

Crystal Growth, Structure and Anisotropic Magnetic Properties of Quasi-2D Materials

DISSERTATION

zur Erlangung des akademischen Grades

Doctor rerum naturalium

(Dr. rer. nat.)

vorgelegt von

M. Sc. Sebastian Selter

geboren am 30.11.1990 in Bietigheim-Bissingen

Institut für Festkörper und Werkstoffforschung, Leibniz IFW Dresden

Fakultät Physik, Bereich Mathematik und Naturwissenschaften,

Technische Universität Dresden

2021

Diese Dissertation wurde in der Zeit von Februar 2017 bis Januar 2021 am Institut für Festkörperforschung des Instituts für Festkörper- und Werkstoffforschung, Leibniz IFW Dresden in der Arbeitsgruppe von Dr. Saicharan Aswartham angefertigt.

Eingereicht am 22.01.2021

Verteidigt am 03.06.2021

Erstgutachter: Prof. Dr. Bernd Büchner
IFW Dresden / TU Dresden
Zweitgutachter: Jun.-Prof. Dr. Anna Isaeva
TU Dresden

Abstract

In this work, the crystal growth as well as structural and magnetic investigations of several metal trichalcogenides compounds with a general formula $M_2X_2Ch_6$ are presented. M stands for a main group metal or transition metal, X is an element of the IV or V main group and Ch is a chalcogen. In particular, these compounds are the phosphorus sulfides $Fe_2P_2S_6$, $Ni_2P_2S_6$ as well as intermediate compounds of the substitution regime $(Fe_{1-x}Ni_x)_2P_2S_6$, the quaternary phosphorus sulfides $CuCrP_2S_6$ and $AgCrP_2S_6$ and the germanium tellurides $Cr_2Ge_2Te_6$ and $In_2Ge_2Te_6$. As members of the metal trichalcogenides, all these compounds have a van der Waals layered honeycomb structure in common. This layered structure in combination with their magnetic properties makes these compounds interesting candidate materials for the production of magnetic monolayers by exfoliation from bulk crystals.

Crystals of the phosphorus sulfides were grown by the chemical vapor transport technique and, for the growth of the germanium tellurides, the self-flux growth technique was used. Crystals of all phases were extensively characterized regarding their morphology, chemical composition and homogeneity as well as regarding their crystal structure. The structural analysis, especially for $Ni_2P_2S_6$, yields insight into details of the stacking order and disorder of the corresponding quasi-two-dimensional layers in the bulk.

Regarding the magnetic properties, both $Fe_2P_2S_6$ and $Ni_2P_2S_6$ order antiferromagnetically but exhibit different magnetic anisotropies (*i.e.* Ising-like anisotropy for $Fe_2P_2S_6$ and XYZ anisotropy for $Ni_2P_2S_6$). In this context, it is surprising to find that compounds in the solid solution regime of $(Fe_{1-x}Ni_x)_2P_2S_6$ up to $x = 0.9$ exhibit an anisotropic magnetic behavior that is comparable to $Fe_2P_2S_6$ and, thus, indicative of Ising-like anisotropy. For $CuCrP_2S_6$ and $AgCrP_2S_6$, the ordering of the two different transition elements on the honeycomb sites yields more complex magnetic structures. The magnetic Cr^{3+} atoms in $CuCrP_2S_6$ order in a triangular arrangement and form an antiferromagnetic ground state with notable ferromagnetic interactions. $AgCrP_2S_6$ exhibits pronounced features of low dimensional magnetism resulting from the (quasi-)one-dimensional stripe-like arrangement of magnetic Cr^{3+} atoms and no onset of long-range magnetic order is unambiguously observed. $Cr_2Ge_2Te_6$ exhibits ferromagnetic order and an anisotropic feature in the temperature dependence of the magnetization. Based on the magnetic phase diagrams for two orientations between the magnetic field and the crystallographic directions, the temperature dependence of the magnetocrystalline anisotropy constant as well as the critical exponents of the magnetic phase transition are extracted. Concluding from this, the magnetic interactions in $Cr_2Ge_2Te_6$ are dominantly of two-dimensional nature and the anisotropy is uniaxial with the before mentioned anisotropic feature resulting from the interplay between magnetocrystalline anisotropy, magnetic field, and temperature. $In_2Ge_2Te_6$ is diamagnetic as to be expected for a closed-shell system.

Additional to the investigations on single crystals, the quasi-binary phase diagram of $(Cu_{1-x}Ag_x)CrP_2S_6$ was investigated for regimes of solid solution behavior based on polycrystalline samples. Accordingly, isostructural substitution is most likely possible in the composition range of $(Cu_{0.25}Ag_{0.75})CrP_2S_6$ to $AgCrP_2S_6$, potentially allowing to tune the magnetic interactions of the Cr sublattice indirectly by substitution on the Cu/Ag sublattice.

Kurzfassung

In dieser Arbeit werden die Kristallzüchtung sowie strukturelle und magnetische Untersuchungen an mehreren Metalltrichalkogenid-Verbindungen mit der allgemeinen Summenformel $M_2X_2Ch_6$ vorgestellt. M steht für ein Hauptgruppen- oder Übergangsmetall, X ist ein Element der IV- oder V-Hauptgruppe und Ch ein Chalkogen. Insbesondere handelt es sich bei diesen Verbindungen um die Phosphorsulfide $Fe_2P_2S_6$, $Ni_2P_2S_6$ sowie um Verbindungen der Substitutionsreihe $(Fe_{1-x}Ni_x)_2P_2S_6$, die quaternären Phosphorsulfide $CuCrP_2S_6$ und $AgCrP_2S_6$ sowie die Germaniumtelluride $Cr_2Ge_2Te_6$ und $In_2Ge_2Te_6$. Als Mitglieder der Metalltrichalkogenide haben alle diese Verbindungen eine van-der-Waals-Schichtstruktur mit Honigwabenmotiv gemein. Diese Schichtstruktur in Kombination mit ihren magnetischen Eigenschaften macht diese Verbindungen zu interessanten Kandidaten für die Herstellung von magnetischen Monolagen durch Exfoliation aus Volumenkristallen.

Kristalle der Phosphorsulfide wurden mit der chemischen Dampfphasentransporttechnik gezüchtet und für die Züchtung der Germaniumtelluride wurde die Selbstflusstechnik verwendet. Die Kristalle aller Phasen wurden sowohl hinsichtlich ihrer Morphologie, chemischen Zusammensetzung und Homogenität als auch hinsichtlich ihrer Kristallstruktur umfassend charakterisiert. Die Strukturanalyse, insbesondere für $Ni_2P_2S_6$, gibt Aufschluss über Details der Stapelordnung und -unordnung der entsprechenden quasizweidimensionalen Schichten im Volumen.

Bezüglich der magnetischen Eigenschaften ordnen sowohl $Fe_2P_2S_6$ als auch $Ni_2P_2S_6$ antiferromagnetisch, zeigen aber unterschiedliche magnetische Anisotropien (d.h. Ising-artige Anisotropie für $Fe_2P_2S_6$ und XYZ-Anisotropie für $Ni_2P_2S_6$). In diesem Zusammenhang ist es überraschend, dass Verbindungen im Mischkristallregime von $(Fe_{1-x}Ni_x)_2P_2S_6$ bis $x = 0.9$ ein anisotropes magnetisches Verhalten zeigen, das mit dem von $Fe_2P_2S_6$ vergleichbar ist und daher auf Ising-artige Anisotropie hindeutet. Bei $CuCrP_2S_6$ und $AgCrP_2S_6$ führt die Anordnung der beiden unterschiedlichen Übergangselemente auf den Gitterplätzen der Wabenstruktur zu komplexeren magnetischen Strukturen. Die magnetischen Cr^{3+} -Atome in $CuCrP_2S_6$ ordnen sich in einer Dreiecksanordnung an und bilden einen antiferromagnetischen Grundzustand mit ausgeprägten ferromagnetischen Wechselwirkungen. $AgCrP_2S_6$ weist deutliche Merkmale von niederdimensionalem Magnetismus auf, welche aus der (quasi-)eindimensionalen, streifenartigen Anordnung der magnetischen Cr^{3+} -Atome resultieren, und das Einsetzen von langreichweitiger magnetischer Ordnung kann nicht eindeutig beobachtet werden. $Cr_2Ge_2Te_6$ weist ferromagnetische Ordnung und einen anisotropen Verlauf der Temperaturabhängigkeit der Magnetisierung auf. Anhand von magnetischen Phasendiagrammen für zwei Orientierungen zwischen Magnetfeld und kristallographischen Richtungen wurden die Temperaturabhängigkeit der magnetokristallinen Anisotropiekonstante sowie die kritischen Exponenten des magnetischen Phasenübergangs extrahiert. Hieraus ergibt sich, dass die magnetischen Wechselwirkungen in $Cr_2Ge_2Te_6$ überwiegend zweidimensionaler Natur sind und die Anisotropie uniaxial ist, wobei der zuvor erwähnte anisotrope Verlauf aus dem Zusammenspiel von magnetokristalliner Anisotropie, Magnetfeld und Temperatur resultiert. $In_2Ge_2Te_6$ ist diamagnetisch, wie es für ein System mit geschlossener Schale zu erwarten ist.

Zusätzlich zu den Untersuchungen an Einkristallen wurde das quasibinäre Phasendiagramm von $(Cu_{1-x}Ag_x)CrP_2S_6$ anhand von polykristallinen Proben auf Bereiche mit Mischkristallverhalten hin untersucht. Folglich ist eine isostrukturelle Substitution höchstwahrscheinlich im Zusammensetzungsbereich von $(Cu_{0.25}Ag_{0.75})CrP_2S_6$ bis $AgCrP_2S_6$ möglich, was es erlauben könnte, die magnetischen Wechselwirkungen des Cr-Untergitters indirekt durch Substitution auf dem Cu/Ag-Untergitter zu beeinflussen.

Contents

1. Introduction	1
1.1. $M_2X_2Ch_6$ Class of Materials	4
1.2. Magnetism in Solid State Materials	8
1.2.1. Diamagnetism	11
1.2.2. Paramagnetism	11
1.2.3. Cooperative Magnetism	13
1.2.4. Magnetic Anisotropy	21
1.2.5. Magnetism in $D < 3$	23
1.2.6. Critical Exponents	24
2. Methods	27
2.1. Synthesis and Crystal Growth	27
2.1.1. Solid State Synthesis	28
2.1.2. Crystal Growth <i>via</i> the Liquid Phase	29
2.1.3. Crystal Growth <i>via</i> the Vapor Phase	31
2.2. X-ray Diffraction	32
2.2.1. Single Crystal X-ray Diffraction	36
2.2.2. Powder X-ray Diffraction	37
2.3. Scanning Electron Microscopy and Energy Dispersive X-ray Spectroscopy	39
2.3.1. Scanning Electron Microscopy	40
2.3.2. Energy Dispersive X-ray Spectroscopy	42
2.4. Magnetometry	44
2.5. Nuclear Magnetic Resonance Spectroscopy	45
2.6. Specific Heat Capacity	46
3. $M_2P_2S_6$	49
3.1. $Ni_2P_2S_6$	50
3.1.1. Crystal Growth	52
3.1.2. Characterization	53
3.1.3. Magnetic Properties	62
3.1.4. ^{31}P -NMR Spectroscopy	66
3.1.5. Stacking (Dis-)Order in $Ni_2P_2S_6$	68
3.2. $(Fe_{1-x}Ni_x)_2P_2S_6$	72
3.2.1. Synthesis and Crystal Growth	73
3.2.2. Characterization	75
3.2.3. Evolution of Magnetic Properties	79
3.3. Summary and Outlook	90

4. $M^{1+}CrP_2S_6$	93
4.1. $CuCrP_2S_6$	96
4.1.1. Crystal Growth	96
4.1.2. Characterization	97
4.1.3. Magnetic Properties	102
4.2. $AgCrP_2S_6$	106
4.2.1. Crystal Growth	106
4.2.2. Characterization	107
4.2.3. Magnetic Properties	111
4.3. Polycrystalline $(Cu_{1-x}Ag_x)CrP_2S_6$	116
4.3.1. Synthesis	116
4.3.2. Phase Analysis	117
4.4. Summary and Outlook	127
5. $M_2(Ge,Si)_2Te_6$	131
5.1. $Cr_2Ge_2Te_6$	131
5.1.1. Crystal Growth	134
5.1.2. Characterization	134
5.1.3. Magnetic Properties	137
5.1.4. Analysis of the Critical Behavior	149
5.2. $In_2Ge_2Te_6$	155
5.2.1. Crystal Growth	155
5.2.2. Characterization	157
5.2.3. Magnetic Properties	160
5.2.4. Specific Heat	161
5.3. Summary and Outlook	163
6. Conclusion	165
Bibliography	167
List of Publications	177
Acknowledgements	179
Eidesstattliche Erklärung	181
A. Appendix	A.1
A.1. Scanning Electron Microscopic Images	A.1
A.1.1. $(Fe_{1-x}Ni_x)_2P_2S_6$	A.1
A.2. scXRD	A.3
A.2.1. $(Fe_{1-x}Ni_x)_2P_2S_6$	A.3

1. Introduction

In 2004, Novoselov and Geim *et al.* reported the experimental discovery of graphene, a stable modification of carbon in atomically thin layers [1], as illustrated in Fig. 1.1. Until then, atomically thin layers were thought to be thermodynamically unstable following from the Mermin-Wagner theorem (and its variants) [2–4], according to which long-range order cannot be stable for an isotropic two-dimensional (2D) system. However, the discovery of graphene demonstrated that stable 2D systems can be realized, which is attributed to crumpling of the layers or interactions with a substrate [5, 6]. The importance of this finding for the scientific community is likely best illustrated by the fact that Novoselov and Geim received the Nobel price in physics 'for groundbreaking experiments regarding the two-dimensional material graphene' in 2010 [7] – only six years after the publication of their initial report on graphene.

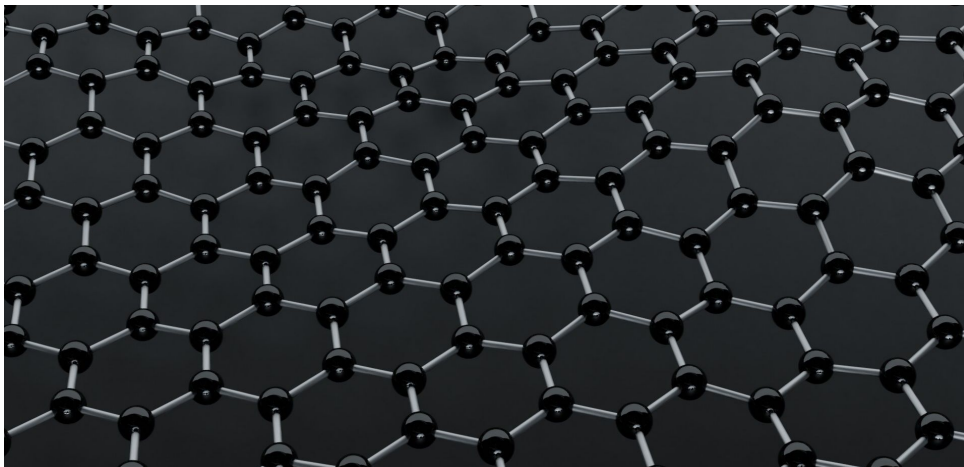


Fig. 1.1.: Illustration of the structure of graphene (*i.e.* a monolayer of graphite). Graphic created with Blender (v2.9) [8].

The discovery of graphene motivated a whole new field in solid state science dealing with monolayer materials, their properties and potential applications [9–12]. Several families of 2D materials were subsequently found, isolated and investigated [13, 14]. Special attention was given to the electronic properties of these materials [15], as the electronic structure in the monolayer limit is affected by quantum confinement along one dimension [16–18]. This yielded a plethora of monolayer materials with different electronic properties, including metals, semimetals, topological insulators, semiconductors and insulators [19–24]. Furthermore, more complex electronic phenomena such as superconductivity, charge density wave or Mott-insulating states could be observed in these 2D materials [25–27]. The combination of materials with different properties in heterostructures is promising to yield new physical effects and develop new devices [9, 28].

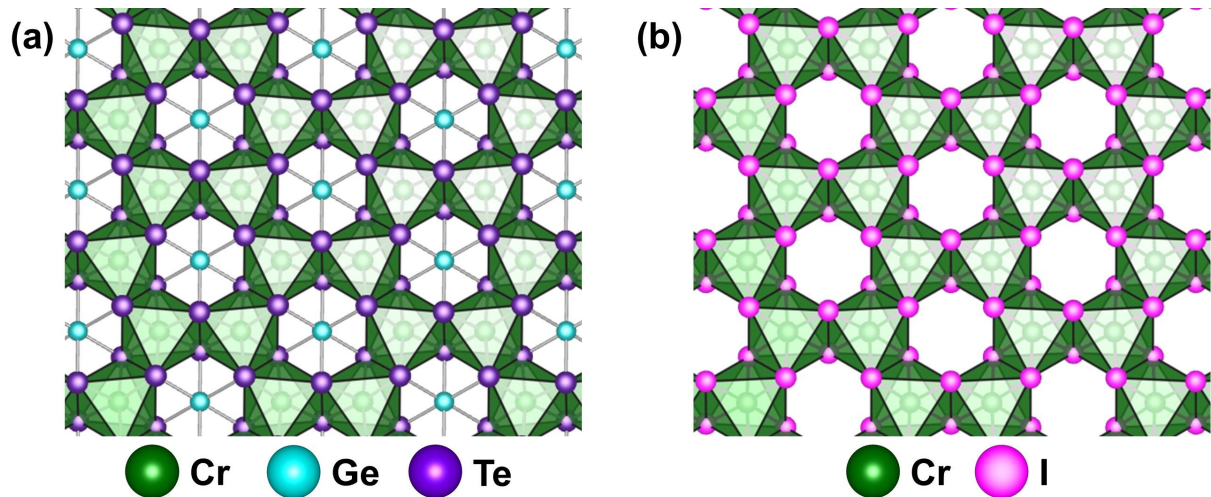


Fig. 1.2.: Perspective drawing of a layer of (a) $\text{Cr}_2\text{Ge}_2\text{Te}_6$ and (b) CrI_3 with view perpendicular to the layer illustrating a honeycomb structure similar to graphene. Structural data according to Carteaux *et al.* [37] and McGuire *et al.* [38].

Over a decade after the discovery of stable monolayers, the realization and subsequent investigation of magnetic monolayer materials became a rapidly growing research area within the 2D materials research. To a substantial part, this is due to the experimental detection of long range ferromagnetic order in atomically thin samples of $\text{Cr}_2\text{Ge}_2\text{Te}_6$ [29] and CrI_3 [30] in 2017 and the potential application of such ferromagnetic monolayers in devices and heterostructures [31–36]. The structure of these two compounds is shown in Fig. 1.2.

In general, materials that exhibit a structure of charge neutral layers in the bulk are suitable to yield monolayer samples in a top-down approach, in analogy to the preparation of graphene from graphite. In the bulk, such layers typically interact only *via* weak van der Waals forces with each other. Consequently, bulk crystals are readily thinned down, potentially to the monolayer, by mechanical or chemical exfoliation [13, 24, 39, 40]. Thus, bulk materials consisting of such layers moved in the focus of research. To additionally exhibit magnetic order, the material has to contain magnetic transition element or rare earth ions [32].

The metal trichalcogenides of the general formula $M_2X_2Ch_6$ (M is a main group metal or transition metal, X is an element of the IV or V main group and Ch is a chalcogen) are a class of compounds exhibiting both a layered structure and containing a wide range of different transition element ions [41, 42]. As all members of the metal trichalcogenides share virtually the same structure in the layer, compounds of this class became model systems to study the influence of different transition metals on 2D magnetism [43]. Additionally, physical properties can be tuned by chemical substitution and physical pressure in metal trichalcogenides compounds.

Regarding 2D magnetism, a property that is of particular interest is the magnetic anisotropy, as it determines the stability of magnetic order on the monolayer. Similar to 2D structural order, magnetic order in 2D may be expected to break down following the Mermin-Wagner theorem [2]. However, this theorem is only valid for isotropic systems and, thus, magnetic anisotropy can stabilize long-range magnetic order in 2D [29, 32]. As an example, illustrat-

ing the role of magnetic anisotropy on the stability of the magnetic order in 2D, magnetic order is experimentally observed for a monolayer of the magnetically strongly anisotropic $\text{Fe}_2\text{P}_2\text{S}_6$ [44], while the bulk magnetic order breaks down for a monolayer of the isostructural but weakly anisotropic $\text{Ni}_2\text{P}_2\text{S}_6$ [45]. For a particular magnetic anisotropy of intermediate strength which can be described by the XY model, a special kind of disordered ground state is expected to be stabilized in 2D systems due to fluctuations described in the Mermin-Wagner theorem. This state is predicted to be accessed *via* a phase transition from the paramagnetic (disordered) state, which is unusual as the transition describes a disorder–disorder transition and, thus, is of topological nature. The prediction and description of such a phase transition and the corresponding states is part of the work of Thouless and Kosterlitz [46, 47] for which they received the Nobel price in physics in 2016 together with Haldane – ‘for theoretical discoveries of topological phase transitions and topological phases of matter’ [48].

This work focuses on different compounds of the class of metal trichalcogenides, namely $\text{Fe}_2\text{P}_2\text{S}_6$, $\text{Ni}_2\text{P}_2\text{S}_6$, CuCrP_2S_6 , AgCrP_2S_6 , $\text{Cr}_2\text{Ge}_2\text{Te}_6$ and $\text{In}_2\text{Ge}_2\text{Te}_6$, as well as the substitution series $(\text{Fe}_{1-x}\text{Ni}_x)_2\text{P}_2\text{S}_6$ and $(\text{Cu}_{1-x}\text{Ag}_x)\text{CrP}_2\text{S}_6$. The conditions for the growth of bulk crystals were investigated and optimized. As exfoliation of such bulk crystals is one of the suitable ways to produce monolayer samples, reliable and reproducible crystal growth conditions are essential. Crystals were extensively characterized to ensure a good crystal quality. Furthermore, the crystal structure and its defects were investigated to obtain a better understanding of the interactions in the structural layers as well as between adjacent layers. The magnetic properties were studied directly on the bulk crystals. Due to the absence of covalent bonds between the layers, no significant interlayer magnetic exchange is expected in such a crystal. Thus, even bulk crystals exhibit characteristic features of 2D magnetism. Furthermore, the material-specific contribution to the magnetic anisotropy (*i.e.* the magnetocrystalline anisotropy) is independent of the dimensionality of the sample. Consequently, the magnetic anisotropy is studied in bulk samples to identify compounds with a suitable magnetic anisotropy for monolayer magnetism. The specific compounds are introduced in more detail in the beginning of the experimental chapters, as listed in the following paragraph.

This work is structured as follows: Hereafter, the introduction chapter continues with the introduction of the class of metal trichalcogenides in more detail regarding structure and properties (Sect. 1.1) and a general introduction to magnetic phenomena in solid state materials (Sect. 1.2). The methods and techniques used in this work for synthesis, crystal growth, characterization and physical measurements are introduced in Chapter 2. Subsequently, the main experimental findings of this work are presented in Chapter 3 for the results on the $M_2\text{P}_2\text{S}_6$ compounds, *i.e.* $\text{Ni}_2\text{P}_2\text{S}_6$ and the substitution series $(\text{Fe}_{1-x}\text{Ni}_x)_2\text{P}_2\text{S}_6$, in Chapter 4 for the results on the $M^{1+}\text{CrP}_2\text{S}_6$ compounds, *i.e.* CuCrP_2S_6 , AgCrP_2S_6 and the substitution series $(\text{Cu}_{1-x}\text{Ag}_x)\text{CrP}_2\text{S}_6$, and in Chapter 5 for the results on the $M_2\text{Ge}_2\text{Te}_6$ compounds, *i.e.* $\text{Cr}_2\text{Ge}_2\text{Te}_6$ and $\text{In}_2\text{Ge}_2\text{Te}_6$. The main results of this work are shortly summarized and concluded in Chapter 6.

1.1. $M_2X_2Ch_6$ Class of Materials

The compounds investigated in this work belong to the class of metal trichalcogenides. Members of this class exhibit a general formula of $M_2X_2Ch_6$ with M being a 2+ main group metal or transition metal and $Ch = S, Se$ for $X = P$, or M being a 3+ metal and $Ch = Te$ for $X = Si, Ge$ [41, 42].

Although X may either be a group IV or group V element with the oxidation state of M adapting accordingly to ensure charge neutrality, all members of this class of materials share a specific structural motif: a X_2 dumbbell octahedrally coordinated by six Ch atoms. This X_2Ch_6 structural unit exhibits interatomic distances that imply covalent $X-X$ and $X-Ch$ bonding. The notation of the chemical formula as $M_2X_2Ch_6$ rather than as $MXCh_3$, as frequently found in literature, expresses the existence of such covalent X_2Ch_6 units in these compounds. In the plane perpendicular to the bond axis of the X_2 dumbbell and through its center of mass, this covalent unit is surrounded by six M atoms forming a hexagon. The M atoms interact with the X_2Ch_6 unit mainly by ionic bonding *via* the Ch atoms. *Vice versa*, each M atom is surrounded by a hexagon of three other M atoms and three X_2Ch_6 units, which results in a honeycomb patterned layer of M with each void occupied by a X_2Ch_6 unit. Such layers are stacked on top of each other with relatively large gaps in between them (*i.e.* van der Waals gaps, as shown in Fig. 1.3), such that adjacent layers interact only *via* weak van der Waals interactions.

Following from this general bonding behavior, the metal trichalcogenides are best understood as $M_2^{2+} [P_2S_6]^{4-}$ and $M_2^{3+} [(Si,Ge)_2Te_6]^{6-}$ regarding their oxidation states. Consequently, these compounds may be described as salts of the hypothetical hexathiohypodiphosphoric acid $H_4P_2S_6$ with divalent cations and of the equally hypothetical hexatellurohypodisilicic and -hypodigermanic acids $H_6(Si,Ge)_2Te_6$ with trivalent cations [49].

This type of structure descends from the structural aristotype CdI_2 in agreement with Seidlmayer [51]. CdI_2 in the space group $P\bar{3}m1$ (No. 164) [52] forms hexagonal closed packed layers of I with the octahedral sites of every second interlayer being fully occupied by Cd. Such CdI_2 layers are stacked on top of each other without any shift between layers (AA stacking). Consequently, the high-symmetry crystal structure of CdI_2 can be understood as idealized parent structure of all metal trichalcogenides with their different space groups being subgroups of the CdI_2 space group. An introduction to the group theory for crystallographic considerations can be found in Ref. [53]. The group-subgroup relationship as well as the relationship between the different structures in the different space groups is illustrated in Fig. 1.3 and 1.4, following the Bärnighausen formalism, and discussed in the following paragraphs.

Compounds of the $Al_2Si_2Te_6$ structure type ($P\bar{3}$; No. 147) [54] exhibit the same hexagonal closed packed layers as CdI_2 but with a chalcogen Ch instead of I. The octahedral sites of every second interlayer are again fully occupied, in this case by 1/3 X_2 dumbbells (*i.e.* the center of mass of the dumbbells is located on the octahedral site) and 2/3 M atoms. In particular, X_2 and M sites order such that each M octahedral site is surrounded by three octahedral sites with X_2 dumbbells and three sites occupied by M , while every X_2 octahedral site is surrounded by six M octahedral sites. This ordering breaks the mirror symmetry of the layers in the CdI_2

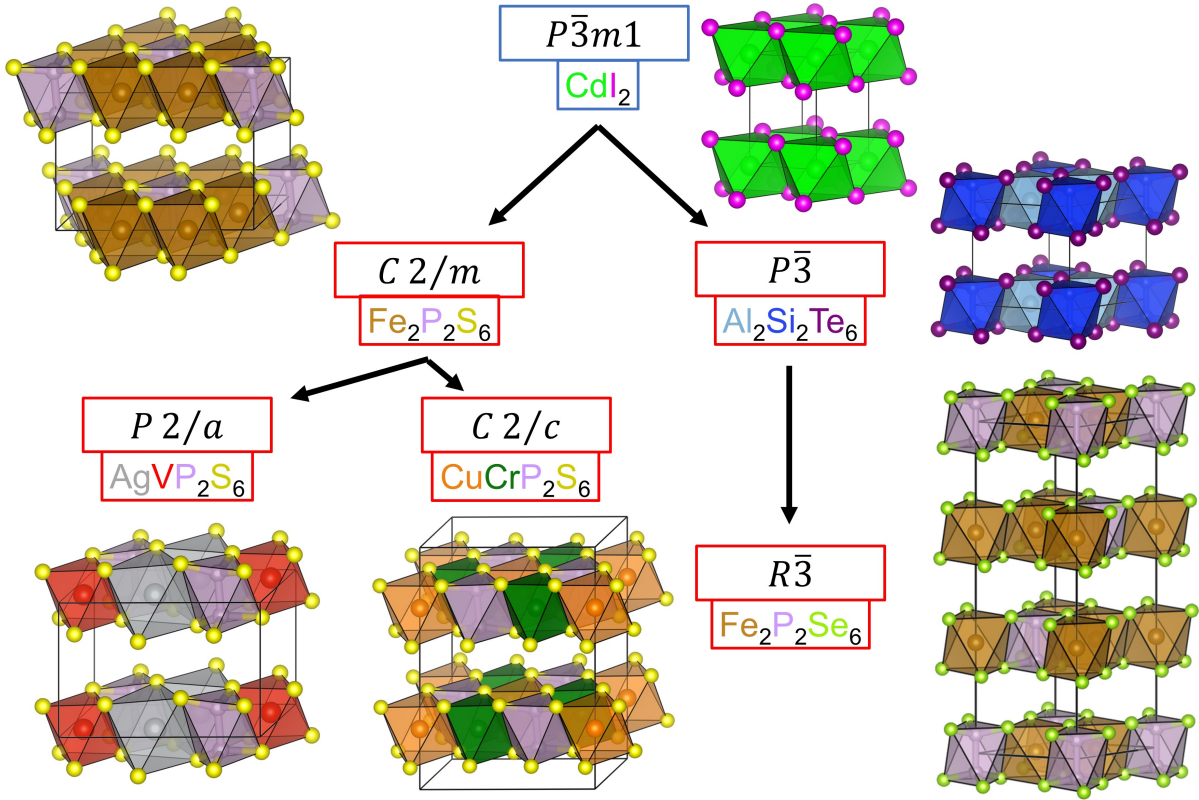


Fig. 1.3.: Graphical illustration of the structural relationship between the CdI_2 structure type in the $P\bar{3}m1$ space group and the different structure types of the metal trichalcogenides. The colors of the atoms corresponds to the colors in Fig. 1.4.

structure and , subsequently, causes a larger unit cell in the in-plane directions, containing three octahedral sites instead of one.

Compounds of the $Fe_2P_2Se_6$ structure type ($R\bar{3}$; No. 148) [55] exhibit the same atomic structure in the layers as the $Al_2Si_2Te_6$ type compounds but ABC stacking (*i.e.* a shift of $1/3a$ and $1/3b$ between adjacent layers) instead of AA stacking. By changing the centering of the space group from primitive to rhombohedral, a three-fold screw axis is obtained. This screw axis together with a tripling of the c parameter and the adjustment of the atomic parameters ensures the ABC stacking in the crystal structure of the $Fe_2P_2Se_6$ structure type.

The $Fe_2P_2S_6$ type compounds exhibit again the same structure of the layer as observed in the $Al_2Si_2Te_6$ structure type. The stacking of layers in these sulfides is similar to the ABC stacking in the $Fe_2P_2Se_6$ structure type. However, the periodicity in c direction is not exactly three layers (as expected for ABC stacking) but differs slightly. The corresponding description yielding the smallest possible unit cell is in the monoclinic space group $C2/m$ (No. 12) [55]. As the angle β between the base plane in ab and the stacking direction c is variable in the monoclinic space group, the relatively small deviations from the ideal ABC stacking can be well accounted for. In particular, $c \cos(\beta)$ defines the distance between layers c^* and $c \sin(\beta)$ defines the shift between adjacent layers along the a direction. The monoclinic space group $C2/m$ is neither a subgroup of the $R\bar{3}$ space group nor of the $P\bar{3}$ space group. Yet it is a subgroup of the $P\bar{3}m1$ space group, demonstrating the important role of the aristotype CdI_2

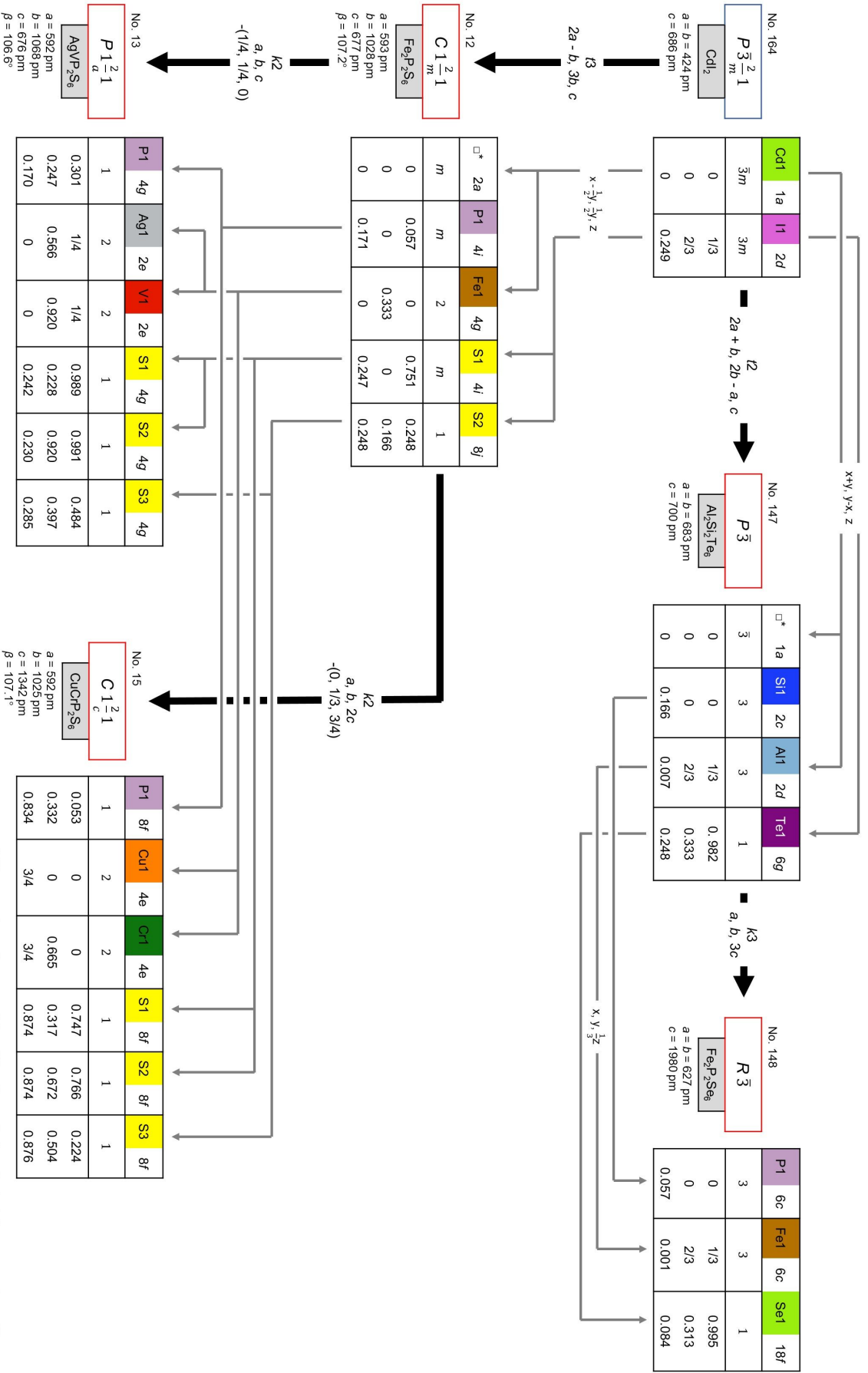


Fig. 1.4.: Bärnighausen diagram demonstrating the structural relationship between the CdI_2 structure type and the structure types of the metal trichalcogenides. The colors for the different atoms correspond to the perspective drawings in Fig. 1.3. The notation on the black arrows between the different space groups indicates the nature of subgroup (i.e. t for 'translationsgleich' and k for 'klassengleich') according to the International Tables of Crystallography [50] followed by the index of the subgroup as well as changes of the lattice parameter and shifts of the origin.

for understanding the structural relationships. The changes of the lattice parameter and the atomic positions between the CdI_2 structure type and the $Fe_2P_2S_6$ structure type are attributed to the change of the crystal system from hexagonal to monoclinic. Furthermore, as the $C2/m$ space group does not contain any threefold rotation axis, two sites are necessary to describe the hexagonal closed packed Ch layer.

A special case for the $M_2P_2S_6$ compounds is observed for M^{2+} being replaced by $M_{0.5}^{1+}M_{0.5}^{3+}$. In such compounds, M^{1+} and M^{3+} either order in stripes or triangular on the honeycomb lattice of M . The driving force for the triangular sublattice arrangement is an optimal separation and distribution of the metal ions regarding the different oxidation states, while the stripe arrangement follows from the minimization of the lattice deformation for notably different ionic sizes of the 1+ and 3+ ions (*i.e.* chemical pressure), as discussed by Brec in more detail [56]. The stripe-like sublattice order violates the mirror symmetry of the $C2/m$ space group parallel to the b direction. Consequently, a unit cell in the space group $P2/a$ (No. 13) is observed, *e.g.*, for $AgVP_2S_6$ [57]. As the mirror symmetry is lost, an additional sulfur position is necessary to describe the sulfur layer. For $CuCrP_2S_6$, Cu and Cr form a triangular arrangement which as well violates the mirror symmetry of the $C2/m$ space group. Additionally, $CuCrP_2S_6$ exhibits an AB stacking with regard to the monoclinic c direction, such that a unit cell in the space group $C2/c$ (No. 15) is found [58].

Following from the common aristotype, all members of the class of metal trichalcogenides share several structural motifs, although they exhibit different space group symmetries. These common structural motifs go along with several physical properties that are comparable between different metal trichalcogenides. As all these structures have a van der Waals gap between adjacent layers, corresponding metal trichalcogenides crystals are ductile and can be easily exfoliated. For some compounds the preparation of monolayer samples by exfoliation was already achieved [44, 45, 59]. Besides these common mechanical properties, metal trichalcogenides are insulators or broad-band semiconductors [37, 41, 42, 60]. The electronic properties of $M_2P_2S_6$ are discussed in the context of Mott insulators and pressure-induced Mott transitions could be observed in some compounds (*e.g.* $V_{1.8}P_2S_6$ [61], $Mn_2P_2S_6$ [62] and $Fe_2P_2S_6$ [63, 64]). A similar scenario is conceivable for the other members of the metal trichalcogenides. With M being a magnetic ion (as explained in Sect. 1.2), the metal chalcogenides exhibit long range magnetic order [41, 42]. While most metal trichalcogenides order antiferromagnetically, some members exhibit ferromagnetic order (such as $Cr_2Ge_2Te_6$) [37]. As the investigation of magnetic properties of some metal trichalcogenides is one focus of this work, details regarding the magnetic properties are discussed in the corresponding introductions to the specific materials at the beginning of each experimental chapter.

1.2. Magnetism in Solid State Materials

The macroscopic magnetic properties of solid state materials originate from the microscopic magnetic moments of atoms. These magnetic moments are, in turn, related to the total angular momentum \mathbf{J} , which is non-zero for atoms with partly filled electron orbitals [65, 66]. \mathbf{J} contains contributions of the orbital angular momentum \mathbf{l}_i and the spin \mathbf{s}_i (i.e. the 'intrinsic angular momentum') of the electrons in these partly filled orbitals. These angular momenta are expressed in units of the reduced Plank constant \hbar , as usual in the literature. The total angular momentum operator $\hat{\mathbf{J}}$ is related to the corresponding quantum number J by Eq. 1.1 and its z component \hat{J}_z (z being defined as the direction of quantization) to its quantum number m_J by Eq. 1.2 with Ψ being the wavefunction of the electron.

$$\hat{\mathbf{J}}^2 \Psi = J(J + 1) \Psi \quad (1.1)$$

$$\hat{J}_z \Psi = m_J \Psi \quad (1.2)$$

Analogous equations relate $\hat{\mathbf{l}}_i$ and $\hat{l}_{i,z}$ to the quantum numbers l and m_l as well as $\hat{\mathbf{s}}_i$ and $\hat{s}_{i,z}$ to the quantum numbers s and m_s . These quantum numbers, together with the primary quantum number n define the electron orbital states in an atom, such that every electron of an atom can be uniquely addressed by its full set of quantum numbers, as shown in Table 1.1.

Fundamentally, the orbital occupation of an atom is determined by the orbital occupation rules, *i.e.* the aufbau principle (or Madlung rule), the Pauli exclusion principle and Hund's rule of maximum multiplicity [67], which consequently severely influence if an atom or ion is magnetic. In this line, closed shell ions like main group ions, strictly following the octet rule, or, *e.g.*, Cu^+ ($[\text{Ar}] 3d^{10}$; closed d subshell) are non-magnetic, while several magnetic ions of the d elements and the rare earth elements with stable oxidation states containing singly occupied d and f orbitals exist.

Additionally in solid state materials, atoms are not isolated but form a crystalline lattice. Assuming the interatomic interactions in such a lattice are well expressed by ionic interactions, the crystal field theory describes the electrostatic influence of an anionic coordination environment of a certain symmetry on the orbital energies of a central cation. Consequently, orbital degeneracies of the highest occupied orbital shell may be lifted which, in turn, can result in a different orbital occupation than expected for an isolated cation in vacuum.

Table 1.1.: Quantum numbers describing an electron in an atom.

Number	Symbol	Possible Values
Principal Quantum Number	n	1, 2, 3, 4, ...
Angular Moment Quantum Number	l	0, 1, 2, 3, ..., $(n - 1)$
Magnetic Quantum Number	m_l	$-l, \dots, -1, 0, 1, \dots, l$
Spin Quantum Number	m_s	$+1/2, -1/2$

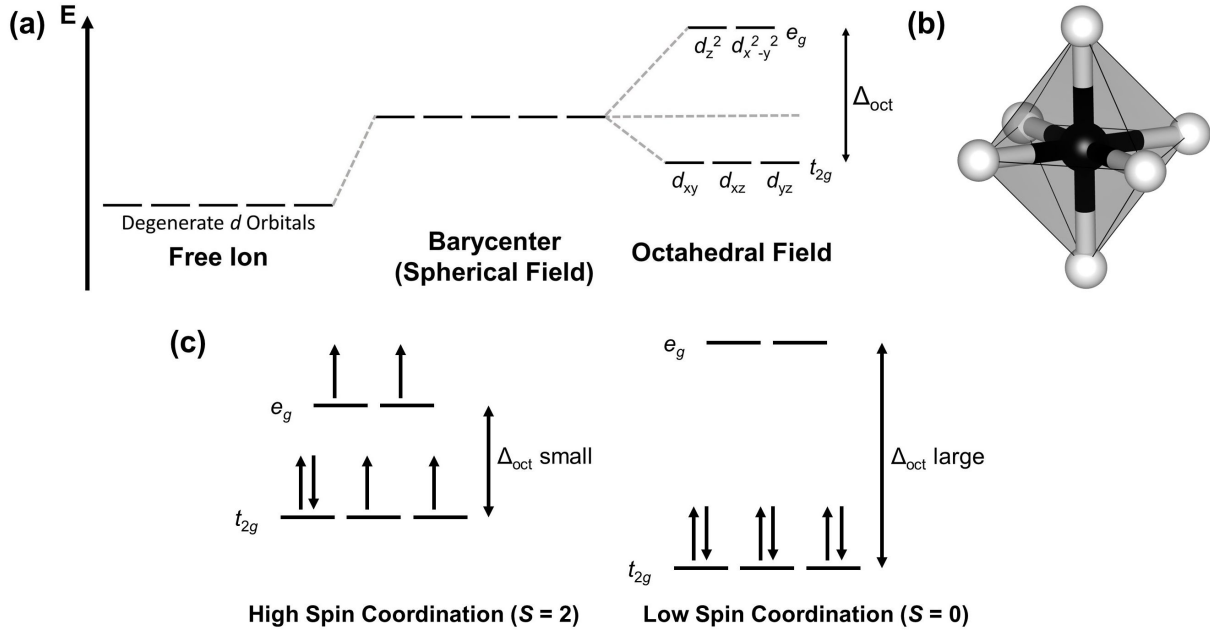


Fig. 1.5.: (a) Crystal field scheme illustrating the effect of the ligand electric field on the d orbital energies of an octahedrally coordinated ion, as shown in (b). (c) d orbital occupation for a electronic $[\text{Ar}] 3d^6$ configuration, as for example observed for Fe^{2+} , assuming octahedral coordination with a small crystal field energy Δ (left) and a large crystal field energy Δ (right).

For example, Fig. 1.5(b) shows an cation of an d element in a octahedral coordination environment, *i.e.* the ligands are located along the x , y and z directions. Consequently, the energy of d orbitals with a strong component of these directions (being the d_{z^2} and $d_{x^2-y^2}$ orbitals) is lifted, while the other orbital energies are lowered, as illustrated in Fig. 1.5(a). The energy difference Δ between the orbitals with lowered and lifted energies is affected by several parameters, such as the nature of the cation and its charge, the arrangement of the coordination environment as well as the nature and number of ligands. If the splitting Δ is sufficiently small, all orbitals of the subshell are first occupied singly, in agreement with Hund's rule of maximum multiplicity. Such complex is called high spin. However, if Δ is larger than the energy necessary to pair electrons in an orbital, first the lower lying orbitals are doubly occupied before the higher orbitals are filled. This configuration is called low spin. For example for Fe^{2+} , Δ decides if unpaired electrons are present or not, as illustrated in Fig. 1.5(c).

The coupling between s_i and l_i of separate electrons to yield \mathbf{J} for the complete ensemble of unpaired electrons of an atom is determined by the strength of the spin-orbit coupling relative to the electrostatic interaction between an electron, the nucleus and the other electrons of the atom. If the spin-orbit coupling is weak compared to the electrostatic interactions, first a total spin $\mathbf{S} = \sum_i \mathbf{s}_i$ and a total orbital angular momentum $\mathbf{L} = \sum_i \mathbf{l}_i$ are formed. These total angular momenta are subsequently coupled to yield $\mathbf{J} = \mathbf{L} + \mathbf{S}$, with its quantum number J taking values of $|L-S|$ to $|L+S|$ (L and S are the quantum numbers of the corresponding total angular momenta). This coupling scheme is called LS coupling. If the spin-orbit coupling in an atom becomes comparable in strength to its electrostatic interactions, the coupling follows another scheme, called jj coupling. As the spin-orbit coupling strength scales with the atomic number Z , the latter scheme is applicable for heavy elements (*i.e.* rare earth elements or $5d$

transition elements). As the compounds in this work exclusively contain magnetic atoms of the relatively light $3d$ transition elements, the LS coupling scheme is assumed.

The relation between the total angular momentum \mathbf{J} and the corresponding total magnetic dipole moment $\boldsymbol{\mu}_J$ of an atom is shown in Eq. 1.3 with the Landé g -factor g_J and the Bohr magneton $\mu_B = \frac{e\hbar}{2m_e}$ with the elementary charge e , the reduced Planck constant \hbar and the electron rest mass m_e . The Landé g -factor g_J is given by Eq. 1.4. The electron orbital angular g -factor g_L is equal to one, while the spin g -factor deviates with $g_S \approx 2.002$ from the ideal value of two obtained from the Dirac equation due to quantum electrodynamical corrections already for the free electron [65]. With the approximation of $g_S = 2$, Eq. 1.4 simplifies to Eq. 1.5.

$$\boldsymbol{\mu}_J = g_J \mu_B \mathbf{J} \quad (1.3)$$

$$g_J = g_L \frac{J(J+1) - S(S+1) + L(L+1)}{2J(J+1)} + g_S \frac{J(J+1) + S(S+1) - L(L+1)}{2J(J+1)} \quad (1.4)$$

$$g_J(g_L = 1, g_S = 2) \approx \frac{3}{2} + \frac{S(S+1) - L(L+1)}{2J(J+1)} \quad (1.5)$$

For a macroscopic sample, the distribution of magnetic moments $\boldsymbol{\mu}_J$ in the sample volume is expressed by the magnetization vector field \mathbf{M} according to Eq. 1.6. The relation between \mathbf{M} , an external magnetic field \mathbf{H} and the magnetic flux density \mathbf{B} is given in Eq. 1.7 with $\mu_0 = 4\pi \times 10^{-7}$ H/m being the permeability of vacuum. The direction of the magnetic field \mathbf{H} with the magnitude $H = |\mathbf{H}|$ defines the direction of quantization and, thus, the z direction of the corresponding coordinate system. For systems with isolated spins (*i.e.* spins are not interacting with each other), usually a linear relation between \mathbf{M} and \mathbf{H} is observed, as in Eq. 1.8, with χ being the magnetic susceptibility. The z component of \mathbf{M} and \mathbf{B} along the direction of quantization (*i.e.* $\parallel \mathbf{H}$) is typically referred to simply as M and B .

$$\boldsymbol{\mu}_J = \iiint \mathbf{M} dV \quad (1.6)$$

$$\mathbf{B} = \mu_0(\mathbf{H} + \mathbf{M}) \quad (1.7)$$

$$\mathbf{M} = \chi \mathbf{H} \quad (1.8)$$

The interaction of a magnetic moment with an external field is given by the Zeeman effect describing the splitting of electronic energy levels in a magnetic field. In this line, the perturbation of the Hamiltonian $\hat{\mathcal{H}}_0$ of the electron system of an atom by the application of a magnetic field is shown in Eq. 1.9 with the constants introduced before and \mathbf{r}_i corresponding to the position of the i^{th} electron of the atom.

$$\hat{\mathcal{H}} = \hat{\mathcal{H}}_0 + \underbrace{\mu_B g_J \mathbf{J} \cdot \mathbf{B}}_{\hat{\mathcal{H}}_{\text{para}}} + \underbrace{\frac{e^2}{8m_e} \sum_i (\mathbf{B} \times \mathbf{r}_i)^2}_{\hat{\mathcal{H}}_{\text{dia}} > 0} \quad (1.9)$$

$\hat{\mathcal{H}}_{\text{para}}$ corresponds to the paramagnetic moment (discussed in Sect. 1.2.2). For the optimal orientation between the magnetic moment and the external field, the scalar product becomes negative and $\hat{\mathcal{H}}_{\text{para}}$ causes a reduction of energy. In contrast, $\hat{\mathcal{H}}_{\text{dia}}$, which corresponds to the field induced diamagnetic moment (discussed in Sect. 1.2.1), is always positive yielding an energy increase. Typically, $\hat{\mathcal{H}}_{\text{para}}$ is the dominant perturbation of $\hat{\mathcal{H}}_0$. However for specific cases, such as $\mathbf{L} = \mathbf{S} = 0$, $\hat{\mathcal{H}}_{\text{para}}$ vanishes and the perturbation is caused purely by $\hat{\mathcal{H}}_{\text{dia}}$ [65].

1.2.1. Diamagnetism

For compounds without unpaired electrons, no interaction with an external magnetic field may be expected, as $\mathbf{J} = 0$. However, typically such systems exhibit a negative magnetic response of χ to the application of a magnetic field, which is caused by diamagnetism. The classical explanation of this effect is that the magnetic field induces loop currents in the electron orbitals which in turn give rise to a magnetic moment which opposes the magnetic field. However, the Bohr-van Leeuwen theorem demonstrates that magnetism is a quantum mechanical effect which cannot be explained by classical mechanics. The quantum mechanical derivation (as *e.g.* presented in Ref. [65]) yields Eq. 1.10 with N ions per volume V , the elementary charge e , the vacuum permeability μ_0 , the electron rest mass m_e and $\langle r^2 \rangle$ being the mean square distance between electrons and nucleus. The same prediction was obtained by Langevin using classical mechanics.

$$\chi = -\frac{N}{V} \frac{e^2 \mu_0}{6m_e} \sum_{i=1}^Z \langle r^2 \rangle \quad (1.10)$$

Consequently, the diamagnetic susceptibility is expected to be negative and temperature independent. In fact, such a contribution is present in all materials and not just in closed shell systems. However, the diamagnetic susceptibility is usually weak compared to other contributions and therefore only clearly observable in systems without unpaired spins due to the lack of other magnetic interactions.

1.2.2. Paramagnetism

For systems containing atoms with unpaired electrons (*i.e.* $\mathbf{J} > 0$), the magnetic moments align with the external magnetic field to reduce the systems energy (as observed based on $\hat{\mathcal{H}}_{\text{para}}$ in Eq. 1.9) while thermal fluctuations disturb the field induced order. The correspondingly expected dependence of the paramagnetic susceptibility χ_{para} on temperature and magnetic

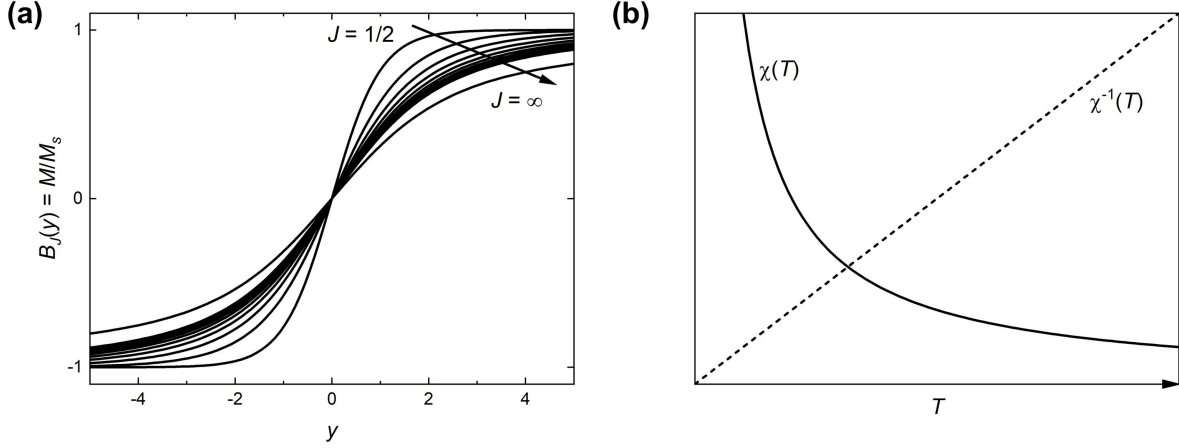


Fig. 1.6.: (a) The evolution of the Brillouin function $B_J(y)$ for several total magnetic quantum numbers $J = 1/2, 1, 3/2, \dots, \infty$. (b) Evolution of the susceptibility and inverse susceptibility of a paramagnet according to the Curie law.

field is given by Eq. 1.11, which can be derived based on the partition function of $\hat{\mathcal{H}}_{\text{para}}$ and the relation between M , B and the free energy F as demonstrated, e.g., in Ref. [65].

$$M = \underbrace{\frac{N}{V} g_J \mu_B J}_{M_s} \cdot \underbrace{\left\{ \frac{2J+1}{2J} \coth\left(\frac{2J+1}{2J} y\right) - \frac{1}{2J} \coth\left(\frac{y}{2J}\right) \right\}}_{B_J(y)} \quad (1.11)$$

$$y \equiv \frac{g_J \mu_B B}{k_B T} J \quad (1.12)$$

$$B_\infty(y) = \coth(y) - \frac{1}{2J} \frac{2J}{y} = \coth(y) - \frac{1}{y} \equiv L(y) \quad (1.13)$$

M_s corresponds to the saturation magnetization and $B_J(y)$ is the Brillouin function with y defined in Eq. 1.12. As $B_J(0) = 0$ and $B_J(\infty) = 1$, for small magnetic fields and high temperatures $M = 0$ while for large magnetic fields and low temperatures $M = M_s$. The evolution of $B_J(y)$ for different total magnetic quantum numbers J is shown in Fig. 1.12(a). As shown in Eq. 1.13, for $J \rightarrow \infty$ the Brillouin function simplifies to the Langevin function $L(y)$. The semiclassically derived Langevin function $L(y)$ assumes a macroscopic magnetic moment μ , instead of magnetic moments that are directly related to the total angular momentum of the electrons by $g_J \mu_B J$, such that $y = \frac{\mu B}{k_B T}$.

For low magnetic fields, the paramagnetic susceptibility can be obtained from the Brillouin function as shown in Eq. 1.14.

$$\chi = \frac{M}{H} \approx \frac{\mu_0 M}{B} = \underbrace{\frac{n \mu_0 \mu_{\text{eff}}^2}{3 k_B T}}_{\equiv C} \cdot \frac{1}{T} \quad (1.14)$$

$$\mu_{\text{eff}} = g_J \mu_B \sqrt{J(J+1)} \quad (1.15)$$

Eq. 1.14 is the Curie law with the Curie constant C and the effective magnetic moment μ_{eff} (as defined in Eq. 1.15). Following from the Curie law is a linear temperature dependence of $1/\chi$, which is characteristic for paramagnetism and illustrated in Fig. 1.12(b).

An additional contribution to the paramagnetic response can be obtained due to the population of excited electronic states at finite temperatures, which may yield a different J (van Vleck paramagnetism) than expected for the groundstate. Furthermore if a system has delocalized electrons (*i.e.* in a metallic state), additional contributions due to Landau diamagnetism and Pauli paramagnetism can be expected [65].

1.2.3. Cooperative Magnetism

Until here, magnetic moments were considered to be isolated and to interact independently with a magnetic field. However for long-range magnetic order as observed in ferromagnets and antiferromagnets, a interaction between spins is necessary.

Exchange Interaction

The interaction between spins is attributed to the quantum mechanical interaction between identical particles and is called the exchange interaction [65]. The spins of two electrons can either align symmetrically ($S = 1$; parallel) or antisymmetrically ($S = 0$; antiparallel) to each other. These states differ in energy, as the different alignments are related to changes in the electrostatic potential of the reference frame, which may be an amount of spins on the same atom or on adjacent atoms.

For two interacting spins \mathbf{S}_1 and \mathbf{S}_2 , the spin dependent effective Hamiltonian can be written as shown in Eq. 1.16 with J being the exchange constant¹.

$$\hat{\mathcal{H}}^{\text{spin}} = -2J\mathbf{S}_1 \cdot \mathbf{S}_2 \quad (1.16)$$

$$\hat{\mathcal{H}} = - \sum_{ij} J_{ij} \mathbf{S}_i \cdot \mathbf{S}_j \quad (1.17)$$

For $J > 0$ the symmetric $S = 1$ state is favored while for $J < 0$ the antisymmetric $S = 0$ is found. As the interaction described in Eq. 1.16 is likely to be the same between all adjacent electrons, for a many-body system the Hamiltonian of the Heisenberg model, as shown in Eq. 1.17, is obtained. Note that in this notation, the factor of 2 has to be omitted as each pair of spins is already counted twice in the sum.

Considering spins on the same atom, J is in general positive, leading to parallel arrangement of spins in one atom. This leads to a maximum spatial separation of the electrons minimizing

¹ J is used as symbol for the exchange constant to distinguish it from the total angular momentum J .

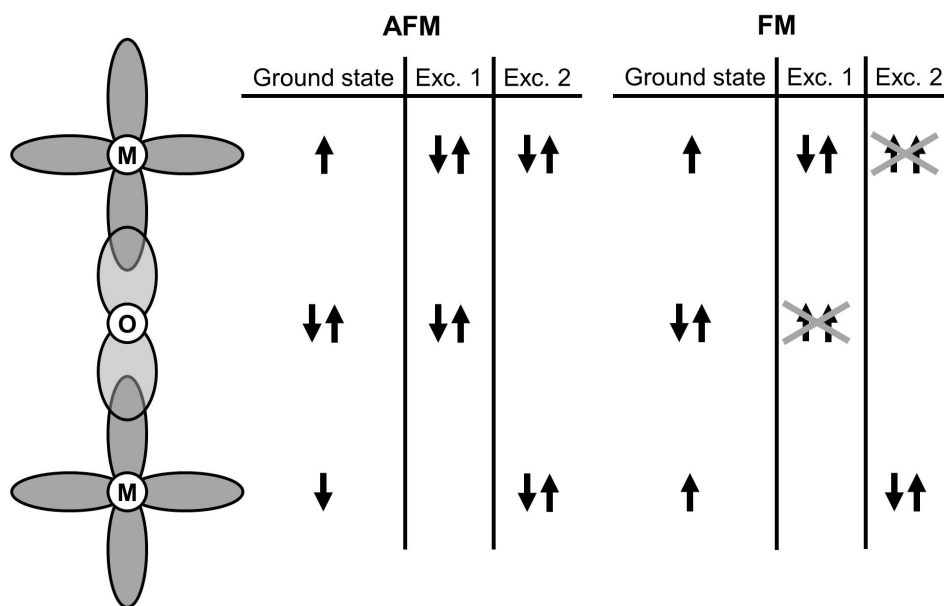


Fig. 1.7.: Left: Linear $M-O-M$ bonding in a magnetic oxide. One unpaired electron of M interacts with an unpaired electron of an adjacent M via super-exchange involving two p electrons of oxygen. Center: Ground state configuration and excited state configuration (Exc. 1 and Exc. 2) assuming antiferromagnetic exchange. Right: Ground state configuration and excited states configuration assuming ferromagnetic exchange. Note that the crossed-out configurations would violate the Pauli exclusion principle and, therefore, do not represent valid configurations.

the Coloumb energy and, thus, is energetically favored in agreement with Hund's rule of maximum multiplicity. Considering adjacent atoms, atomic orbitals overlap and bonds are formed. Consequently, molecular orbitals have to be considered with bonding orbitals with lowered energy and antibonding orbitals which are lifted in energy. To occupy the energetically favored bonding orbital together, the spin of two electrons must be aligned antisymmetrically (Pauli exclusion principle). Consequently, often negative exchange constants are found for interatomic exchange [65].

If electrons of adjacent atoms directly interact with each other via an exchange interaction, then this is called direct exchange. However, this direct interaction is rarely dominant, as it relies on the direct overlap of magnetic orbitals. For example for rare earth elements, the magnetic $4f$ orbitals are strongly localized and close to the nucleus so that no sufficient $4f$ orbital overlap between adjacent rare earth atoms is expected [65].

A similar scenario is observed for MnO. This ionic solid exhibits antiferromagnetic order, although the Mn^{2+} atoms are spatially well separated from each other such that no direct overlap of the magnetic $3d$ orbitals is possible. However, in this case the nonmagnetic O^{2-} acts as mediator for the antiferromagnetic exchange interaction, which is consequently considered as an indirect super-exchange.

As illustrated in Fig. 1.7, such a super-exchange favors an antiferromagnetic $M-O-M$ interaction, as this arrangement allows for more excited states than a ferromagnetic arrangement, which lowers the kinetic energy for this state. This is however only the case for a 180° bond

angle between two singly occupied orbitals, as in MnO. For different bond angles or an interaction between a singly occupied and an empty orbital *via* super-exchange, also ferromagnetism may be stabilized. Furthermore, in some materials a super-super-exchange mechanism is discussed. Although the corresponding large distance between two magnetic atoms should cause this interaction to be relatively weak, it is proposed to explain the magnetic coupling in some materials [65].

The super-exchange mechanism is likely to be the most important exchange interaction for the materials investigated in this work. However, there are also further indirect exchange mechanisms. For example for materials with delocalized electrons, the RKKY (Ruderman, Kittel, Kasuya and Yosida) interaction as well as the double exchange interaction are of importance. Furthermore, the Dzyaloshinsky-Moriya interaction may cause a weak ferromagnetic component in antiferromagnetically coupled materials due to the influence of spin-orbit coupling [65].

Ferromagnetism

For $J > 0$, spins of neighboring atoms align parallel to each other. Consequently, such a system exhibits a spontaneous magnetization even without the application of a magnetic field and is called a ferromagnet. The Hamiltonian describing a ferromagnet in a magnetic field B is given in Eq. 1.18. For simplicity, $L = 0$ and, consequently, $\mathbf{J} = \mathbf{S}$ are assumed.

$$\hat{\mathcal{H}} = \underbrace{-\sum_{ij} J_{ij} \mathbf{S}_i \cdot \mathbf{S}_j}_{\text{Heisenberg Exchange Term}} + \underbrace{g\mu_B \sum_j \mathbf{S}_j \cdot \mathbf{B}}_{\text{Zeeman Term}} \quad (1.18)$$

$$\hat{\mathcal{H}} = g\mu_B \sum_i \mathbf{S}_i \cdot (\mathbf{B} + \mathbf{B}_{\text{mf}}) \quad (1.19)$$

The Weiss model of ferromagnetism assumes that every spin in the system experiences a field \mathbf{B}_{mf} (the molecular field) additional to \mathbf{B} due to the parallel arrangement of all surrounding magnetic moments. Consequently, Eq. 1.18 can be reformulated to Eq. 1.19 as demonstrated in detail in Ref. [65]. Thus, a ferromagnet can be treated as a paramagnet placed in a magnetic field $(\mathbf{B} + \mathbf{B}_{\text{mf}})$ with $\mathbf{B}_{\text{mf}} = \lambda \mathbf{M}$ and λ expressing the strength of the molecular field in terms of the magnetization \mathbf{M} [65]. Consequently, solving the Brillouin function with an adapted expression for y , as shown in Eq. 1.21, yields the stable states for a ferromagnet according to the Weiss model.

$$\frac{M}{M_s} = B_J(y) \quad (1.20)$$

$$y = \frac{g_J \mu_B J (B + \lambda M)}{k_B T} \quad (1.21)$$

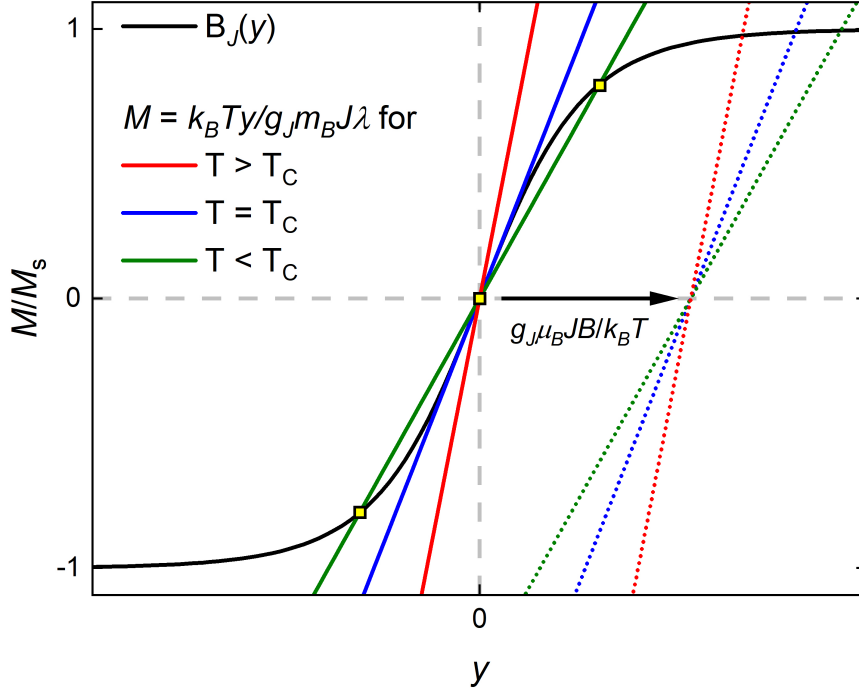


Fig. 1.8.: Graphical solution of Eq. 1.20 and Eq. 1.21 for $J = 1$ and $B = 0$ for different temperatures. The intersections (*i.e.* the solutions) are marked with yellow squares. Additionally, the effect of increasing B is shown as dotted lines.

Assuming $B = 0$ and consequently $M = k_B T y / g_J m_B J \lambda$, the equations can be solved graphically. The simultaneous solutions of both equations are given by the intersections of the linear function of $M(y)$ with the Brillouin function, as shown in Fig. 1.8. Above a critical temperature, the only valid solution is $M = 0$. However, below this critical temperature two additional solutions are found with M being \pm a non-zero value. In fact in the presence of non-zero solutions, the $M = 0$ solution describes no longer a stable state, as any fluctuations in the system drive the system into a state corresponding to one of the two non-zero solutions. Consequently, a ferromagnet exhibits a spontaneous magnetization at $B = 0$ up to a critical temperature. Above this temperature the spontaneous magnetization vanishes [65]. This transition temperature, the Curie temperature T_C , is defined as shown in Eq. 1.22.

$$T_C = \frac{g_J \mu_B (J + 1) \lambda M_s}{3k_B} = \frac{n \lambda \mu_{\text{eff}}^2}{3k_B} \quad (1.22)$$

From the graphical solution of the model, the thermal evolution of M can be extracted, as shown in Fig. 1.9(a). The evolution is continuous approaching T_C , but the first derivative (corresponding to the second derivative of the free energy) is not. Thus, the phase transition at T_C is of second order.

The application of a magnetic field shifts the linear functions in Fig. 1.8 along y by $g_J \mu_B J B / k_B T$. Consequently, a common non-zero solution for Eq. 1.20 and Eq. 1.21 can be found at all temperatures. This means that it is always favorable for a ferromagnet to align

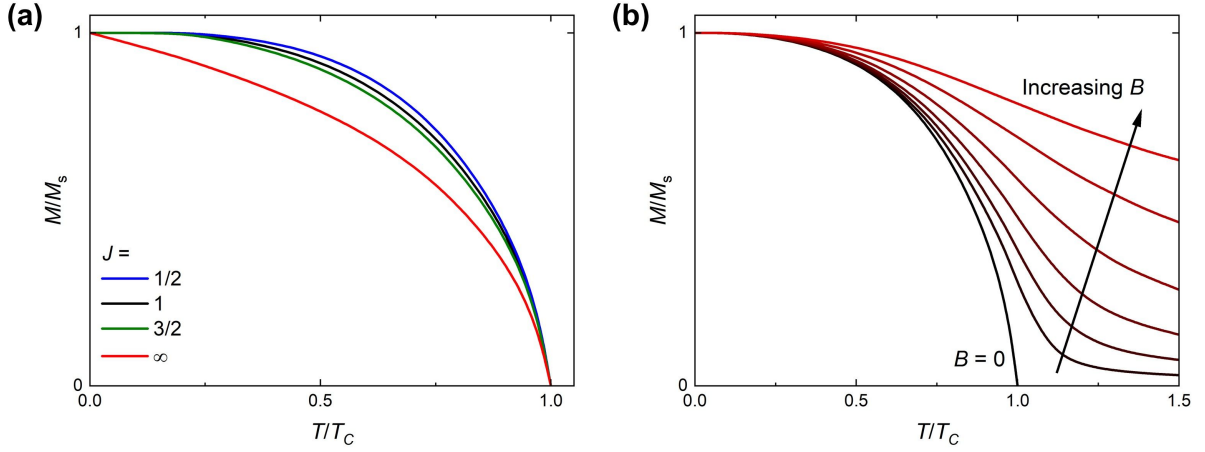


Fig. 1.9.: (a) Thermal evolution of M/M_s for several total magnetic moments J and $B = 0$. (b) Thermal evolution of M/M_s for $J = 1$ under increasing magnetic fields B .

its moments parallel to the external field. Furthermore, the difference between $T \geq T_C$ and $T < T_C$ vanishes, *i.e.* the phase transition is removed [65]. This is demonstrated in Fig. 1.9(b) for increasing magnetic fields.

For a small magnetic field B and at $T \geq T_C$ the Curie-Weiss law can be obtained from the Brillouin function, analogous to the Curie law for a paramagnet.

$$\chi \approx \frac{\mu_0 M}{B} = \frac{C}{T - T_C} \quad (1.23)$$

The molecular field parameter λ is related to the exchange constant J as shown in Eq. 1.24 for $S = J$, as initially assumed and sufficient for $3d$ ions, as their angular momentum L is quenched [68]. Here, z is the number of nearest neighbors of an ion over which J is effective.

$$\lambda = \frac{2zJ}{ng_J^2\mu_B^2} \quad (1.24)$$

However, if L strongly contributes to J (*e.g.*, as in $4f$ ions), S is no longer a good quantum number and additional contributions to J need to be considered [65]. However, this is not further elaborated here, as the materials in this work exclusively contain magnetic $3d$ ions.

Antiferromagnetism

For $J < 0$, the molecular field leads to a favored antiparallel alignment of adjacent magnetic moments, which is called antiferromagnetism. The antiferromagnetic order can be considered as two interpenetrating sublattices each with parallel magnetic moments, as illustrated in Fig. 1.10(a). Assuming the arrangement as shown in Fig. 1.10(a), any atom has the opposite spin to all of its direct neighbors [65]. Consequently, the molecular field on one sublattice

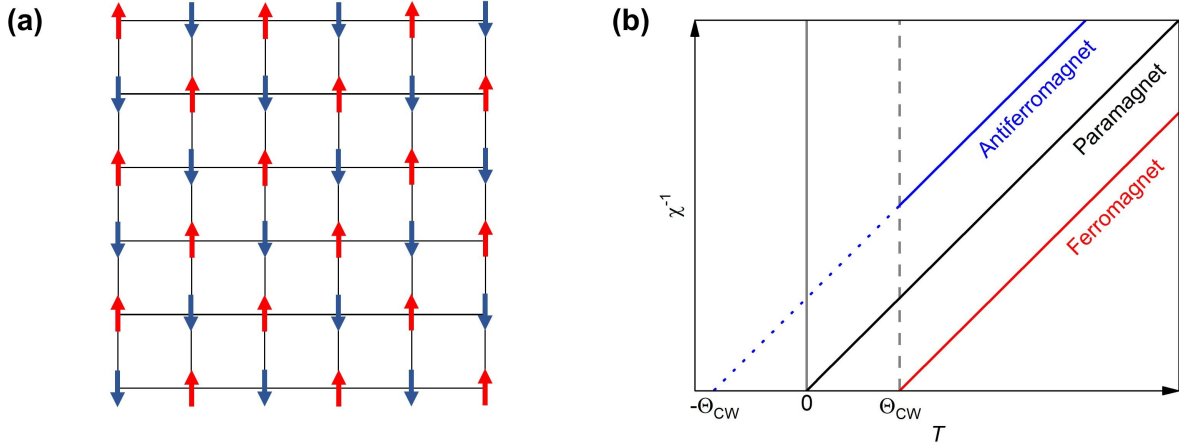


Fig. 1.10.: (a) Antiferromagnetic moments on a square net lattice. The different moment directions have different colors to illustrate the two sublattices with parallel magnetic moments. (b) Thermal evolution of the invers suceptibility χ^{-1} for a paramagnet with $\Theta_{\text{CW}} = 0$, a ferromagnet with $\Theta_{\text{CW}} > 0$ and a antiferromagnet with $\Theta_{\text{CW}} < 0$.

is proportional to the magnetization of the other sublattice. Labeling one sublattice + and the other one -, the molecular field on each sublattice is given by Eq.1.25 with λ being the molecular field constant which is negative for antiferromagnets.

$$B_+ = -|\lambda|M_-; B_- = -|\lambda|M_+ \quad (1.25)$$

Analogous to the considerations for the ferromagnetic order, the magnetization on each sublattice can be expressed by the Brillouin function as shown in Eq. 1.26.

$$\frac{M_{\pm}}{M_s} = B_J \left(-\frac{gJ\mu_B J |\lambda| M_{\mp}}{k_B T} \right) \quad (1.26)$$

$$\frac{M}{M_s} = B_J \left(\frac{gJ\mu_B J |\lambda| M}{k_B T} \right) \quad (1.27)$$

As both sublattices are identical ($M_+ = M_- = M$) except for the direction of the magnetic moment, Eq. 1.26 simplifies to Eq. 1.27. This relation is virtually the same as introduced for ferromagnetic order before. Consequently, the thermal evolution of the molecular field on each sublattice in an antiferromagnet is the same as for the magnetization in a ferromagnet (shown in Fig. 1.9(a)) and it vanishes above a critical temperature [65]. This temperature is called Néel temperature T_N and is defined in Eq. 1.28 (analogous to T_C).

$$T_N = \frac{gJ\mu_B(J+1)|\lambda|M_s}{3k_B} = \frac{n|\lambda|\mu_{\text{eff}}^2}{3k_B} \quad (1.28)$$

Although each sublattice behaves independently like a ferromagnet, the netmagnetization of an antiferromagnet at $B = 0$ is zero, as both sublattices negate each other.

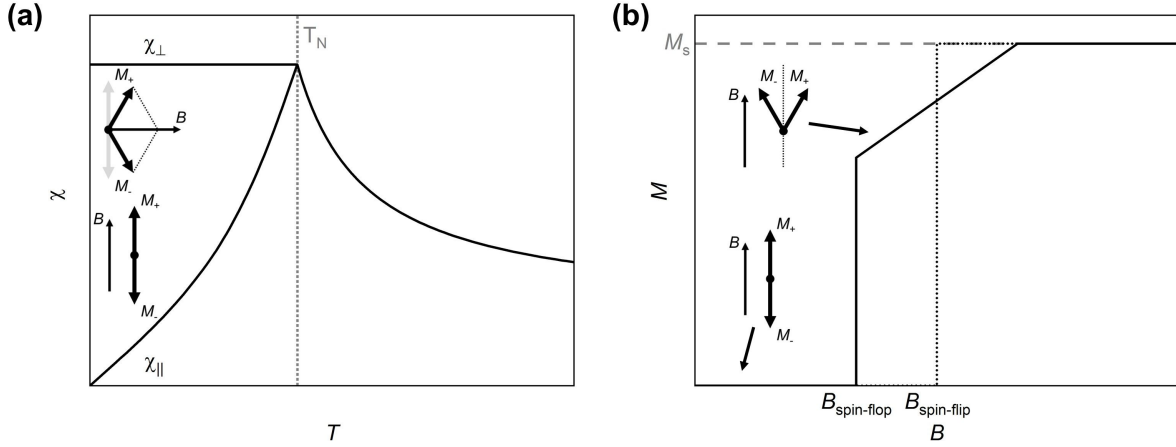


Fig. 1.11.: (a) Thermal evolution of the magnetic susceptibility of an antiferromagnet for magnetic fields applied parallel and perpendicular to the zero-field magnetization direction. (b) Field dependence of the magnetization of an antiferromagnet for magnetic fields applied parallel to the initial magnetization direction. The black dotted line shows the evolution of the magnetization in case of a spin flip in a strongly anisotropic antiferromagnet. The horizontal dashed grey line indicates the saturation magnetization M_s .

Analogous to ferromagnets above the ordering temperature and at small magnetic fields, for antiferromagnets Eq. 1.29 is obtained, which is again the Curie-Weiss law but with $+T_N$ instead of $-T_C$.

$$\chi = \frac{C}{T + T_N} \quad (1.29)$$

Consequently, the Curie-Weiss law may be generalized as shown in Eq. 1.30 with Θ_{CW} being the Weiss temperature.

$$\chi = \frac{C}{T - \Theta_{CW}} \quad (1.30)$$

The susceptibility of a magnetic systems can be expressed by Eq. 1.30 above the magnetic ordering temperature in the paramagnetic state. Following the considerations above, Θ_{CW} indicates if a system is paramagnetic ($\Theta_{CW} = 0$), ferromagnetic ($\Theta_{CW} > 0$) or antiferromagnetic ($\Theta_{CW} < 0$) with corresponding intercepts with $\chi^{-1} = 0$ as shown in Fig. 1.10(b). For the two latter cases, the long range magnetic ordering temperature (T_C or T_N) is expected to be at $|\Theta_{CW}|$. However, Θ_{CW} often significantly deviates from the magnetic ordering temperature in experiments (especially common for antiferromagnets). This can be attributed to the assumptions that were made above and more complex magnetic interactions in real systems. Consequently, the sign of Θ_{CW} indicates the dominant magnetic interactions in a system while its value may be rather used as an estimate for the strength of the magnetic interactions [65].

The effect of a magnetic field on an antiferromagnetically ordered system strongly depends on the direction of the magnetic field relative to the direction of the magnetic moments, as

illustrated in Fig. 1.11(a). Assuming $T = 0$, applying a small magnetic field parallel to the magnetization direction of one sublattice (*i.e.* antiparallel to the other sublattice), slightly increases the energy of the antiparallel sublattice and slightly lowers the energy of the parallel sublattice. However, since both sublattices are already saturated, the external field has no effect and the netmagnetization remains zero. But if the field is applied perpendicular to the magnetization direction of the sublattices, it causes a small tilt of the magnetization of both sublattices and a small magnetization component along the field direction is obtained [65].

Increasing the temperature to $T < T_N$, the observed magnetization for the magnetic field (anti-)parallel to the magnetization direction increases gradually. While the molecular field decreases for both sublattices by increasing T , the magnetization for the parallel sublattice is energetically lowered and, thus, less affected from thermal fluctuations than the energetically lifted antiparallel sublattice. For the magnetic field perpendicular to the initial magnetization directions of the sublattices, no notable temperature dependence is expected, as both sublattices are affected equally by the temperature increase [65].

Furthermore the field dependence of this direction dependence in the antiferromagnetic state has to be considered. For a magnetic field applied perpendicular to the initial direction of the magnetization of both sublattices, increasing the field yields a gradually increasing tilt of the magnetization direction of both sublattices and, thus, a gradually increasing magnetization along the field direction.

For a magnetic field applied (anti-)parallel to the initial magnetization direction, zero magnetization is obtained up to a critical field as explained before, as illustrated in Fig. 1.11(b). However, increasing the magnetic field above the critical value causes a spontaneous rotation of both sublattice magnetization directions so that both sublattices have their main component of the magnetization parallel to the field, while still having an angle between each other. This field driven (metamagnetic) reorientation of the magnetization direction is called spin-flop transition. Further increasing the magnetic field gradually decreases the remaining angle between the two sublattice magnetization directions until the saturation magnetization is reached for an angle of zero. As, *e.g.*, demonstrated in Ref. [65], at fields above the spin-flop field $B_{\text{spin-flop}}$, no longer the antiparallel antiferromagnetic phase but the spin-flop phase is energetically stabilized by the applied magnetic field.

The initial direction of the magnetization of a material in the ground state (*i.e.* $T = 0$ and $B = 0$) is given by its magnetic anisotropy. However, if the magnetic anisotropy is very strong, no intermediate spin-flop phase is stabilized. Instead zero magnetization is observed up to a critical field at which the spins of the antiparallel sublattice flip around by 180° immediately, shown as a dotted line in Fig. 1.11(b). This transition is called spin-flip transition. Regardless of spin-flop or spin-flip, the typical behavior in the field dependent magnetization allows to identify the preferred direction of the magnetization in an antiferromagnet [65].

In Fig. 1.10(a), an antiferromagnetic square net lattice was considered. The corresponding antiferromagnetic order is called G-type or checkerboard order. Yet, depending on *e.g.* the underlying atomic lattice, the magnetic ions and the exchange mechanism, several different types of antiferromagnetic order can be stabilized. One example are ferromagnetic planes which align antiferromagnetically to adjacent planes (A-type antiferromagnetism) as observed, *e.g.*,

in LaMnO_3 . Such an interplay between different exchange interactions can pose a challenge for the investigation of antiferromagnetic systems, as it can cause deviations from the expected behavior presented before [65].

Further Magnetic Ordering Phenomena

Beyond pure ferromagnetic or antiferromagnetic order, magnetic systems may exhibit other magnetic ordering phenomena. For example, ferrimagnets contain two sublattices, which are antiferromagnetically coupled (as illustrated in Fig. 1.10(a) for antiferromagnetism) but do not have the same sublattice magnetization.

In some magnetic systems, not all magnetic exchange interactions can be satisfied at once, leading to magnetic frustration. This can be due to the geometric arrangement of magnetic ions (*i.e.* geometric frustration; *e.g.* antiferromagnetic arrangement in a plane triangle or tetrahedron) or due to different exchange interactions between different magnetic ions that cannot be simultaneously fulfilled. In a frustrated system, no unique magnetic ground state exists which ideally causes the absence of magnetic order down to zero temperature. However in many frustrated systems, metastable magnetic arrangements are formed and below a critical temperature the system adopts randomly one of these metastable states. Such states exhibit magnetic order only on a short range, similar to the structural order in glasses. Thus, the low temperature state in such systems is called spin glass with the freezing temperature T_f being the critical temperature [65].

1.2.4. Magnetic Anisotropy

As already mentioned in the context of the temperature and field dependence of an antiferromagnet in Sect. 1.2.3, magnetic systems often exhibit a preferred direction of the magnetization in the ordered ground state. This direction is defined relative to the high symmetry directions of the underlying crystal lattice and it may originate from the magnetocrystalline anisotropy, which is a material specific property and/or from the shape of the specific sample.

Magnetocrystalline Anisotropy

The magnetocrystalline anisotropy arises mainly from spin-orbit coupling and causes a direction dependent change of the energy of the magnetic system. In first approximation, this direction dependence is often well expressed as uniaxial, as shown in Eq. 1.31 for a ferromagnetic system, with K_U being the uniaxial magnetocrystalline anisotropy constant, φ being the angle between direction of the magnetic field and the magnetization direction and θ corresponding to the direction dependence of the magnetocrystalline anisotropy energy.

$$F = \underbrace{-\mu_0 \cdot M_s \cdot H \cdot \cos(\varphi)}_{\text{Zeeman Energy}} + \underbrace{K_U \cdot \sin^2(\varphi - \theta)}_{\text{Uniaxial Anisotropy Energy}} \quad (1.31)$$

At $\theta = 0$, the magnetocrystalline energy is either minimized for $K_U > 0$ or maximized for $K_U < 0$. If it is minimized, $\theta = 0$ is the magnetic easy axis (*i.e.* preferred orientation) and the perpendicular plane is the magnetic hard plane. However if the energy has a maximum at $\theta = 0$, this direction is the magnetic hard axis with the perpendicular plane being the magnetic easy plane [65].

Shape Anisotropy

A magnetic sample with a non-zero netmagnetization generates a magnetic field (the demagnetizing field), which may even be the case for antiferromagnetic compounds (*e.g.* due to the sample surface, other crystallographic defects or ferromagnetic contributions to the exchange interactions). If such a sample is not perfectly spherical, the energy of the demagnetizing field may differ for different magnetization directions. For example, a ferromagnetic thin plate favors any in-plane direction of the magnetization over the out-of-plane direction, as the latter orientation causes a larger magnetic stray field, which is energetically unfavorable. This direction dependence of the demagnetizing energy is called shape anisotropy. As it is a property of the specific sample, the effect of the shape anisotropy has to be considered separately to obtain the material-specific magnetic properties [65].

The demagnetizing field effectively reduces the magnetic field that the material experiences. For a principle direction i , this is described by Eq. 1.32, with H_i being the effective magnetic field, $(H_0)_i$ being the applied magnetic field and N_i being the demagnetizing factor for this direction, which is given by the shape of the sample.

$$H_i = (H_0)_i - N_i M_i, \quad i = x, y, z \quad (1.32)$$

By approximating the sample shape as an ellipsoid, demagnetizing factors can be obtained as reported by Osborn [70]. One limiting case, which is especially relevant for this work, is the infinite thin plate (*i.e.* an ellipsoid with relative radii of $r_y/r_x = 1$ and $r_z/r_x = 0$). The corresponding demagnetizing factors are $N_x = N_y = 0$ and $N_z = 1$ according to Osborn. Consequently, the maximum demagnetizing field is observed for $H \parallel z$ while no effect of the shape anisotropy is obtained for $H \perp z$. This is in agreement with the aforementioned behavior for a ferromagnetic thin plate.

Theoretical Models

Systems with different magnetic anisotropies are typically discussed in terms of different theoretical models to describe the magnetic interactions. The classical Heisenberg model was

already introduced before in Eq. 1.17. In this model, the dimensionality of the spins is $d = 3$, as a spin is classically expressed by a three-dimensional vector. Consequently in the ground state, the spin can rotate in any direction as it is the case for an isotropic magnetic system. This is in contrast to the Ising model, in which $d = 1$. Thus, spins can only align (anti-)parallel to a defined axis, as expected for a magnetic system with a well pronounced magnetic easy axis. The anisotropic magnetic behavior of a system with easy plane anisotropy can be well described by the XY model for which $d = 2$.

$$\hat{\mathcal{H}} = - \sum_{ij} J_{ij} \mathbf{S}_i \cdot \mathbf{S}_j \quad (1.33)$$

$$\hat{\mathcal{H}} = - \sum_{ij} (J_{ij}^x \mathbf{S}_i^x \cdot \mathbf{S}_j^x + J_{ij}^y \mathbf{S}_i^y \cdot \mathbf{S}_j^y + J_{ij}^z \mathbf{S}_i^z \cdot \mathbf{S}_j^z) \quad (1.34)$$

This is generalized in the n -vector model, with the Hamiltonian shown in Eq. 1.33 and the dimensionality of spins being $d = n$ with the special cases discussed before. Furthermore, the Heisenberg model may be generalized by assuming a direction dependence of the exchange constant J , as shown in Eq. 1.34. Consequently in the generalized Heisenberg model, the anisotropy is not expressed by the dimensionality of the spins but by the anisotropy of the exchange coupling. A special case of this model is known as the XXZ model for $J_{ij}^x = J_{ij}^y \neq J_{ij}^z$ [65].

Fundamentally, real systems can be classified by the theoretical model that expresses the experimental behavior most accurately, allowing for an easier comparison between different systems. Furthermore, predictions for the real system can be made based on results obtained for the model from theoretical considerations (*i.e.* the critical behavior around a phase transition). Also for some models under specific conditions, exotic physical phenomena are predicted (*e.g.*, the Berezinskii-Kosterlitz-Thouless transition for the XY model in 2D) which have to be experimentally realized and investigated in order to further improve the corresponding model. Thus, investigating which model corresponds best to the experimental magnetic behavior of a system is worthwhile and the magnetic anisotropy can be a good indicator for this. Another method to investigate which model corresponds best to the experimental magnetic behavior of a system is *via* the critical exponents, as discussed in Sect. 1.2.6.

1.2.5. Magnetism in $D < 3$

Additional to the dimensionality of the spins d , the dimensionality of the underlying atomic lattice D plays an important role for the behavior of a model. While long range order can occur in the isotropic Heisenberg model on a 3D lattice, the isotropic Heisenberg model cannot order for reduced dimensions of the atomic lattice at finite temperatures. This was demonstrated by Mermin and Wagner [2]. The reason for the absence of an ordered state in this model is that spin waves can be excited and disturb any long range ordered state at all finite temperatures for reduced lattice dimensions. In a simplified approach, the direction of all spins can be globally rotated in an isotropic system without energy differences between directions. Consequently,

to excite a long wavelength spin wave (*i.e.* the difference in the direction of adjacent spins is small) virtually no energy is necessary. These spin fluctuations destroy any long range order. However, if the system is anisotropic, the rotation of spins away from the direction in the ground state costs energy. Thus for the Ising model on a 2D lattice, an ordered state can be theoretically be formed. This demonstrates the importance of the magnetic anisotropy for the magnetic order in 2D systems [65, 66].

Another exotic physical behavior is predicted for the XY model in a 2D system. As demonstrated by Berezinskii [71] as well as Kosterlitz and Thouless [46] (BKT), this model does not exhibit long-range order but a phase transition between two disordered phases. Above the transition temperature $T_{\text{BKT}} = \pi J/2k_{\text{B}}$, the system may spontaneously forms vortices and the spin–spin correlation decays exponentially as expected for a disordered phase. Below the transition, the spin–spin correlation decays with a power law behavior which does not agree with the behavior expected for a long range ordered state. The low temperature phase is discussed as previously independent vortices and anti-vortices being bound together in pairs. In this context, the BKT transition is considered a topological phase transition as it is not related to any symmetry breaking.

Reducing the dimensions of the magnetic lattice further yields 1D spin chains. If such chains are magnetically well isolated from each other, no long range order is stable at finite temperatures due to magnetic fluctuations. As a disordered state is entropically favored for a 1D system, not even magnetic anisotropy can stabilize long range order. Yet in real systems, magnetic chains are potentially not completely isolated from each other and interchain interactions cause deviations from the expected behavior at low temperatures, such as the existence of long range magnetic order. In the disordered state, 1D spin chains allow the investigation of complex excitations [65, 66].

1.2.6. Critical Exponents

The evolution of the spontaneous magnetization approaching the ordering temperature in a ferromagnet can be experimentally found to be proportional to $(T_{\text{C}} - T/T_{\text{C}})^{\beta}$. As the spontaneous magnetization in a ferromagnet corresponds to existence of the ordered phase and vanishes in the disordered paramagnetic phase, it can be defined as order parameter for the ferromagnetic state. In fact, also the thermal evolution of the magnetic susceptibility approaching T_{C} from above as well as the field dependence of the magnetization at T_{C} can be described by a similar exponential behavior [65]. The corresponding exponents are called critical exponents [72]. According to Griffiths' hypothesis of universality [73], these exponents are independent of system specific details and only depend on general features of a physical system. These general features are the dimensionality of the system D , the internal dimensionality d (*e.g.* spin dimensionality for magnetic systems) and the range of the interaction.

For a ferromagnetic–paramagnetic phase transition, the spontaneous magnetization M_{s} below, the initial magnetic susceptibility χ_0 above and the field dependence of the magnetization $M(H)$ at the critical temperature T_{C} can be described by critical exponents β , γ and δ as shown in Eq. 1.35, Eq. 1.36 and Eq. 1.37, respectively.

$$M_s(T) = M_0(-\varepsilon)^\beta \text{ for } T < T_C \quad (1.35)$$

$$\chi_0^{-1}(T) = (h_0/m_0)\varepsilon^\gamma \text{ for } T > T_C \quad (1.36)$$

$$M(H) = DH^{1/\delta} \text{ for } T = T_C \quad (1.37)$$

Here, $\varepsilon = (T - T_C)/T_C$ is the reduced temperature while M_0 , h_0/m_0 and D are the critical amplitudes [74]. Using the scaling hypothesis, the magnetic equation of state can be written as shown in Eq. 1.38 with the regular functions f_+ for $T > T_C$ and f_- for $T < T_C$.

$$M(H, \varepsilon) = \varepsilon^\beta f_\pm(H/\varepsilon^{\beta+\gamma}) \quad (1.38)$$

$$m = f_\pm(h) \quad (1.39)$$

Defining a renormalized magnetization $m \equiv \varepsilon^{-\beta} M(H, \varepsilon)$ and a renormalized magnetic field $h \equiv \varepsilon^{-(\beta+\gamma)} H$ and substituting in Eq. 1.38 yields Eq. 1.39. The latter implies that for correct values of β , γ and δ , $m(h)$ exhibits two universal behaviors, one above and one below the critical temperature.

The critical exponents for different models depending on the aforementioned general features, such as the Ising model ($d = 1$) or the Heisenberg model ($d = 3$) on a $D = 2$ or $D = 3$ lattice, are known. Thus, the extraction of such exponents from experimental data allows to identify which model expresses the physical behavior of a real system most accurately.

2. Methods

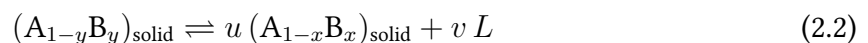
2.1. Synthesis and Crystal Growth

In solid state science, each compound corresponds to a phase with a defined elemental composition (or range of composition) and a certain atomic structure. The structure may be only short-range (amorphous) or exhibit a long-range order (crystalline). In this line, these phases are stable arrangements of atoms in the solid state in the thermodynamical equilibrium at a certain temperature and pressure [67, 75].

For example, different atomic structures (allotropes) for elemental iron are known in the solid state which are stable at different temperatures and pressures. At a pressure of 1 bar, liquid iron solidifies in the δ -Fe phase with body-centered cubic arrangement of atoms below approximately 1540 °C. Below approximately 1400 °C, the γ -Fe phase with face-centered cubic structure becomes thermodynamically stable and, thus, the δ -Fe phase transforms to the γ -Fe phase in equilibrium. Below approximately 910 °C, the body-centered cubic α -Fe phase corresponds to the stable structure [76].

The relation between different phases are illustrated in phase diagrams. While for pure elements, the dependence of the phase on both temperature and pressure can be shown as an x-y plot, for binary compounds different phases may be stable for different elemental ratios and, thus, the phase diagram contains three parameters (elemental ratio, temperature, pressure). To simplify the graphical representation from three dimensions to two, one parameter is typically fixed [67, 75]. A schematic binary phase diagram at constant pressure between the elements A and B with the binary phases $A_{1-x}B_x$ and $A_{1-y}B_y$ is shown in Fig. 2.1.

The phases A, B and $A_{1-x}B_x$ melt congruently, *i.e.* a liquid phase of the same composition as the solid phase is formed during the solid-liquid phase transition at the melting point T_m , which is the case for the phases A, $A_{1-x}B_x$ and B in Fig. 2.1 (*i.e.* $T_m(A)$ is the melting point of phase A, *etc.*). This is illustrated in Eq. 2.1 for $A_{1-x}B_x$ as an example.



In difference, $A_{1-y}B_y$ decomposes at T_{decomp} , forming a solid phase and a liquid phase, both of different composition than $A_{1-y}B_y$. This is illustrated in Eq. 2.2 and, consequently, $A_{1-y}B_y$ is considered an incongruently melting phase [67, 75].

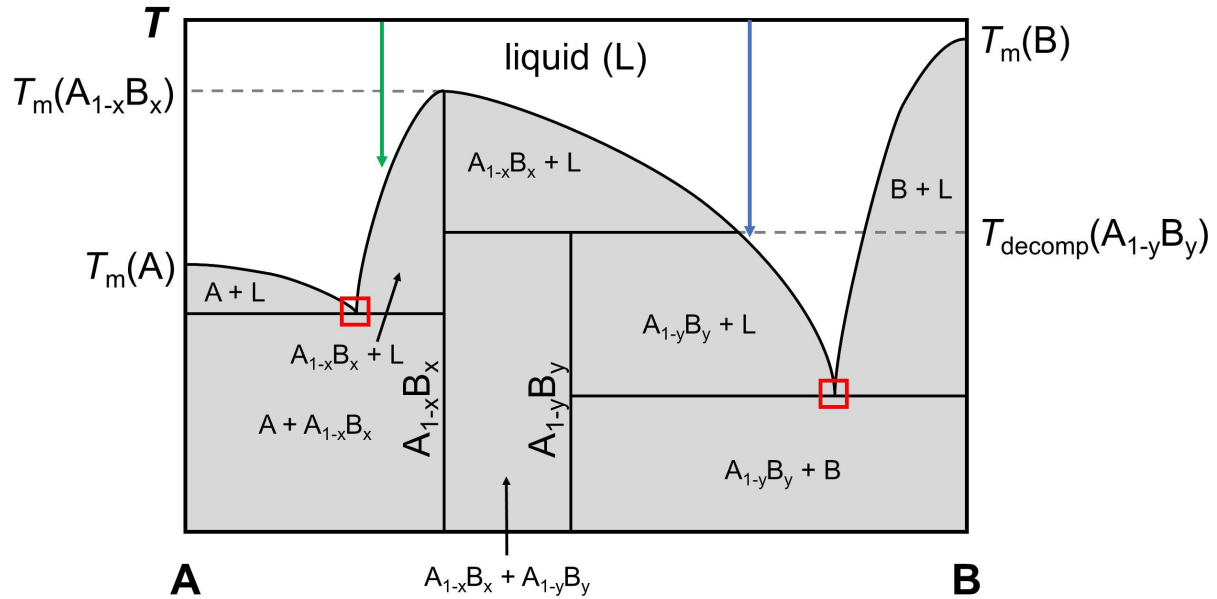


Fig. 2.1.: Schematic phase diagram of a binary system AB as function of temperature T . The grey areas correspond to twophase regions. Eutectic points are marked by red squares. Two specific compositions referred to in the text are marked by the green and blue arrows.

According to the position in the phase diagram and, consequently, the relation to adjacent phases, different phases may be synthesized and crystals may be grown by different techniques [77]. To form a phase as polycrystalline material (*i.e.* a bulk or powder sample containing a large amount of independent, small and randomly oriented crystals) solid state synthesis is used, as introduced in Sect. 2.1.1. As in this technique the crystal growth speed is limited, specialized methods are used to grow larger crystals which employ a liquid phase and high temperatures to improve the growth speed (Sect. 2.1.2). Such crystal growth methods yield good results for phases with a low vapor pressure (*e.g.* for intermetallics and some oxides). For compounds with high vapor pressure components, crystal growth *via* the vapor phase is widely used. Compounds containing some non-volatile component may also be grown *via* the vapor phase using a so-called transport agent in the chemical vapor transport technique. This is introduced in Sect. 2.1.3.

2.1.1. Solid State Synthesis

According to thermodynamics, any solid state phase can be formed by an elemental mixture with the stoichiometry of the phase which is exposed to a temperature and pressure at which the phase is stable. However, the process of formation may take a while due to the corresponding kinetics. In the solid state, diffusion is limited. Consequently, it may take a long time until an atom arrives at the correct place in the structure of the phase. This is especially true if a loose powder of elemental educts is considered as starting material [75].

Thus, for solid state synthesis, high temperatures (in the stability region of the desired phase) and short diffusion paths between particles of the different educts are preferable. The former is

achieved by a furnace resulting in faster kinetics and the latter by grinding the educts to a fine homogeneous powder and subsequent pressing of the powder to a pellet. The close packing of particles in a pellet without large cavities minimizes the diffusion paths. The heat treatment is typically performed under an inert atmosphere to avoid reactions with the atmosphere or in an atmosphere that contains a constituent of the phase (e.g. oxygen or air for oxides). During the heat treatment, the phase formation starts randomly at several points in the pellet (nucleation) and slowly a large number of small crystallites form. Thus, a polycrystalline sample is obtained.

To ensure a good intermixing of the educts, intermediately formed phases and the target phase, the heat treatment may be interrupted by a regrinding and repressing of the pellet. During such a synthesis, stoichiometry has to be ensured. Changes in the composition of the sample (*i.e.* due to partial evaporation) may cause the formation of secondary phases due to the shift of the overall sample composition into a multiphase region in the corresponding phase diagram. A technique to investigate the phase composition of a sample after the synthesis is pXRD (as explained hereafter in Sect. 2.2.2) [75].

Although this technique is in general suitable to form any solid state phase, it rarely yields large crystals in a reasonable amount of time. Crystallites from solid state synthesis are typically in the size of several tens of μm , which may be sufficient for a determination of the crystal structure by scXRD (as explained hereafter in Sect. 2.2.1) but are too small for most physical measurements techniques [75].

In this work, solid state synthesis was used to synthesize polycrystalline precursors for the growth of $(\text{Fe}_{1-x}\text{Ni}_x)_2\text{P}_2\text{S}_6$ (Sect. 3.2.1) and polycrystalline samples of the substitution series of $(\text{Cu}_{1-x}\text{Ag}_x)\text{CrP}_2\text{S}_6$ (Sect. 4.3.1).

2.1.2. Crystal Growth *via* the Liquid Phase

To accelerate the crystal growth process compared to the solid state synthesis, the kinetics of the phase formation have to be improved. In the solid state, a limiting factor is the diffusion, which is much higher in a liquid phase. Accordingly, forming the desired phase directly from the melt or a solution can notably improve the crystal growth speed and potentially allows to grow large crystals in reasonable time frames [77, 78].

For congruently melting phases, a melt of the same stoichiometry as the phase can be used to grow crystals. By slowly reducing the temperature below the corresponding melting temperature, the melt crystallizes. If such a melt is cooled homogeneously, it is likely that multiple nuclei form as the nucleation conditions are fulfilled everywhere in the melt simultaneously. Consequently, a sample containing several crystals is obtained after the complete solidification of the melt. To minimize the amount and, thus, maximize the size of crystals obtained from such a melt growth, the melt can be cooled with a spatial temperature gradient, as used in several melt growth techniques (e.g. the Bridgeman-Stockbarger technique, the Czochralski technique and the floating zone technique). Using a spatial temperature gradient, the melt solidifies at one spot first and crystallizes from there continuously. Due to the initial local

solidification, only few (ideally one) nucleation centers are created from which only few crystallites grow. As the crystallization front is moved through the material, a grain selection process takes place, which yields even less large crystals in the resolidified melt [77].

If the desired phase does not melt congruently or the congruent melting point is too high and, thus, not practical for a melt growth, solution growth techniques are used. Instead of growing a crystal of the phase $A_{1-x}B_x$ in Fig. 2.1 from a stoichiometric melt at high temperatures around $T_m(A_{1-x}B_x)$, adding a small amount of the phase A in the starting mixture reduces the solidification temperature along the curved line above the two phase regime ' $A_{1-x}B_x + L$ ', called liquidus line. Assuming a homogeneous melt with the composition corresponding to the green arrow, if the temperature is reduced below the liquidus line, the two phase region ' $A_{1-x}B_x + L$ ' is accessed. Thus, solid $A_{1-x}B_x$ forms and the stoichiometry of the liquid phase shifts along the liquidus line under further cooling [78].

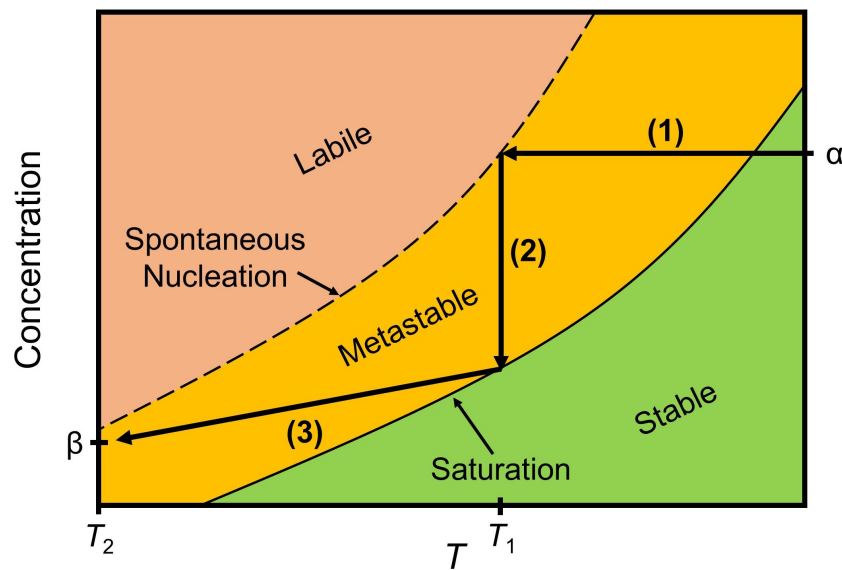


Fig. 2.2.: Temperature dependence of the concentration of a solution or melt containing a stable, metastable (Ostwald-Miers) and labile regime. The black arrows illustrate the evolution of the concentration of a solution from a concentration α to β under cooling as discussed in the corresponding section. In the style of Ref. [78].

For the crystal growth, this solidification process is of interest. The starting mixture can be considered as a solution of the solute $A_{1-x}B_x$ in the solvent L with a temperature dependent solubility, as illustrated in Fig. 2.2. The liquidus line corresponds to the the temperature at which the equilibrium solubility is reached. However, if the temperature is initially reduced slightly below the liquidus line, no solidification happens as the solution supersaturates (Fig. 2.2 (1)). Only if the temperature is reduced further, stable nucleation centers form. This behavior is observed as nucleation centers have to reach a critical radius to be stable, which is only possible below the regime of supersaturation (*i.e.* Ostwald-Miers regime). Consequently, the concentration of the solution is reduced until it is again stable (Fig. 2.2 (2)). In the Ostwald-Miers regime, only growth of already present nucleation centers or crystals takes place. Thus after the initial nucleation, the temperature change of the liquid can be adjusted to the growth speed of the crystal to keep the solution supersaturated but avoid the spontaneous formation

of additional nucleation (Fig. 2.2 (3)). In practice, slow cooling (typically in the order of 1 °C/h or less) is used if detailed thermodynamic data on the system is missing [78].

The temperature limit of this growth towards low temperatures is determined by the eutectic point between A and $A_{1-x}B_x$ marked by a red square in Fig. 2.1. By cooling below the corresponding temperature, the two phase region of 'A + $A_{1-x}B_x$ ' is accessed and the residual melt abruptly solidifies as a phase mixture. To minimize the presence of secondary phases on the crystal, the temperature is slowly reduced to just above the eutectic point and then the residual melt can be separated from the grown crystals (*e.g.* by centrifugation) [78].

The growth of $A_{1-x}B_x$ from ' $A_{1-x}B_x$ + A' is called self flux growth, as the solvent A is a constituent of the target phase. By a self flux growth with the solvent B and the starting composition marked by the blue arrow in Fig. 2.1, crystals of the incongruently melting phase $A_{1-y}B_y$ can be grown. The scenario is in general the same for a conventional solution growth, like the growth of NaCl crystals from water as a solvent [79]. In this specific case, it is also possible to keep the temperature constant and remove solvent *via* slow evaporation to influence the solubility of the solution [77, 78].

In this work, self flux growth experiments were performed for the growth of $Cr_2Ge_2Te_6$ and $In_2Ge_2Te_6$ crystals from a GeTe rich starting composition. Details are discussed in Sect. 5.1.1 and Sect. 5.2.1.

2.1.3. Crystal Growth *via* the Vapor Phase

Elements and compounds with high vapor pressures pose a challenge to high temperature solution and melt growth techniques, as the overall stoichiometry of the liquid phase changes due to evaporation. In some techniques, high pressure reaction atmospheres are used to suppress evaporation with some success [77].

Yet, it is also possible to use such high vapor pressures and grow crystals directly from the vapor phase. For this, the high vapor pressure reactants are evaporated at high temperatures and precipitated at another spot in the reaction volume at lower temperatures. Based on Le Chatelier's principle, the reactants are gradually transported to the colder spot *via* the vapor phase providing the matter for the growth of large crystals. The vapor phase exhibits an Ostwald-Miers regime, too and, thus, acts analogous to a melt or solution by supersaturating and the formation of nucleation centers and crystals under certain system-specific conditions. For example, crystals of iodine and arsenic are grown *via* the vapor phase to purify these elements [80].

The chemical vapor transport (CVT) technique differs from the scenario mentioned before, as it is used to transport a *per se* non-volatile (low vapor pressure) element or compound *via* the vapor phase, which is illustrated schematically in Fig. 2.3. In CVT, a so-called 'transport agent' is added to the system, which forms volatile intermediate species with the reactant at certain temperatures. At different temperatures, this intermediate vapor species is no longer stable and decomposes back to the transport agent and the reactant. By spatially separating the two temperature zones and thermodynamically controlling the decomposition reaction,

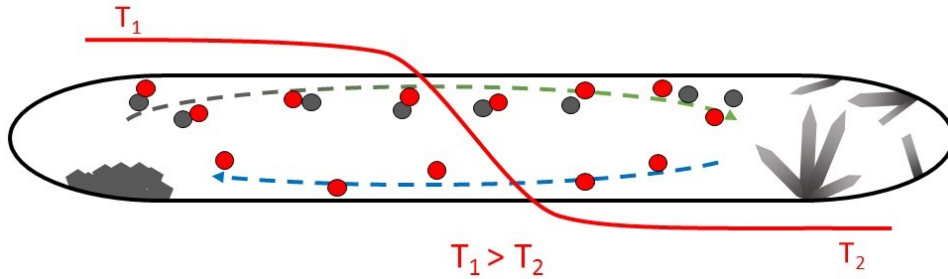


Fig. 2.3.: Schematic drawing of the processes during a chemical vapor transport reaction for an endothermic formation of the intermediate species ($T_1 > T_2$). Grey: transported material; red: transport agent. In the style of Ref. [80].

the transport of material based on Le Chatelier's principle and the growth of crystals of the reactant can be achieved. In this process, the transport agent acts as a catalyst and, thus, may only be added in low amounts. Depending on the nature of the formation and decomposition of the intermediate vapor species, the crystal growth in CVT takes place either in the colder or in the hotter zone [80].

For example, Fe_2O_3 crystals can be grown by CVT using HCl as transport agent by transport from hot (approx. 1000°C) to cold (approx. 800°C) as the formation of the transport species FeCl_3 is endothermic [81]. In contrast, the purification of Ni by the Mond process with CO as transport agent is based on the exothermic formation of gaseous $\text{Ni}(\text{CO})_4$ at low temperatures (approx. $50\text{--}60^\circ\text{C}$) and its decomposition to solid Ni and CO at higher temperatures (approx. $220\text{--}250^\circ\text{C}$) [75, 82].

In this work, CVT was used to grow $M_2\text{P}_2\text{S}_6$ crystals with M being a $3d$ transition element as well as for crystals of the quarternary phases CuCrP_2S_6 and AgCrP_2S_6 . As P and S are relatively volatile, these constituents readily evaporate. However, the transition element exhibits a low vapor pressure and a transport agent is necessary to bring it in the vapor phase at the growth temperatures (approximate temperature range: $600\text{--}900^\circ\text{C}$). For the CVT of $3d$ transition elements, halogens are suitable transport agents forming volatile MX_3 species. Consequently, iodine was added as transport agent. Details are discussed in Sect. 3.1.1, Sect. 3.2.1, Sect. 4.1.1 and Sect. 4.2.1.

2.2. X-ray Diffraction

Electromagnetic radiation interacts with a periodic arrangement of optical slits (*i.e.* an optical grating) under diffraction, if the width of the slits is in the same order of magnitude as the wavelength of the electromagnetic radiation λ . In this line, the periodic arrangement of atoms in a crystal can act as three dimensional grating for electromagnetic radiation in the X-ray region of the optical spectrum (*i.e.* $10\text{ pm} < \lambda < 10\text{ nm}$)¹. Thus for any orientation

¹It may be mentioned that also other types of radiation (*i.e.* matter waves, such as neutrons or electrons) may exhibit a similar wavelength and, thus, can interact with a crystal lattice under diffraction.

of the crystal to the (incoming) primary beam, measuring the intensity of the X-ray radiation in a sphere around the crystal yields a spatial distribution of the intensity, *i.e.* a diffraction pattern [53, 83].

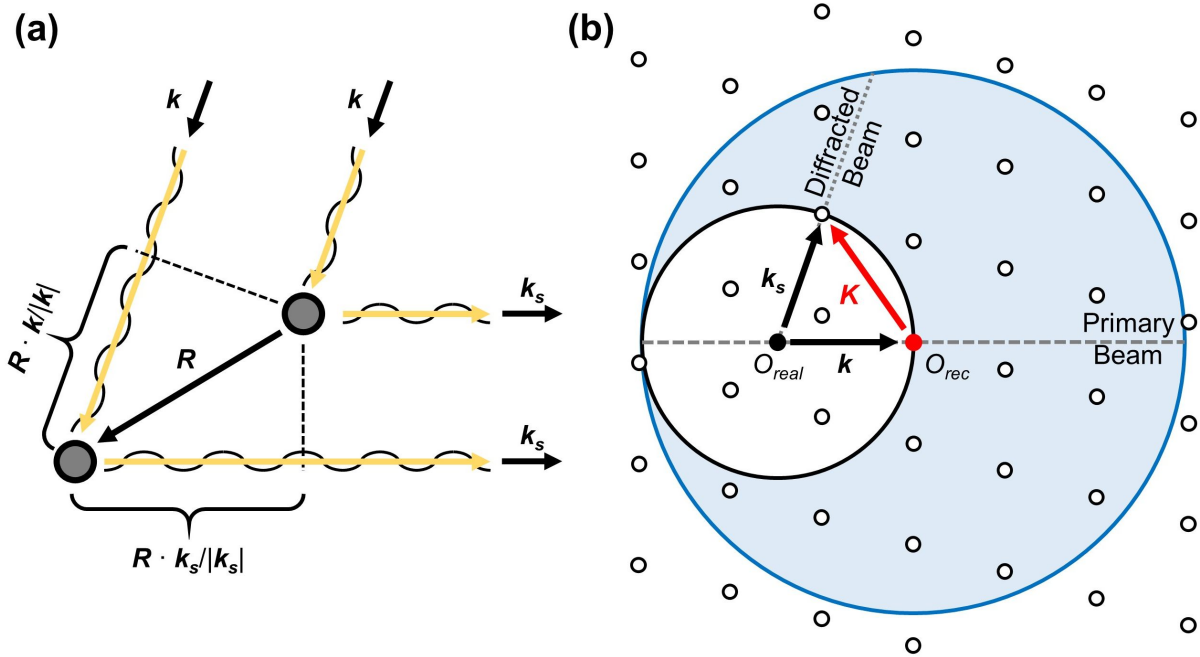


Fig. 2.4.: (a) Graphical representation of the Laue condition for diffraction for radiation with the initial wave vector \mathbf{k} and the wave vector \mathbf{k}_s after elastic scattering on two scattering centers with the distance \mathbf{R} . (b) Ewald sphere for the illustration of the Laue condition in reciprocal space. Details are explained in the text. In the style of Ref. [83].

For certain angles, reflections (*i.e.* maxima of the X-ray intensity) are found, which are obtained due to constructive interference of the X-ray beam which was elastically scattered on different scattering centers in the crystal. The condition for constructive interference is given by the Laue description. Fundamentally, a crystal can be defined as an infinite three dimensional array generated by a set of translation operations acting on a basis, *i.e.* a Bravais lattice. The crystal's basis may be an atom, an ensemble of atoms, molecules or polymer strings with a certain point group symmetry and acts as one homogeneous scattering center in the Laue description of diffraction. As illustrated in Fig. 2.4(a), the lattice vector \mathbf{R} describes the distance between two of these scattering centers. With the wave vector \mathbf{k} of the primary radiation and \mathbf{k}_s of the scattered radiation, the path difference Δx is obtained as in Eq. 2.3.

$$\Delta x = \mathbf{R} \cdot \frac{\mathbf{k}}{|\mathbf{k}|} - \mathbf{R} \cdot \frac{\mathbf{k}_s}{|\mathbf{k}_s|} \quad (2.3)$$

$$n\lambda = \mathbf{R} \cdot \left(\frac{\mathbf{k}}{|\mathbf{k}|} - \frac{\mathbf{k}_s}{|\mathbf{k}_s|} \right) \quad (2.4)$$

$$\mathbf{R} \cdot (\mathbf{k} - \mathbf{k}_s) = 2\pi n \Rightarrow e^{i\mathbf{R} \cdot (\mathbf{k} - \mathbf{k}_s)} = 1 \quad (2.5)$$

As constructive interference is only observed if the path difference is an integer multiple of the wavelength ($\Delta x = n\lambda$, n being an integer), Eq. 2.4 is obtained. For elastic scattering ($|\mathbf{k}| = |\mathbf{k}_s| = 2\pi\lambda^{-1}$) this simplifies to Eq. 2.5. This is equal to the relation between a lattice vector \mathbf{R} and the corresponding reciprocal lattice vector \mathbf{K} ($e^{i\mathbf{R}\cdot\mathbf{K}} = 1$). Consequently, constructive interference is observed if the change of the wave vector $\Delta\mathbf{k}$ from \mathbf{k} to \mathbf{k}_s due to scattering is equal to a reciprocal lattice vector, as shown in Eq. 2.6 [53, 83].

$$\Delta\mathbf{k} = \mathbf{k} - \mathbf{k}_s = \mathbf{K} \quad (2.6)$$

This can be illustrated by the Ewald sphere, as shown in Fig. 2.4(b) [84]. In the center of a sphere, the origin of real space is located. The sphere has a radius of λ^{-1} and, thus, describes all wave vectors \mathbf{k} with $|\mathbf{k}| = \lambda^{-1}$. The origin of the reciprocal space is defined at the intersection of the primary X-ray beam with the sphere, such that the primary beam is always parallel to a diameter of the sphere. Rotating the crystal around the origin of real space causes a rotation of the reciprocal lattice around its origin. However, the relative position of these origins in this construction is not affected. For certain rotations of the crystal in real space, a second lattice point of the reciprocal lattice is on the surface of the sphere (the first one always being at the origin of reciprocal space). For such an orientation of the crystal to the primary X-ray beam, the corresponding wave vector fulfills the Laue condition with the reciprocal lattice parameter \mathbf{K} and, thus, elastic scattering is observed in the direction of \mathbf{k}_s . Consequently, the diffraction process describes a Fourier transform of the crystal lattice into a direct image of its reciprocal lattice as diffraction pattern [53, 83].

The maximum possible \mathbf{K} corresponding to a scattering direction different from the direction of the primary beam is $|\mathbf{K}| < 2|\mathbf{k}_s| = 2\lambda^{-1}$ (*i.e.* less than the diameter of the sphere). In this line, only lattice points with a distance from the origin of reciprocal space of less than $2|\mathbf{k}_s|$ can at all fulfill the Laue condition (*i.e.* be rotated on the surface of the Ewald sphere by rotation of the crystal in real space). As $2|\mathbf{k}_s| = 2\lambda^{-1}$, increasing λ reduces the number of reciprocal lattice points that can fulfill the Laue condition. If λ becomes too large, the Laue condition is no longer fulfilled for any \mathbf{K} and, thus, no diffraction can be observed anymore [53, 83].

According to Laue, the reciprocal lattice vector \mathbf{K} can be expressed as a linear combination of the primitive lattice vectors of the reciprocal lattice \mathbf{b}_i with the Laue indices h , k and l as shown in Eq. 2.7.

$$\mathbf{K} = h\mathbf{b}_1 + k\mathbf{b}_2 + l\mathbf{b}_3 \quad (2.7)$$

As shown by the Ewald sphere, the reciprocal lattice vector \mathbf{K} describes the translation from the origin to a lattice point in reciprocal space. Each lattice point in reciprocal space corresponds to a family of lattice planes in real space. In this line, a reciprocal lattice vector with the Laue indices h , k and l describes the lattice point at $h\mathbf{b}_1$, $k\mathbf{b}_2$ and $l\mathbf{b}_3$ in reciprocal space, yielding the reflection hkl and corresponding to the family of lattice planes with the Miller indices (hkl) in real space. These lattice planes have a distance d between each other. According to the Bragg equation, as shown in Eq. 2.8, for such lattice planes, a reflection is

observed at an angle θ [85], which is half the angle that is obtained in the Ewald sphere for the aforementioned reciprocal lattice vector. Accordingly, the Laue description and the Bragg description of diffraction are equivalent [53, 83].

$$n\lambda = 2d \sin(\theta) \quad (2.8)$$

Both descriptions relate the position of a reflection to the crystal lattice. Thus, the symmetry of a crystal can be determined by the positions of the reflections. However following from Friedel's law [86], the diffraction pattern is always centrosymmetric, regardless of the actual point group of the crystal. Adding an inversion center to each of the 32 point groups yields 11 Laue classes. Based on the position of reflection in the diffraction pattern, only the Laue class of a crystal can be determined additional to the translation symmetry. Due to anomalous (*i.e.* inelastic) scattering, which is always observed to some degree, Friedel pairs (the reflections hkl and $\bar{h}\bar{k}\bar{l}$ unrelated by the Laue class) may exhibit slightly different intensities. This allows to identify the presence or absence of inversion symmetry and to determine the space group [53, 83].

The intensity of a reflection hkl is determined by the structure factor F_{hkl} , which describes the scattering potential of the crystals basis, *i.e.* the unit cell. It is given by the structure of the unit cell as well as the scattering potential and thermal motion of the contained atoms. In the case of X-ray scattering, the electromagnetic radiation interacts with the electrons of the atoms in the unit cell and, thus, the structure factor is the Fourier transform of the electron density distribution. While F_{hkl} contains the amplitude and phase of the diffracted beam, only the intensity of the diffracted beam $I \propto |F_{hkl}|^2$ is obtained as result of the diffraction experiment and the phase information is lost. Yet, the phase information of the Fourier transform is necessary to gain access to the electron density distribution of the unit cell *via* an inverse Fourier transformation and, subsequently, to determine the atomic structure (phase problem of X-ray crystallography). Therefore, several methods were developed to initially estimate the phase information exploiting general properties of the Fourier transformation and of specific details of the diffraction pattern (*e.g.* direct methods, Patterson method, charge flipping) [53, 83].

After an initial estimate for the phases is obtained, the electron density distribution can be calculated and an initial structural model can be constructed. Based on this structural model, a new set of phases is simulated, which can be used to recalculate the electron density distribution from the diffraction pattern. According to the new electron density distribution, the initial structural model is optimized. This iterative process is called a refinement. The agreement between experimental and simulated reflection intensities is expressed by reliability factors, which are optimized over several refinement cycles [53, 83].

2.2.1. Single Crystal X-ray Diffraction

For single crystal X-ray diffraction (scXRD), a crystal is mounted in the optical path of an X-ray beam. In laboratory devices, the X-ray beam is generated by an X-ray anode. An electron beam is emitted on an anode, which consequently emits X-ray white light, *i.e.* *bremsstrahlung* together with the characteristic X-ray spectrum of the anode material (most commonly Co, Cu, Mo). *Via* a monochromator or an X-ray filter all wavelengths except of a narrow wavelength regime, typically corresponding to the high intensity characteristic K_{α} transitions, are filtered out before the beam interacts with the crystal [83].

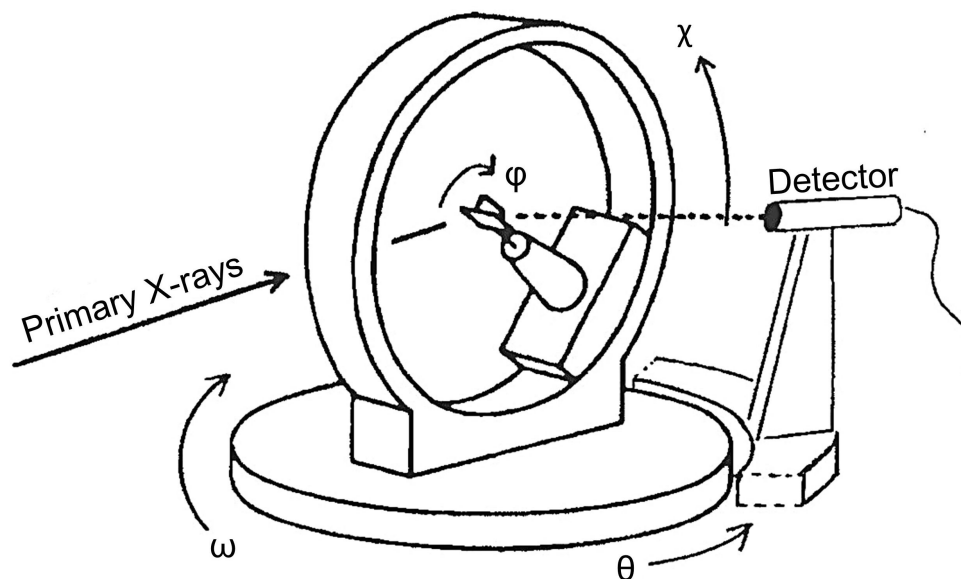


Fig. 2.5.: Schematic drawing of a 4-circle goniometer as used in scXRD, illustrating the rotations along the ϕ , χ , ω and θ circle [83].

The sample mount, as illustrated in Fig. 2.5, allows a precise rotation of the crystal in the beam along three circles (ϕ , χ and ω) while the X-ray detector (typically a CCD point or area detector) moves on a fourth circle with the sample in its center (θ). Consequently, this setup corresponds to a 4-circle diffractometer and allows to detect sections of the diffraction pattern (corresponding to sections of reciprocal space) for any orientation of the crystal to the primary X-ray beam [83].

Depending on its symmetry, the crystal needs to be rotated step-by-step through an angle of up to 180° (*e.g.* for crystals with low symmetry) to reconstruct all necessary details of reciprocal space. To avoid blind spots of the reciprocal space, rotations around independent axis are necessary. Additionally, a high amount of measured reflections is of advantage for the structural solution process, allowing for additional degrees of freedom for the initial phase estimation as well as for the structural refinement and, thus, improves the reliability of the resulting crystal structure model [83].

After the measurement, the indices of the reflections of the separate sections have to be determined (indexing) before the sections can be combined together (integrated) to obtain a single datafile containing all reflection indices and corresponding intensity information. Based on

the integrated data, initial phases for the inverse Fourier transform are estimated as mentioned before and a model for the crystal structure of the unit cell is determined and refined [83].

In this work, scXRD was performed at room temperature on a Bruker X8 Apex2 CCD4K diffractometer with Mo- K_α radiation. The data collection consists of large ω and ϕ scans of the reciprocal space. The frames were integrated with the Bruker SAINT software package [87] using a narrow-frame algorithm in APEX2 [88]. The data were corrected for absorption effects using a semiempirical method based on redundancy with SADABS program [89], developed for scaling and absorption corrections of area detector data. The symmetry determination, structural determination and refinement were performed using charge flipping with the Superflip algorithm [90] within Jana2006 [91] and SHELXL [92].

2.2.2. Powder X-ray Diffraction

Instead of a single crystal, a crystalline powder can be used as a sample in diffraction experiments (powder X-ray diffraction; pXRD). Such a powder consists of a large number of small crystals (crystallites) that are randomly oriented to each other. While the reciprocal space of a single crystal exhibits distinct lattice points, continuous spheres are formed for a powder due to the overlap of the reciprocal space lattices of all differently oriented crystallites. This is illustrated in Fig. 2.6(a). Considering such spheres instead of well defined lattice points in the Ewald sphere shows that for every orientation of the sample to the primary beam every reciprocal lattice vector \mathbf{K} (up to the maximum \mathbf{K} with $|\mathbf{K}| < 2\lambda^{-1}$) fulfills the Laue condition for a certain scattering angle. Correspondingly, the orientation between the sample and the primary beam does not affect the diffraction pattern for a powder sample. Thus, in pXRD only one circle is needed, which is the θ circle with the detector moving around the sample in the center. This simplifies the experimental setup and reduces the measurement time. However, the spatial resolution of the reflections in reciprocal space cannot be observed in pXRD. All reflections corresponding to the same length $|\mathbf{K}|$ overlap as the direction of \mathbf{K} is lost due to the smearing of reciprocal space [83, 93].

The considerations before assume an ideal powder with a homogeneous distribution of every possible orientation for the crystallites. In reality, often some orientation of the crystallites to the primary beam is preferred following from their shape (*e.g.* plate-like crystallites for layered compounds). As consequently not all reflection conditions are fulfilled by the same fraction of the powder, some reflections exhibit a higher and other reflections a lower intensity than expected for the ideal powder [83, 93].

pXRD can be measured in different geometries with the most common one being the Bragg-Brentano reflection geometry, as shown in Fig. 2.6(b). In this geometry, the sample is prepared as a film by mixing powder and an X-ray amorphous glue and applying this mixture as a film on an X-ray amorphous substrate. This film is placed in the center of the goniometer circle on which the X-ray source and the detector are located. The angle between source, sample and detector is changed such that the sample is always tangent to an imaginary circle through source and detector (focusing circle). This is called parafocusing and can be achieved either by moving the source and the detector on the goniometer circle (fixed sample, θ - θ geometry) or by

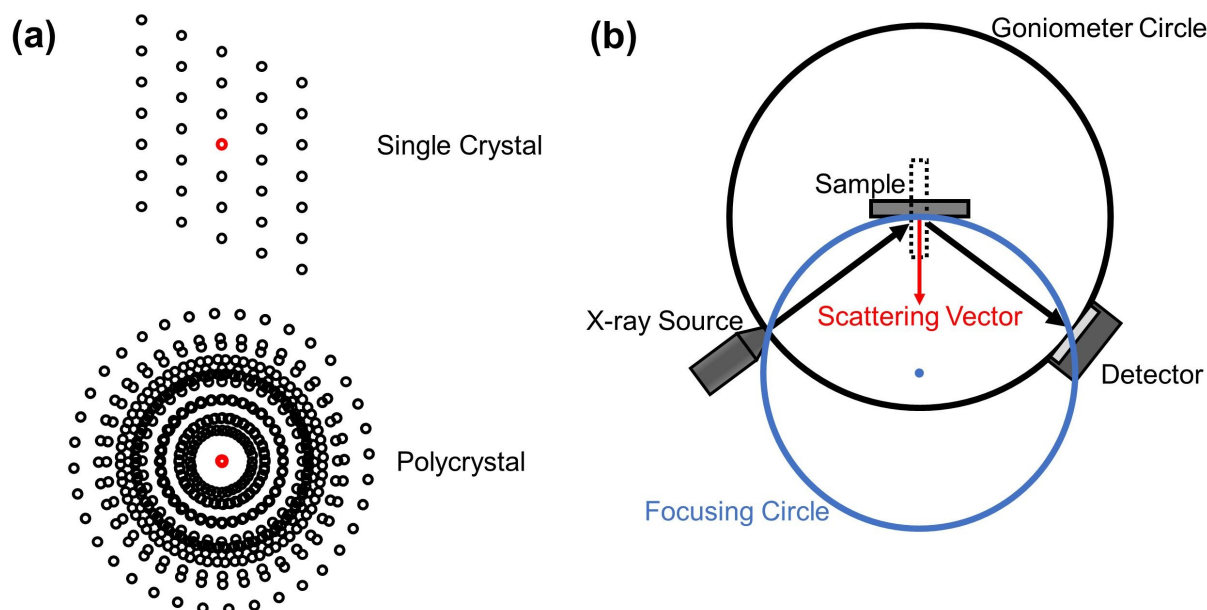


Fig. 2.6.: (a) Top: Schematic two dimensional cut through the reciprocal space lattice of a single crystal. Bottom: Smearing of reciprocal space due to the superposition of the reciprocal lattices of several crystallites. Note that the smearing is much stronger in a real powder with a higher number of crystallites. (b) Illustration of the Bragg-Brentano geometry for pXRD. The arrangement with the solid grey square as sample corresponds to the reflection geometry, while the dotted square corresponds to the transmission geometry.

moving only the detector and simultaneously rotating the sample (fixed source). This reflection geometry ensures that the scattering vector is always perpendicular to the film surface [53, 93].

In the Bragg-Brentano transmission geometry (also shown in Fig. 2.6(b)), the sample is a thin film of a mixture of powder and X-ray amorphous glue which is applied to an X-ray amorphous foil. This sample is placed between source and detector as before. However, for the transmission geometry the thin film is kept always normal to the focusing circle. Consequently, the scattering vector is parallel to the film surface. This geometry was mostly used for the pXRD investigations in this work [53, 93].

The difference in the orientation of the scattering vector relative to the surface of the sample can be exploited to investigate preferred orientation effects. As the scattering vectors for the reflection and the transmission geometry are perpendicular to each other, reflections, which exhibit increased intensity due to preferred orientation of the crystallites in one geometry, are expected to show reduced intensity in the other geometry and *vice versa* [53, 93].

In addition to the aforementioned geometries, the Debye-Scherrer transmission geometry as well as the Guinier geometry are used in pXRD devices. The Debye-Scherrer transmission geometry may be understood as a special case of the Bragg-Brentano transmission geometry for samples with a homogeneous, angle independent shape in the primary beam (*e.g.*, powder in a capillary). Some geometries that do not rely on parafocusing, such as the Zeeman-Bolin, Preston or Guinier geometries, are less commonly used in modern pXRD devices [53, 93].

In general, a powder diffraction pattern allows to be indexed and a Laue group can be determined. Due to the averaging of reciprocal space over the Friedel pairs in powder samples, the absence of inversion symmetry cannot be observed. Furthermore, the phase problem can rarely be solved based on pXRD data alone. Due to the smearing of reciprocal space, the intensity of too less independent reflections is known to analyze the structure factor. However, a pXRD pattern can be used for phase analysis by comparison with pXRD pattern of known phases using corresponding databases. Furthermore, multiphase powders can be investigated and phase fractions can be quantified. Based on the shape of the reflections, information on the size and the strain of crystallites in the sample can be obtained [53, 93].

An initial assumption for the crystal symmetry and the unit cell parameters can be further refined using the Le Bail method which additionally involves several instrumental parameters. With this method, the whole diffraction pattern is fitted using a least square method. However, the reflection intensity is not obtained based on the structure factor of a crystal structure model but rather scaled to fit the experiment. If an initial model for the crystal structure of a compound is already known, a structural refinement is possible based on pXRD data using the Rietveld method. Using this method, a pXRD pattern is simulated with accurate intensities based on the initial structural model. The agreement between the simulated and the experimental pXRD pattern is improved using a least square method by tuning the corresponding structural parameters as well as several instrumental parameters [53, 83, 93].

In this work, pXRD was performed at room temperature on a STOE STADI laboratory diffractometer in transmission geometry with Cu- $K_{\alpha 1}$ radiation from a curved Ge(111) single crystal monochromator and detected by a MYTHEN 1K 12.5°-linear position sensitive detector manufactured by DECTRIS. For the investigation of preferred orientation in $Ni_2P_2S_6$, the transmission pXRD experiment was performed on a STOE STADI device with the same detector and monochromator setup but with Co- $K_{\alpha 1}$ radiation, while the reflection measurement was done on a PANanalytical X'Pert Pro PW3050/60 diffractometer with X'Celerator 1D detector in Bragg-Brentano θ - θ geometry with Co- K_{α} radiation. Jana2006 [91] was used to analyze the pXRD diffraction pattern by the Le Bail method and for structural refinements by the Rietveld method.

2.3. Scanning Electron Microscopy and Energy Dispersive X-ray Spectroscopy

The minimal resolution in microscopy is proportional to the wavelength λ of the radiation. In order to resolve objects in the nm- μ m regime, radiation with a wavelength shorter than visible light has to be used. For this, an electron beam can be used instead of a beam of short wavelength electromagnetic radiation (*i.e.* ultraviolet or X-rays). This has the advantage that an electron beam can be well manipulated by magnetic fields owed to its charge nature, while optical elements for short-wavelength/high-energy electromagnetic radiation pose a challenge for modern science and are subject of ongoing research [94, 95].

To produce such an electron beam, a cathode (*i.e.* a filament of, *i.e.*, tungsten or LaB₆) is heated under vacuum until it emits electrons thermo-ionically. Applying additional high electrostatic fields to the cathode increases the electron yield by Schottky emission. It is even possible to induce electron emission purely by an extremely strong electrostatic field, *i.e.* cold field emission. The free electrons are subsequently accelerated towards the anode with an acceleration voltage U_b . As a matter wave, the wavelength of an electron beam is $\lambda = h/p = h/(m_e v_e)$ according to de Broglie. With $v_e = \sqrt{2U_b e/m_e}$ and $U_b = 10$ kV, this yields $\lambda \approx 10^{-11}$ m, which is in the range of X-ray radiation and allows for a smaller spatial resolution than visible light [95].

The electron beam is focused on a sample *via* electromagnetic lenses and apertures under vacuum. Depending on the setup, either the transmitted electron beam is refocused and imaged *via* an image plate (transmission electron microscopy; TEM) or the sample is scanned with the electron beam and for every spot the radiation products of the interaction between primary electron beam and sample are detected (scanning electron microscopy; SEM). The latter technique of SEM was employed in this work and is explained in more detail in the following section [95].

2.3.1. Scanning Electron Microscopy

As mentioned before, in SEM a sample is scanned by the primary electron beam and the radiation products of the interactions between sample and beam are detected. The interaction between the primary electron beam and the sample causes an energy loss of the primary beam *via* several different mechanisms, as shown in Fig. 2.7. Besides energy being converted into heat, light (cathodoluminescence), X-ray radiation or by emitting Auger electrons, low-energy secondary electrons (SE) are emitted or primary electrons are scattered back from the sample (*i.e.* backscattered electrons; BSE) [95].

SE are low-energy electrons (< 50 eV), which are emitted due to inelastic scattering interactions between the samples conduction or valence bands and the primary beam. Due to their low energy, only SE that emerge close to the sample surface can escape the material before getting absorbed. Consequently, detecting the SE at every spot on the sample during scanning yields information about the texture of the surface, *i.e.* a topographic sample image. To detect these SE, a scintillator in a Faraday cage is used (Everhart-Thornley detector), which is typically mounted slightly above and at one site of the sample [96]. The Faraday cage is charged positively by a small voltage to attract the SE, while higher energy electrons are not significantly affected due to the small charge. The attracted SE in the vicinity of the detector are subsequently attracted to the scintillator by a high positive voltage and converted into photons. The photons are focused to a lightguide and guided out of the vacuum chamber, where an electrical signal is obtained *via* a photomultiplier. The position of the SE detector affects the 'illumination' of the corresponding image. If there is an obstacle (*e.g.* a step or a grain on the surface of the sample) on the direct line between a spot on the sample and the detector, SE will collide with the obstacle and be absorbed. Thus, such spots appear darker (*i.e.* less electrons reach the detector) on the SEM(SE) image than spots without such an obstacle. In

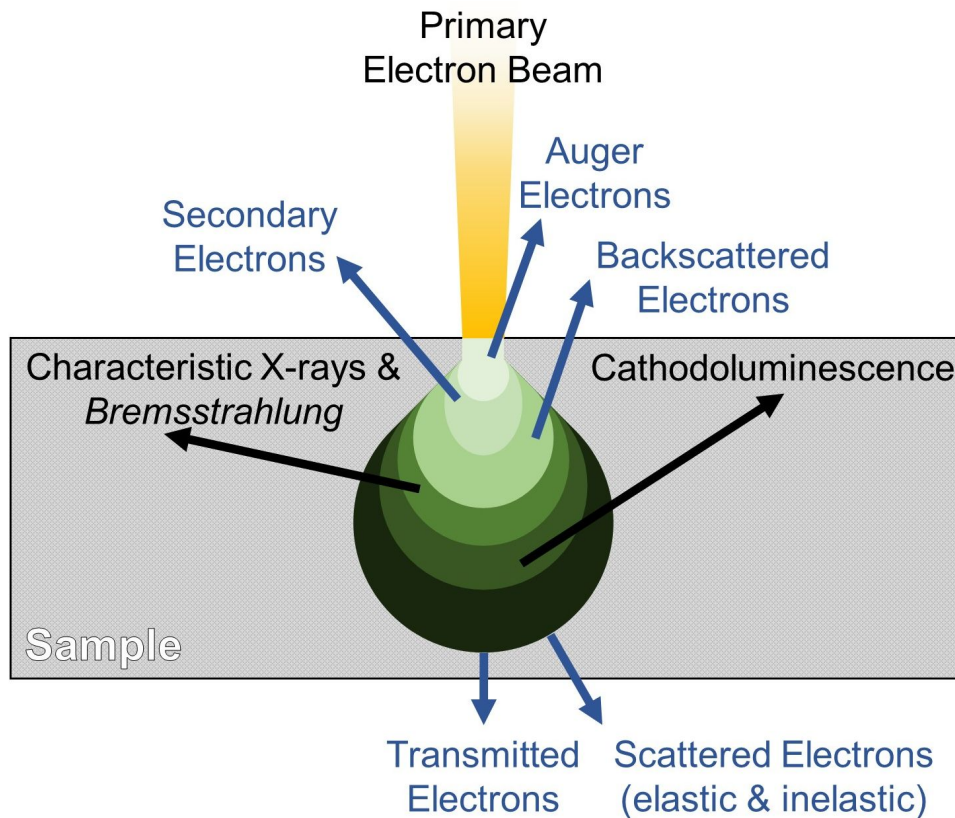


Fig. 2.7.: Schematic illustration of the interaction between the primary electron beam and a sample in an electron microscope. Blue arrows correspond to matter (*i.e.* electron) signals from the sample due to the interaction with the primary electron beam and black arrows correspond to electromagnetic signals. Signals with an arrow pointing to the top can be probed in SEM, while signals with an arrow pointing towards the bottom of the scheme can only be investigated in TEM.

this line, an SEM(SE) image appears to be taken from the direction of the primary beam but illuminated from the detector [95].

BSE are high-energy primary electrons, which are reflected or backscattered from the sample due to elastic scattering with the atoms in the sample. Atoms with a high atomic number cause an increased backscattering of electrons than atoms with a low atomic number. Consequently, spots with a composition corresponding to a higher mean atomic number appear brighter in an SEM(BSE) image than spots with a lower mean atomic number. Thus, the BSE detector yields a chemical contrast. Due to their high energy, BSE can emerge deeper in the sample than SE and still reach the sample surface without being absorbed and they are not affected by the small charge of the Everhart-Thornley detector. Therefore, BSE are detected by a separate detector positioned above the sample as a ring through which the primary beam is guided. This detector is either made of a scintillator or a semiconductor to detect the electrons. Following from the position of the BSE detector above the sample, SEM(BSE) images seem to be illuminated from the direction of which the image is taken [95].

As the SEM image is not directly obtained from the primary beam, the resolution of this technique is not directly dependent on the wavelength of the primary beam but rather on the

interaction volume between primary beam and sample. This volume is influenced by the spot size of the beam on the sample and the energy (*i.e.* wavelength) of the primary beam [95].

2.3.2. Energy Dispersive X-ray Spectroscopy

As mentioned before, the energy loss of the primary beam due to the interaction with the sample causes, *inter alia*, the emission of X-ray radiation. This radiation contains two contributions: *bremsstrahlung* and characteristic X-ray radiation. The *bremsstrahlung* is obtained due to the deceleration of primary electrons in the sample and yields a continuous contribution to the X-ray spectrum with a maximum energy corresponding to the energy of the primary electron (*i.e.* a primary electron is abruptly stopped in the sample and all kinetic energy is emitted as an X-ray photon) [95, 97].

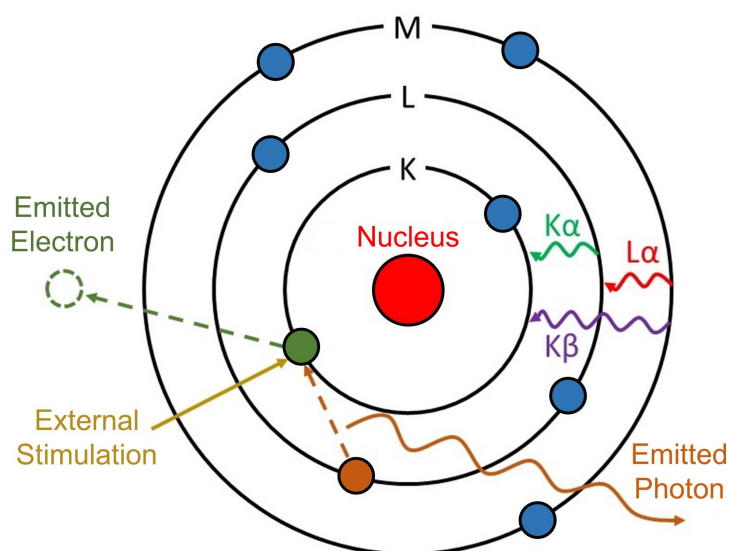


Fig. 2.8.: Schematic illustration of the generation of characteristic X-ray radiation. The labeling of the possible transitions is shown on the left. In the style of Ref. [97].

X-ray radiation of a characteristic energy is emitted if an outer shell electron in an atom fills a vacant inner shell hole and releases the difference in energy. This process follows up on the ejection of an inner shell electron due to the bombardment with high energy particles (here: primary electrons) and is illustrated in Fig. 2.8. The energy of such transitions between an electron in a certain outer shell and a certain inner shell is characteristic to each element and, thus, each element has its characteristic X-ray spectrum [97].

In energy dispersive X-ray spectroscopy (EDX) this effect is used to determine the elements and estimate the composition of a sample. Accordingly, irradiating a spot on the sample with the primary electron beam and measuring the emitted X-ray spectrum yields the superimposed characteristic spectra of all elements present at a spot on the sample together with the *bremsstrahlung*. After subtracting the contribution from the *bremsstrahlung*, the superimposed X-ray spectra can be deconvoluted and, based on the intensity of the separate characteristic spectra, an estimate for the relative atomic composition is obtained [95, 97].

The reliability of this estimate depends on a homogeneous yield of X-ray photons generated by the different elements. In the sample, the X-ray photons are emitted in all directions homogeneously, such that only a fraction of generated X-rays leave the sample at all. X-rays that do not leave the sample can potentially cause the ejection of another core electron somewhere in the sample and, consequently, the emission of characteristic X-ray radiation from outside the measured spot. In general, the mean distance that an X-ray photon can travel in a material before strongly interacting with it depends on the energy of the photon as well as the density and composition of the material. Thus, the lower the energy the higher the fraction of X-rays that are absorbed before leaving the sample. Consequently, the reliability for light elements (corresponding to low energy characteristic transitions) is low and the measured X-ray spectrum has to be corrected due to absorption and related effects in the sample. Furthermore, a flat sample surface is important for EDX measurements to ensure a homogeneous interaction volume for the X-ray emission as well as consistent conditions for X-rays to leave the sample. Further inaccuracies may arise from elements with similar characteristic transition energies and the corresponding overlap of peaks in the X-ray spectrum affecting the deconvolution process [97].

Nevertheless, EDX also exhibits several advantages over more precise methods to determine the elemental composition, such as mass spectrometry. EDX is non-destructive and allows to investigate the homogeneity of the elemental composition in a sample by several measurements on different spots. Especially for samples with a flat surface, changes in the elemental composition can be probed with a good reliability, although the absolute elemental ratios are less reliable due to the aforementioned reasons. Combining EDX with SEM allows to detect areas of different composition by BSE and to locally quantify their elemental composition, while SE can be used to identify suitable flat surfaces. Furthermore, spatial resolved information on the elemental distribution can be obtained by EDX line scans or mapping. For these techniques, a line or an area on the sample are divided into pixel and for each pixel an EDX spectrum is measured under the same conditions. Consequently, the spatial distribution of the intensity at a characteristic energy of each element color-coded illustrates the spatial distribution of all elements over the investigated line or area [95, 97].

In this work, a ZEISS EVO MA 10 scanning electron microscope was used for electron microscopic images either with a SE detector for topographic contrast or a BSE detector for chemical contrast. EDX was measured with the same device using an energy dispersive X-ray analyzer. For an investigation on a layered single crystal, such a crystal was initially exfoliated to obtain a flat and pristine surface and, subsequently, attached to a sample holder with sticky carbon tape. For polycrystalline samples (as investigated in Sect. 4.3), grains of the polycrystalline material were embedded in an epoxy resin mixed with fine Ni powder to ensure conductivity. Such a resin puck was, subsequently, ground and polished until a flat surface containing several polycrystalline grains was obtained. These samples were investigated in the SEM initially at low magnification using the SE and BSE detectors to obtain an overview of the morphology and phase composition. At several locations of interest, the study was resumed at higher magnification. Furthermore, SEM images were captured at different magnifications in this phase. After a general overview of the sample and its phase composition was obtained from SEM, areas that fulfill the requirement of a flat surface area and are representative of the samples phase composition were located and subjected to several EDX measurements. This procedure was repeated on several areas on one sample. If this EDX investigation revealed inhom-

genities of the chemical composition that were not expected from the corresponding BSE images, EDX mappings were conducted to reveal their origins (as, *i.e.*, for $(\text{Cu}_{0.75}\text{Ag}_{0.25})\text{CrP}_2\text{S}_6$ and $(\text{Cu}_{0.50}\text{Ag}_{0.50})\text{CrP}_2\text{S}_6$ in Sect. 4.3).

2.4. Magnetometry

A superconducting quantum interference device (SQUID) magnetometer was used for the measurements of the magnetic properties. The SQUID is a superconducting ring with two Josephson junctions on opposite sites (dc-SQUID). The magnetic flux through a superconducting ring is quantized as a multiple of the magnetic flux quantum $\Phi_0 = h/(2e)$. Changing the magnetic field induces a loop current in the superconducting ring, which compensates the magnetic flux through the ring to the closest $n \Phi_0$ [98]. Applying an external dc-current to the system induces a voltage over the Josephson junctions, which is affected by the loop current in the ring. Consequently, a periodic flux–voltage dependence is observed with the periodicity of exactly one magnetic flux quantum. The same dependence can be observed for a superconducting ring with only one Josephson junction and an applied ac-current in the range of several 10 MHz (rf-SQUID). To measure changes of the magnetic flux that are larger than Φ_0 , the voltage over the SQUID is detected and kept constant by a feedback loop. *Via* an induction coil close to the SQUID the change of the magnetic flux through the ring is compensated. Consequently, the feedback current through the induction coil is proportional to the external magnetic flux [65, 98, 99].

This setup is used in SQUID magnetometry to measure the magnetic moment of a sample at high sensitivity. For this, a sample is moved through a pickup coil, inducing a current. Following from Faraday’s law of induction, only the magnetization component along the direction of movement of the sample can be measured. The induced current flows through an induction coil close to the SQUID changing the flux through the superconducting ring. *Via* the setup described before, this change in flux is compensated and transformed in a measurable current. The sample is moved through the pickup coil repeatedly and the output current is measured as function of the sample position. Such a flux profile is fitted by the expected flux profile of a point dipole to obtain the magnetic moment [65, 99].

The SQUID can be also used as amplifier in a vibrating sample magnetometer (VSM), in which a sample is vibrated in a homogeneous magnetic field with a certain frequency. The periodic oscillation of the sample causes a detectable change in the magnetic flux. In classical VSM this signal is amplified and measured by a lock-in amplifier, while in SQUID VSM a SQUID is used, improving the sensitivity of the device. To relate the measured current from a VSM to magnetic moments, the device is calibrated with a standard of known magnetic properties (*e.g.* a Pd cube of defined dimensions) [65, 99].

For both devices described before, the pickup coil with the sample is inside a (superconducting) magnet such that the external magnetic dc- or ac-field is homogeneous and parallel to the axis of sample movement. Furthermore, the temperature in the sample space can be varied over a wide range (*e.g.* 1.8–400 K) to allow for field and temperature dependent measurements. In a conventional SQUID magnetometer, for each value of temperature and field a

full flux profile is measured, while in a SQUID VSM a magnetic moment can be deduced from each oscillation of the sample, allowing for a faster measurement [99].

In this work, DC magnetization was measured as a function of temperature and magnetic field using a SQUID VSM and a conventional SQUID magnetometer, both from Quantum Design. The conventional SQUID magnetometer was equipped with a 5.5 T magnet and could be stabilized at a minimum temperature of 5 K for an elongated time. This device was only used for the magnetic measurements on CuCrP_2S_6 (excluding the $M(H)$ dependence at 1.8 K and up to 7 T, which was measured at the SQUID VSM). For the magnetic measurements on all other compounds, a SQUID VSM with a 7 T magnet and the capability of heating up to 400 K as well as stabilizing 1.8 K over elongated times was used. For the measurements with the conventional SQUID magnetometer, samples were glued to a paper stripe with Duosan such that the sample was in the desired orientation to the field in the SQUID. The paper stripe with the sample was fixed inside a plastic straw and the setup was mounted to the SQUID sample rod and introduced in the sample chamber. For the measurements with the SQUID VSM, samples were glued with Duosan to a quartz sample holder in the desired orientation. The quartz holder was mounted to the sample rod and introduced into the sample chamber. In both cases, the background contribution from the sample holder setup was not explicitly taken into account. However, for the measurements of ferromagnetic $\text{Cr}_2\text{Ge}_2\text{Te}_6$ on the VSM, a shape correction was performed due to the high magnetic moments and the large sample size which led to notable deviations from the behavior of a point dipole. This correction followed a procedure described by the device manufacturer Quantum Design [100].

2.5. Nuclear Magnetic Resonance Spectroscopy

Nuclei exhibit a non-zero nuclear spin, if they contain either an odd number of protons or neutrons or an odd number of both nucleons. As the magnetic dipole moment of a particle is inversely proportional to its mass, the nuclear magnetic moment is orders of magnitude smaller than the electron magnetic moment and, thus, was neglected in the considerations about the magnetic properties before [101].

In an external magnetic field B , the energy levels of a spin split up due to the Zeeman effect. This is the case for both electron spins and nuclear spins. The energy difference between states due to the Zeeman splitting is $\Delta E = \hbar\gamma B$ with the reduced Planck constant \hbar and the gyromagnetic ratio $\gamma = g\mu/\hbar$ with the gyromagnetic factor (Landé factor) g and the magnetic moment μ of the particle. As the nuclear magnetic moment is orders of magnitude smaller than the electron magnetic moment, also the energy differences in the Zeeman effect differ notably. Applying ΔE to a system of spins induces transitions between the split spin states in the Zeeman effect. Consequently, a spectrum with distinct absorption lines can be obtained as function of the applied energy. This is exploited in electron spin resonance (ESR) spectroscopy probing the electronic system and in nuclear magnetic resonance (NMR) probing the spins of certain nuclei [101].

In modern NMR a fourier transform process is used. The excitation energy is applied by an oscillating magnetic field using a radio frequency pulse *via* a coil around a sample. Due to

the bandwidth of the pulse, a whole range of energies are excited at once. The phase of the radio frequency pulse causes the nuclear magnetic moments to precess in phase around the external magnetic field B with the Larmor frequency $f = \gamma B/2\pi$. Thus, an oscillating voltage is induced in the coil around the sample. The induced voltage as function of time is called the free induction decay and yields the NMR spectrum of the excited bandwidth via Fourier transformation [101].

As γ is known for each nucleus, ΔE and the Larmor frequency f can be calculated for a magnetic field B . However, the absorption line for a certain nucleus is found at slightly different energies/frequencies than expected from the gyromagnetic ratio. This effect is called chemical shift δ and is caused by a slight change of the magnetic field experienced by the nucleus due to its local electronic environment via hyperfine fields. As different coordination environments or bonding situations change the electronic environment and, thus, the chemical shift δ , structural information can be extracted from the spectrum. Furthermore, changes in the electron spin system as well as in the electronic band structure can be probed by NMR [101]. Additionally, the time dependent relaxation of the nuclear spin system to thermal equilibrium yields information on changes in the local environment of the nuclei, *e.g.* as function of temperature.

In this work, NMR spectroscopy was measured on the ^{31}P nuclei of $\text{Ni}_2\text{P}_2\text{S}_6$ single crystals. These experiments were conducted in a 7 T superconducting magnet using a home-built probe with a single-axis goniometer for sample rotation and alignment. The sample temperature was controlled using a flow cryostat from Janis (sample in helium gas) with a calibrated Lakeshore Cernox temperature sensor. NMR measurements were performed with an Apollo spectrometer from Tecmag. For the spectral measurements shown in Sect. 3.1.4, a standard spin-echo pulse sequence ($\pi/2-\pi$) was used. The delay time between the $\pi/2$ and π pulses was $\tau = 500 \mu\text{s}$ for the measurements in the normal state and $\tau = 50 \mu\text{s}$ for the measurements in the magnetic state.

2.6. Specific Heat Capacity

The specific heat capacity at constant pressure C_p is related to the free energy of a system F as shown in Eq. 2.9.

$$C_p = T(\partial S/\partial T)_p = -T(\partial^2 F/\partial T^2)_p \quad (2.9)$$

Thus, a second order phase transition according to Ehrenfest, such as a magnetic phase transition, causes a discontinuity in the evolution of the specific heat [72]. Consequently, the specific heat can be used to investigate the nature and evolution of phase transitions. Furthermore, the evolution of the specific heat corresponds to the entropy change and, thus, contains contributions of the phononic, electronic and spin systems for a solid system [102].

In this work, the specific heat was measured using a relaxation technique. *Via* a heat pulse of an electrical heater, a defined amount of heat is induced in the sample, which is connected to a thermal reservoir. Subsequently, the temperature decay is measured as function of time with a thermometer. The temperature decay follows an exponential behavior corresponding to Eq. 2.10 and with the specific heat capacity C can be obtained according to Eq. 2.11 [103].

$$\Delta T = \Delta T_{\max}[1 - \exp(-t/\tau)] \quad (2.10)$$

$$C = P\tau/\Delta T_{\max} \quad (2.11)$$

For the measurements of the specific heat capacity of $\text{Cr}_2\text{Ge}_2\text{Te}_6$ as function of temperature and magnetic field, a Physical Property Measurement System (PPMS) from Quantum Design was used which in principle allows for measurements at temperatures down to 0.5 K and under applied magnetic fields of up to 9 T. For measurements with the magnetic field out-of-plane of a plate-like $\text{Cr}_2\text{Ge}_2\text{Te}_6$ crystal (*i.e.* $H \perp ab$), the crystal was directly mounted to the specific heat puck. However for measurements with $H \parallel ab$, the crystal was mounted to a copper block, which was subsequently mounted on the specific heat puck to achieve the desired orientation between the crystal and the magnetic field. The specific heat from the platform, the copper block and grease used for mounting the sample were measured separately and subtracted from the experimental data.

3. $M_2P_2S_6$

The $M_2P_2S_6$ compounds (M being a main group metal or transition metal with a 2+ oxidation state) are a subclass of the family of metal trichalcogenides crystallizing in the monoclinic space group $C2/m$ (No. 12), as introduced in Sect. 1.1. The corresponding monoclinic structure was first discovered for the structural archetype $Fe_2P_2S_6$ by Klingen *et al.* [104]. Following on this report, Taylor *et al.* [105] as well as Brec *et al.* [106] found that most other $M_2P_2S_6$ compounds are isostructural to $Fe_2P_2S_6$.

The ICSD¹ lists ten $M_2P_2S_6$ compounds in the $C2/m$ space group, as summarized in Table 3.1. $Hg_2P_2S_6$ (ICSD Code: 639130; [104]) differs from the other compounds as it exhibits the triclinic space group $P\bar{1}$ (No. 2) and a distorted $Fe_2P_2S_6$ structure [108]. Additionally, substitution between two of the before mentioned isostructural compounds has been successfully performed, as for example demonstrated for $(Zn_{1-x}Fe_x)_2P_2S_6$ and $(Zn_{1-x}Ni_x)_2P_2S_6$ [41].

Table 3.1.: Isostructural $M_2P_2S_6$ compounds in the monoclinic $C2/m$ space group according to the ICSD.

Compound	ICSD Code	Ref.
Main-group metal compounds		
$Mg_2P_2S_6$	642729	[109]
$Sn_2P_2S_6$	648056	[110]
Transition metal compounds		
$V_{1.56}P_2S_6$	648076	[111]
$Mn_2P_2S_6$	61391	[112]
$Fe_2P_2S_6$	27307	[104]
$Co_2P_2S_6$	61394	[112]
$Ni_2P_2S_6$	259148	[43]
$Zn_2P_2S_6$	79557	[113]
$Pd_2P_2S_6$	647926	[110]
$Cd_2P_2S_6$	79556	[113]

$M_2P_2S_6$ compounds are, in general, insulators or broad-band semiconductors [41, 60]. Magnetically, the main group metal compounds as well as $Zn_2P_2S_6$, $Cd_2P_2S_6$ and $Hg_2P_2S_6$ are expected to be diamagnets as they are closed shell systems ($S = 0$). However, for the transition element compounds $Mn_2P_2S_6$ ($S = 5/2$), $Fe_2P_2S_6$ ($S = 2$), $Co_2P_2S_6$ ($S = 3/2$) and $Ni_2P_2S_6$ ($S = 1$) an antiferromagnetic ground state was found in bulk samples [114]. Above their magnetic ordering temperature, all these compounds exhibit a short range magnetic correlated regime typical for low-dimensional magnets. The $M_2P_2S_6$ compounds with $M = Mn, Fe, Co, Ni$ exhibit different magnetic anisotropy strengths making them model systems to investigate the influence of magnetic anisotropy on low-dimensional magnetism [43]. $Mn_2P_2S_6$ is isotropic [115], $Fe_2P_2S_6$ is Ising-like (*i.e.* strongly anisotropic) [116] and $Co_2P_2S_6$ as well as $Ni_2P_2S_6$ exhibit an intermediate anisotropy strength [117, 118]. Substitution between these compounds may yield exotic magnetic states resulting from the interplay of different magnetic anisotropies, as demonstrated by a spin glass state in $(Mn_{0.5}Fe_{0.5})_2P_2S_6$ [119], .

¹Inorganic Crystal Structure Database (<http://icsd.fiz-karlsruhe.de>) [107], accessed July 2020.

In the course of this work, a substitution series between the two transition metal compounds $Fe_2P_2S_6$ and $Ni_2P_2S_6$ was produced. Both parent compounds as well as four intermediate compounds of the general composition $(Fe_{1-x}Ni_x)_2P_2S_6$ were grown as single crystals and investigated regarding their structure and magnetic behavior. Hereafter, $Ni_2P_2S_6$ as well as the substitution series $(Fe_{1-x}Ni_x)_2P_2S_6$ are introduced comprehensively and the findings of the experimental studies are presented.

It should be noted that the synthesis of the $(Fe_{1-x}Ni_x)_2P_2S_6$ substitution series and the corresponding magnetic measurements were done in close cooperation with Yuliia Shemerliuk in the course of her master thesis at the Institute for Solid State Research, Leibniz IFW Dresden and are therefore reported as part of her master thesis [120]. However, the detailed structural analysis and the extensive discussion of the evolution of the magnetic properties of these compounds are unique to the work at hand. Following the results presented here, preliminary experiments including synthesis and growth experiments with focus on the substitution degree of $0.9 \leq x \leq 1$ in $(Fe_{1-x}Ni_x)_2P_2S_6$ were done by Tamara Holub at the Institute for Solid State Research, Leibniz IFW Dresden and are consequently part of her master thesis [121].

3.1. $Ni_2P_2S_6$

$Ni_2P_2S_6$ is a member of the class of $M_2P_2S_6$ compounds and was first synthesized by Hahn and Klingens in 1965 [122]. First macroscopic single crystals of $Ni_2P_2S_6$ were reported by Taylor *et al.* [105] in 1973 using the chemical vapor transport technique. The general structural motifs are the same as for $Fe_2P_2S_6$ described in Sect. 1.1. However, additionally site disorder between M and the P_2 dimer has been reported for $Ni_2P_2S_6$ (as well as for $Co_2P_2S_6$) by Ouvrard *et al.* [112] based on scXRD. More recent reports by Lançon *et al.* [117] as well as Goossens *et al.* [123] question if the site disorder in $Ni_2P_2S_6$ is real or rather an artifact in the structural solution process due to the presence of a large number of stacking faults. Such crystallographic defects are commonly found in layered compounds with vanishing interlayer interactions such as $Ni_2P_2S_6$ [124].

$Ni_2P_2S_6$ is an insulator with an optical gap of approximately 1.8 eV [125] and antiferromagnetic order sets in below $T_N \approx 155$ K [43, 114, 126]. In the magnetically ordered state, $Ni_2P_2S_6$ forms ferromagnetic chains along the a direction, which couple antiferromagnetically to adjacent chains in the ab plane (stripe-like antiferromagnetic order). Such layers are coupled ferromagnetically along the monoclinic c direction. The preferred orientation of the magnetic Ni-moments is found mostly along the a direction with a weak contribution in c direction [43]. A perspective drawing of the crystal structure with the orientation of the magnetic moments at 2 K according to Wildes *et al.* [43] is shown in Fig. 3.1. Please note, that the structure is shown without Ni- P_2 site disorder in agreement with Wildes *et al.* who reported that only the moments on the Ni-majority sites gave a robust refinement while moments on the Ni-minority sites did not refine reliably. Above T_N , a broad maximum in the thermal evolution of the susceptibility is ascribed to low-dimensional short range magnetic correlations [66, 114]. Compared to its sister $M_2P_2S_6$ compounds with $M = Mn, Fe$ and Co , $Ni_2P_2S_6$ exhibits the highest ordering temperature as well as the broadest regime of low-dimensional magnetic correla-

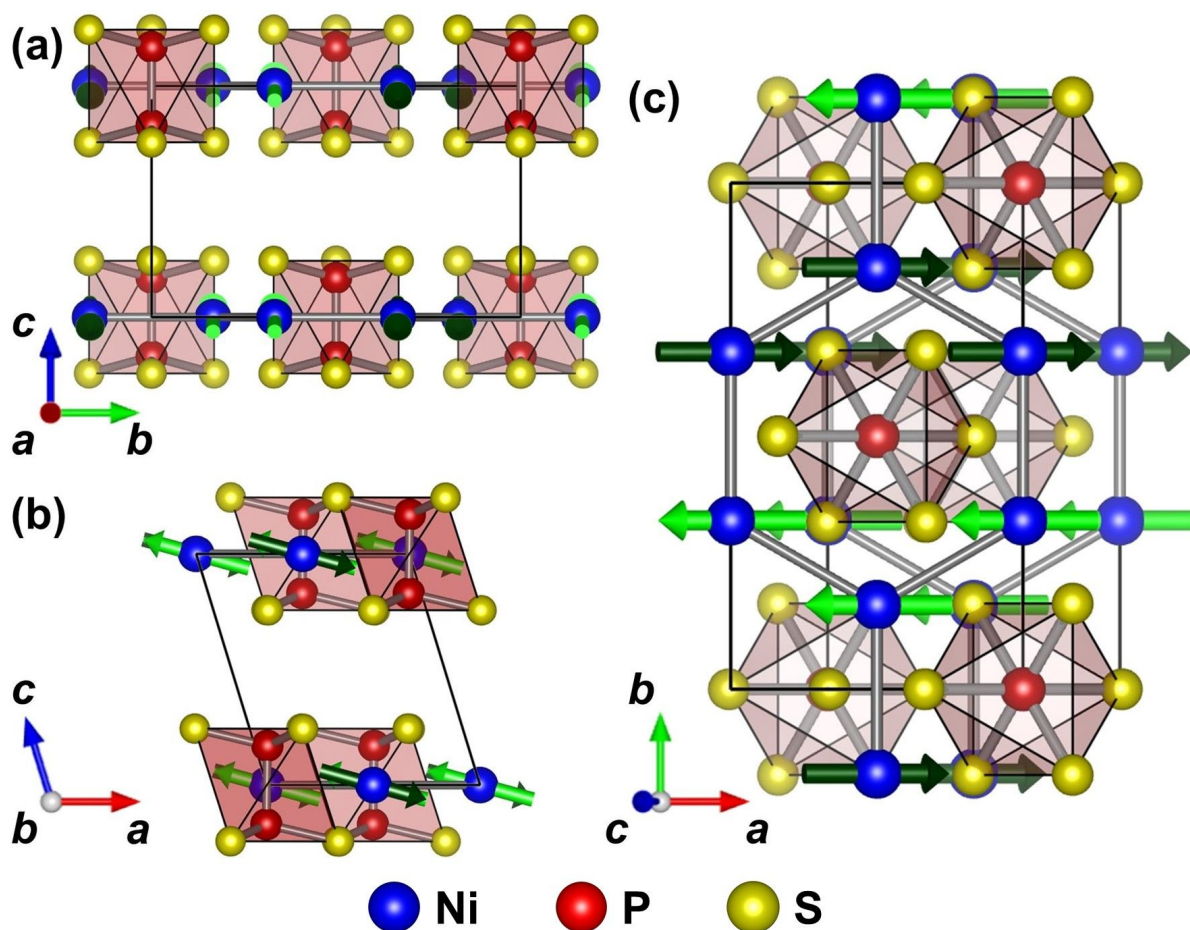


Fig. 3.1.: Perspective drawing of the crystal structure of $\text{Ni}_2\text{P}_2\text{S}_6$ and orientation of the magnetic moments of Ni at 2 K according to Wildes *et al.* [43]. View along (a) the a direction ($\perp bc$ plane), (b) the b direction ($\perp ac$ plane) and (c) the c^* direction ($\perp ab$ plane). The red octahedra illustrate the P_2S_6 structural units. Bright and dark green arrows illustrate the moment orientations and are drawn in different colors to improve the visibility of the stripe-like antiferromagnetic order.

tions. However, not only the relatively high ordering temperature but also the intermediate anisotropy strength make $\text{Ni}_2\text{P}_2\text{S}_6$ an interesting compound for investigations of magnetism in low-dimensional compounds. Furthermore, the intermediate magnetic anisotropy combined with a low-dimensional system is promising to yield access to exotic magnetic states, such as the highly unusual short range correlated ground state that was demonstrated by Berezinskii [71] as well as Kosterlitz and Thouless [46] for the XY model in 2D [45], as introduced in Sect. 1.2.5. While such a state may not be realized in $\text{Ni}_2\text{P}_2\text{S}_6$ itself or, at least, was not found until now, it may be a good starting candidate for tuning the magnetic anisotropy towards the desired XY-anisotropy.

Nevertheless, before being able to fully understand and subsequently tune the physical properties of $\text{Ni}_2\text{P}_2\text{S}_6$, the open structural questions, such as the presence or absence of Ni-P₂ site disorder as well as the role of stacking faults, have to be addressed.

Single crystals of $\text{Ni}_2\text{P}_2\text{S}_6$ were grown by chemical vapor transport using iodine as transport agent as presented in Sect. 3.1.1. These crystals were extensively characterized by SEM and

EDX regarding their morphology and composition and scXRD and pXRD were used to investigate the crystal structure (see Sect. 3.1.2). This combination of characterization techniques allowed to address the Ni-P₂ site disorder and stacking faults in the Ni₂P₂S₆ crystals grown in this work as well as general challenges of pXRD on highly textured samples. In Sect. 3.1.3, the bulk magnetic properties of Ni₂P₂S₆ are discussed which were measured for magnetic fields along three specific in-plane and one out-of-plane directions. The in-plane directions imply an unexpected angular dependence of the magnetization, which is discussed in the context of a potential 120° rotational twinning in Ni₂P₂S₆. As a complementary local probe technique to both the X-ray structural analysis as well as the bulk magnetization investigation, ³¹P NMR spectroscopy was used to obtain further insight into the local structure as well as the local magnetic behavior. As discussed in Sect. 3.1.4, NMR spectroscopy does not exhibit any indication for the Ni-P₂ site disorder and agrees with the unexpected in-plane angular dependence observed in the magnetic study explainable by twinning. In Sect. 3.1.5, the 120° rotational twinning in Ni₂P₂S₆ is derived from the crystal structure of a single layer in interplay with the monoclinic stacking in form of a thought experiment. Consequently, the three possible monoclinic stacking directions of the $C2/m$ space group with respect to the adjacent layer favor 120° rotational twinning.

Parts of the following section (characterization and results from ³¹P NMR spectroscopy) are published in A. P. Dioguardi, S. Selter *et al.*, Physical Review B **102**, 064429 (2020) [127].

3.1.1. Crystal Growth

Single crystals of Ni₂P₂S₆ were grown using the chemical vapor transport (CVT) technique with iodine as the transport agent. The temperature profile of the growth was adopted from Taylor *et al.* [105].

In a glove box under argon atmosphere, the elemental educts nickel (powder -100 mesh, Sigma Aldrich, 99.99%), phosphorus (red, lumps, Alfa Aesar, 99.999%) and sulfur (pieces, Alfa Aesar, 99.999%) were weighed out to yield a molar ratio of Ni : P : S = 2 : 2 : 6 and homogenized in an agate mortar. 0.5 g of reaction mixture were loaded in a quartz ampule (6 mm inner diameter, 2 mm wall thickness, which was previously baked out at 800 °C for at least 12 h) together with a small quantity (approx. 5 mol-% with respect to Ni) of the transport agent iodine (re-sublimed crystals, Alfa Aesar, 99.9985%). The ampule was then transferred to a vacuum pump and evacuated to a residual pressure of 10⁻⁸ bar. To suppress the unintended sublimation of the transport agent during evacuation, the lower end of the ampule containing the reaction mixture was cooled with liquid nitrogen. After reaching the desired internal pressure, the valve to the vacuum pump was closed, the cooling was stopped and the ampule was sealed under static pressure at a length of approximately 12 cm.

The ampule was placed horizontally in a two-zone tube furnace in such a way that the elemental mixture was only at one side of the ampule which is called the charge side. The furnace was heated homogeneously to 750 °C at 100 °C/h. The charge side was kept at this temperature for 394.5 h while the other side of the ampule which is the sink side was initially heated up to 800 °C at 100 °C/h, dwelled at this temperature for 24 h and then cooled back to

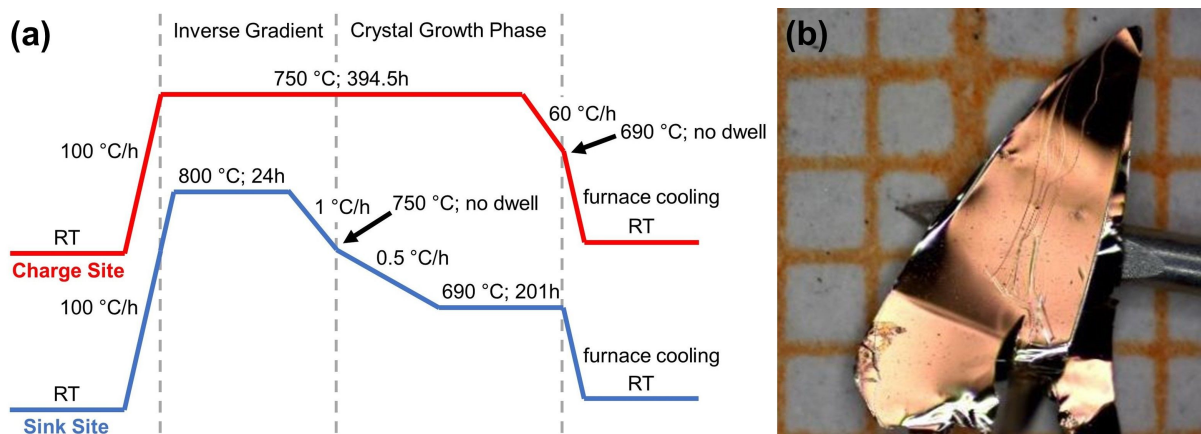


Fig. 3.2.: (a) Schematic representation of the temperature profile as function of time for the single crystal growth of $Ni_2P_2S_6$ using CVT. The charge site temperature profile is shown in red and the sink site profile in blue. (b) Photographic image of a plate-like crystal obtained from the CVT growth experiment with iodine as transport agent. One orange square equals 1 mm \times 1 mm for scale. The same image as in (b) is shown in the master thesis of Shemerliuk [120].

750 °C at 1 °C/h. An inverse transport gradient is formed, *i.e.* transport from sink to charge, to clean the sink side of particles which stuck to the walls of the quartz ampule during filling. This ensures improved nucleation conditions in the following step. Then the sink side was cooled to 690 °C at 0.5 °C/h to slowly form the thermal transport gradient resulting in a controlled nucleation. Then the ampule was dwelled with a transport gradient of 750 °C (charge) to 690 °C (sink) for 200 h. After this the charge side was cooled to the sink temperature in 1 h before both sides were furnace cooled to room temperature. This temperature profile is graphically illustrated in Fig. 3.2(a).

Shiny plate-like crystals of $Ni_2P_2S_6$ of up to 4 mm \times 3 mm \times 200 μ m were obtained. Fig. 3.2(b) shows an exemplary as-grown single crystal. The crystals exhibit a layered morphology and a ductile nature. Furthermore, the crystals are easily exfoliated which is a typical feature of these layered compounds. Further crystal growth experiments without the addition of any halogen yielded no notable formation of crystals. This implies that $Ni_2P_2S_6$ (and, in extension, most likely all $M_2P_2S_6$) grows *via* a chemical vapor transport mechanism and not *via* a physical transport mechanism following a phase formation in the solid state (*i.e.* sublimation and recondensation).

3.1.2. Characterization

Crystal Morphology and Compositional Analysis

Fig. 3.3 shows SEM images of an as-grown crystal with topographical contrast (using an SE detector) and with chemical contrast (BSE detector). In the SEM(SE) image, a flat surface is observed with some layers peeling off from the bulk of the crystal. Additionally, several crystalline edge facets forming angles of $\approx 120^\circ$ illustrate the hexagonal crystal habitus (*e.g.* bot-

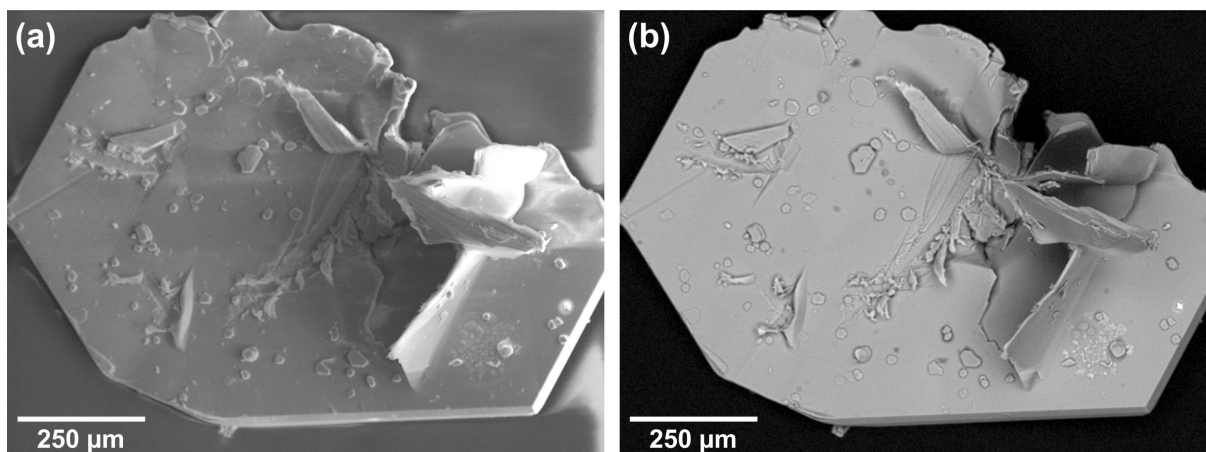


Fig. 3.3.: SEM images of a crystal obtained from the aforementioned growth experiment with (a) topographical contrast (SE detector) and (b) chemical contrast (BSE detector).

tom right). The SEM(BSE) image exhibits a homogeneous contrast of the crystal surface. Some spots of different contrast can be clearly attributed to particles on the surface of the crystal rather than intrinsic impurities by comparing SEM(BSE) and SEM(SE) images. Accordingly, the crystal exhibits a homogeneous elemental distribution on the shown surface.

The mean elemental composition was quantified from EDX spectroscopy which was performed on several spots on multiple crystals of the same crystal growth experiment. The obtained mean elemental composition of $Ni_{20.5(1)}P_{20.3(1)}S_{59.2(1)}$ is in ideal agreement with the expected composition of $Ni_{20}P_{20}S_{60}$. The low standard deviations of the mean ratios are exemplary for a homogeneous elemental distribution. Furthermore, no iodine was found incorporated in the crystals.

Structural Analysis

All reflections obtained from scXRD² on a $Ni_2P_2S_6$ single crystal are well indexed by a monoclinic unit cell with space group $C2/m$ (No. 12) with the lattice parameters given in Table 3.2 in agreement with literature [106, 112]. Brec *et al.* initially reported $Ni_2P_2S_6$ to be isostructural to $Fe_2P_2S_6$ [106]. Using the corresponding structural model (hereafter named the ordered model) as a model for the structural refinement of the scXRD data yields the refined atomic positions, occupancies and thermal displacement parameters given in Table 3.3 (top) together with the reliability factors shown at the bottom of Table 3.2. While the refined atomic positions are in agreement with the starting model and the thermal displacement parameters are physically reasonable, the reliability values are unusually high and a notable residual electron density is not assigned to any atoms. As shown in Fig. 3.4 (left), the residual electron density is rather localized implying missing atomic sites in the model. Residual density is found in the center of mass between the two P atoms of the P_2 dimer in the common (001) plane of Ni

²scXRD experiments were carried out by Dr. Mihai-Ionut Sturza (IFW Dresden) and are shown with his kind permission.

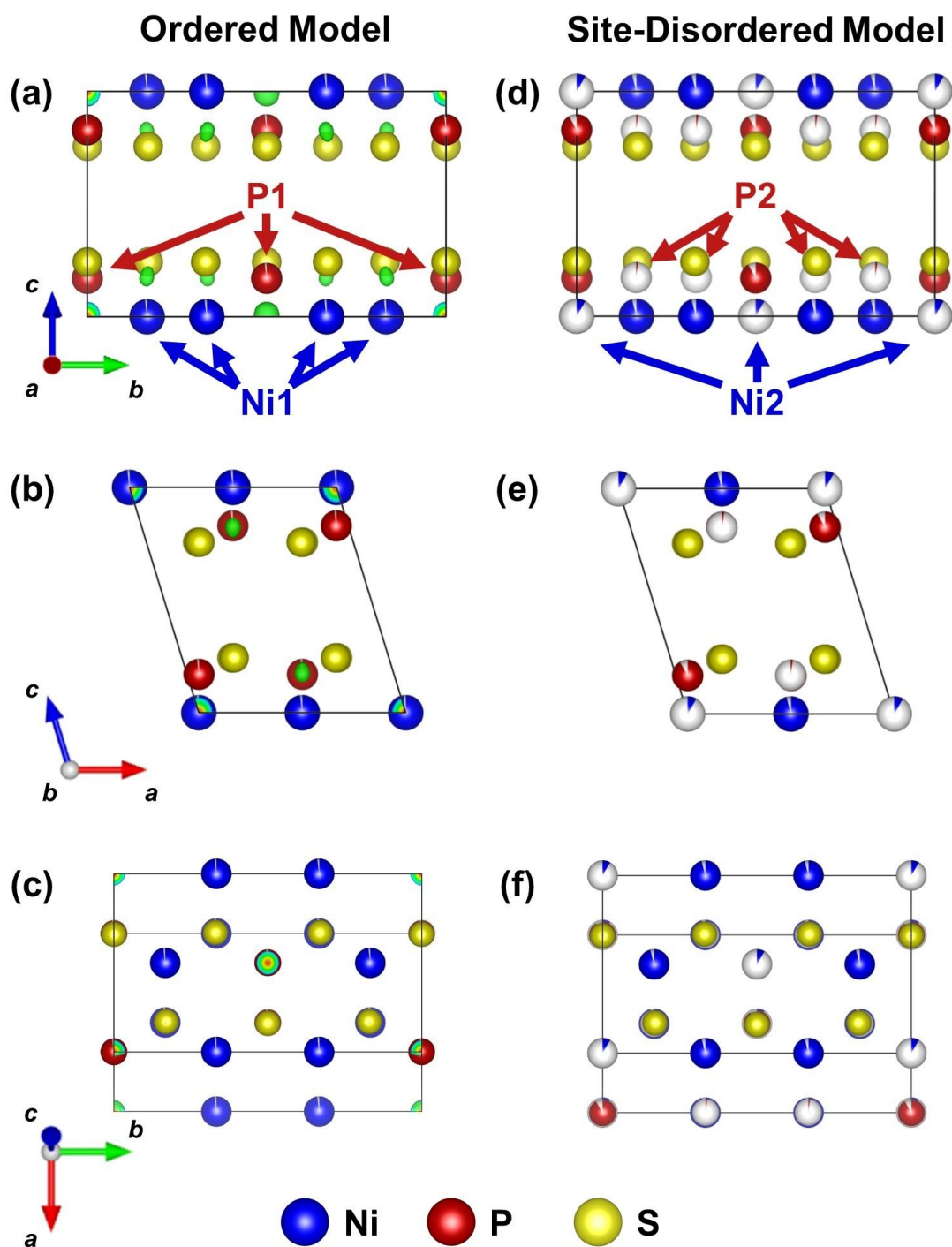


Fig. 3.4.: Perspective drawings of the refined crystal structure of $Ni_2P_2S_6$ based on scXRD using the ordered model (left) and using the site-disordered model (right). (a) and (d) showing the view along the a direction, (b) and (e) the view along the b direction and (c) and (f) the view along the c^* direction (perpendicular to the ab planes). In (a) and (d), the different Ni and P sites are labeled. The color filling of the atoms corresponds to the occupancy of the respective Wyckoff sites. All drawings show the positive residual electron density after the structural refinements of the scXRD data. The green isosurface corresponds to the lower cutoff value of $2 e/\text{\AA}^3$. The color gradient (e.g. see the corners of the unit cell in (a)) indicates the increasing residual electron density up to $14 e/\text{\AA}^3$ in red.

Table 3.2.: Summary and comparison of the crystallographic data and structural refinement for $Ni_2P_2S_6$ from scXRD at 293(2)K using the ordered structural model proposed for the $Fe_2P_2S_6$ structure type and adopted for $Ni_2P_2S_6$ [106] as well as the site-disordered model for $Ni_2P_2S_6$ proposed by Ouvrard *et al.* [112].

Structural Model	Ordered Model	Site-Disordered Model
<i>Experiment & Data Collection</i>		
Temperature (K)		293(2)
Radiation Type & Wavelength (Å)		Mo-K $_{\alpha 1}$; 0.71073
θ_{\min} (°)		3.22
θ_{\max} (°)		43.23
Completeness to θ (%)		100 ($\theta = 26.64^\circ$)
Reflections Collected		19885
Independent Reflections		1438
R_{int} (%)		4.47
Index Ranges		$-11 \leq h \leq 11$ $-19 \leq k \leq 19$ $-12 \leq l \leq 12$
$F(000)$		361
Absorption Coefficient (mm^{-1})		7.075
<i>Crystal Data</i>		
Crystal System		Monoclinic
Space Group		$C2/m$ (No. 12)
a (Å)		5.8165(7)
b (Å)		10.0737(12)
c (Å)		6.6213(8)
β (°)		107.110(6)
Volume (Å ³)		370.79(8)
Empirical Formula	$Ni_{1.96}P_{1.97}S_{6.00}$	$Ni_{2.00}P_{1.96}S_{6.00}$
Formula Weight (g mol^{-1})	368.6	370.2
Z	2	2
Density (calculated) (g cm^{-3})	3.301	3.315
<i>Refinement</i>		
Method	Full-matrix least squares on F^2	
Data / Restraints / Parameters	1438 / 0 / 29	1438 / 0 / 39
Goodness-Of-Fit	2.92	1.28
R_{obs} (%)	5.19	2.17
wR_{obs} (%)	10.95	4.64
R_{all} (%)	6.10	2.97
wR_{all} (%)	11.13	4.87
Largest Diff. Peak and Hole ($e \text{ \AA}^{-3}$)	13.98 and -1.70	1.07 and -0.87

Table 3.3.: Fractional atomic coordinates, occupancies, equivalent isotropic displacement parameters U_{eq} and anisotropic displacement parameters U_{ij} for $Ni_2P_2S_6$ at 293(2)K using the ordered structural model [106] (top) as well as the site-disordered model for $Ni_2P_2S_6$ [112] (bottom). Estimated standard deviations are given in parentheses. Please note that $U_{ij}(P1) = U_{ij}(P2)$ had to be set during refinement of the site-disordered model to obtain physically reasonable ADPs for P2.

Label	Type	Wyck	x	y	z	Occ (%)	U_{eq}	U_{11}	U_{22}	U_{33}	U_{12}	U_{13}	U_{23}
Ordered Model													
Ni1	Ni	4g	0	0.3331(1)	0	98(1)	8(1)	7(1)	7(1)	12(1)	0	3(1)	0
P1	P	4i	0.0578(1)	0	0.1702(1)	99(1)	8(1)	7(1)	6(1)	11(1)	0	3(1)	0
S1	S	4i	0.7419(1)	0	0.2434(1)	100(1)	8(1)	6(1)	7(1)	10(1)	0	4(1)	0
S2	S	8j	0.2518(1)	0.1700(1)	0.2436(1)	100	8(1)	7(1)	6(1)	10(1)	-1(1)	2(1)	-1(1)
Site-Disordered Model													
Ni1	Ni	4g	0	0.3331(1)	0	96(1)	9(1)	8(1)	8(1)	13(1)	0	4(1)	0
P1	P	4i	0.0578(1)	0	0.1702(1)	91(1)	7(1)	6(1)	6(1)	9(1)	0	3(1)	0
S1	S	4i	0.7421(1)	0	0.2432(1)	100	9(1)	8(1)	9(1)	11(1)	0	4(1)	0
S2	S	8j	0.2517(1)	0.1699(1)	0.2433(1)	100	9(1)	8(1)	7(1)	12(1)	-1(1)	3(1)	-1(1)
Ni2	Ni	2a	0	0	0	8(1)	12(1)	11(2)	8(2)	16(2)	0	5(1)	0
P2	P	8j	0.0574(10)	0.3329(6)	0.1734(9)	3(1)	7(1)	6(1)	6(1)	9(1)	0	3(1)	0

atoms as well as above and below the Ni atoms in c^* direction in the corresponding common (001) planes of P atoms.

Ouvrard *et al.* proposed to treat the residual electron density by introducing a site disorder of Ni between majority 4g (Ni1) and minority 2a sites (Ni2) and of P between majority 4i (P1) and minority 8j sites (P2) [112]. Using this structural model (hereafter referred to as site-disordered model) as starting point yields significantly improved reliability factors for the refined structural model (see Table 3.2). The corresponding atomic positions, occupancies and thermal displacement parameters are shown in Table 3.3 (bottom).

Comparing Fig. 3.4 left and right shows the additionally introduced minority sites of Ni2 and P2 in ideal agreement with the position of the residual electron density for the ordered model. Based on the occupancies of the majority and minority sites, approximately 4% of Ni atoms are found at a site where a P_2 dimer would be expected and *vice versa*. Accordingly, this structural model with disorder in the ab planes appears to be a sufficient to describe the scXRD data well.

Fig. 3.5 shows two sections through reciprocal space with thermal diffuse scattering of $Ni_2P_2S_6$. As seen in Fig. 3.5(a), the $hk0$ layer exhibits well resolved reflections. In contrast, the $0kl$ layer (Fig. 3.5(b)) shows a significant streaking of reflections in the l direction. As the l direction in reciprocal space corresponds to the c^* direction in real space, this broadening implies a highly defective structure in the stacking direction. Stacking faults, known defects in van der Waals layered compounds, are well suited to cause broadening of such form and direction.

As discussed by Goossens *et al.* [123] and Lançon *et al.* [117], it is likely that the displaced electron density resulting from stacking faults is misinterpreted in the structural solution and

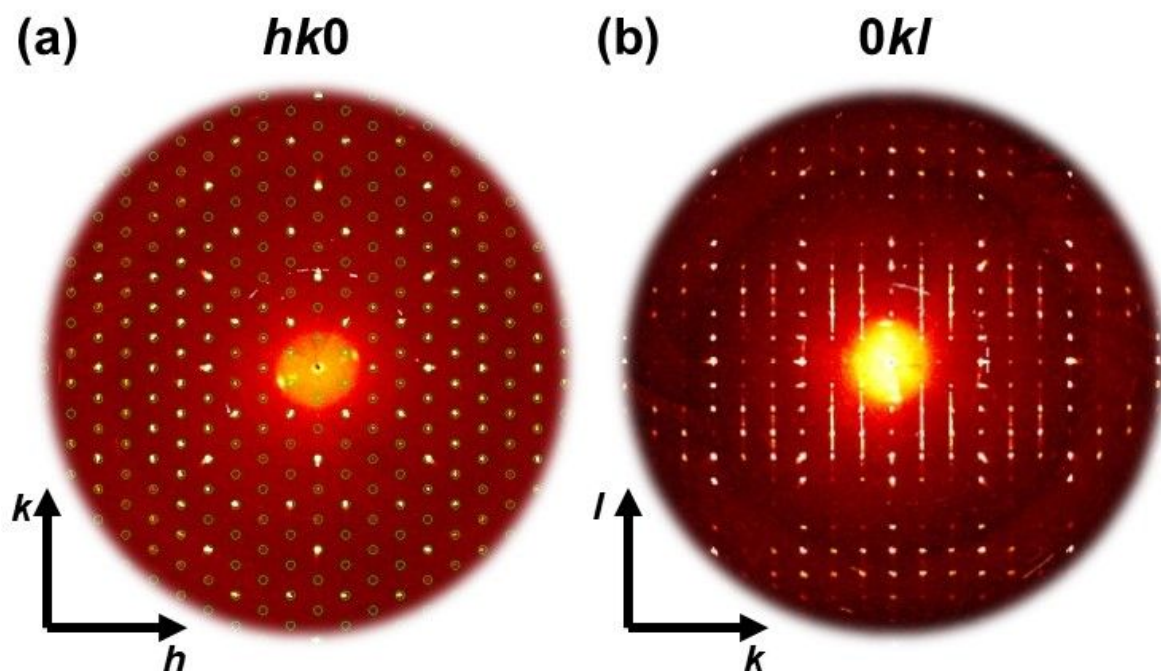


Fig. 3.5.: Cuts through reciprocal space from scXRD on a single crystal of $Ni_2P_2S_6$ showing the (a) $hk0$ and (b) $0kl$ planes.

falsely leads to a crystal structure model involving site disorder. Lançon *et al.* further support this assumption by their refinement of the magnetic structure of $Ni_2P_2S_6$ which they find unimproved by including the aforementioned site disorder.

Fundamentally, the Ni- P_2 site disorder may also be questioned regarding its influence on the chemical bonding nature and charge distribution in $Ni_2P_2S_6$. As introduced before (see Sect. 3), the $[P_2S_6]^{4-}$ structural unit is considered to be internally covalently bound. Accordingly, atoms in this complex anion are best understood to be charge neutral with the negative charges being delocalized over the whole unit. The $Ni^{2+}-[P_2S_6]^{4-}$ interaction, however, is considered as ionic. Subsequently, replacing a P_2 unit in the lattice by a Ni atom, in the course of a site disorder, formally leads to a local clustering of positive charges. *Vice versa*, a P_2 dimer on a majority site of Ni would be located in direct vicinity to three other $[P_2S_6]^{4-}$ anions. While a site disorder may be entropically favored, such charge clustering can be expected to be energetically undesired. Additionally the bonding nature of the sulfur atoms in the first coordination shell around such a disorder site would change from one ionic and one covalent bonding partner to either two ionic (Ni on P_2 site) or two covalent (P_2 on Ni site) bonding partners. Such a change in the bonding nature should result in changes of bond angles and subsequently in the position of these S atoms. However, corresponding shifts of electron density are not observed for $Ni_2P_2S_6$ from scXRD.

Additional to scXRD, pXRD was measured on pulverized crystals of $Ni_2P_2S_6$. The corresponding pattern is shown in Fig. 3.6 in comparison to the calculated pattern for the site-disordered structural model adjusted by the Rietveld method. The resulting structural parameters as well as the refined structural model from the Rietveld method are shown in Table 3.4 and Table 3.5, respectively.

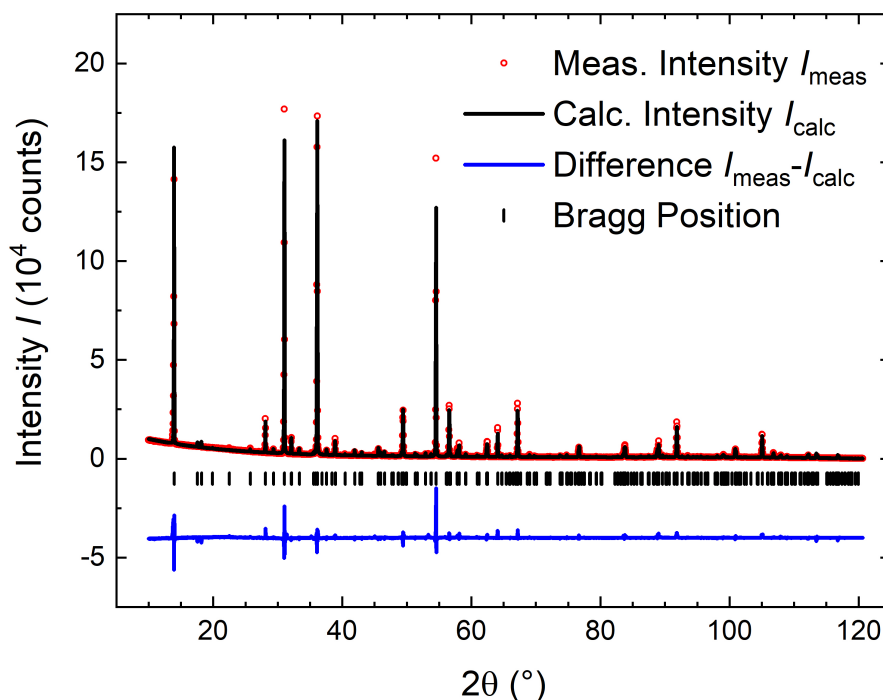


Fig. 3.6.: pXRD pattern from $Cu-K\alpha_1$ radiation ($\lambda = 1.54059 \text{ \AA}$) of pulverized $Ni_2P_2S_6$ crystals (red dots) in comparison to the calculated pXRD pattern for the refined crystal structure model of $Ni_2P_2S_6$ including Ni- P_2 site disorder obtained by the Rietveld method.

Comparing the structural parameters from Rietveld refinement (pXRD) to the values obtained from structural refinement of the scXRD experiments shows a significantly increased unit cell volume (scXRD: $370.80(1) \text{ \AA}^3$; pXRD: $372.40(1) \text{ \AA}^3$) as result of an increase of all lattice parameters. Also with approximately 16% of the Ni atoms being located on the minority site $2a$, the structure obtained from the model corresponding to the pXRD measurement exhibits more disorder than the structure obtained from scXRD with 4%. However, these deviations should be critically questioned as they go hand in hand with relatively high reliability factors, implying a non-ideal agreement between experiment and model.

As shown by the difference curve (blue) in Fig. 3.6, the relative intensities of reflections is not ideally reproduced by the model. This may be attributed to strong preferred orientation effects. Van der Waals layered systems such as $Ni_2P_2S_6$ are prone to exhibit this kind of sample effect in pXRD experiments. Grinding a macroscopic crystal of such kind to a powder yields mainly plate-like powder particles resulting from the preferred breaking of the weak stacking interactions. As these plate-like particles tend to lie flat on the sample holder, a non-homogeneous distribution of crystallographic orientations of the powder is obtained. This results in relative intensities of the crystallographic reflections that are significantly different compared to *e.g.* a calculated pattern. Furthermore it may be mentioned that grinding ductile compounds partly leads to a deformation of crystallites rather than breaking them into smaller particles. This deformation induces strain into the crystal lattice which causes deviations of the pXRD pattern from the expected pattern for an ideal powder.

Table 3.4.: Summary and reliability factors of the Rietveld analysis of the pXRD pattern of $Ni_2P_2S_6$.

Structural Analysis (Rietveld)	
<i>Experiment & Data Collection</i>	
Temperature (K)	293(2)
Radiation Type & Wavelength (Å)	Cu-K $_{\alpha 1}$; 1.54059
θ_{\min} (°)	10.00
θ_{step} (°)	0.03
θ_{\max} (°)	120.64
<i>Crystal Data</i>	
Crystal System	monoclinic
Space Group	$C2/m$ (No. 12)
a (Å)	5.8227(1)
b (Å)	10.0846(2)
c (Å)	6.6354(1)
β (°)	107.103(1)
<i>Refinement</i>	
Goodness-Of-Fit	5.79
R_p (%)	7.57
wR_p (%)	11.24
R_F (%)	8.72

Table 3.5.: Fractional atomic coordinates, occupancies and isotropic displacement parameters U_{iso} of $Ni_2P_2S_6$ at 293 K with estimated standard deviations in parantheses after Rietveld refinement.

Label	Type	Wyck	x	y	z	Occ (%)	U_{iso} ($\times 10^{-3} \text{Å}^2$)
Ni1	Ni	4g	0	0.3329(4)	0	84(1)	15(1)
P1	P	4i	0.0586(15)	0	0.1699(13)	84(1)	30(2)
S1	S	4i	0.7426(10)	0	0.2405(8)	100	18(1)
S2	S	8j	0.2515(7)	0.1696(4)	0.2415(5)	100	18(1)
Ni2	Ni	2a	0	0	0	32(1)	15(1)
P2	P	8j	0.0630(110)	0.3330(60)	0.1940(80)	8(1)	30(2)

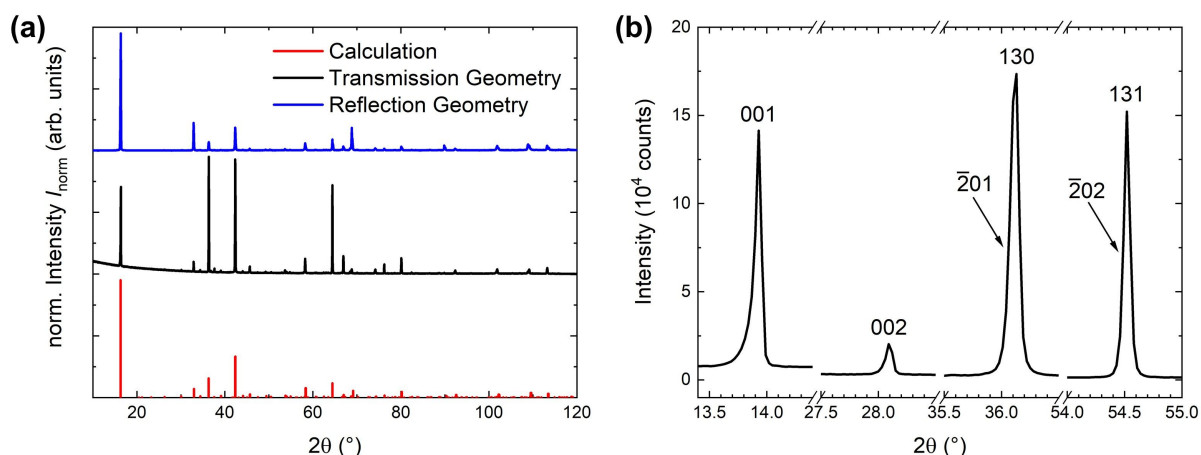


Fig. 3.7.: (a) Experimental pXRD pattern of $\text{Ni}_2\text{P}_2\text{S}_6$ measured with $\text{Co-K}\alpha$ radiation ($\lambda = 1.79026 \text{ \AA}$) in transmission (black) and reflection geometry (blue) in comparison to a calculated pXRD pattern (red) based on the structural model of Ouvrard *et al.* [112]. Intensities are normalized to the main intensity reflection of each pattern. (b) Comparison of the shape of the 001, 002, 130 and 131 reflections of the pXRD pattern used for the Rietveld refinement in Fig. 3.6 ($\text{Cu-K}\alpha_1$; $\lambda = 1.54059 \text{ \AA}$).

As mentioned in Sect. 2.2.2, the effect of preferred orientation on a pXRD pattern can be qualitatively demonstrated by performing diffraction experiments in different geometries (*i.e.* reflection and transmission) on the same sample and comparing the resulting patterns, as shown for $\text{Ni}_2\text{P}_2\text{S}_6$ in Fig. 3.7(a). While the 2θ angle of the reflections are in agreement with the calculated pattern based on the site-disordered structural model of Ouvrard *et al.* [112], the relative intensities differ between both experiments and the calculation. For plate-like crystallites, as expected for $\text{Ni}_2\text{P}_2\text{S}_6$, reflections with a strong l component have lower relative intensities in transmission geometry than expected from a calculation assuming spherical powder particles. *Vice versa*, in reflection geometry reflections with a strong l component exhibit increased relative intensities. For the experiment in transmission geometry, the intensity is found altered so much that the main intensity reflection is no longer the 001 reflection at 16.3° but the $1\bar{3}0$ reflection at 36.3° . For ideally spherical particles, the relative intensity of both experimental patterns are expected to match.

This sample effect is of course considered in the Rietveld refinement to a certain degree using the method proposed by March [128] and extended by Dollase [129]. However, any additional parameter during refinement (*e.g.*, parameters describing the preferred orientation) makes the overall model more complex and allows for additional correlations between parameters. Furthermore, such a strong preferred orientation as observed in $\text{Ni}_2\text{P}_2\text{S}_6$ might be in the limit of what the semi-empirical March-Dollase model is capable of describing accurately.

Besides the discrepancy between experimental and calculated intensities attributed to preferred orientation, a pronounced asymmetric shape of the $00l$ reflections can be observed (see Fig. 3.7(b)). This asymmetry has to be considered separately from the overall reflection asymmetry of the pattern, as the latter is considered in the Rietveld refinement by the correction proposed by Bézar and Baldinozzi [130] which yields a good overall description of the asymmetry for all but the $00l$ reflections. While the overall asymmetry is caused by the diffractometer

setup, the additional asymmetry of the $00l$ reflections is likely attributed to effects obtained from the sample itself.

Paterson [131] discusses shifts of the reflection positions and the asymmetric broadening of certain reflections resulting from stacking faults for the case of a highly symmetric cubic crystal system. For lower symmetric crystal systems (*e.g.*, monoclinic for $Ni_2P_2S_6$) the fundamental effects of stacking faults on a pXRD pattern can be expected to be the same. Consequently, the asymmetry of the $00l$ reflections may be well attributed to stacking faults. The broadening of $00l$ reflections observed in the scXRD experiment (see Fig. 3.5(b)) further supports this interpretation. However, an accurate modeling of a pXRD pattern influenced by stacking faults is challenging and not in the scope of a typical Rietveld refinement based on a lab-quality pXRD pattern.

Accordingly, two sample effects - preferred orientation and stacking faults - mainly cause the residual deviations between experiment and model and the relatively high reliability factors. In the presence of these sample effects, the absolute accuracy of the structural model obtained from Rietveld refinement should not be overestimated. These sample effects are not unique to $Ni_2P_2S_6$ but pose a challenge for an accurate structural refinement of pXRD pattern of many $M_2P_2S_6$ compounds, as, for example, discussed in Sect. 3.2.2 for the substitution series of $(Fe_{1-x}Ni_x)_2P_2S_6$.

In summary of the structural analysis of $Ni_2P_2S_6$, the phase adopts a monoclinic structure (space group $C2/m$) in agreement with the reported crystal structures of $Ni_2P_2S_6$. A notable contribution of stacking faults is observed in the scXRD and pXRD diffraction patterns. Regarding the atomic structure, the honeycomb structure proposed for $Fe_2P_2S_6$ [55] alone is not sufficient to describe the measured electron density distribution in scXRD. The addition of a Ni- P_2 site disorder to the aforementioned model significantly improves the agreement between experiment and model. However, whether this site disorder really exists or if it is an artifact obtained from stacking faults in the crystal, as discussed in literature [117, 123], cannot be determined unambiguously from scXRD alone. In pXRD, stacking faults and preferred orientation of the crystallites in the sample make an accurate structural refinement difficult. Apparently, the Ni- P_2 site disorder is more prominent in the model obtained from pXRD than in the scXRD structural model. Yet, above considerations regarding the relation between stacking faults and site disorder for scXRD have to be also applied to the refinement based on pXRD.

3.1.3. Magnetic Properties

The thermal evolution of the normalized magnetization $MH^{-1}(T)$ of $Ni_2P_2S_6$ measured at a magnetic field of 10 kOe for fields applied consecutively parallel to four crystallographic directions is shown in Fig. 3.8(a). The corresponding field dependence of the magnetization $M(H)$ measured at 1.8 K for the same four magnetic field directions is presented in Fig. 3.8(b). For the in-plane directions, a crystal was oriented using X-ray Laue diffraction and subsequently glued to the sample holder of the SQUID magnetometer such that the magnetic field is applied parallel to $[010]$ (*i.e.* b direction). After the measurements of $MH^{-1}(T)$ and $M(H)$, the crystal

was carefully detached from the holder, rotated in-plane by an angle of 30° (i.e. $[120]$), glued again to the sample holder and measured. This procedure was then repeated with a 60° rotation in the same direction ($[100]$, i.e. a direction) before the crystal finally was prepared for the measurement with the field along $[103]$ (i.e. c^* direction, perpendicular to the ab -plane).

In the temperature dependence (see Fig. 3.8(a)) above 156 ± 2 K, the normalized magnetization is isotropic for all magnetic field directions, with a maximum of the magnetization at $T_{\max} \approx 260$ K. This maximum is a distinctive feature observed in low-dimensional antiferromagnets which is attributed to a regime of low-dimensional short-range spin correlations above the long-range magnetic ordering temperature. Above the maximum, the magnetization decreases isotropically. However, the investigated temperature range above T_{\max} with an upper limit of 400 K due to device limitations does not allow for a Curie-Weiss analysis with sufficient statistics to ensure reliability.

At 156 ± 2 K, the temperature dependence of MH^{-1} exhibits an inflection point for all measured directions of the magnetic field. The inflection is accompanied by an abrupt change of the slope. While for all magnetic field directions with respect to the crystal orientation the slopes above the inflection match, they differ below resulting in anisotropic magnetization. Out of the three perpendicular directions $[100]$, $[010]$ and $[103]$, $H \parallel [100]$ exhibits the lowest, $H \parallel [103]$ the highest and $H \parallel [010]$ an intermediate magnetization at all temperatures below 156 ± 2 K. Wildes *et al.* [43] show the same general dependence of the magnetic susceptibility on the direction of the magnetic field with respect to the crystal orientation. For $H \parallel [120]$, the magnetization is slightly lower in the thermal evolution than for $H \parallel a$.

Although the absolute values of the magnetization differ below 156 ± 2 K, the general course of the thermal evolution is the same for all magnetic field directions. The magnetization decreases under cooling before reaching a minimum. Towards lowest temperatures, again a slight increase of the magnetization is observed, which can be likely attributed to Curie impurities (Curie tail). The overall decrease of magnetization below the inflection point indicates antiferromagnetic ordering with the inflection point corresponding T_N . Antiferromagnetic order as well as the specific T_N are in agreement with other studies of the magnetic behavior of $Ni_2P_2S_6$ by magnetometry [43, 126] as well as neutron diffraction [43].

As shown in Fig. 3.8(b), the field dependence of the magnetization of $Ni_2P_2S_6$ $M(H)$ at 1.8 K and up to 70 kOe exhibits a linear evolution for $H \parallel [103]$, while for $H \parallel [100]$ a curved $M(H)$ behavior is observed. This curvature in the field dependent magnetization is most likely attributed to a spin-flop transition, as introduced in Sect. 1.2.3. This indicates that $[100]$ is the magnetic easy axis of $Ni_2P_2S_6$ (not considering $H \parallel [120]$ for the moment). This is in agreement with the magnetic structure model proposed for $Ni_2P_2S_6$ by Wildes *et al.* based on single crystal neutron diffraction [43].

However, a $M(H)$ behavior similar to $H \parallel [100]$ is observed for $H \parallel [120]$, implying a comparable magnetic hardness for this direction. This is in agreement with $MH^{-1}(T)$, for which the evolution for $H \parallel [120]$ is similar to $H \parallel [100]$ below the ordering temperature, too. Yet, the observed field dependency for $H \parallel [120]$ is in apparent contradiction to the aforementioned model of the magnetic structure. From the model, a 180° rotational symmetry with respect to the easy axis in the ab plane is expected. In more detail, a monotonic decrease of

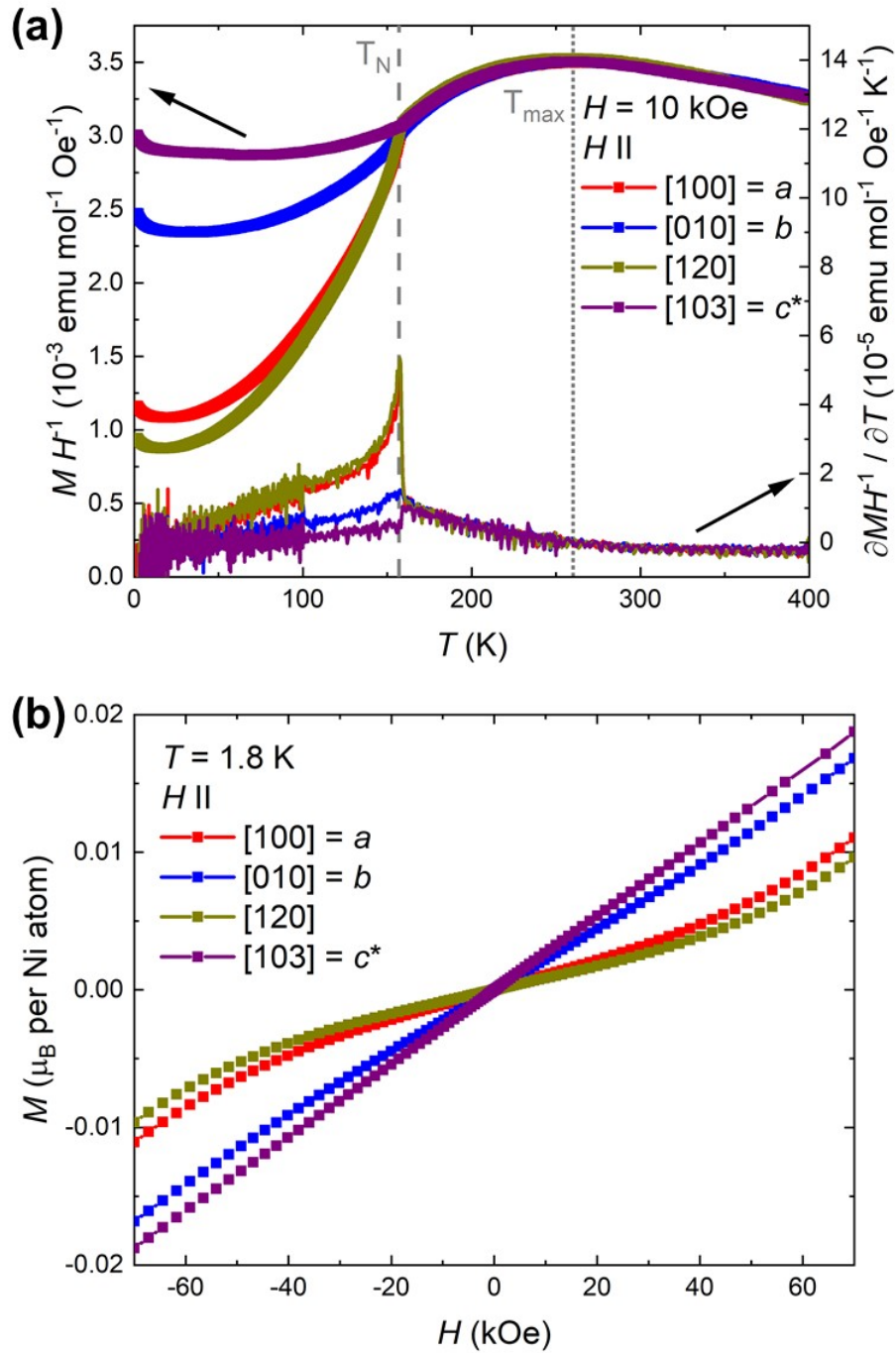


Fig. 3.8.: (a) Top: Normalized magnetization of $Ni_2P_2S_6$ as function of temperature $MH^{-1}(T)$ measured at a magnetic field of 10 kOe applied parallel to the crystallographic directions [100], [010], [120] and [103] direction, respectively (left y-axis). Bottom: First derivative of $MH^{-1}(T)$ for all four crystallographic directions (right y-axis). The grey dashed line indicates the temperature of inflection in $MH^{-1}(T)$ corresponding to a maximum in $\partial MH^{-1} / \partial T$ and the afm ordering temperature T_N of $Ni_2P_2S_6$. The grey dotted line shows the temperature of the maximum in $MH^{-1}(T)$ corresponding to $\partial MH^{-1} / \partial T = 0$. (b) Field dependence of the magnetization $M(H)$ at 1.8 K for magnetic fields applied along the same crystallographic directions.

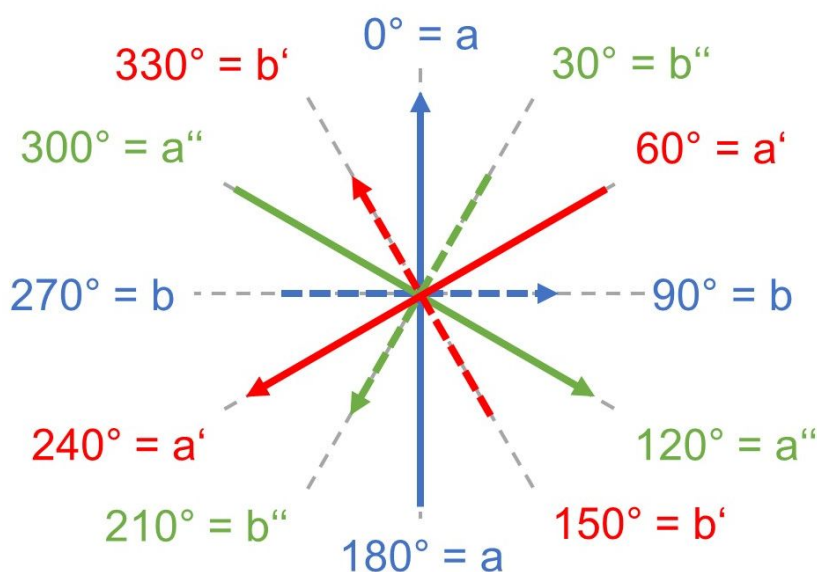


Fig. 3.9.: Schematic illustration of the consequences of 120° rotational twinning in the ab plane on the observed directions. Blue corresponds to the 'unrotated' domains, red to the domains rotated by 120° and green those rotated by 240° . The longer arrows indicate the magnetically easy a directions of the domains while the shorter, dashed arrows correspond to the magnetically harder b directions.

the magnetization is expected from 0° ($H \parallel [010]$) to 90° ($H \parallel [100]$), followed by a monotonic increase from 90° to 180° (again $H \parallel [010]$), as result of the change of the magnetic hardness. The $M(H)$ behavior for $H \parallel [120]$ rather suggests a 60° (i.e. six-fold) rotational symmetry of the easy axis in the ab plane which is also suitable to describe a hard axis for $H \parallel [010]$ at 90° rotated from $[100]$.

A potential scenario that can explain the observation of a 6-fold rotation symmetry of the magnetic easy axis in the ab plane while still relying on the magnetic structure proposed by Wildes *et al.* [43] is the formation of 120° rotational twins along the c^* direction of $Ni_2P_2S_6$. Accordingly, a crystal may contain several twin domains with 0° , 120° and 240° rotated directions in the ab plane but a common c^* direction, as illustrated in Fig. 3.9. Considering this, each of these domains intrinsically exhibits the expected two-fold symmetry regarding the magnetic easy axis. However, due to the rotation around the c^* direction, overall the sample has an easy axis every 60° . Yet, if the magnetic field is applied along the easy axis of one of these domains, for the other two domains the field is applied 30° to the harder b direction. Consequently, only a fraction of the whole sample experiences the field parallel to the local easy axis and causes the corresponding behavior, while for the other twin domains additional contributions from the harder magnetic directions are observed. These additional contributions may explain the broadness of the metamagnetic transition in the field dependence for magnetic fields applied along an 'easy axis' in $Ni_2P_2S_6$.

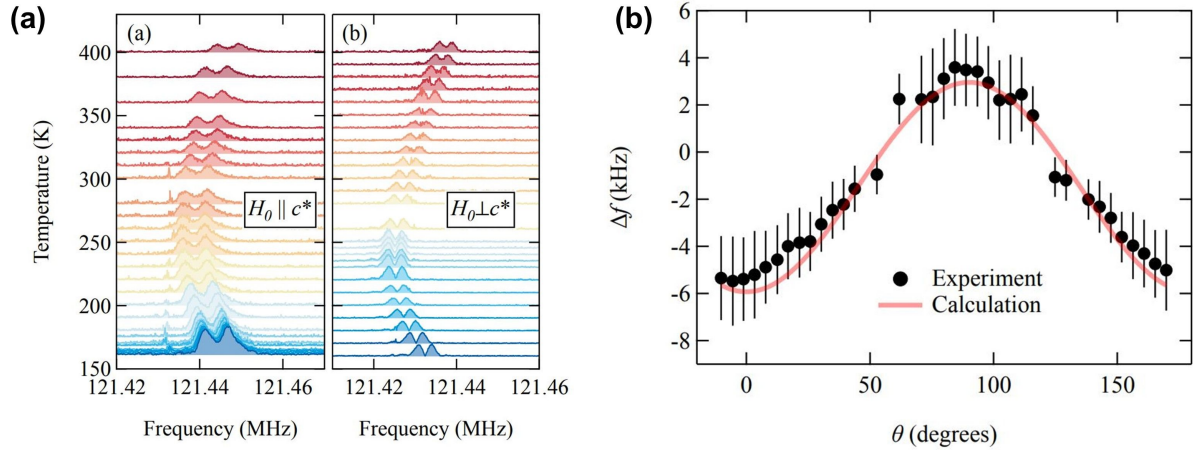


Fig. 3.10.: (a) Evolution of the ^{31}P NMR spectrum as function of temperature above the magnetic ordering temperature for a magnetic field of 70 kOe applied parallel and perpendicular to the ab planes. (b) The peak splitting Δf as function of the out-of-plane angle θ measured at 300 K and 70 kOe. The line corresponds to the expected behavior according to Eq. 3.1.

3.1.4. ^{31}P -NMR Spectroscopy

In addition to the study of the magnetization by SQUID magnetometry, solid state ^{31}P -NMR spectroscopy³ was performed on $\text{Ni}_2\text{P}_2\text{S}_6$ single crystals in a field of 70 kOe. This local probe technique allowed for further insights regarding the local structure and the magnetic interactions in $\text{Ni}_2\text{P}_2\text{S}_6$ taking advantage of the excellent properties of the ^{31}P nuclei in the compound ($S = 1/2$, high gyromagnetic ratio $\gamma_n \approx 17.235$ MHz/T and 100% abundance). Furthermore, the ^{31}P nuclei are sensitive to changes in the spin system *via* hyperfine coupling to the electron magnetic moments. The observation of appreciable transferred hyperfine coupling in $\text{Ni}_2\text{P}_2\text{S}_6$ [127] is in line with the covalent bonding picture of the $[\text{P}_2\text{S}_6]^{4-}$ anions, implying noticeable orbital hybridization between P and S. Furthermore, this agrees with the Ni–S–Ni super-exchange and Ni–S–S–Ni super-super-exchange coupling being dominant, which was proposed to explain the large nearest-neighbor and third-nearest neighbor exchange couplings J_1 and J_3 from inelastic neutron spectroscopy [117].

Here, the focus is on the local structure part of this investigation and on the angular behavior of the NMR signal in the magnetically ordered state as this is found complementary to the angular dependence of the magnetization discussed before (Sect. 3.1.3). Additionally, a K - χ anomaly (where K is the NMR shift) was observed in $\text{Ni}_2\text{P}_2\text{S}_6$ which is likely related to low-dimensional magnetic correlations at temperatures around the maximum in $MH^{-1}(T)$ [127]. However, a discussion of this specific part of the NMR study is beyond the scope of this work.

The thermal evolution of the ^{31}P NMR spectra above the magnetic ordering temperature $T_N = 156 \pm 2$ K is shown in Fig. 3.10(a) for magnetic fields applied parallel to the ab planes and along the c^* direction, respectively. At all temperatures, a spectrum with two narrow peaks is observed for both field directions. As observed in the crystal structure, $\text{Ni}_2\text{P}_2\text{S}_6$ exhibits two P

³Solid state ^{31}P -NMR spectroscopy on $\text{Ni}_2\text{P}_2\text{S}_6$ was measured and analyzed by Dr. Adam P. Dioguardi (IFW Dresden) and the corresponding spectra are shown with his kind permission.

atoms with a nuclear spin of $S = 1/2$ in close proximity to each other ($d(P-P) = 2.1534 \text{ \AA}$). For such an atomic arrangement of $S = 1/2$ nuclei, a 'Pake doublet' is expected, which is a peak splitting due to homonuclear dipolar coupling [132]. Investigating the out-of-plane angular dependence of the peak splitting Δf yields the dependence shown in Fig. 3.10(b). For a Pake doublet a angular dependence of the splitting in accordance with Eq. 3.1 is expected, where μ_0 is the vacuum permeability, \hbar the reduced Planck's constant, γ the gyromagnetic ratio and r the distance between the nuclear spins.

$$\Delta f(\theta) = f_1 - f_2 = \frac{3\mu_0\hbar\gamma^2}{8\pi r^3}(1 - 3\cos^2\theta) \quad (3.1)$$

As seen in Fig. 3.10(b), the experimental Δf as function of the out-of-plane angle θ is found in good agreement with the calculated dependence following from Eq. 3.1. Consequently, the split doublet in the NMR spectra above the magnetic ordering temperature is consistent with homonuclear dipolar coupling rather than, *e.g.*, from different chemical environments.

The absence of any further appreciable peaks in the NMR spectra implies that virtually all P nuclei experience the same hyperfine field and accordingly share the same chemical environment. Considering the Ni-P₂ site disorder, which was extensively discussed in Sect. 3.1.2, additional peaks in the ³¹P NMR spectra would be expected to be visible as a result of the different local P environments and the respectively different hyperfine fields. Corresponding signals are not observed in these spectra, indicating that site disorder does not play a significant role in the structure of the Ni₂P₂S₆ crystals grown in the course of this work. However, it should be noted that a small amount of site disorder corresponding to broad, low intensity signals in the NMR spectra cannot be completely ruled out.

Fig. 3.11(a) and (b) show the dependence of the NMR spectrum in the magnetically ordered state at 150 K on the out-of-plane angle θ and the in-plane angle φ , respectively. The 'Pake doublet' that was well observed above T_N can no longer be seen due to a significant broadening of the peaks. Instead, six resonances can be identified in the angular-dependent spectra. The spectral weights and evolution as function of the angles θ and φ of these signals allow them to be assigned to three doublets. These doublets result from the appearance of an internal hyperfine field in the magnetic state that leads to in-plane symmetry breaking. To take into account slight crystal misalignment with respect to the rotation and external magnetic field axes, the spectra were simulated *via* numerical exact diagonalization of the nuclear spin Hamiltonian including an internal hyperfine field interaction. The results of these simulations are shown in Fig. 3.11(c)-(e) as blue, green and red lines.

For the out-of-plane rotation shown in Fig. 3.11(a) and (c), all resonances virtually overlap at around 0° ($H \parallel c^*$). Furthermore, a maximum splitting is observed at approximately 90° ($H \parallel ab$), implying a 180° out-of-plane rotational symmetry. This behavior is in agreement with the magnetic structure proposed by Wildes *et al.* [43].

The evolution the NMR spectrum as function of the in-plane angle φ is shown in Fig. 3.11(b) and (d). While for one signal the doublet splitting becomes zero, the other two signal pairs exhibit an intermediate splitting. This behavior is in agreement with the scenario of 120° rota-

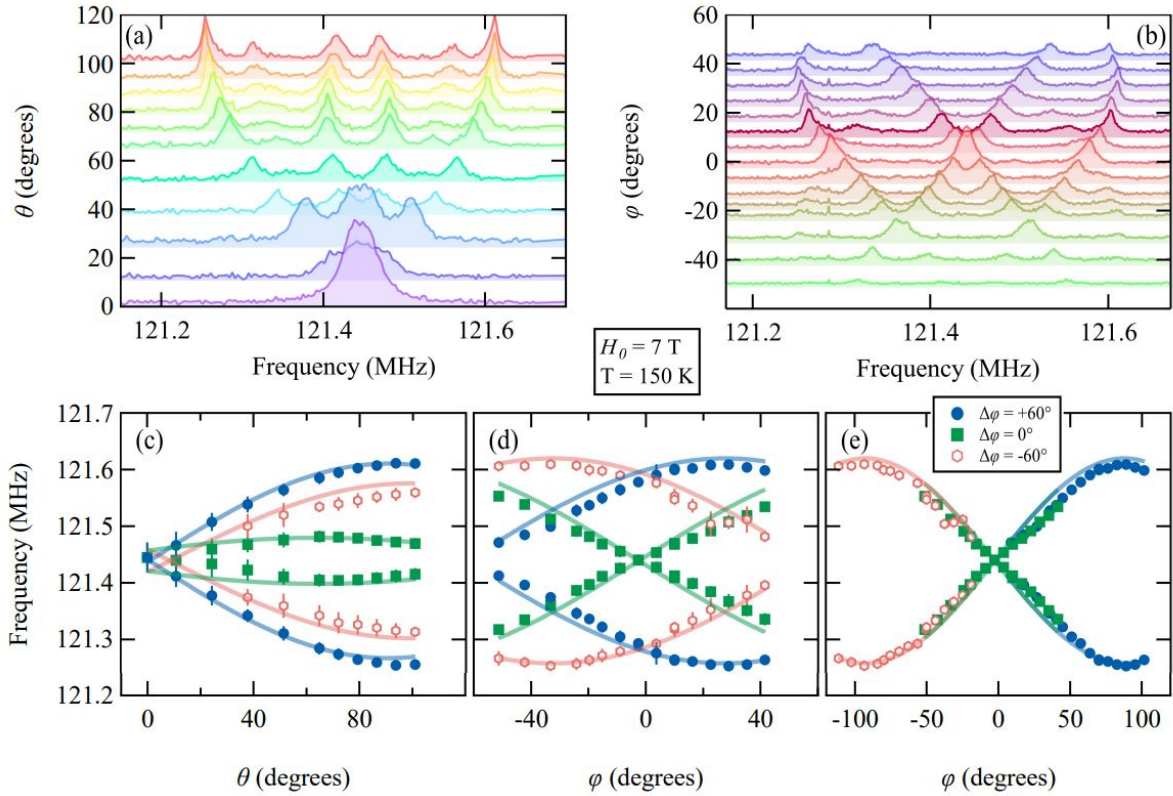


Fig. 3.11.: Evolution of the NMR spectrum measured in the magnetic state at 150 K at 7 T as function of (a) the out-of-plane rotation angle θ and (b) the in-plane rotation angle φ . Dependence of the position of each resonance on (c) θ and (d) φ as extracted from multipeak fits to the spectra in (a) and (b), respectively. (e) Same as (d) with offsets of -60° , 0° and 60° .

tional twinning discussed before in Sect. 3.1.3 to explain the magnetic behavior of $\text{Ni}_2\text{P}_2\text{S}_6$ for 0° , 30° and 90° in-plane rotation from the b direction. The three doublets exhibit an angular dependence that follows the magnetic six-fold rotational symmetry based on the aforementioned rotational twinning as shown in Fig. 3.11(e). A continuous evolution of the in-plane angular dependence can be obtained assuming one doublet (blue) is shifted by $+60^\circ$ and another doublet (red) is shifted by -60° . The relative spectral weights of the three pairs are $S_{red} = 16 \pm 1\%$, $S_{blue} = 37 \pm 1\%$ and $S_{green} = 47 \pm 1\%$ reflecting the twin fractions of the three domains in the measured crystal.

3.1.5. Stacking (Dis-)Order in $\text{Ni}_2\text{P}_2\text{S}_6$

Considering only one layer of $\text{Ni}_2\text{P}_2\text{S}_6$ (or any other $M_2\text{P}_2\text{S}_6$ compound in the monoclinic $C2/m$ space group) and for now ignoring the translation in c direction, the symmetry of this layer can be expressed in the form of a wallpaper group. As shown in Fig. 3.12(a), the smallest unit cell of such a layer is in the wallpaper group $p3$ (black). Another possible unit cell with slightly larger area can be constructed in the wallpaper group pm . This unit cell corresponds to the ab base plane of the monoclinic unit cell in $C2/m$. As pm is lower in symmetry, the lost symmetry elements compared to the higher symmetric $p3$ (i.e. three-fold rotation) transfer the

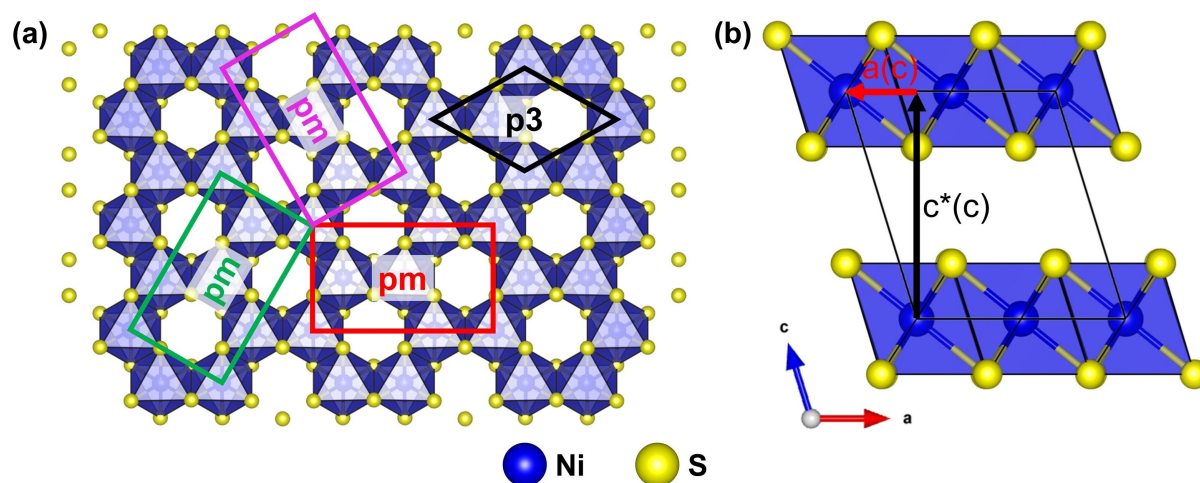


Fig. 3.12.: (a) Perspective drawing of a single layer of $Ni_2P_2S_6$ illustrating the honeycomb structure made from NiS_6 octahedra. The black parallelogram as well as the red, green and magenta rectangles correspond to the 2D unit cells for the different wallpaper groups as indicated in the drawing and discussed in the text. P atoms are omitted for clarity. (b) Perspective drawing of the monoclinic 3D unit cell of $Ni_2P_2S_6$ with view parallel to the b direction. Assuming a Cartesian coordinate system, the black arrow shows the component of the monoclinic c vector perpendicular to the ab plane called c^* while the red arrow illustrates the component of c in a direction which is referred to as monoclinic shift in the text.

different settings of the lower symmetrical unit cell into each other. Correspondingly, three possible settings for the pm unit cell are found in Fig. 3.12(a) rotated by 120° in regard to each other (red, green, magenta).

Turning towards more than one layer, the three-fold rotation symmetry is broken by the stacking and a monoclinic unit cell in $C2/m$ is found. The monoclinic angle of the $M_2P_2S_6$ unit cell results in an offset between atoms of each layer along the a direction additional to the stacking in c^* direction as illustrated in Fig. 3.12(b). However, each of the pm unit cells results in another direction for this monoclinic shift resulting in three equivalent orientations for a possible second layer. This is shown in Fig. 3.13. Considering all three orientations of the second layer at the same time yields a hexagonal closed packed layer of atomic positions. Each of these sites is occupied for two out of three orientations by Ni and for the residual orientation by P_2 . This is shown in Fig. 3.13 for the center triangle of atomic positions of the second layer by half-and-half colored spheres and black arrows indicating for which orientation a P_2 dimer occupies the corresponding position. Another way of approaching the stacking over multiple layers is that the direction of the offset between atoms of two layers defines the a and b direction locally.

Adding a third layer on top opens up the question if this new layer follows the monoclinic directions defined by the offset between layer 1 and layer 2 or not. More fundamentally, two potential scenarios can be distinguished in accordance with this question, which are illustrated in Fig. 3.14(a) and (b): for every new layer, i) the three possible orientations either correspond to the same conformation energy (*i.e.* each new layer takes one of the three orientations randomly) or ii) the orientation with the same monoclinic direction as for the layers below

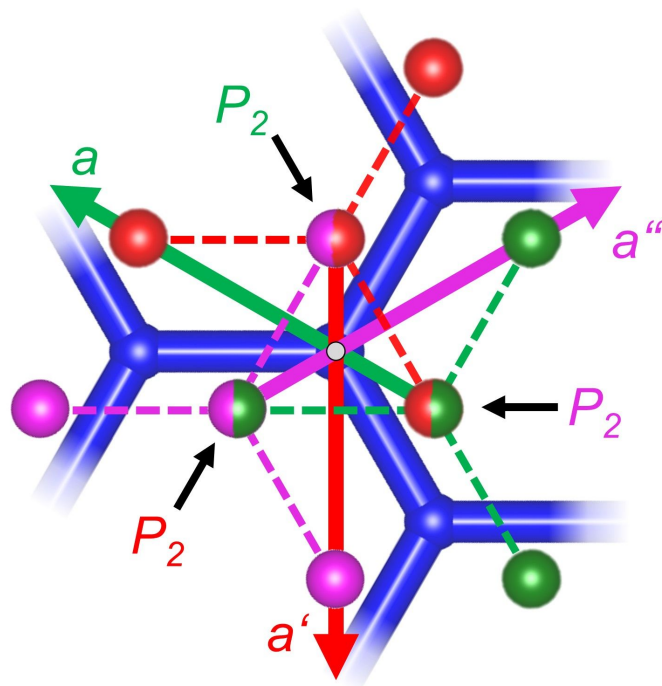


Fig. 3.13.: Schematic drawing of the three possible 120° rotated orientations in which a second layer of $Ni_2P_2S_6$ (red, green, magenta) may be added to a first layer (blue). The drawing only shows Ni atoms as spheres, while P and S atoms are omitted for clarity. Assuming the origin of the coordinate system is at the center Ni atom of the first layer in blue (gray circle), the a , a' and a'' directions are marked in the same colors as the second layer orientations and correspond to the a directions of the pm unit cells in Fig. 3.12(a) of the same color. Further details are described in the text.

is energetically favored. For scenario i), the monoclinic direction is expected to randomly change between layers by 120° rotations, while for scenario ii) the monoclinic direction would be preserved over multiple layers. However, crystallographic defects, such as stacking faults, may affect the energy difference between the different orientations and, subsequently, cause a change of the monoclinic direction. Thus, scenario ii) yields macroscopic domains of the same monoclinic direction, which are related to adjacent domains in the stacking direction by the twin condition of a 120° rotation.

Each of the scenarios above is capable to explain the six-fold in-plane rotational symmetry observed in magnetization experiments and the angular evolution of the ^{31}P NMR spectrum. However, the twin fractions obtained from the spectral weights from NMR are more consistent with scenario ii). For scenario i), fractions of roughly 33% for each orientation would be expected as result from the random changes of orientations in a large number of layers. The fractions being significantly different from 33% rather agrees with larger twin domains resulting from scenario ii).

In the context of scenario ii), a close relation between 120° twinning and the Ni- P_2 site disorder that improves the agreement between crystal structure model and XRD experiments in Sect. 3.1.2 can be recognized in Fig. 3.13. Consider the stacking of a certain crystal in the bulk is defined by the monoclinic shift given by the green set of Ni atoms. However, between the topmost layer and the layer below twinning occurs and the shift corresponding to the

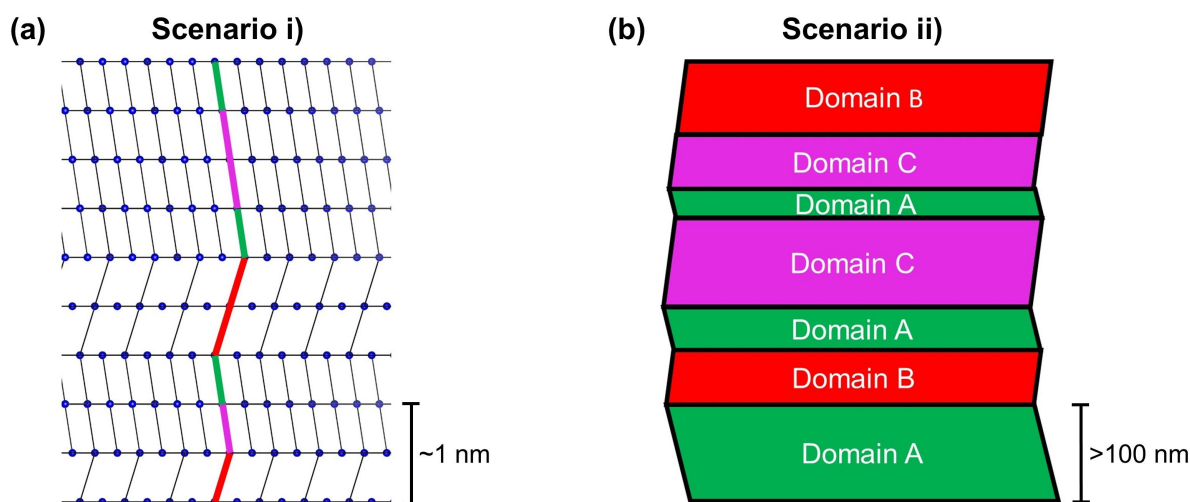


Fig. 3.14.: Schematic drawing of multilayer $Ni_2P_2S_6$ considering twinning resulting from (a) scenario i) and (b) scenario ii). Please note that a) is in the scale of interatomic distances while the scale of b) is orders of magnitude larger.

red layer is realized (instead of the shift that corresponds to green). As a result, instead of having a P_2 dimer on the position marked P_2 (green), a Ni atom is found at these coordinates. *Vice versa*, a P_2 dimer (marked in red) is found where a Ni atom would be expected from the bulk monoclinic direction. Accordingly it is imaginable that the Ni- P_2 site disorder actually describes the twin boundaries. Considering this, the roughly 4% of site disorder found for the $Ni_2P_2S_6$ crystal investigated by scXRD in this work (Sect. 3.1.2) imply a low amount of twin boundaries with respect to the ordered fractions of the crystal in agreement with large twin domains as expected to be obtained from scenario ii) discussed before.

To summarize this thought experiment, the intrinsic three-fold symmetry of a single layer is broken by the monoclinic stacking of layers. This opens up three possible orientations to add a new layer which are rotated by 120° with respect to each other. These different orientations in combination with only weak interactions between adjacent layers give rise to the formation of 120° rotational twin domains. Such a structural behavior is sufficient to explain the angular dependence of the magnetization and the NMR spectrum in the ab plane of $Ni_2P_2S_6$. It should be noted, that this angular dependence of the magnetic lattice is not likely to be observable in $M_2P_2S_6$ with $M = Mn, Fe$. The reason for this is due to only $M = Ni$ exhibiting anisotropic in-plane behavior (a direction is magnetic easy axis) [43, 117], while for $M = Mn$ and Fe the ab plane is reported to be isotropic. For $M = Fe$, ab is reported as intrinsically isotropic magnetic hard plane [116, 117], and for $M = Mn$ no appreciable magnetic anisotropy is observed [115, 117], as introduced in Sect. 3. Accordingly, $Ni_2P_2S_6$ can be considered a model system for investigating the structural disorder in the class of $M_2P_2S_6$ compounds, not only by means of XRD but also by probing the angular dependence of the magnetic lattice. The twin fractions extracted from NMR spectroscopy in Sect. 3.1.4 agree with twin domains of notable size rather than fully random stacking. Furthermore, a close relation between the 120° twinning and the Ni- P_2 site disorder, which improves the agreement between crystal structure model and XRD experiments in Sect. 3.1.2, suggests that the site disorder in the model may actually originate from the borders of twin domains.

3.2. $(Fe_{1-x}Ni_x)_2P_2S_6$

As mentioned in Sect. 3, substitution series between two magnetic $M_2P_2S_6$ parent compounds may yield intermediate compounds with exotic magnetic states as result of the interplay of different magnetic anisotropies. In this line, partly replacing Ni in $Ni_2P_2S_6$ by another transition element may yield similarly interesting results as reported for $(Mn,Fe)_2P_2S_6$ [119, 133]. For this purpose, Fe is the most promising element, as the corresponding parent compound, $Fe_2P_2S_6$, exhibits a distinctly different magnetic anisotropy (*i.e.* Ising-like [116]) from $Ni_2P_2S_6$ (*i.e.* Heisenberg-like with single ion anisotropy contribution [117]).

In expectancy of a structural solid solution behavior and, thus, a gradual evolution of the physical properties over the substitution series, also the magnetic anisotropy would be tunable by the degree of Fe/Ni substitution. As mentioned in Sect. 3.1, for a specific strength of the magnetic anisotropy (*i.e.* XY-type), 2D magnetic systems are expected to stabilize a highly unusual short range correlated ground state as proposed by Berezinskii [71] as well as Kosterlitz and Thouless [46]. While for $Ni_2P_2S_6$ such a state could not be found, it may be stabilized by tuning the magnetic anisotropy. Additional to the changes in the magnetic anisotropy, also the magnetic easy axis changes from parallel to a for $Ni_2P_2S_6$ [43] to parallel to c^* for $Fe_2P_2S_6$ [116]. Furthermore, although both compounds exhibit a stripe-like antiferromagnetic order in the layers, for $Fe_2P_2S_6$ these layers are ordered antiferromagnetically in the c direction [116], as shown in Fig. 3.15, in difference to the ferromagnetic stacking in $Ni_2P_2S_6$ [43], as illustrated in Fig. 3.1. Also, the magnetic ordering temperature is reduced from $T_N \approx 155$ K for $Ni_2P_2S_6$ [43, 114, 126] to $T_N \approx 119$ K for $Fe_2P_2S_6$ [116, 126].

It should be noted that Rao and Raychaudhuri [134] already synthesized polycrystalline $(Fe_{1-x}Ni_x)_2P_2S_6$ and reported an unusual evolution of the magnetic behavior. However, their polycrystalline samples do not allow for a study on the evolution of the magnetic anisotropy. To be able to directly investigate the evolution of the magnetic anisotropy over the substitution, single crystals of the intermediate compounds are required.

Single crystals of $(Fe_{1-x}Ni_x)_2P_2S_6$ with $x = 0, 0.3, 0.5, 0.7$ & 0.9 were grown from presynthesized polycrystalline precursors by CVT using iodine as transport agent as illustrated in Sect. 3.2.1. Crystals of all compounds were comprehensively characterized by SEM and EDX regarding their morphology and composition and scXRD and pXRD were used to investigate the crystal structure (see Sect. 3.2.2). The solid solution nature of $(Fe_{1-x}Ni_x)_2P_2S_6$ is validated by the investigation of structural properties. In Sect. 3.2.3, the evolution of the bulk magnetic properties are discussed as function of the Fe/Ni substitution. Hereby, the following magnetic aspects are discussed in more detail: the evolution of the magnetic anisotropy in the ordered state, the evolution of the short range correlated regime above the ordering temperature as well as the evolution of the magnetic anisotropy in the paramagnetic state. Furthermore, $(Fe_{1-x}Ni_x)_2P_2S_6$ is investigated for the existence of a potential spin glass state and $(Fe_{0.5}Ni_{0.5})_2P_2S_6$ specifically is investigated for a magnetic glass state due to a corresponding report in literature [135].

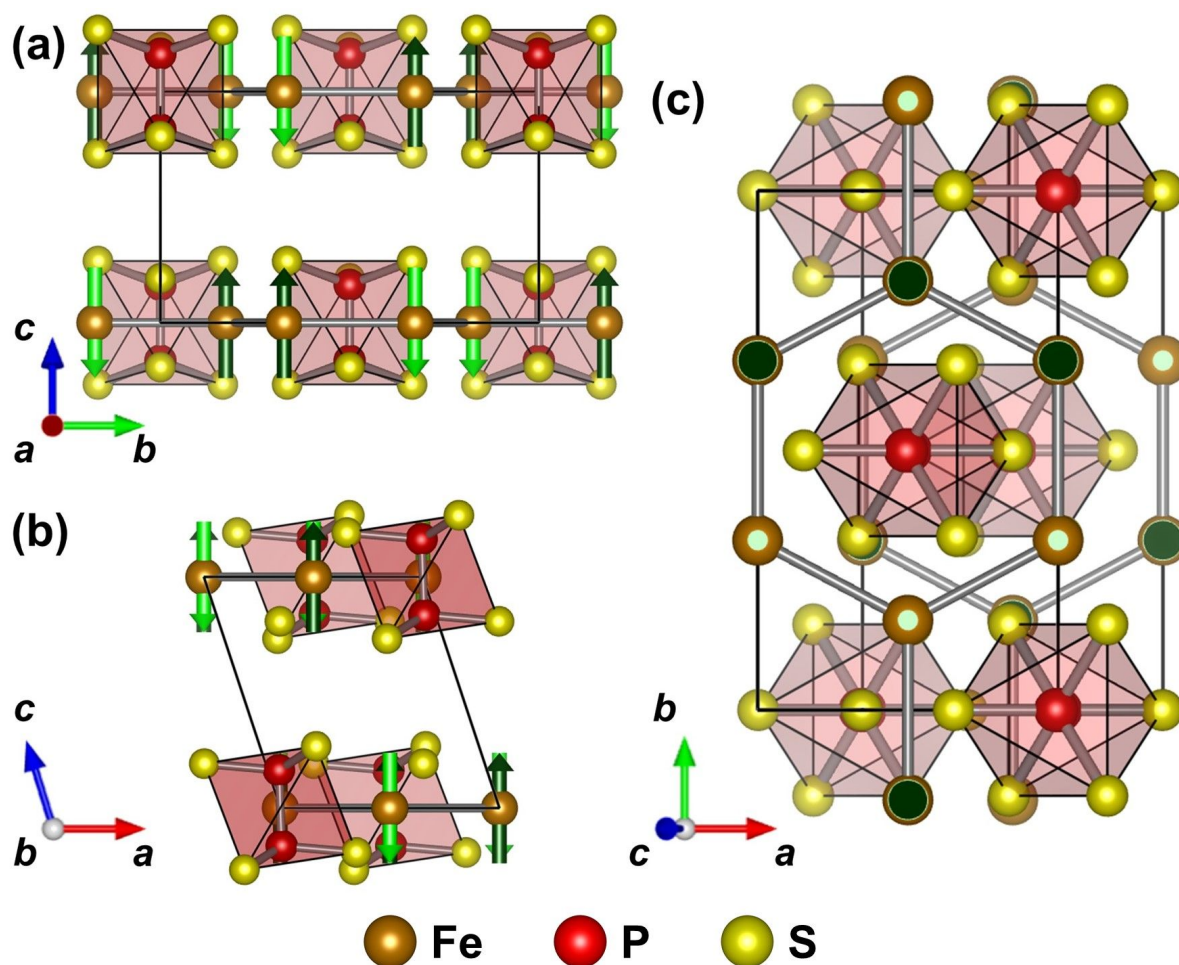


Fig. 3.15.: Perspective drawing of the crystal structure of $\text{Fe}_2\text{P}_2\text{S}_6$ and orientation of the magnetic moments of Fe at 2 K according to Lancon *et al.* [116]. View along (a) the a direction ($\perp bc$ plane), (b) the b direction ($\perp ac$ plane) and (c) the c^* direction ($\perp ab$ plane). The red octahedra illustrate the P_2S_6 structural units. Bright and dark green arrows illustrate the moment orientations and are drawn in different colors to improve the visibility of the stripe-like antiferromagnetic order.

The following section is the subject of a manuscript in preparation as S. Selzer *et al.*, 'Influence of Chemical Substitution on the Magnetic Anisotropy in Single Crystals of the 2D van der Waals System $(\text{Fe}_{1-x}\text{Ni}_x)_2\text{P}_2\text{S}_6$ ' (2020).

3.2.1. Synthesis and Crystal Growth

Single crystals of $(\text{Fe}_{1-x}\text{Ni}_x)_2\text{P}_2\text{S}_6$ were obtained by a two-step process, as also mentioned in the master thesis of Shemerliuk [120]. First, stoichiometric polycrystalline powders were obtained by solid state synthesis from the elements. In a second step, crystals were grown from these polycrystalline precursors by the chemical vapor transport (CVT) technique. This two-step process has proven necessary to obtain homogeneous single crystals with the desired degree of substitution.

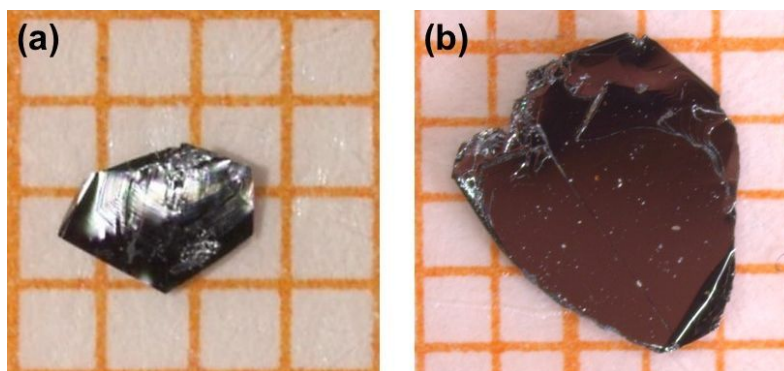


Fig. 3.16.: (a) $Fe_2P_2S_6$ single crystal and (b) $(Fe_{0.7}Ni_{0.3})_2P_2S_6$ single crystal as obtained from the CVT growth experiments. A orange square in the background is $1\text{ mm} \times 1\text{ mm}$ for scale. These images are also shown in the master thesis of Shemerliuk [120].

Synthesis of Polycrystalline Precursors

The elemental constituents iron (powder -70 mesh, Acros Organics, 99%), nickel (powder -100 mesh, Sigma Aldrich, 99.99%), red phosphorus (lumps, Alfa Aesar, 99.999%) and sulfur (pieces, Alfa Aesar, 99.999%) were weighed out in stoichiometric quantities with respect to $(Fe_{1-x}Ni_x)_2P_2S_6$ ($x = 0, 0.3, 0.5, 0.7, 0.9$). The elemental mixtures were homogenized in an agate mortar and pressed to pellets (1 cm diameter) at approximately 25 kN using a hydraulic press. Typically 2 g of pellets were loaded in a quartz ampoule (10 mm inner diameter, 3 mm wall thickness) which was previously baked out at $800\text{ }^\circ\text{C}$ for at least 12 h. All preparation steps up to here were performed under argon atmosphere inside a glove box. The ampoule was then sealed under an internal pressure of approximately 0.3 bar Ar (at $20\text{ }^\circ\text{C}$). Finally, samples were sintered in a tube furnace. Initially, the samples were heated to $300\text{ }^\circ\text{C}$ at $50\text{ }^\circ\text{C/h}$ and dwelled for 24 h to ensure prereaction of the more volatile elements P and S with the transition elements. Then the samples were heated to $600\text{ }^\circ\text{C}$ at $100\text{ }^\circ\text{C/h}$ and dwelled at this temperature for 72 h. After this, the furnace was turned off and the samples were furnace-cooled to room temperature. The formation of the desired monoclinic phase was confirmed by pXRD.

Crystal growth

Single crystals were grown by CVT with iodine as transport agent. The experimental procedure as well as the temperature profile are the same as presented for the single crystal growth of $Ni_2P_2S_6$ in Sect. 3.1.1.

After the growth, plate-like crystals of $(Fe_{1-x}Ni_x)_2P_2S_6$ of up to $5\text{ mm} \times 5\text{ mm} \times 200\text{ }\mu\text{m}$ were extracted from the ampoule. As shown in Fig. 3.16, the crystals are shiny and exhibit a layered morphology. Similar to $Ni_2P_2S_6$, the $(Fe_{1-x}Ni_x)_2P_2S_6$ crystals are ductile and can be easily exfoliated.

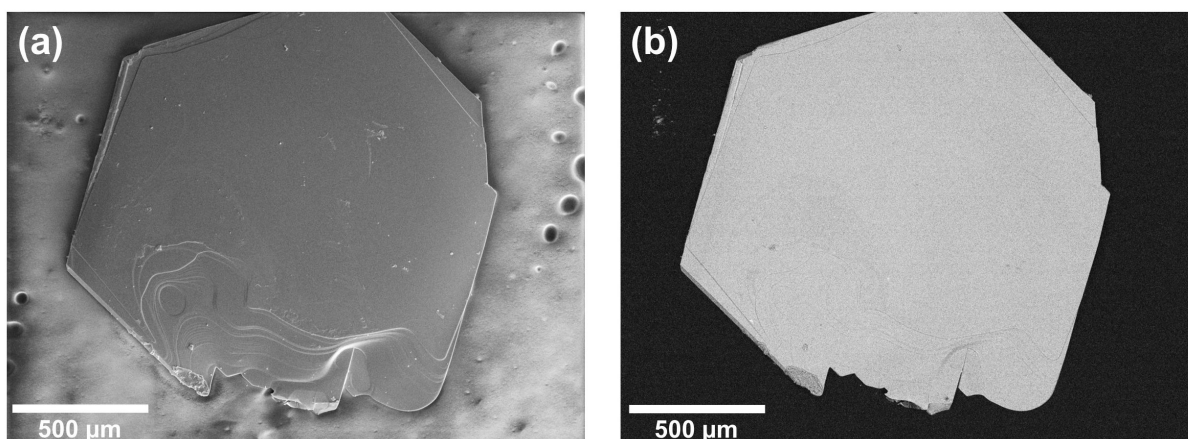


Fig. 3.17.: Electron microscopy images of a $(\text{Fe}_{0.7}\text{Ni}_{0.3})_2\text{P}_2\text{S}_6$ crystal in topographic mode (SE detector) in (a) and in chemical contrast mode (BSE detector) in (b).

3.2.2. Characterization

Crystal Morphology and Compositional Analysis

From the SEM images using the topographic contrast mode (*i.e.* SE detector), crystals of all degrees of substitution exhibit the typical features of layered systems, such as steps and terraces, as shown for example in Fig. 3.17(a) for $(\text{Fe}_{0.7}\text{Ni}_{0.3})_2\text{P}_2\text{S}_6$. Using the chemical contrast mode (*i.e.* BSE detector), no changes in contrast are observed on the crystal surface. This lack of contrast change indicates a homogeneous elemental composition on the respective area of the crystal. An according SEM(BSE) image of $(\text{Fe}_{0.7}\text{Ni}_{0.3})_2\text{P}_2\text{S}_6$ is shown in Fig. 3.17(b). SEM(SE) and SEM(BSE) images of $\text{Fe}_2\text{P}_2\text{S}_6$ as well as the other intermediate $(\text{Fe}_{1-x}\text{Ni}_x)_2\text{P}_2\text{S}_6$ compounds are found as Fig. A.1–A.4 in the Appendix. SEM(SE) and SEM(BSE) for $\text{Ni}_2\text{P}_2\text{S}_6$ are shown in Fig. 3.3 of Sect. 3.2.2.

To quantify the elemental composition, EDX was measured on at least 10 different spots on the surface of several crystals for each nominal degree of substitution x_{nom} . As seen in Table 3.6, the elemental compositions are close to the expected composition of the $M_2\text{P}_2\text{S}_6$ phase for all crystals. Furthermore, the respective compositions are found homogeneously on different locations on the crystals as indicated by small standard deviations given in parentheses in Table 3.6. Moreover, for all crystals the degree of Fe/Ni substitution is found in the range of the nominal value considering a systematic uncertainty on this ratio of approximately 5%.

Structural Analysis

All scXRD⁴ patterns could be indexed in the monoclinic space group $C2/m$ (No. 12) with the lattice parameters given in Table 3.7 top. Regarding the structural refinements, including the Ni-P₂ site disorder in the structural model as proposed by Oувrard *et al.* [112] improves the

⁴scXRD experiments were carried out by Dr. Mihai-Ionut Sturza (IFW Dresden) and are shown with his kind permission.

Table 3.6.: Expected and mean experimental composition measured by EDX as well as the corresponding experimental degree of substitution x_{exp} for crystals with different nominal degrees of substitution x_{nom} . Standard deviations are given in parentheses.

x_{nom}	Expected Composition	Composition from EDX	x_{exp}
0	$\text{Fe}_{20}\text{P}_{20}\text{S}_{60}$	$\text{Fe}_{20.7(3)}\text{P}_{20.3(1)}\text{S}_{59.0(3)}$	0
0.3	$\text{Fe}_{14}\text{Ni}_6\text{P}_{20}\text{S}_{60}$	$\text{Fe}_{14.5(4)}\text{Ni}_{5.9(1)}\text{P}_{20.4(2)}\text{S}_{59.3(3)}$	0.29
0.5	$\text{Fe}_{10}\text{Ni}_{10}\text{P}_{20}\text{S}_{60}$	$\text{Fe}_{11.1(3)}\text{Ni}_{9.6(3)}\text{P}_{20.2(1)}\text{S}_{59.1(6)}$	0.46
0.7	$\text{Fe}_6\text{Ni}_{14}\text{P}_{20}\text{S}_{60}$	$\text{Fe}_{6.5(1)}\text{Ni}_{14.0(2)}\text{P}_{20.3(1)}\text{S}_{59.2(2)}$	0.68
0.9	$\text{Fe}_2\text{Ni}_{18}\text{P}_{20}\text{S}_{60}$	$\text{Fe}_{2.3(3)}\text{Ni}_{18.7(8)}\text{P}_{20.2(2)}\text{S}_{58.7(8)}$	0.89
1	$\text{Ni}_{20}\text{P}_{20}\text{S}_{60}$	$\text{Ni}_{20.5(1)}\text{P}_{20.3(1)}\text{S}_{59.2(1)}$	1

agreement between model and experiment as already discussed in the context of the structural analysis of $\text{Ni}_2\text{P}_2\text{S}_6$ in Sect. 3.1.2. However, the site disorder is most likely an artifact in the structural refinement caused by stacking faults. For $(\text{Fe}_{1-x}\text{Ni}_x)_2\text{P}_2\text{S}_6$ with $x = 0, 0.7, 1$, significant broadening of reflections in the l direction of the $0kl$ section of reciprocal space is observed as shown in Fig. 3.18. This effect in the scXRD pattern is indicative of high amounts of (stacking) disorder perpendicular to the ab -planes.

However, a crystal structure model, which explicitly considers these stacking faults in the model, is lacking by now. Therefore, the model with site disorder was used. Using this structural model allowed to obtain comparable structural parameters throughout the whole substitution series as it yields the best possible agreement with experiment. This is in consonance with the approach of Goossens *et al.* [123] and Lançon *et al.* [117] for $\text{Ni}_2\text{P}_2\text{S}_6$. Yet, it should be emphasized again, that the site disorder is most likely not real but rather an artifact attributed to stacking faults.

For the parent compounds, $\text{Fe}_2\text{P}_2\text{S}_6$ and $\text{Ni}_2\text{P}_2\text{S}_6$, using the site disorder model proposed by Ouvrard *et al.* [112] allowed for a refinement of all atomic coordinates, anisotropic displacement parameters (ADPs) as well as the occupancy of all but the sulfur sites without any restraints. For all intermediate compounds, the structural model had to be extended in order to take the substitution of Fe by Ni into account. Starting from the structural model for $\text{Fe}_2\text{P}_2\text{S}_6$, two new positions were generated (Ni1 and Ni2) which are restrained to have the same fractional coordinates and the same ADPs as the Fe1 (4g) and Fe2 (2a) positions and are occupied by Ni atoms. Additionally, the occupancy of Ni1 and Ni2 were restraint to the occupancy of Fe1 and Fe2, respectively, to always yield the nominal Fe/Ni ratio (*e.g.* for $(\text{Fe}_{0.3}\text{Ni}_{0.7})_2\text{P}_2\text{S}_6$: $f_{\text{Ni1}} = f_{\text{Fe1}} \cdot 7/3$ and $f_{\text{Ni2}} = f_{\text{Fe2}} \cdot 7/3$). Without further restraints, this model was sufficient to describe all intermediate compounds. Only for $(\text{Fe}_{0.7}\text{Ni}_{0.3})_2\text{P}_2\text{S}_6$, additionally the occupancy of the minority sites in the site disorder description, Fe2/Ni2 (2a) and P2 (8j), had to be fixed to zero to obtain a physically reasonable structural model. As an example, the crystal structure of $(\text{Fe}_{0.3}\text{Ni}_{0.7})_2\text{P}_2\text{S}_6$ corresponding to the refined scXRD model in Table 3.7 is shown in Fig. 3.19.

Using the model with site disorder, a disorder ratio r_{disorder} may be defined as in Eq. 3.2, which corresponds to ratio of transition element atoms between the majority and minority sites and takes into account the different site multiplicities.

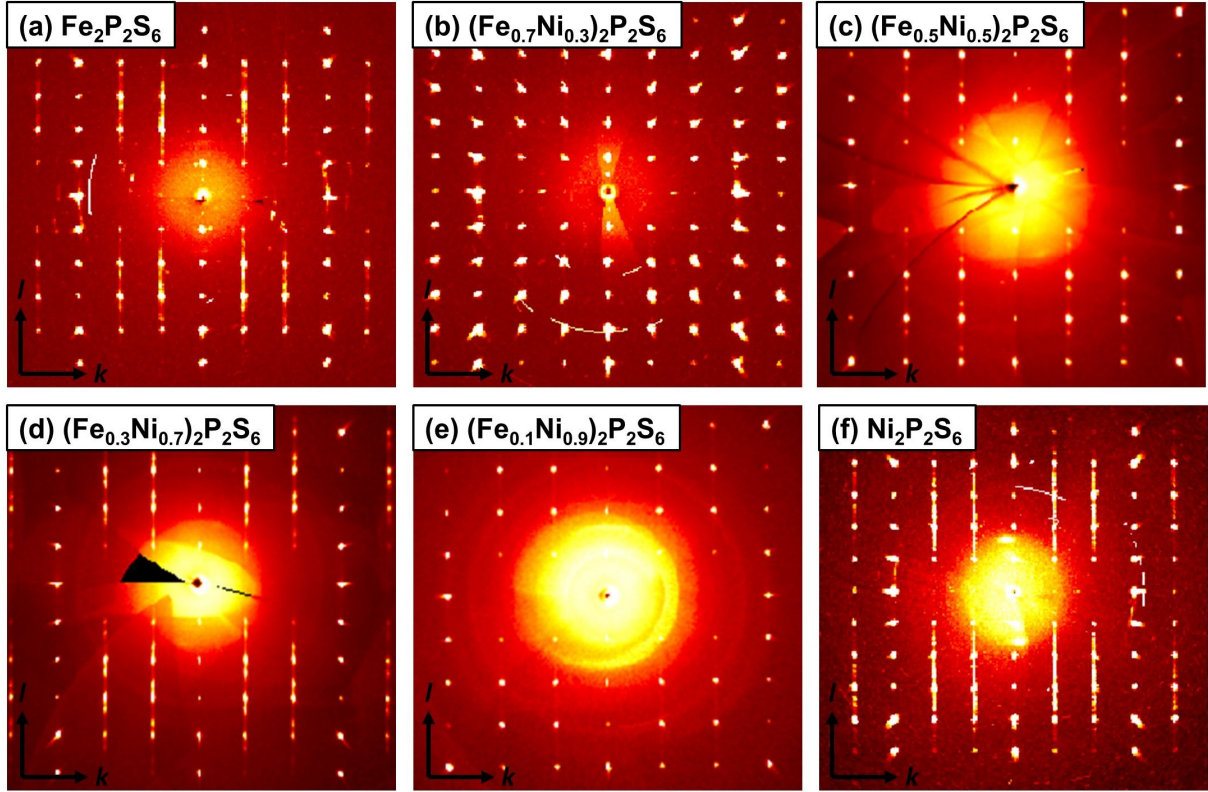


Fig. 3.18.: $0kl$ cuts through reciprocal space from scXRD on $(Fe_{1-x}Ni_x)_2P_2S_6$ single crystal with (a) $x = 0$, (b) $x = 0.3$, (c) $x = 0.5$, (d) $x = 0.7$ and (e) $x = 0.9$. (f) shows the $0kl$ cut for $Ni_2P_2S_6$ from Fig. 3.5(b) in Sect. 3.1.2 for comparison.

$$r_{\text{disorder}} = \frac{f_{\text{Fe2}} + f_{\text{Ni2}}}{2(f_{\text{Fe1}} + f_{\text{Ni1}}) + f_{\text{Fe2}} + f_{\text{Ni2}}} \quad (3.2)$$

In the line of the argumentation before, the disorder ratio r_{disorder} may be best understood as a measure of stacking faults rather than a measure for site disorder. That at least a qualitative correlation between the site disorder ratio and the amount of stacking faults exists, can be observed by comparing the scXRD patterns (*i.e.* Fig. 3.18(d) and (e)) and r_{disorder} of $(Fe_{0.3}Ni_{0.7})_2P_2S_6$ and $(Fe_{0.1}Ni_{0.9})_2P_2S_6$. For $(Fe_{0.3}Ni_{0.7})_2P_2S_6$, strong streaking in l direction is observed and $r_{\text{disorder}} = 14\%$, while for $(Fe_{0.1}Ni_{0.9})_2P_2S_6$ virtually no streaking can be seen and $r_{\text{disorder}} = 2\%$. However, the evolution of r_{disorder} as function of the degree of substitution x shows no clear trend. This may implies that the stacking fault density is heavily sample dependent and less material dependent. In this line, measuring another crystal - even of the same batch - is likely to yield a different value of r_{disorder} .

pXRD patterns for the complete substitution series are shown in Fig. 3.20 and could be indexed in the same monoclinic space group $C2/m$ (No. 12) as the scXRD pattern. As already observed for the pXRD pattern of $Ni_2P_2S_6$ (Fig. 3.6 and Fig. 3.7 in Sect. 3.1.2), strong preferred orientation and stacking faults also influence the powder patterns of $Fe_2P_2S_6$ and the intermediate $(Fe_{1-x}Ni_x)_2P_2S_6$ compounds. While a reliable structural refinement using the Rietveld method is challenging in the presence of these sample effects, a reasonable description for the

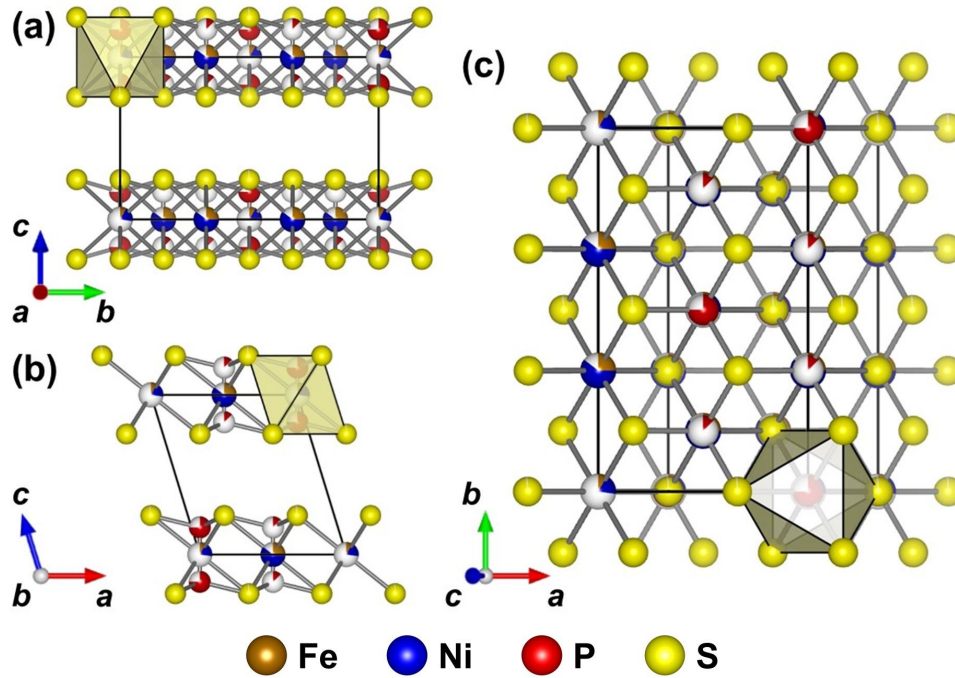


Fig. 3.19.: Perspective drawing of the crystal structure of $(\text{Fe}_{0.3}\text{Ni}_{0.7})_2\text{P}_2\text{S}_6$ according to the structural parameters obtained from scXRD (see Table 3.7). (a) shows the bc plane (view along a), (b) shows the ac plane (view along b) and (c) shows the ab plane (view along c^*). Each S_6 octahedron either hosts a transition metal atom or a P_2 dumbbell in its center, as indicated by the yellow octahedron. Less than half occupied atomic sites correspond to the minority transition element $2a$ and P $8j$ sites.

Table 3.7.: Summary of lattice parameters and volume obtained from modelling the scXRD and pXRD pattern. A selection of reliability values are shown as well. A more comprehensive table of the scXRD analysis is found in the Appendix.

scXRD						
x_{nom}	0.0	0.3	0.5	0.7	0.9	1
Crystal System	Monoclinic					
Space Group	$C2/m$ (No. 12)					
a (Å)	5.9345(10)	5.8544(2)	5.8602(2)	5.8671(2)	5.8481(3)	5.8165(7)
b (Å)	10.2942(17)	10.1487(2)	10.1497(4)	10.1658(3)	10.1219(3)	10.0737(12)
c (Å)	6.7092(11)	6.6563(2)	6.6518(2)	6.6663(2)	6.6534(3)	6.6213(8)
β (°)	107.069(11)	107.139(4)	107.069(3)	107.086(3)	107.127(6)	107.110(6)
Volume (Å ³)	391.82(11)	377.92(2)	378.22(2)	380.06(2)	376.38(3)	370.80(10)
r_{disorder} (%)	6	0 (fixed)	2	14	2	4
Goodness-Of-Fit	1.13	2.30	1.61	2.55	1.93	1.28
R_{obs} (%)	1.70	2.32	3.50	2.67	2.93	2.17
pXRD (Le Bail)						
Crystal System	Monoclinic					
Space Group	$C2/m$ (No. 12)					
a (Å)	5.9349(1)	5.8919(7)	5.8501(1)	5.8513(2)	5.8071(8)	5.8224(2)
b (Å)	10.2812(2)	10.1809(12)	10.1308(2)	10.1337(3)	10.0569(15)	10.0831(3)
c (Å)	6.7180(2)	6.6779(9)	6.6567(2)	6.6571(3)	6.6105(10)	6.6332(2)
β (°)	107.309(2)	107.244(3)	107.199(2)	107.204(2)	107.263(3)	107.096(2)
Volume (Å ³)	391.35(2)	382.57(8)	376.87(2)	377.07(2)	368.67(9)	372.22(2)
Goodness-Of-Fit	1.69	2.04	2.31	1.97	1.97	2.77
R_p	1.78	1.84	2.31	2.73	2.97	3.30
wR_p	2.63	2.74	3.65	4.41	4.43	5.39

pattern profiles could be found and lattice parameters could be extracted using the Le Bail method. Corresponding lattice parameters are shown in Table 3.7 (bottom).

The evolution of the lattice parameters a , b and c as well as the monoclinic angle β and the unit cell volume V extracted from pXRD and scXRD experiments are shown in Fig. 3.21(a) and (b), respectively. The lattice parameters become shorter and the volume smaller by increasing x in $(\text{Fe}_{1-x}\text{Ni}_x)_2\text{P}_2\text{S}_6$ as expected from the ionic radius of Fe^{2+} (0.78 Å) in comparison to Ni^{2+} (0.69 Å) [136]. Overall a linear trend is observed, in agreement with Vegard's law [137]. The monoclinic angle β virtually stays constant as function of the degree of substitution x . However, all these structural parameters exhibit small deviations from the general trend. It is likely that the structural faults in the real structure of $(\text{Fe}_{1-x}\text{Ni}_x)_2\text{P}_2\text{S}_6$ induce additional inaccuracy in the determination of the lattice parameters, which results in the observed deviations.

To conclude the structural analysis, both scXRD and pXRD confirm the solid solution nature of $(\text{Fe}_{1-x}\text{Ni}_x)_2\text{P}_2\text{S}_6$. On the one hand, all scXRD pattern could be modeled using the same structural model only adjusting the Fe/Ni ratio. On the other hand, lattice parameters extracted from both scXRD and pXRD pattern overall follow Vegard's law.

3.2.3. Evolution of Magnetic Properties

The normalized magnetization as function of temperature $MH^{-1}(T)$ is shown in Fig. 3.22 for crystals of $(\text{Fe}_{1-x}\text{Ni}_x)_2\text{P}_2\text{S}_6$ of all acquired degrees of substitution with a field of $H = 10$ kOe applied parallel to three crystallographic directions a , b and c^* , respectively. Please note that $MH^{-1}(T)$ for $\text{Ni}_2\text{P}_2\text{S}_6$ in Fig. 3.22(f) corresponds to the same measurement as discussed before in Sect. 3.1.3.

The generic behavior of $MH^{-1}(T)$ is the same for all compositions and field directions. From 400 K towards lower temperatures, first an increase in MH^{-1} is observed, followed by a decrease. Subsequently, a maximum of MH^{-1} is obtained at a composition dependent temperature T_{max} . Below T_{max} , an inflection point is found at a composition dependent temperature $T_{\text{inflection}}$. Below $T_{\text{inflection}}$, MH^{-1} approaches a minimum and either saturates around this minimum (for $0 \leq x \leq 0.7$) or shows again a slight increase towards lowest temperatures ($T < 20$ K; for $0.9 \leq x \leq 1$). Likely, this increase towards lowest temperatures is related to Curie impurities.

As already mentioned for $\text{Ni}_2\text{P}_2\text{S}_6$ in Sect. 3.1.3, this generic temperature dependence is well known for low-dimensional antiferromagnets. As shown in Table 3.8, the inflection point corresponds to the long-range antiferromagnetic ordering temperature T_N in agreement with complementary techniques (NMR spectroscopy [138] and neutron diffraction [43, 139, 140]). The maximum around T_{max} is typically attributed to short range magnetic correlations above T_N [65, 66].

For all compositions, T_N is isotropic with respect to the direction of H . For the parent compounds $\text{Fe}_2\text{P}_2\text{S}_6$ and $\text{Ni}_2\text{P}_2\text{S}_6$, T_N is in good agreement with literature [126] as $T_N(\text{Fe}_2\text{P}_2\text{S}_6) = 119 \pm 2$ K and $T_N(\text{Ni}_2\text{P}_2\text{S}_6) = 156 \pm 2$ K. Overall, a gradual increase of T_N is observed increasing the degree of Ni substitution in $(\text{Fe}_{1-x}\text{Ni}_x)_2\text{P}_2\text{S}_6$, as seen in Fig. 3.22.

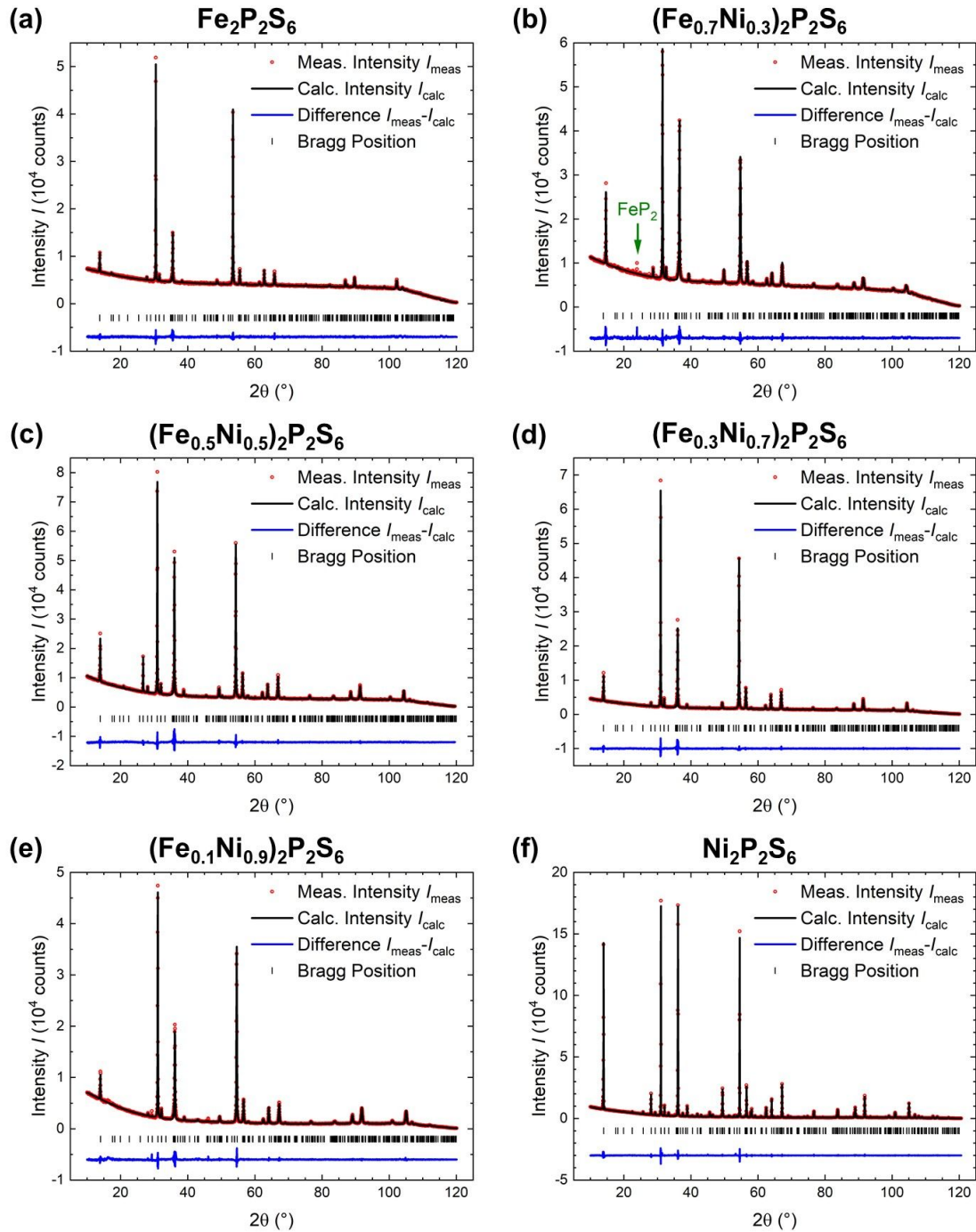


Fig. 3.20.: pXRD pattern from Cu- K_{α_1} radiation ($\lambda = 1.54059 \text{ \AA}$) of pulverized crystals of $(Fe_{1-x}Ni_x)_2P_2S_6$ with (a) $x = 0$, (b) $x = 0.3$, (c) $x = 0.5$, (d) $x = 0.7$, (e) $x = 0.9$ and (f) $x = 1$ as red circles. For comparison, the black line shows the Le Bail fit of the pattern based on the monoclinic space group $C2/m$. The obtained lattice parameters of the monoclinic unit cell as well as the reliability factors of the fit are shown in Table 3.7 (bottom). The green arrow in (b) marks a secondary phase reflection from FeP_2 . The decrease of intensity above approximately 100° is attributed to the measurement setup.

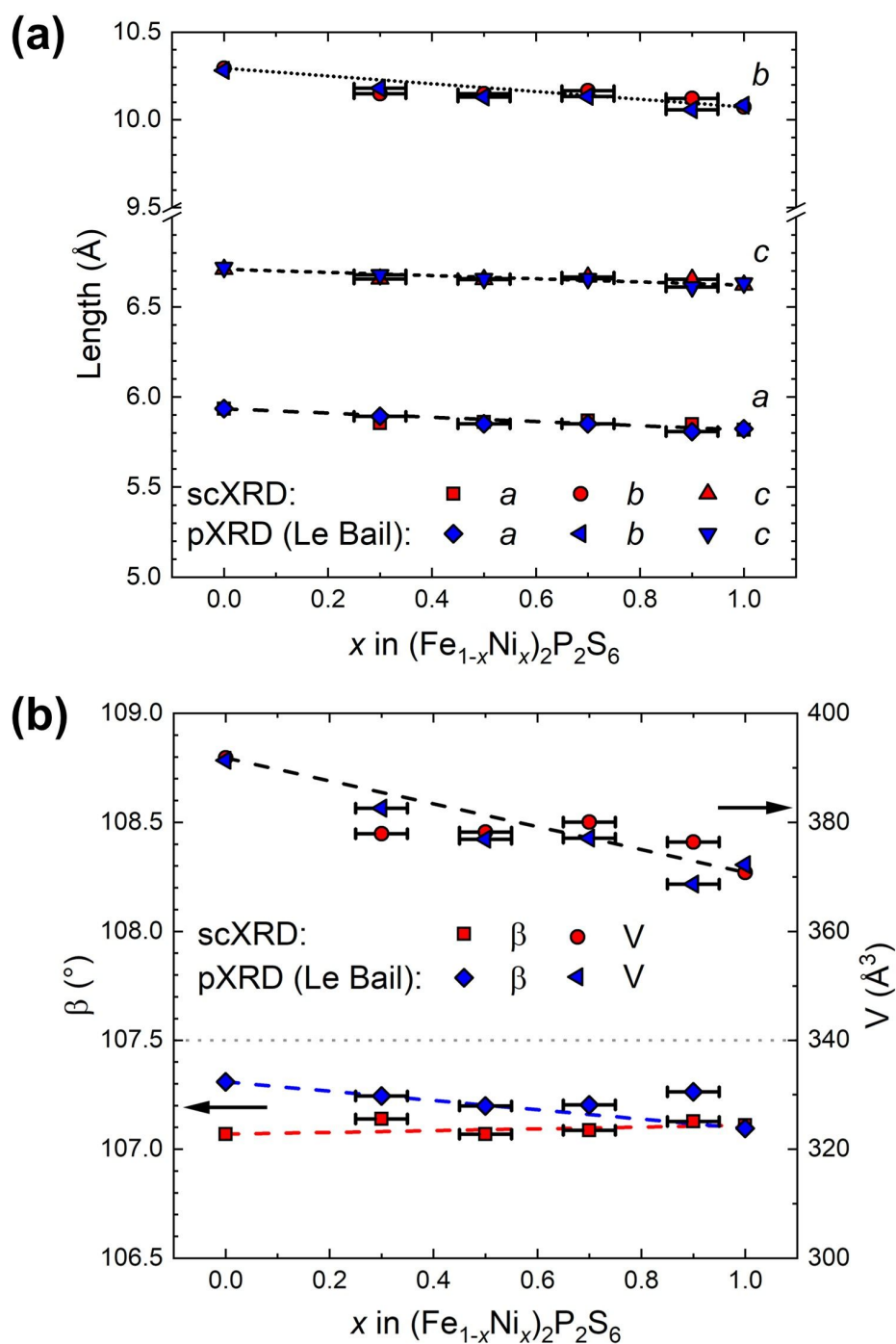


Fig. 3.21.: (a) Evolution of the lattice parameters (from top to bottom) b , c and a as function of the degree of substitution in $(\text{Fe}_{1-x}\text{Ni}_x)_2\text{P}_2\text{S}_6$. (b) Evolution of the unit cell volume (top, right y-axis) and the monoclinic angle β (bottom, left y-axis). Red symbols correspond to values extracted from scXRD experiments and blue symbols correspond to values extracted from Le Bail fits of the pXRD data. The lines indicate the linear trend expected from the parent compounds $\text{Fe}_2\text{P}_2\text{S}_6$ and $\text{Ni}_2\text{P}_2\text{S}_6$. Errorbars in y-direction are smaller than the symbols and are therefore omitted. Note the break of the y-axis between 7.5 Å and 9.5 Å in (a).

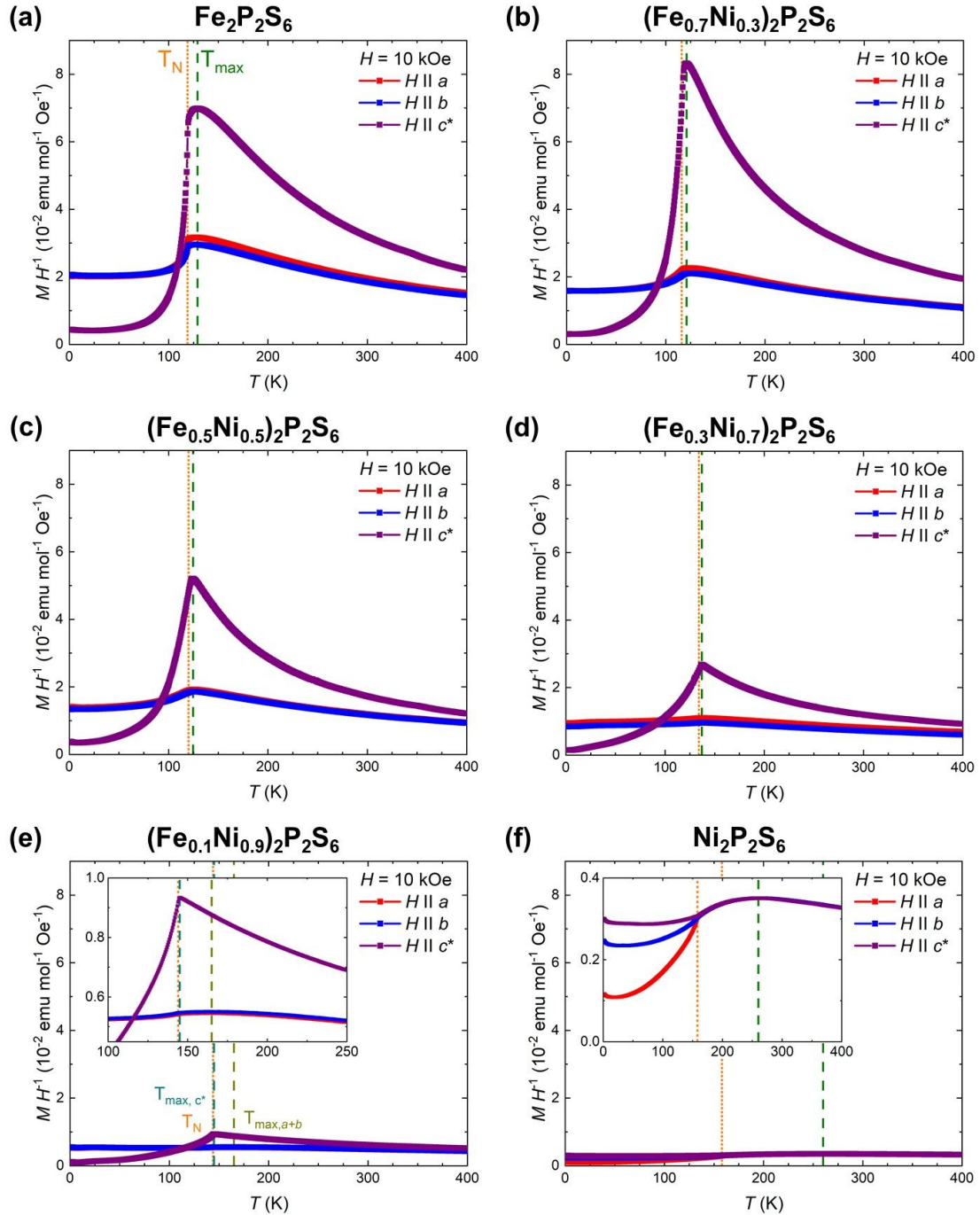


Fig. 3.22.: Normalized magnetization as function of temperature $MH^{-1}(T)$ with a magnetic field of 10 kOe applied along three perpendicular crystallographic directions a , b and c^* for (a) $Fe_2P_2S_6$, (b) $(Fe_{0.7}Ni_{0.3})_2P_2S_6$, (c) $(Fe_{0.5}Ni_{0.5})_2P_2S_6$, (d) $(Fe_{0.3}Ni_{0.7})_2P_2S_6$, (e) $(Fe_{0.1}Ni_{0.9})_2P_2S_6$ and (f) $Ni_2P_2S_6$. The MH^{-1} axes are scaled the same for best comparability. The inset in (f) shows a zoomed-in view on the thermal evolution of MH^{-1} of $Ni_2P_2S_6$. The orange dotted lines indicate the Néel temperature T_N for each compound. The green dashed lines in (a), (b), (c), (d) and (f) denote the isotropic temperature of the maximum in $MH^{-1}(T)$ T_{max} . For (e) $(Fe_{0.1}Ni_{0.9})_2P_2S_6$, T_{max} is anisotropic and accordingly the yellow line indicates T_{max} for $H \parallel a$ and $H \parallel b$ while the cyan line marks T_{max} for $H \parallel c^*$. The inset in (e) shows the two anisotropic temperatures of maximum magnetization for $(Fe_{0.1}Ni_{0.9})_2P_2S_6$ in a zoomed-in view.

Table 3.8.: Comparison of the magnetic ordering temperature T_N of $Fe_2P_2S_6$ and $Ni_2P_2S_6$ extracted in this work with literature values based on several techniques. ND corresponds to neutron diffraction.

$Fe_2P_2S_6$	$Ni_2P_2S_6$	Technique	Reference
119 ± 2 K	156 ± 2 K	Magnetometry	this work
111 K	151 K	Magnetometry	[134]
123 K	155 K	Magnetometry	[126]
	155 K	Magnetometry	[43]
	159 K	ND	[43]
120 K		ND	[139]
117 K		ND	[140]
116 K	155 K	^{31}P -NMR	[138]

T_{max} is found isotropic with regard to the direction of the external magnetic field H for all compounds except $(Fe_{0.1}Ni_{0.9})_2P_2S_6$. For the latter a rather sharp maximum centered at $T_{max} = 145$ K is found for $H \parallel c^*$, while a distinctly broader maximum centered at $T_{max} = 165$ K is observed for both $H \parallel a$ and $H \parallel b$. The sharp maximum resembles the shape of the maximum obtained for the Fe-rich compounds ($0 \leq x \leq 0.7$), while the broader maximum observed for magnetic fields in-plane are similar in shape to the maximum of $Ni_2P_2S_6$. Subsequently, the evolution of T_{max} for $H \parallel a$ and $H \parallel b$ can be considered to be gradual while for $H \parallel c^*$ a drastic change is observed at $x = 0.9$.

Evolution of the Magnetic Anisotropy in the Antiferromagnetic State

In general, the evolution of the magnetization as function of the direction of the magnetic field (with respect to crystallographic directions) is a direct measure for the magnetic anisotropy of a system. For example for $Ni_2P_2S_6$, the magnetic easy axis was identified in Sect. 3.1.3 from the field dependent magnetization for fields applied along the three perpendicular crystallographic directions a , b and c^* , in agreement with literature [43]. For this, the fingerprint of the metamagnetic spin-flop transition was found which occurs for fields applied along the easy axis, as explained in Sect. 1.2.3. However the magnetic hardness of a direction for the intermediate $(Fe_{1-x}Ni_x)_2P_2S_6$ compounds must be identified by other means, since the fingerprint of the metamagnetic spin-flop transition is not found up to 70 kOe as shown in the field dependent magnetization $M(H)$ in Fig. 3.23.

Applying a weak magnetic field (*i.e.* magnetic fields below the metamagnetic transition) to a collinear antiferromagnet parallel to its magnetic easy axis, ideally results in zero magnetization in field direction. However, applying the same field perpendicular to its magnetic easy axis results in canting of spins towards the field direction and thus to a non-zero magnetization in this direction [65]. Although in a real sample the magnetization for $H \parallel$ easy axis might differ from zero, it is still expected to be significantly smaller than for $H \perp$ easy axis. Accordingly, the magnetic easy axis in a collinear antiferromagnet corresponds to the direction for which

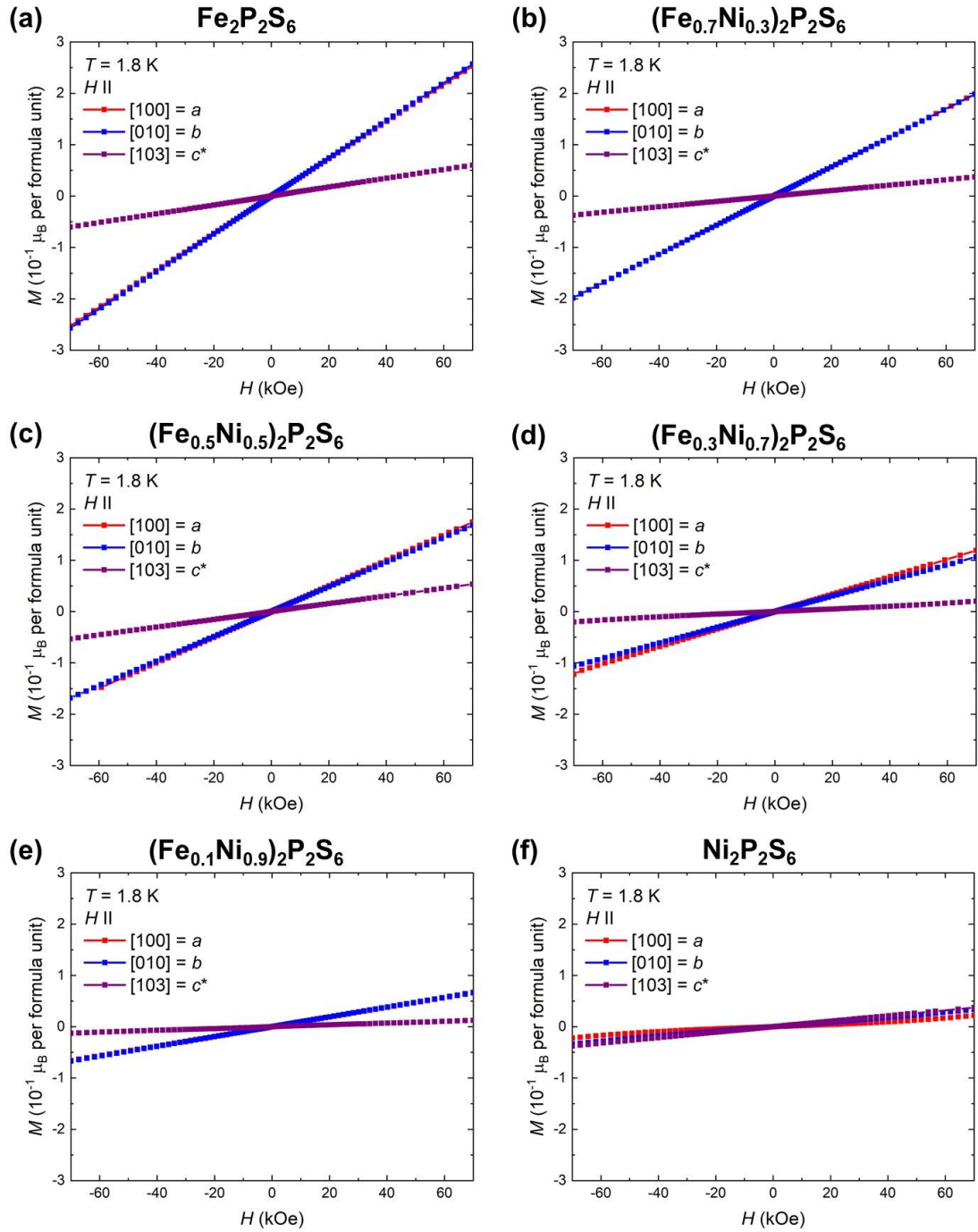


Fig. 3.23.: Field dependent magnetization $M(H)$ at 1.8 K with magnetic fields applied along three perpendicular crystallographic directions a , b and c^* for (a) $\text{Fe}_2\text{P}_2\text{S}_6$, (b) $(\text{Fe}_{0.7}\text{Ni}_{0.3})_2\text{P}_2\text{S}_6$, (c) $(\text{Fe}_{0.5}\text{Ni}_{0.5})_2\text{P}_2\text{S}_6$, (d) $(\text{Fe}_{0.3}\text{Ni}_{0.7})_2\text{P}_2\text{S}_6$, (e) $(\text{Fe}_{0.1}\text{Ni}_{0.9})_2\text{P}_2\text{S}_6$ and (f) $\text{Ni}_2\text{P}_2\text{S}_6$. The M axes are scaled the same for best comparability.

the smallest magnetization is obtained at a given magnetic field and temperature. This can be applied to both the thermal evolution of the magnetization and the field dependent magnetization at temperatures in the ordered state and at magnetic fields below the metamagnetic transition.

Regarding the substitution series of $(\text{Fe}_{1-x}\text{Ni}_x)_2\text{P}_2\text{S}_6$ both the thermal evolution as well as the field dependence of the magnetization yield the same magnetic anisotropy for each compound. For $0 \leq x \leq 0.9$ in $(\text{Fe}_{1-x}\text{Ni}_x)_2\text{P}_2\text{S}_6$, the magnetic easy axis is parallel to c^* . For magnetic fields along the other directions a and b , the magnetization is approximately equal which implies an intrinsically isotropic magnetic hard plane. This behavior is in agreement with Ising-type anisotropy. For $\text{Fe}_2\text{P}_2\text{S}_6$, this type of anisotropy is also found by inelastic neutron spectroscopy [116].

Only $\text{Ni}_2\text{P}_2\text{S}_6$ distinctly deviates from this behavior with the lowest magnetization obtained for $H \parallel a$, which subsequently is the easy axis. Also the magnetization for $H \parallel b$ and $H \parallel c^*$ are anisotropic in regard to each other, with c^* being the magnetically hardest axis. This magnetization behavior clearly speaks against Ising-like anisotropy with an easy axis and defined hard plane. Joy and Vasudevan [126] as well as Lançon *et al.* [117] found an Heisenberg Hamiltonian with a single ion anisotropy contribution suitable to describe the magnetism in $\text{Ni}_2\text{P}_2\text{S}_6$. Likely, such a description of the anisotropic behavior is also suitable for the direction dependence observed in this work. In line with Kim *et al.* [45], this XYZ-type anisotropy may be approximated as XXZ-type at first instance.

Evolution of the Short Range Correlated Regime

As seen in Fig. 3.22, the shape of the maximum around T_{max} changes as function of the degree of substitution. E.g. for $H \parallel c^*$, the maximum is pronounced but rather rounded around T_{max} for $\text{Fe}_2\text{P}_2\text{S}_6$. Increasing the degree of Ni substitution, the maximum gradually gets sharper up to $x = 0.9$. Finally for $\text{Ni}_2\text{P}_2\text{S}_6$, a broad rounded maximum is observed.

The shape of the maximum is dominated by the difference between its center (T_{max}) and the inflection point at lower temperatures at $T_{\text{inflection}} = T_{\text{N}}$. The smaller the difference between T_{N} and T_{max} are, the sharper the maximum becomes. As low-dimensional magnetic short range correlations (SRC) set in below T_{max} , the regime between T_{N} and T_{max} is dominated by these correlations before three dimensional magnetic order is established below T_{N} . Accordingly, the evolution of $T_{\text{max}}/T_{\text{N}}$ can be considered a quantitative measure for the sharpness of the maximum and thus the broadness of the SRC regime over the substitution series. Subsequently, the evolution of $T_{\text{max}}/T_{\text{N}}$ as function of the degree of Ni substitution x in $(\text{Fe}_{1-x}\text{Ni}_x)_2\text{P}_2\text{S}_6$ is shown in Fig. 3.24 in good qualitative agreement with the values from Rao and Raychaudhuri [134] from polycrystalline samples.

The evolution of the broadness of the SRC regime in $(\text{Fe}_{1-x}\text{Ni}_x)_2\text{P}_2\text{S}_6$ resembles similarities to the evolution of the magnetic anisotropy as discussed before. In particular, Ising anisotropy and a sharp maximum with $T_{\text{max}}/T_{\text{N}} \leq 1.1$ is found for $0 \leq x \leq 0.9$ while XYZ anisotropy and a distinctly broader maximum with $T_{\text{max}}/T_{\text{N}} = 1.65$ is obtained for $\text{Ni}_2\text{P}_2\text{S}_6$. As shown in Table 3.9, such a relation between the magnetic anisotropy and the broadness of the SRC

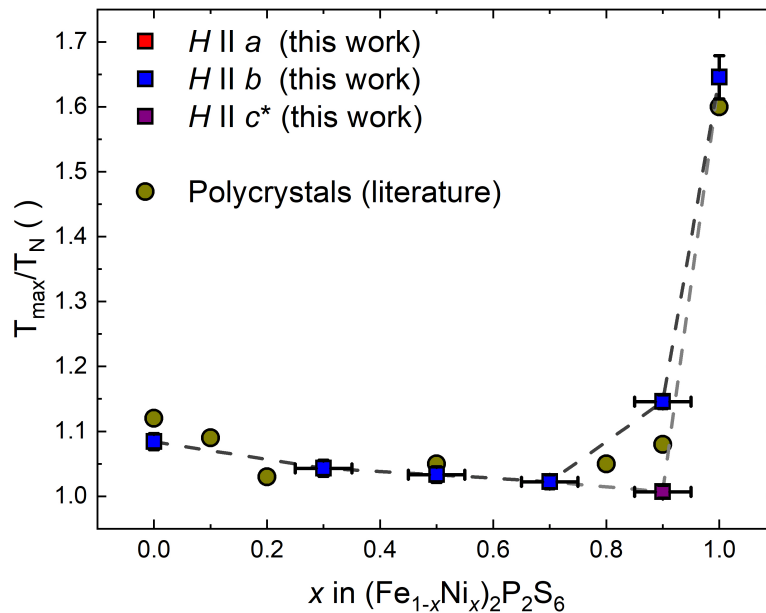


Fig. 3.24.: Evolution of the ratio of T_{max} to T_N (T_{max}/T_N) for an applied magnetic field of 10 kOe along the three perpendicular crystallographic directions a , b and c^* for $(Fe_{1-x}Ni_x)_2P_2S_6$. Literature values for polycrystalline samples [134] are shown as yellow circles.

regime is not only found for $(Fe_{1-x}Ni_x)_2P_2S_6$ but also for other (low-dimensional) antiferromagnets. In general, strongly anisotropic antiferromagnets (*i.e.* Ising-like) exhibit only a small SRC regime with T_{max}/T_N close to unity regardless of the dimensionality. A distinctly broader SRC regime can be found for low-dimensional weakly anisotropic antiferromagnets (*i.e.* XYZ- or Heisenberg-like).

However, the relation between the magnetic anisotropy and the broadness of the SRC regime in low-dimensional systems is not well understood. While T_{max} is a good estimate for the coupling strength in 1D system with exclusively nearest neighbor magnetic exchange coupling [66, 145], for more complex systems this approach fails. Accordingly, details such as the origin for the slight decrease of T_{max}/T_N from 1.08 for $Fe_2P_2S_6$ to 1.01 for $(Fe_{0.3}Ni_{0.7})_2P_2S_6$ as well as the origin for the anisotropy of T_{max}/T_N for $(Fe_{0.1}Ni_{0.9})_2P_2S_6$ still remain elusive. However regarding the latter, it should be noted that similar anisotropies were already observed in other antiferromagnets as shown in Table 3.9.

In conclusion, both the evolution of the anisotropic magnetic behavior as well as the evolution of the SRC regime imply that the magnetic properties of $(Fe_{1-x}Ni_x)_2P_2S_6$ do not evolve gradually between the behaviors of the parent compounds $Fe_2P_2S_6$ and $Ni_2P_2S_6$. Rather, the evolution of the magnetic properties for $(Fe_{1-x}Ni_x)_2P_2S_6$ with $0 \leq x \leq 0.9$ follows a certain trend with the magnetic behavior of $Ni_2P_2S_6$ being distinctly different.

Table 3.9.: Comparison of $T_{\text{max}}/T_{\text{N}}$ of $\text{Fe}_2\text{P}_2\text{S}_6$ and $\text{Ni}_2\text{P}_2\text{S}_6$ with different 2D and 3D magnetic systems exhibiting a comparable magnetic anisotropy. H_{\parallel} indicates an applied magnetic field parallel to the magnetic easy axis, while H_{\perp} indicates a magnetic field applied in the magnetic hard plane.

Compound	Magn. Anisotropy	Dim.	$T_{\text{max}}/T_{\text{N}}$	Reference
$\text{Fe}_2\text{P}_2\text{S}_6$	Ising	2D	1.08	this work
K_2CoF_4	Ising	2D	1.21 (H_{\perp}) 1.48 (H_{\parallel})	Ref. [141]
MnF_2	Ising	3D	1.03 (H_{\perp}) 1.05 (H_{\parallel})	Ref. [142]
$\text{Ni}_2\text{P}_2\text{S}_6$	XYZ	2D	1.65	this work
MnTiO_3	Heisenberg	2D	1.56	Ref. [143]
K_2NiF_4	Heisenberg	2D	2.27	Ref. [144]

Evolution of the Magnetic Anisotropy in the Paramagnetic State

For $\text{Fe}_2\text{P}_2\text{S}_6$, anisotropic magnetization is not only observed in the antiferromagnetically ordered state but also in the paramagnetic state (see Fig. 3.22(a)). This is in contrast to $\text{Ni}_2\text{P}_2\text{S}_6$ which exhibits isotropic magnetization above T_{N} (see Fig. 3.22(f)).

As discussed by Joy and Vasudevan [126], a trigonal distortion of the TS_6 octahedra may lead to an additional splitting of the electron orbital levels in the crystal field scheme depending on the spin configuration of T . Subsequently, an orbital doublet ground state is expected to form for $T = \text{Fe}$, while a singlet ground state is found for $T = \text{Ni}$. A singlet ground state results in an isotropic g -factor and a magnetic easy axis in the ab -plane, in agreement with the magnetization behavior of $\text{Ni}_2\text{P}_2\text{S}_6$. However, the doublet ground state in $\text{Fe}_2\text{P}_2\text{S}_6$ gives a magnetic easy axis perpendicular to the ab -plane and may allow the anisotropic values of g . A potential g -factor anisotropy is suitable to explain the anisotropic magnetization above T_{N} in $\text{Fe}_2\text{P}_2\text{S}_6$.

Anisotropic magnetization in the paramagnetic state is observed for $(\text{Fe}_{1-x}\text{Ni}_x)_2\text{P}_2\text{S}_6$ with $0 \leq x \leq 0.9$ as shown in Fig. 3.22(a)–(e). However, increasing the degree of nickel substitution x in $(\text{Fe}_{1-x}\text{Ni}_x)_2\text{P}_2\text{S}_6$ results in a monotonic reduction of the anisotropy in the paramagnetic state as shown for the normalized magnetization at 400 K in Fig. 3.25 as an example. Increasing the Ni content in $(\text{Fe}_{1-x}\text{Ni}_x)_2\text{P}_2\text{S}_6$ replaces Fe-moments with a locally anisotropic g -factor by Ni-moments which locally have an isotropic g -factor. In this line, the observed trend of the anisotropy in the paramagnetic state with the Fe content in $(\text{Fe}_{1-x}\text{Ni}_x)_2\text{P}_2\text{S}_6$ agrees well with the aforementioned g -factor anisotropy caused by the crystal field splitting of the Fe coordination sphere. Furthermore, the linear decreasing magnetic moment by increasing x in Fig. 3.25 can mainly be attributed to a linear decrease of the effective spin from $S = 2$ for $\text{Fe}_2\text{P}_2\text{S}_6$ to $S = 1$ for $\text{Ni}_2\text{P}_2\text{S}_6$ as function of substitution.

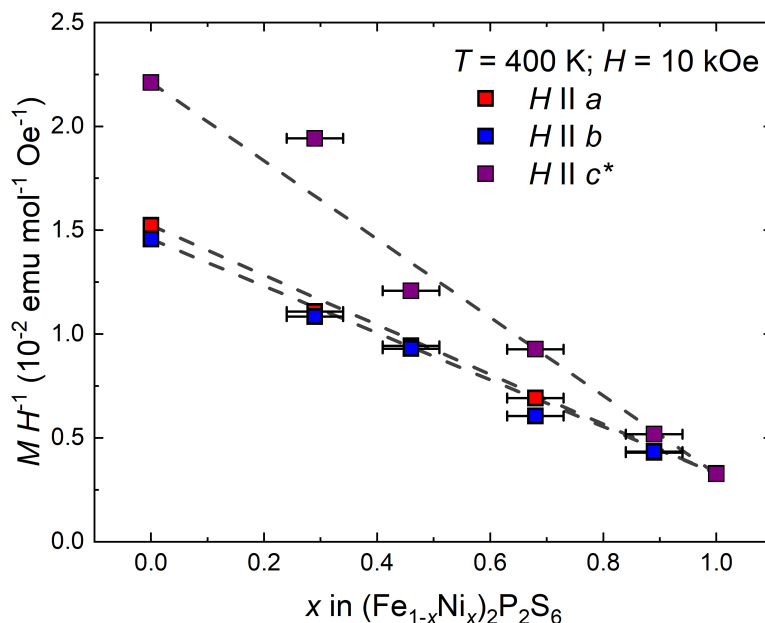


Fig. 3.25.: Evolution of MH^{-1} at 400 K and an external magnetic field of 10 kOe applied along three different crystallographic directions in $(Fe_{1-x}Ni_x)_2P_2S_6$.

Investigation for Spin Glass and Magnetic Glass in $(Fe_{0.5}Ni_{0.5})_2P_2S_6$

As mentioned in Sect. 3.2, mixed transition metal $M_2P_2S_6$ compounds may yield exotic ground states such as spin glass states as *e.g.* found in $(MnFe)P_2S_6$ [119]. Typically, a spin glass state can be detected by a splitting of zero-field cooled (zfc) and field cooled (fc) measurements of the thermal evolution of the magnetization or by displacements in the field dependent magnetization.

Based on the measurements in this work, the first criterion cannot be evaluated as all thermal magnetization measurements were exclusively performed field cooled. However, the field dependent magnetization measurements, as shown in Fig. 3.23, do not exhibit any anomaly corresponding to a spin glass state for any compound of the substitution series at 1.8 K. In agreement with this, Rao and Raychaudhuri [134] investigated the zfc/fc magnetic behavior as well as the field dependence, however only for a polycrystalline $(Fe_{0.5}Ni_{0.5})_2P_2S_6$ sample, finding no indication for a spin glass state down to 10 K.

Goossens *et al.* [135] reported a magnetic glass state in polycrystalline $(Fe_{0.5}Ni_{0.5})_2P_2S_6$. A magnetic glass is a state of randomly oriented (larger) clusters of magnetic moments in contrast to a spin glass state where individual moments or small clusters are frozen with random orientations. The former state is magnetically not identified by the typical characteristics of a spin glass but most prominently by a hysteresis between field cooled warming and field cooled cooling measurements [135, 146]. Such a hysteresis was found for polycrystalline $(Fe_{0.5}Ni_{0.5})_2P_2S_6$ [135].

To investigate if this behavior is specific to the material or dependent on the sample, the thermal evolution of MH^{-1} was measured zfc heating, fc heating and fc cooling on a single

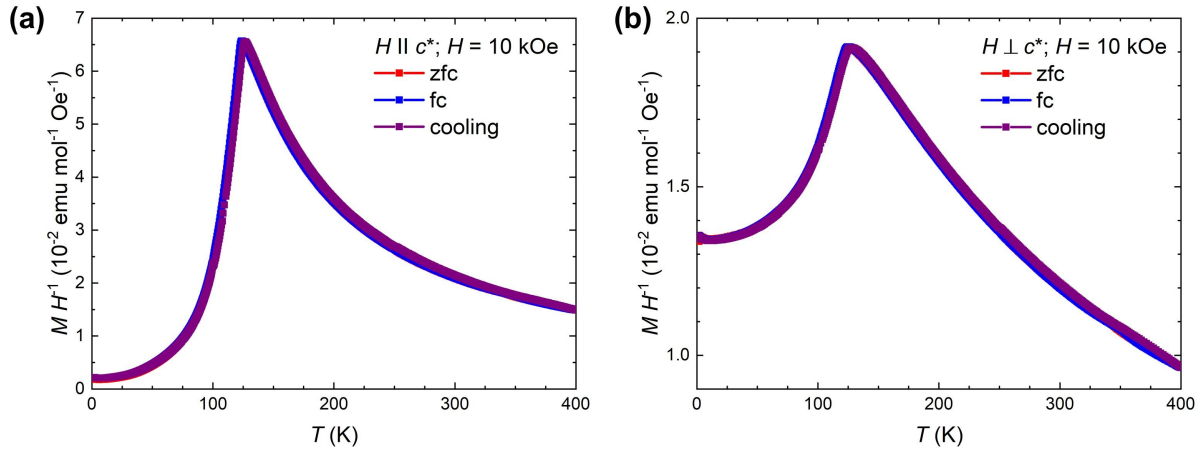


Fig. 3.26.: Normalized magnetization of $(\text{Fe}_{0.5}\text{Ni}_{0.5})_2\text{P}_2\text{S}_6$ as function of temperature $MH^{-1}(T)$ measured during cooling, heating after zfc and heating after fc with an external magnetic field of 10 kOe applied (a) parallel and (b) perpendicular to the magnetic easy axis c^* .

crystal of $(\text{Fe}_{0.5}\text{Ni}_{0.5})_2\text{P}_2\text{S}_6$ with fields applied parallel and perpendicular to the magnetic easy axis c^* , as shown in Fig. 3.26. The same external field of 10 kOe as in the work of Goossens *et al.* [135] was applied. For both directions of the magnetic field, all curves (zfc heating, fc heating and fc cooling) match and no splitting is observed down to 1.8 K. Consequently, the $(\text{Fe}_{0.5}\text{Ni}_{0.5})_2\text{P}_2\text{S}_6$ single crystals investigated in this work do not exhibit magnetic glass behavior and the behavior observed in the work of Goossens *et al.* [135] is most likely not intrinsic.

Accordingly, no indication for a spin glass state or a magnetic glass state could be found for $(\text{Fe}_{1-x}\text{Ni}_x)_2\text{P}_2\text{S}_6$ with $0 \leq x \leq 1$ based on the measurements on single crystals in this work. Nevertheless, measurements of the frequency dependence of the ac-susceptibility may be worthwhile in the future to further investigate the existence of such short range correlated states in single crystals of $(\text{Fe}_{1-x}\text{Ni}_x)_2\text{P}_2\text{S}_6$ at lowest temperatures.

3.3. Summary and Outlook

Two members of the $M_2P_2S_6$ class of materials, $Fe_2P_2S_6$ and $Ni_2P_2S_6$, as well as four intermediate mixed transition element compounds of the general formula $(Fe_{1-x}Ni_x)_2P_2S_6$ (with $x = 0.3, 0.5, 0.7$ & 0.9) have been successfully grown as single crystals by CVT with iodine as transport agent. For the mixed transition element compounds it has proven to be crucial to use polycrystalline stoichiometric precursors as starting mixture for the crystal growth to obtain homogeneous single crystals with the desired degree of substitution. Composition and phase purity are confirmed by EDX spectroscopy and pXRD.

For $Ni_2P_2S_6$ a monoclinic unit cell in the space group $C2/m$ is found by scXRD and pXRD. Furthermore, the X-ray patterns exhibit broadening of certain reflections indicative of strong disorder in the stacking direction c^* . Regarding the atomic structure, a model containing a Ni- P_2 site disorder results in significantly better agreement with the scXRD experiment than a model without this structural disorder as reported by Ouvrard *et al.* [112]. However, ^{31}P NMR spectroscopy finds no indication for such as site disorder in $Ni_2P_2S_6$. Consequently, site disorder does not play a significant role in the structure of the $Ni_2P_2S_6$ crystals grown in the course of this work. It is more likely that the displaced electron density resulting from stacking faults is misinterpreted in the structural solution of scXRD and falsely leads to a crystal structure model involving site disorder, as already speculated in literature [117, 123].

The magnetic behavior of $Ni_2P_2S_6$, as probed by magnetometry and ^{31}P NMR spectroscopy, is found in agreement with literature [43, 126] for magnetic fields along the three perpendicular directions a , b and c^* . However, the magnetic behavior for magnetic fields along additional directions in the ab plane implies an in-plane angular dependence that is in apparent contradiction to the magnetic structure reported by Wildes *et al.* [43]. Instead of a two-fold rotation symmetry of the easy axis expected from the magnetic structure, a six-fold rotation symmetry is found. Yet assuming 120° rotational twinning along the stacking direction c^* in the $Ni_2P_2S_6$ crystals, the observed angular dependence is brought in line with the magnetic structure.

The monoclinic stacking in the $C2/m$ structure breaks the three-fold symmetry of the layers (wallpaper group $p3$), which results in three potential directions for the monoclinic axis. Following from this in combination with only weak interactions between adjacent layers, 120° rotational twinning is likely observed in the monoclinic $M_2P_2S_6$ compounds. For this investigation of the real structure of these compounds, $Ni_2P_2S_6$ is a model system as the magnetic structure with an easy axis in-plane allows to investigate the structural in-plane behavior by means of magnetic properties additional to X-ray diffraction techniques.

For $Fe_2P_2S_6$ as well as for the intermediate mixed transition element compounds of the substitution series $(Fe_{1-x}Ni_x)_2P_2S_6$, scXRD and pXRD are well indexed by a unit cell in the monoclinic space group $C2/m$. Single crystal XRD patterns for all these compounds are well described by the structural model with Ni- P_2 site disorder proposed by Ouvrard *et al.* [112]. Although this site disorder is most likely not real but rather an artifact obtained from stacking faults (as discussed extensively for $Ni_2P_2S_6$), using this model allowed to obtain comparable structural parameters throughout the whole substitution series as it yields the best possible

agreement with experiment - in lack of a crystal structure model for $M_2P_2S_6$ that takes stacking faults explicitly into account.

Lattice parameters and cell volumes extracted from scXRD and pXRD patterns exhibit an overall linear evolution in agreement with Vegard's law [137]. Slight deviations of the structural parameters from linearity are likely observed due to inaccuracies in their determination caused by stacking faults. As one structural model is sufficient to model the scXRD patterns throughout the whole substitution series and Vegard's law is followed, $(Fe_{1-x}Ni_x)_2P_2S_6$ is a solid solution.

$Fe_2P_2S_6$, $Ni_2P_2S_6$ and the intermediate $(Fe_{1-x}Ni_x)_2P_2S_6$ compounds all exhibit a long-range antiferromagnetic ground state as well as a regime of SRC above the ordering temperature which is typical for low-dimensional antiferromagnets. Nevertheless, several aspects of the magnetic behavior differ between both parent compounds. $Fe_2P_2S_6$ is an Ising-like antiferromagnet with the magnetic easy axis parallel to c^* and it exhibits only a narrow regime of SRC above $T_N = 119 \pm 2$ K. However, $Ni_2P_2S_6$ is a XYZ-like antiferromagnet with the magnetic easy axis along the a direction and a broad SRC regime above $T_N = 156 \pm 2$ K. For both compounds, these magnetic properties are in agreement with literature [43, 116, 117, 126]. Surprisingly for all intermediate compounds of $(Fe_{1-x}Ni_x)_2P_2S_6$ with $0.3 \leq x \leq 0.9$, the magnetic behavior resembles the behavior of $Fe_2P_2S_6$. While the Néel temperature evolves gradually, the magnetic behavior of the intermediate compounds is best described as Ising-like with the magnetic easy axis along the c^* direction. Also, the SRC regime above the ordering temperature remains narrow as expressed by the ratio T_{max}/T_N . Based on the behavior of $(Fe_{1-x}Ni_x)_2P_2S_6$ as well as other compounds from literature, the broadness of the SRC regime seems to be dominantly affected by the strength of the magnetic anisotropy in low-dimensional systems. In this line of argumentation, the magnetic anisotropy in $(Fe_{1-x}Ni_x)_2P_2S_6$ stays comparable for $0 \leq x \leq 0.9$ and then abruptly changes between $x = 0.9$ and $x = 1$. Nevertheless, the origin of this behavior remains elusive and calls for further investigations.

Furthermore, the magnetization is anisotropic in the paramagnetic regime for the whole substitution series except of $Ni_2P_2S_6$. As discussed by Joy and Vasudevan for $Fe_2P_2S_6$ [126], an anisotropic Landé g -factor emerges from the crystal field splitting of Fe in its distorted octahedral coordination sphere. This is suitable to explain the normal state anisotropy in $Fe_2P_2S_6$. The evolution of the anisotropy in the paramagnetic state as function of the Fe/Ni substitution can be understood in the context of replacing Fe with an anisotropic g -factor by Ni with an isotropic g -factor. Moreover, no indications for a spin glass state or a magnetic glass state are found for any compound of $(Fe_{1-x}Ni_x)_2P_2S_6$ based on the single crystals investigated in this work. This is in contrast to a report on a magnetic glass state in polycrystalline $(Fe_{0.5}Ni_{0.5})_2P_2S_6$ [135].

In conclusion, the real structure of the $M_2P_2S_6$ compounds likely is better understood by involving 120° twinning rather than M - P_2 site disorder. $(Fe_{1-x}Ni_x)_2P_2S_6$ was identified as solid solution with a rather unusual evolution of the magnetic behavior, which is most likely attributed to the magnetic anisotropy. This work demonstrates that the magnetic anisotropy in $(Fe_{1-x}Ni_x)_2P_2S_6$ does not significantly change in the range of $0 \leq x \leq 0.9$ but then is found heavily altered for $x = 1$. In this line, $(Fe_{1-x}Ni_x)_2P_2S_6$ may only allow for a narrow window between $x = 0.9$ and $x = 1$ to tune the magnetic anisotropy to stabilize exotic ground states

in this low-dimensional magnet. The origin of this non-continuous change in the magnetic anisotropy as well as the potential (narrow) regime for tuning the magnetic anisotropy in $(\text{Fe}_{1-x}\text{Ni}_x)_2\text{P}_2\text{S}_6$ call for further investigation of this system.

4. $M^{1+}CrP_2S_6$

The material class of $M_2P_2S_6$ compounds exhibits a certain flexibility in the oxidation state of M [41]. This is well observed in vanadium containing compound, which does not form the stoichiometric phase but rather the off-stoichiometric phase $V_{1.56}P_2S_6$. As reported by Ouvrard *et al.* [111], in this compound vanadium occurs in an mixed valence state and the phase may be better expressed as $(V_{0.68}^{2+} V_{0.88}^{3+} \square_{0.44})P_2S_6$ (\square indicates vacant M sites).

This flexibility in the oxidation state led to the idea of replacing M^{2+} by $M_{0.5}^{1+}M_{0.5}^{3+}$ in $M_2P_2S_6$ to synthesize new compounds in this material class. Subsequently, the compounds shown in Table 4.1 could be obtained *via* solid state synthesis by Colombet *et al.* [57, 58, 147, 148]. Similar to the structure of $M_2^{2+}P_2S_6$ discussed before, all these compounds form honeycomb layers of edge sharing MS_6 antiprisms (*i.e.* distorted octahedra) with a P_2 dumbbell in the void of the honeycomb. Furthermore, the stacking of these layers is comparable to $M_2^{2+}P_2S_6$ and of van der Waals nature [41].

The main difference between $M_2^{2+}P_2S_6$ and $M^{1+}M^{3+}P_2S_6$ is that, for the latter, the two different metals of different oxidation state arrange in an orderly manner on the vortices of the honeycomb layer. As illustrated in Fig. 4.1, either an alternating, triangular arrangement (*e.g.* $CuCrP_2S_6$ in the space group $C2/c$ (No.15)) or an arrangement in stripes (*e.g.* $AgCrP_2S_6$ in the space group $P2/a$ (No. 13)) is formed on the honeycomb lattice [41]. As introduced in Sect. 1.1, the different sublattice arrangements depend mainly on the relative ionic sizes of the two M ions in regard to each other and lead to the different space groups. This is in stark contrast to *e.g.* the homocharge substitution series of $(Fe_{1-x}^{2+}Ni_x^{2+})_2P_2S_6$ (see Sect. 3.2), in which Fe and Ni were randomly distributed on the honeycomb lattice.

Specifically for $CuCrP_2S_6$, a deviation from the planar honeycomb lattice of M in $M_2P_2S_6$ is reported. According to Colombet *et al.* [58], a fraction of Cu atoms are displaced along the c^* direction in their S_6 octahedra while the Cr atoms and the remaining Cu atoms are located in the center of their S_6 octahedra. This yields two different coordination environments for Cu:

Table 4.1.: Quarternary phosphorus sulfides of the general formula $M^{1+}M^{3+}P_2S_6$. The triangular and stripe-like sublattice arrangements are illustrated in Fig. 4.1.

Compound	Space Group	Sublattice Ordering	Reference
$CuCrP_2S_6$	$C2/c$ (No. 15)	triangular	[58]
$AgInP_2S_6$	$P\bar{3}1c$ (No. 163)	triangular	[147]
$AgCrP_2S_6$	$P2/a$ (No. 13)	stripes	[148]
$AgVP_2S_6$	$P2/a$ (No. 13)	stripes	[57]

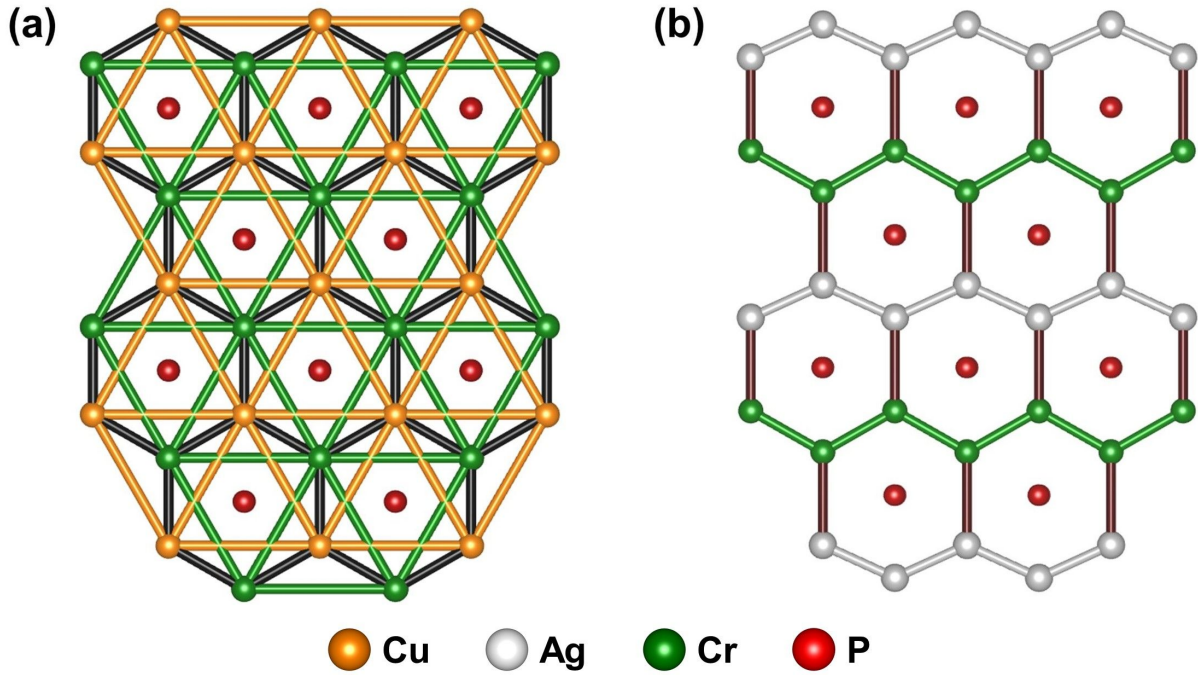


Fig. 4.1.: Perspective drawing (view $\parallel c^*$) of a layer of (a) $CuCrP_2S_6$ as example for the triangular ordering of M^{1+} and M^{3+} and (b) $AgCrP_2S_6$ with the ordering of M^{1+} and M^{3+} as zig-zag chains on the honeycomb network. S omitted for clarity. The black connections illustrate the honeycomb network, while the colored connections further emphasize the sublattices of M^{1+} and M^{3+} .

octahedrally coordinated Cu for the position in the center and a coordination environment which is close to trigonal planar for the displaced Cu atoms. For the latter, the Cu–S bond lengths were similar to those typically observed in CuS_4 tetrahedra [58].

If M^{3+} is not a closed shell cation (such as Cr^{3+} or V^{3+}), then $M^{1+}M^{3+}P_2S_6$ may exhibit magnetic order with an unusual magnetic structure due to the triangular or stripe-like arrangement of the magnetic ions on the honeycomb lattice. The triangular magnetic arrangement in the layer is supposed to yield a 2D magnetic character similar to the $M_2P_2S_6$ compounds. However, the stripe-like arrangement can be expected to result in 1D magnetic behavior, as the magnetic stripes of M^{3+} are well isolated from each other by stripes of non-magnetic M^{1+} cations.

Furthermore, specifically Cr^{3+} can be used as magnetic ion, which is known to exhibit a 90° Cr–X–Cr super-exchange coupling (X is a chalcogenide) of ferromagnetic nature [149, 150]. Consequently, it is not surprising that several quasi-2D ferromagnetic systems (e.g. $Cr_2Ge_2Te_6$ [29] (also discussed in Sect. 5.1), $Cr_2Si_2Te_6$ [151], CrI_3 [152], $CrBr_3$ [152]) contain Cr^{3+} as magnetic ion. In this line, the layered $M^{1+}Cr^{3+}P_2S_6$ compounds are promising candidates to exhibit ferromagnetic order, potentially down to the monolayer. Thus, the focus in this work is on the chromium containing compounds $CuCrP_2S_6$ and $AgCrP_2S_6$. The former is reported to yield a triangular arrangement of Cu and Cr [58], while the latter exhibits zig-zag chains of Ag and Cr according to literature [148].

In the context of the potential for long range magnetic order down to the monolayer limit, the magnetic anisotropy plays a crucial role, as introduced in Sect. 1.2.5. To reliably investigate the magnetic anisotropy of a system, single crystals are of first choice. However for the aforementioned compounds of CuCrP_2S_6 and AgCrP_2S_6 , only solid state synthesis conditions are reported [58, 148]. Although Kleemann *et al.* [153] reported the investigation of CuCrP_2S_6 crystals grown by the Bridgeman technique and Mutka *et al.* [154] mentioned that the AgCrP_2S_6 crystals used in their work had been grown by chemical vapor transport (CVT), both did not specify nor cite any details on the crystal growth. Thus in this work, the single crystal growth of CuCrP_2S_6 and AgCrP_2S_6 by CVT was attempted and optimized starting from the growth conditions used for the $M_2\text{P}_2\text{S}_6$ compounds. Based on the similarities between $M_2\text{P}_2\text{S}_6$ and $M^{1+}\text{CrP}_2\text{S}_6$ with respect to the bonding behavior and the crystal structure, the same crystal growth technique and conditions were promising as a starting point. Nevertheless, optimizing the conditions for the CVT growth of quaternary compounds is ambitious due to the large amount of species that possible contribute to the vapor phase and the transport mechanism.

Considering the severe effect that the size of the non-magnetic M^{1+} ion has on the magnetic order in $M\text{CrP}_2\text{S}_6$, it is of interest to investigate how a gradual substitution of a M^{1+} with a similar size as Cr^{3+} by another M^{1+} ion with a notably different size affects the magnetic order. Such a substitution is expected to induce chemical pressure on the compound by deforming the local $M^{1+}\text{S}_6$ environments, which indirectly affects the bonding behavior and distorts the octahedral coordination environment of the adjacent Cr^{3+}S_6 units. As seen based on the example of CuCrP_2S_6 and AgCrP_2S_6 , this yields two completely different arrangements of the two sublattices in case of the complete substitution of Cu by Ag. With smaller degrees of substitution, however, one may expect changes in the exchange coupling mechanism, as the Cr–S–Cr super-exchange pathways are affected by the chemical pressure, while the triangular or stripe-like sublattice arrangements remains. This may offer a way of tuning the magnetic properties of these quaternary compounds without inducing chemical disorder in the magnetic Cr sublattice.

However as CuCrP_2S_6 and AgCrP_2S_6 crystallize in different space groups, a structural phase transition has to be present in the quasi-binary phase diagram of $(\text{Cu}_{1-x}\text{Ag}_x)\text{CrP}_2\text{S}_6$. Such a phase transition goes along with a regime of immiscibility and, thus, $(\text{Cu}_{1-x}\text{Ag}_x)\text{CrP}_2\text{S}_6$ cannot exhibit solid solution behavior over the full range of substitution. Thus, this quasi-binary phase diagram has to be examined to locate regimes of miscibility and immiscibility and, consequently, identify regimes which are suitable to follow the aforementioned magnetic behavior under substitution. For an initial investigation of the $(\text{Cu}_{1-x}\text{Ag}_x)\text{CrP}_2\text{S}_6$ phase diagram, a polycrystalline sample series with the nominal compositions of $(\text{Cu}_{1-x}\text{Ag}_x)\text{CrP}_2\text{S}_6$ with $x = 0, 0.25, 0.50, 0.75$ & 1 was synthesized and investigated regarding its structural evolution.

Hereafter, the results of the single crystal growth experiments of CuCrP_2S_6 and AgCrP_2S_6 via CVT with iodine as transport agent are reported in Sect. 4.1 and Sect. 4.2, respectively. Additionally, the results of the compositional, structural and magnetic investigation based on these crystals are presented. In Sect. 4.3, the synthesis and structural evolution of the polycrystalline sample series of $(\text{Cu}_{1-x}\text{Ag}_x)\text{CrP}_2\text{S}_6$ with $x = 0, 0.25, 0.50, 0.75$ & 1 is presented.

4.1. $CuCrP_2S_6$

Details and results of the single crystal growth experiments of $CuCrP_2S_6$ via chemical vapor transport (CVT) with iodine as transport agent are presented hereafter in Sect. 4.1.1. Single crystals that were obtained from these growth experiments were comprehensively investigated regarding their morphology and composition by SEM and EDX and regarding their crystal structure by pXRD as shown in Sect. 4.1.2. The pXRD pattern is sufficiently modeled by structures in two different space groups. Consequently, the different possible structures are discussed in the context of literature and physical properties. In Sect. 4.1.3, the magnetic properties of $CuCrP_2S_6$ are presented and discussed. Single crystals of $CuCrP_2S_6$ enabled measurements with magnetic fields applied parallel and perpendicular to the ab planes which allows insight in the magnetic anisotropy of this compound. Ferromagnetic interactions are dominant in the planes of $CuCrP_2S_6$, while adjacent planes couple antiferromagnetically at sufficiently low temperatures.

4.1.1. Crystal Growth

Single crystals of $CuCrP_2S_6$ were grown using the CVT technique with iodine as transport agent which was not reported until now. As mentioned in Sect. 4, the preparation and growth procedure as well as the temperature profile are adapted from the crystal growth of $Ni_2P_2S_6$ as described in Sect. 3.1.1.

Under argon atmosphere in a glove box, the elemental educts copper (powder -100+325 mesh, Alfa Aesar, 99.9%), chromium (powder -100+325 mesh, Alfa Aesar, 99.99%), red phosphorus (lumps, Alfa Aesar, 99.999%) and sulfur (pieces, Alfa Aesar, 99.999%) were weighed out to yield a molar ratio of $Cu : Cr : P : S = 1 : 1 : 2 : 6$ and homogenized in an agate mortar. 0.5 g of reaction mixture were loaded in a quartz ampule (6 mm inner diameter, 2 mm wall thickness, previously baked out at 800 °C for at least 12 h) together with approx. 50 mg of the transport agent iodine (resublimed crystals, Alfa Aesar, 99.9985%). The ampule was then transferred to a vacuum pump and evacuated to a residual pressure of 10^{-8} bar. To suppress the unintended sublimation of the transport agent during evacuation, the lower end of the ampule containing the material was cooled with liquid nitrogen. After reaching the desired internal pressure, the valve to the vacuum pump was closed, the cooling was stopped and the ampule was sealed under static pressure at a length of approximately 12 cm.

Following the same procedure for the heat treatment as described in Sect. 3.1.1 for $Ni_2P_2S_6$ with the temperature profile shown in Fig. 4.2, shiny plate-like crystals of $CuCrP_2S_6$ in the size of up to $3\text{ mm} \times 3\text{ mm} \times 200\text{ }\mu\text{m}$ were obtained. Fig. 4.3(a) shows such an as-grown single crystal. The crystals exhibit a layered morphology and are easy to exfoliate. Such a freshly exfoliated crystal with a highly reflective surface is shown in Fig. 4.3(b).

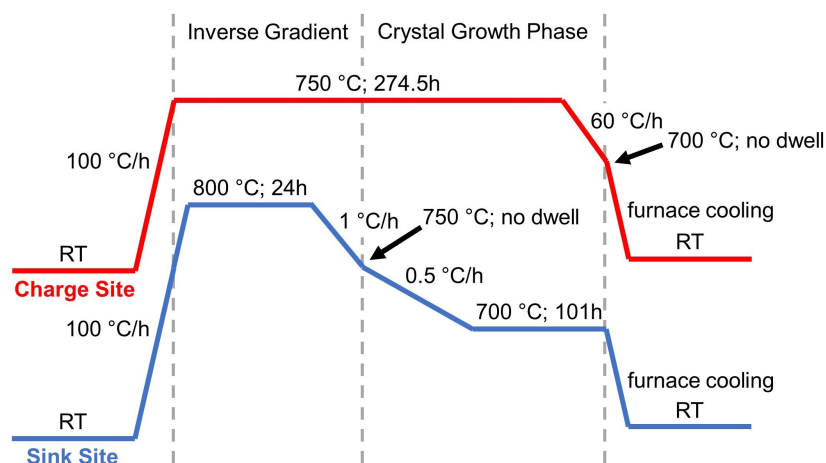


Fig. 4.2.: Schematic representation of the temperature profile for the single crystal growth of CuCrP_2S_6 using CVT. The charge site temperature profile is shown in red and the sink site profile in blue.

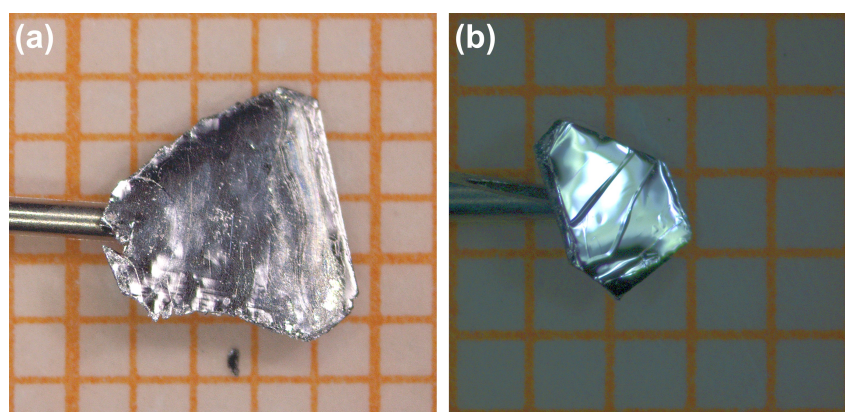


Fig. 4.3.: Single crystals of CuCrP_2S_6 obtained from the chemical vapor transport growth with iodine as transport agent - (a) as-grown and (b) freshly exfoliated. One orange square in the background corresponds to $1 \times 1 \text{ mm}^2$ for scale.

4.1.2. Characterization

Crystal Morphology and Compositional Analysis

The crystal morphology was further investigated by SEM. Using the SE detector (*i.e.* topographic contrast), the CuCrP_2S_6 crystals exhibit flat surfaces and well developed edge facets, as, *e.g.*, illustrated in Fig. 4.4(a). The edge facets indicate a hexagonal crystal habitus. In the lower central part of Fig. 4.4(a), the surface of the crystal was scratched and several layers peel off, demonstrating the layered nature of the crystal with only weak van der Waals interactions between layers. Using the chemical contrast mode (BSE detector) as shown in Fig. 4.4(b), the crystal surface overall shows a homogeneous contrast. Comparing the SEM(SE) and SEM(BSE) images, the few spots of different contrast can be clearly attributed to particles on the crystal surface and not to intrinsic impurities in the crystal. Subsequently, the crystals have a homogeneous composition.

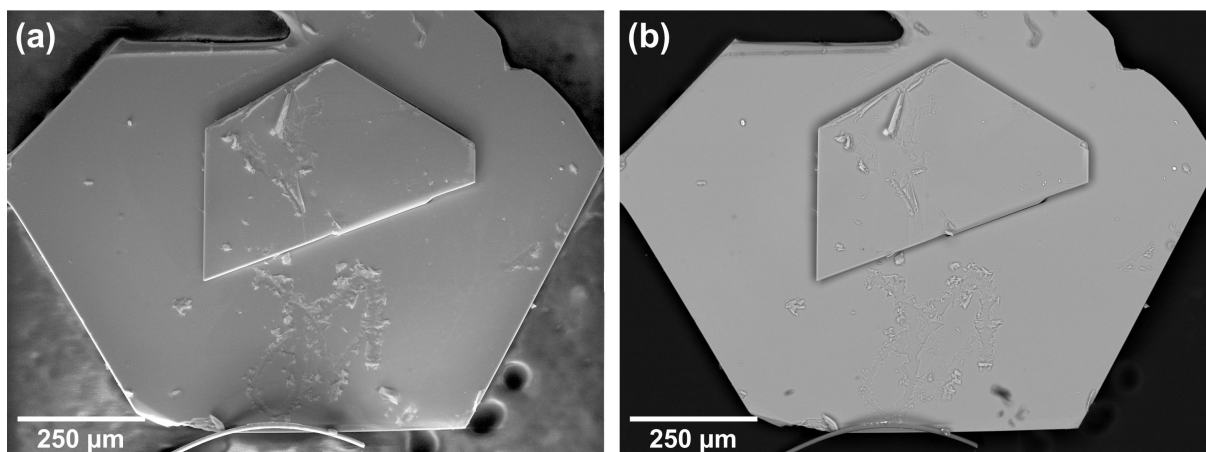


Fig. 4.4.: SEM images of a $CuCrP_2S_6$ crystal using (a) the topographic contrast mode (*i.e.* SE-detector) and (b) the chemical contrast mode (*i.e.* BSE-detector).

In more detail, the elemental composition was investigated by EDX on 30 spots on several crystals of the same crystal growth experiment. The mean elemental composition is $Cu_{10.5(3)}Cr_{10.4(2)}P_{20.3(1)}S_{58.8(4)}$, in agreement with the expected composition of the $M^{1+}CrP_2S_6$ phase of $Cu_{10}Cr_{10}P_{20}S_{60}$. The low standard deviations further indicate the high homogeneity of the elemental composition over several crystals. Moreover, no significant amount of iodine was found in any crystal.

Structural Analysis

The crystal structure of $CuCrP_2S_6$ was investigated by pXRD at 293(2) K and the corresponding pattern is shown in Fig. 4.5. According to the structural solution of $CuCrP_2S_6$ based on scXRD by Colombet *et al.* [58], Cu and Cr alternately occupy the corners of the honeycomb lattice in $CuCrP_2S_6$. This arrangement on the honeycomb lattice breaks the mirror symmetry of the $C2/m$ space group. However by doubling the c parameter, a glide plane is found instead of a mirrorplane for $CuCrP_2S_6$ and thus this structure fulfills the symmetry of the $C2/c$ space group (No. 15). Yet, the symmetry breaking is caused by having two $3d$ elements order on the honeycomb lattice which most likely affects the structure factor only barely. Therefore, it is challenging to distinguish the ordered $C2/c$ structure as illustrated in Fig. 4.6(b) from a $C2/m$ structure with random distribution of Cu and Cr on the honeycomb as shown in Fig. 4.6(a) based on pXRD. The latter type of structure is discussed in the context of $(Fe_{1-x}Ni_x)_2P_2S_6$ in Sect. 3.2.2. As shown in Fig. 4.5, both structural models yield a calculated pXRD pattern that is in good agreement with the measured pattern of $CuCrP_2S_6$ and very similar reliability factors as shown in Table 4.2. The refined structural models are shown in Table 4.3 (top and mid).

The model in $C2/c$ in Fig. 4.6(b) assumes that Cu atoms and Cr atoms occupy two different $4e$ Wyckoff sites and therefore lie in a plane parallel to ab in similarity to the $C2/m$ structure. However, Colombet *et al.* [58] also reported that the Cu atoms are displaced along the c^* direction in their S_6 octahedra as mentioned before in Sect. 4.

Table 4.2.: Summary and reliability factors of the Rietveld analysis of the pXRD pattern of CuCrP_2S_6 using different structural models.

Structural Model	Random $C2/m$	Idealized $C2/c$	Disordered $C2/c$
<i>Experiment & Data Collection</i>			
Temperature (K)		293(2)	
Radiation Type & Wavelength (Å)		Cu- $K_{\alpha 1}$; 1.54059	
θ_{\min} (°)		10.00	
θ_{step} (°)		0.03	
θ_{\max} (°)		119.62	
<i>Crystal Data</i>			
Crystal System		Monoclinic	
Space Group	$C2/m$	$C2/c$	$C2/c$
a (Å)	5.9128(3)	5.9117(3)	5.9133(3)
b (Å)	10.2386(8)	10.2392(6)	10.2362(5)
c (Å)	6.6965(7)	13.3934(12)	13.3907(11)
β (°)	107.265(8)	107.289(7)	107.285(5)
<i>Refinement</i>			
Goodness-Of-Fit	2.82	2.45	2.14
R_p (%)	4.81	4.13	3.82
wR_p (%)	7.11	6.15	5.39
R_F (%)	14.04	12.28	11.45

Table 4.3.: Fractional atomic coordinates, occupancies and isotropic displacement parameters U_{iso} of the three structural models for CuCrP_2S_6 after Rietveld refinement. Estimated standard deviations given in parantheses.

Label	Type	Wyck	x	y	z	Occ (%)	U_{iso} ($\times 10^{-3} \text{Å}^2$)
Random $C2/m$							
Cu1	Cu	4g	0	0.3319(9)	0	50	84(2)
Cr1	Cr	4g	0	0.3319(9)	0	50	84(2)
P1	P	4i	0.0484(17)	0	0.1501(15)	100	5(1)
S1	S	4i	0.7544(15)	0	0.2455(19)	100	20(2)
S2	S	8j	0.2626(10)	0.1720(5)	0.2412(11)	100	19(1)
Idealized $C2/c$							
Cu1	Cu	4e	0	0.0025(9)	0.25	100	39(2)
Cr1	Cr	4e	0	0.3360(12)	0.25	100	93(4)
P1	P	8f	0.0616(15)	0.3366(9)	0.8386(7)	100	3(1)
S1	S	8f	0.2527(15)	0.1679(9)	0.3705(7)	100	15(2)
S2	S	8f	0.2662(16)	0.1575(9)	0.8749(8)	100	18(2)
S3	S	8f	0.7405(17)	0.0019(10)	0.3713(9)	100	30(2)
Disordered $C2/c$							
Cu1	Cu	8f	0.0512(14)	0.0017(13)	0.3267(7)	50	9(2)
Cr1	Cr	4e	0	0.3314(9)	0.25	100	18(2)
P1	P	8f	0.0500(20)	0.3353(12)	0.8216(9)	100	61(3)
S1	S	8f	0.2530(18)	0.1736(12)	0.3711(8)	100	27(2)
S2	S	8f	0.2666(17)	0.1769(10)	0.8749(8)	100	18(2)
S3	S	8f	0.7378(12)	0.9962(12)	0.3739(8)	100	15(2)

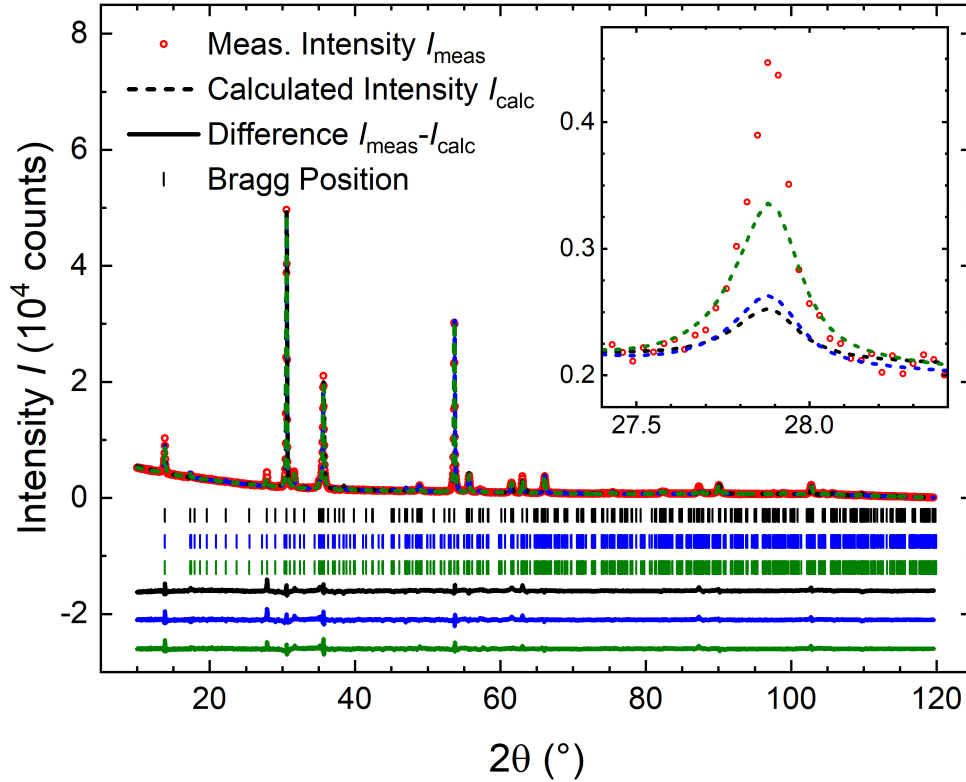


Fig. 4.5.: pXRD pattern from Cu- $K_{\alpha 1}$ radiation (1.54059 Å) of pulverized $CuCrP_2S_6$ crystals (red circles) in comparison to calculated pattern based on different structural models (dashed lines). Black: $C2/m$ structure with random distribution of Cu and Cr on the honeycomb lattice. Blue: Idealized $C2/c$ structure with Cu and Cr occupying two different $4e$ sites. Green: $C2/c$ structure with Cu occupying one $8f$ site. The marks below the pattern indicate the Bragg positions and the solid line on the bottom corresponds to the difference between experiment and model. The inset shows a zoomed-in view on the small reflection at 27.9° (002 for $C2/m$ and 004 for $C2/c$) for which the three models yield visibly different intensities.

This disorder is taken into account by shifting Cu on two partially occupied $8f$ Wyckoff sites in the structural model, Cu1 being refined close to the center of the S_6 octahedron and Cu2 closer to the face of the octahedron perpendicular to c^* . Due to the partial occupation and the statistical distribution only one of both positions is considered to be occupied for each CuS_6 unit.

Using the structural model proposed by Colombet *et al.* with two $8f$ Wyckoff sites of Cu to model the experimental pXRD pattern yields either a negative isotropic displacement parameter for Cu1 or for both Cu sites (after restricting their isotropic displacement parameters to be equal). However using only one $8f$ site for the disordered Cu, the refinement of the structural model succeeds with non-restricted, physically reasonable parameters as shown in Table 4.2 (bottom). The Cu $8f$ site is found close to the Cu2 site of the model of Colombet *et al.* with trigonal planar coordination environment as shown in Fig. 4.6(c). As shown in Fig. 4.5, a good agreement between the calculated pattern based on this model and the experiment is

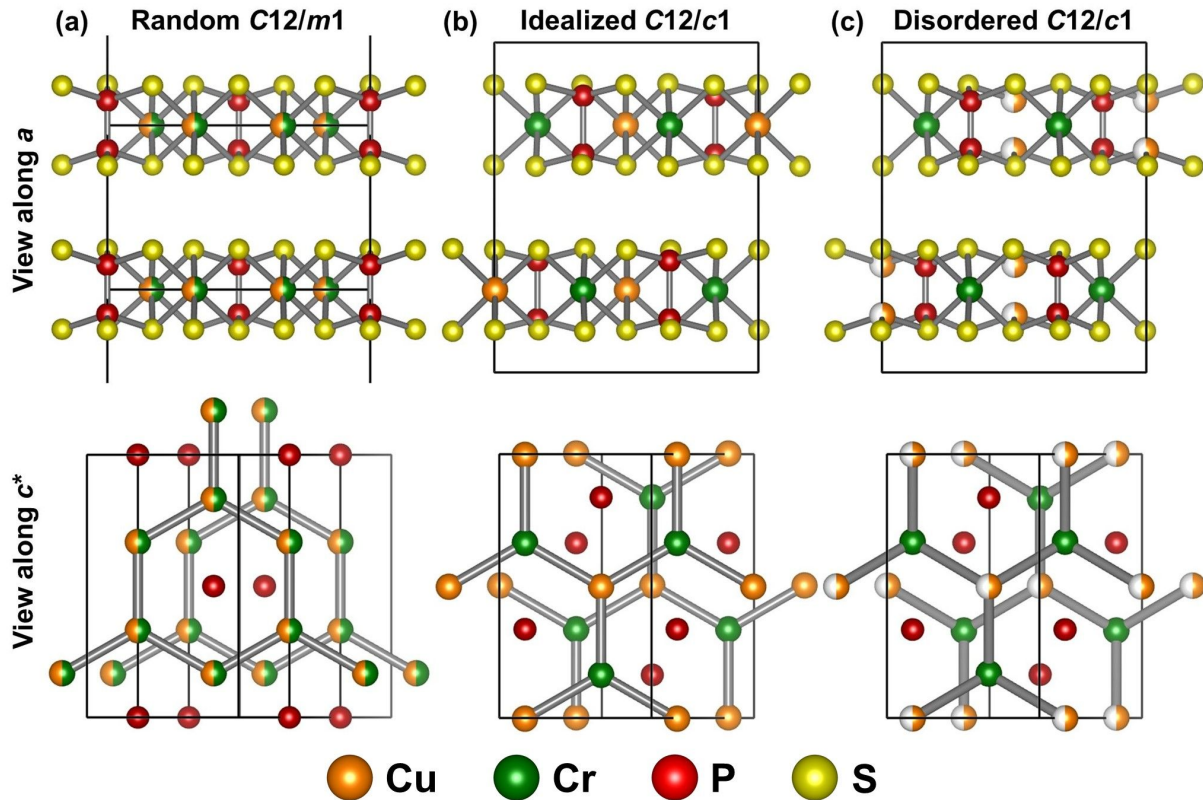


Fig. 4.6.: Perspective drawing of the crystal structure of CuCrP_2S_6 with view parallel a (top) and parallel c^* (bottom) for different structural models. (a) $C2/m$ structure with random distribution of Cu and Cr on the honeycomb lattice. (b) Idealized $C2/c$ structure with Cu and Cr occupying two different $4e$ sites. (c) $C2/c$ structure with Cu occupying one $8f$ site. For the bottom drawings S and chemical bonds are omitted and the honeycomb network is emphasized in grey.

achieved. Furthermore, this model yields the best reliability factors out of the three structural models discussed for CuCrP_2S_6 as shown in Table 4.2.

Maisonneuve *et al.* [155] reported a structural phase transition below 200 K in CuCrP_2S_6 . According to this work, the triangular arrangement of CrS_6 and CuS_6 units on the honeycomb lattice with a P_2 dumbbell in the resulting voids is still valid at low temperatures. Also, Cu is found not in the center but either closer to the top or the bottom of the S_6 octahedra as discussed for the disordered $C2/c$ structure shown in Fig. 4.6(c). However, the main difference between the disordered $C2/c$ structure and the low temperature structure is that at low temperatures Cu is no longer randomly occupying the position closer to the top or the bottom of the S_6 octahedra as in Fig. 4.6(c) but order alternating along the (110) direction (*i.e.* top position for Cu on the unit cell edge and bottom position for the center Cu in a layer in Fig. 4.6(c), or *vice versa*). Due to this ordering, the unit cell symmetry is described by the space group $P1c1$ at low temperatures. The similarities between the low temperature structure reported by Maisonneuve *et al.* and the $C2/c$ model in Fig. 4.6(c) are further supporting that the $C2/c$ model is depicting the crystal structure at room temperature best.

To summarize, it is challenging to distinguish between the crystal structure in $C2/c$ with ordered CrS_6 and CuS_6 units, as proposed by Colombet *et al.* [58], and a structure in $C2/m$

with random distribution of CrS_6 and CuS_6 on the honeycomb lattice by pXRD alone. Adding the disordered Cu sites to the $C2/c$ crystal structure model further improves the reliability factors of the refinement slightly, but overall all three models yield reasonable agreement between model and experiment. However considering the existence of the low temperature structure proposed by Maisonneuve *et al.* [155], the $C2/c$ structures are likely to depict reality better than the $C2/m$ structure for $CuCrP_2S_6$ at room temperature. Furthermore, the magnetic behavior (as discussed hereafter in Sect. 4.1.3) strongly suggests the oxidation states $Cu^{1+}Cr^{3+}P_2S_6$. As mentioned in Sect. 1.1, these different oxidation states are expected to yield the $C2/c$ structure with a triangular sublattice ordering allowing for an ideal charge separation of the two ions with different oxidation states instead of a local charge clustering as expected for the random distribution in the $C2/m$ structure.

4.1.3. Magnetic Properties

The normalized magnetization of $CuCrP_2S_6$ as function of temperature $MH^{-1}(T)$ is shown in Fig. 4.7(a) for a magnetic field of 1 kOe applied parallel and perpendicular to the ab planes (*i.e.* parallel to a random direction in the ab plane and parallel to c^*). Additionally, on the bottom of Fig. 4.7(a) the first derivative of $MH^{-1}(T)$ is shown. From 300 K towards lower temperatures, the normalized magnetization monotonically increases. A maximum in $MH^{-1}(T)$ is observed at ~ 31 K followed by a decrease towards lower temperatures. Close below the maximum in $MH^{-1}(T)$ at 30 ± 2 K, an inflection point is observed corresponding to a maximum in the first derivative. The normalized magnetization becomes strongly anisotropic below the maximum. However, a slightly anisotropic behavior can be observed already below 50 ± 5 K. The downturn below the maximum at approximately 31 K indicates a transition into an antiferromagnetically ordered state at low temperatures with the transition temperature $T_N = 30 \pm 2$ K corresponding to the anomaly (*i.e.* maximum) in the first derivative. This is in agreement with literature [58, 153].

The inverse of the normalized magnetization of $CuCrP_2S_6$ as function of temperature is shown in Fig. 4.7(b). At high temperatures a linear evolution is observed in agreement with the Curie-Weiss law. Accordingly, a Curie-Weiss analysis of the temperature regime 100–300 K yields $\Theta_{CW} = 35 \pm 1$ K and $\mu_{\text{eff}} = 3.78 \pm 0.05 \mu_B$ per $CuCrP_2S_6$ for $H \parallel ab$ and $\Theta_{CW} = 33 \pm 1$ K and $\mu_{\text{eff}} = 3.89 \pm 0.05 \mu_B$ per $CuCrP_2S_6$ for $H \perp ab$. For the latter direction of the external field, this is in good agreement with the values reported by Kleemann *et al.* [153] (who reported on the magnetic behavior of $CuCrP_2S_6$ only for this direction of the magnetic field with respect to the crystal orientation). The positive values of Θ_{CW} indicate dominantly ferromagnetic interactions in $CuCrP_2S_6$. However considering the antiferromagnetic ground-state, a positive Θ_{CW} is unexpected. Regarding μ_{eff} , both values are close to the magnetic moment expected for Cr^{3+} assuming the free electron g -factor and the absence of spin orbit coupling (*i.e.* spin only moment) $\mu_{\text{so}}(Cr^{3+}) = 3.88 \mu_B$. This implies that the oxidation states are $Cu^{1+}Cr^{3+}[P_2S_6]^{4-}$ (since Cu^{1+} is closed shell with zero magnetic moment) rather than $Cu^{2+}Cr^{2+}[P_2S_6]^{4-}$. For the latter, a magnetic moment of around $\mu \approx 6.63 \mu_B$ per $CuCrP_2S_6$ would be expected ($\mu_{\text{so}}(Cr^{2+}) = 4.90 \mu_B$ and $\mu_{\text{so}}(Cu^{2+}) = 1.73 \mu_B$).

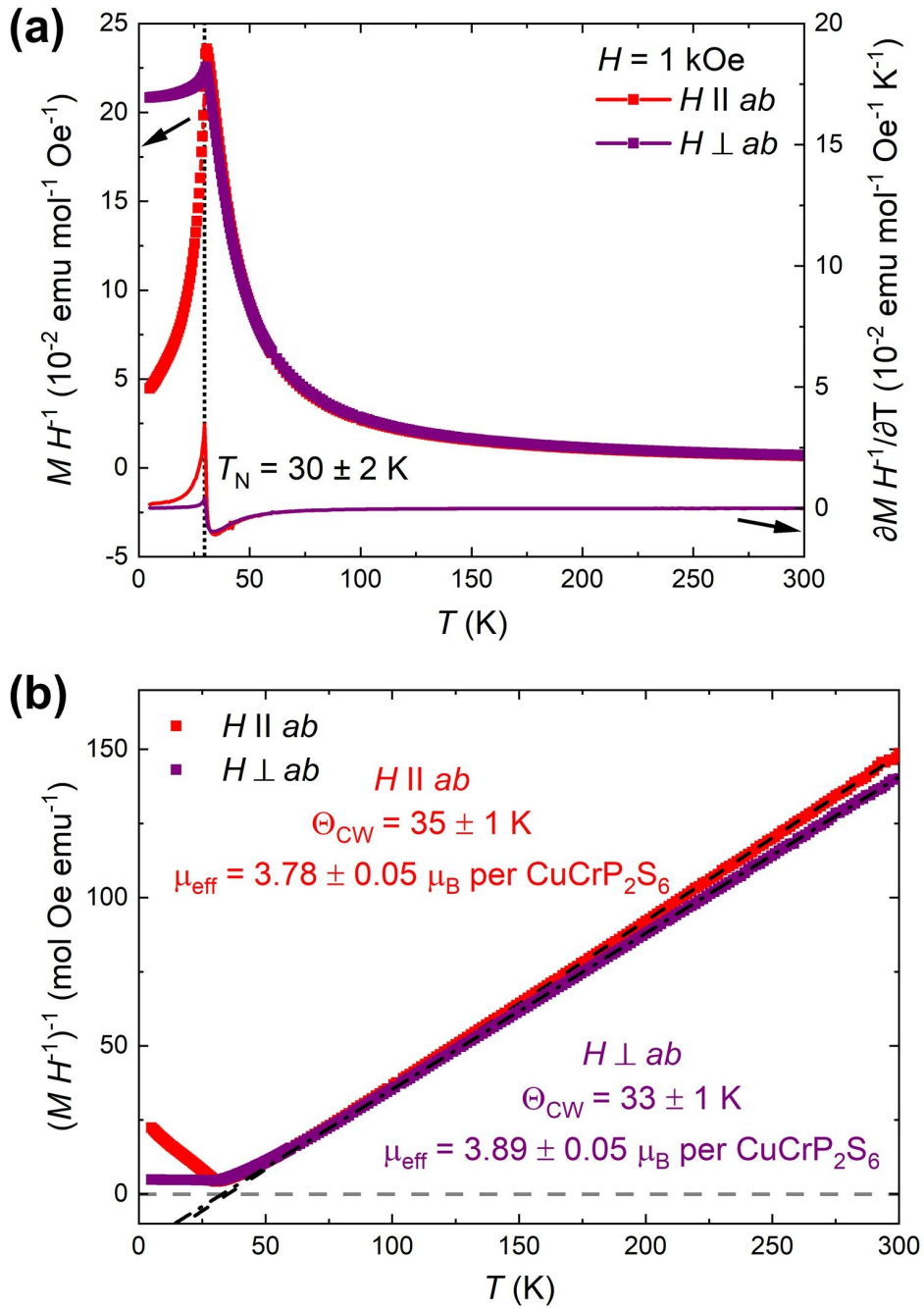


Fig. 4.7.: (a) Normalized magnetization as function of temperature $MH^{-1}(T)$ (left y-axis) and its first derivative (right y-axis) of CuCrP_2S_6 for a magnetic field of 1 kOe applied parallel and perpendicular to the crystallographic ab plane. The black dotted line marks the inflection point in $MH^{-1}(T)$ (i.e. the maximum in the first derivative) which corresponds to T_N . (b) Inverse of the normalized magnetization as function of temperature $(MH^{-1})^{-1}(T)$. The black dashed lines correspond to linear regressions of the paramagnetic regime in the range of 100–300 K.

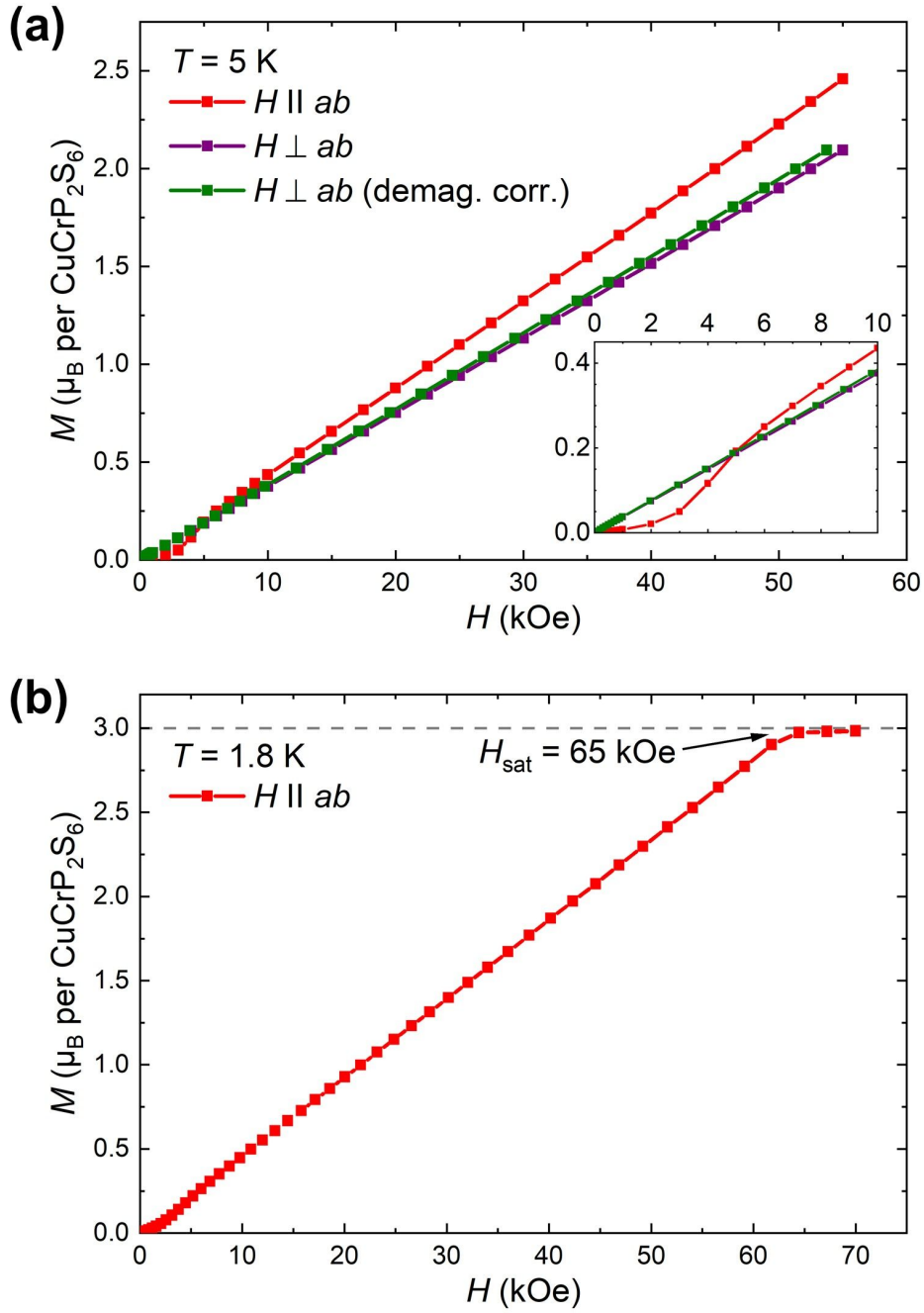


Fig. 4.8.: (a) Magnetization as function of magnetic field $M(H)$ of $CuCrP_2S_6$ at 5 K with a magnetic field up to 55 kOe applied parallel (red) and perpendicular (violet) to the ab plane. The green curve shows $M(H)$ for $H \perp ab$ after demagnetizing field correction as explained in the text. The inset shows a zoomed-in view on the low field regime up to 10 kOe. (b) $M(H)$ of $CuCrP_2S_6$ at 1.8 K with a magnetic field up to 70 kOe applied parallel to the ab plane (black). The grey dotted line marks the spin-only saturation moment for Cr^{3+} assuming $S = 3/2$ and $g = 2$.

The field dependent evolution of the magnetization $M(H)$ of CuCrP_2S_6 at 5 K and up to 55 kOe is shown in Fig. 4.8(a) for fields applied parallel and perpendicular to the ab plane. The in-plane direction of the magnetic field is the same as for the thermal evolution discussed before. The influence of a demagnetizing field due to an anisotropic shape of the sample (*i.e.* thin plate-like crystal) was estimated following the corresponding procedure introduced in Sect. 1.2.4 using the demagnetizing factors for an infinite thin platelet ($N_x = N_y = 0$ and $N_z = 1$). For $H \perp ab$, the field dependence of the magnetization is linear in agreement with Kleemann *et al.* [153] and the demagnetizing field correction causes a slight increase of the slope. For $H \parallel ab$, the magnetization is not affected by this correction and a curved $M(H)$ behavior is observed at low fields centered around approximately 4 kOe. Above ~ 10 kOe, the field dependence for $H \parallel ab$ becomes linear, however with a higher slope than for $H \perp ab$ (with and without demagnetizing field correction). The curvature at low fields is attributed to a spin-flop transition. On one hand, this indicates that the ground state of CuCrP_2S_6 is antiferromagnetic and on the other hand shows that CuCrP_2S_6 is either a magnetic easy plane system or that it has a magnetic easy axis in the ab plane, as for example observed for $\text{Ni}_2\text{P}_2\text{S}_6$ in Sect. 3.1.3. The magnetic anisotropy is likely attributed to magnetocrystalline anisotropy, as the magnetization remains notably anisotropic even after the effect of shape anisotropy was considered.

Additionally, $M(H)$ at 1.8 K and up to 70 kOe parallel to the ab plane is shown in Fig. 4.8(b) indicating magnetic saturation above $H_{\text{sat}} \approx 65$ kOe with a saturation magnetization of $M_{\text{sat}} \approx 3 \mu_{\text{B}}$ per CuCrP_2S_6 . This saturation magnetization is in agreement with $S = 3/2$ and the free electron g -factor. As Cr^{3+} in an octahedral crystal field is $S = 3/2$, this further supports the before mentioned oxidation states of $\text{Cu}^{1+}\text{Cr}^{3+}[\text{P}_2\text{S}_6]^{4-}$. The saturation field is relatively low for a system with antiferromagnetic ground state. For example, $\text{Ni}_2\text{P}_2\text{S}_6$ in Sect. 3.1.3 and $(\text{Fe}_{1-x}\text{Ni}_x)_2\text{P}_2\text{S}_6$ in Sect. 3.2.3 exhibit a magnetization which is at least an order of magnitude below the expected saturation magnetization at 70 kOe. This implies that the spin system in CuCrP_2S_6 is easily polarized by an external magnetic field which may hints at the presence of ferromagnetic interactions in CuCrP_2S_6 , in agreement with the positive values of Θ_{CW} .

This magnetization behavior of CuCrP_2S_6 is in good agreement with Colombet *et al.* [58]. They discussed this specific evolution of the magnetic properties in the context of dominantly ferromagnetic interactions in the layers, while adjacent layers interact antiferromagnetically. Such a magnetic order is already well established for several layered compounds with Cr^{3+} as magnetic ion (*i.e.* $M\text{CrX}_2$ with $M = \text{Li}, \text{Na}, \text{K}, \text{Cu}, \text{Ag}$ and $X = \text{S}, \text{Se}$ [156–159] as well as CrCl_3 [160, 161]) and yields the same characteristic behavior in the evolution of the magnetization as function of field and temperature as observed for CuCrP_2S_6 . Thus, it may be speculated that also CuCrP_2S_6 exhibits such a magnetic order, although more detailed investigations of the magnetic behavior of CuCrP_2S_6 are necessary to confirm this assumption.

4.2. $AgCrP_2S_6$

The single crystal growth experiments for $AgCrP_2S_6$ via chemical vapor transport (CVT) using iodine as transport agent are introduced in Sect. 4.2.1. As shown in Sect. 4.2.2, these crystals were carefully analyzed regarding their morphology, composition and the formation of secondary phases by SEM and EDX as well as regarding their crystal structure by pXRD. Many crystals exhibit a surface impurity in form of bubbles of a iodine-rich phase. Based on this finding, opportunities to optimize the growth procedure are proposed and discussed. The magnetic properties of $AgCrP_2S_6$ are shown and discussed in Sect. 4.2.3. A broad maximum in the thermal evolution of the normalized magnetization at around 260 K indicates the presence of low dimensional magnetic correlations in agreement with literature. However, the anisotropic magnetic behavior indicates a more complex magnetic behavior than only nearest neighbor Heisenberg exchange as assumed in literature.

4.2.1. Crystal Growth

Single crystals of the quaternary compound $AgCrP_2S_6$ were grown by CVT using iodine as transport agent, in similarity to the successful single crystal growth of $CuCrP_2S_6$ (as discussed before in Sect. 4.1.1). Until now, Colombet *et al.* [148] reported only on the crystal growth of $AgCrP_2S_6$ via solid state synthesis. Despite Mutka *et al.* [154] mentioned that the crystals used in their work had been grown by CVT, neither they specify nor cite any growth conditions. Thus, this is the first report on the CVT growth of $AgCrP_2S_6$.

Using the same procedure as described for the CVT growth of $CuCrP_2S_6$ in Sect. 4.1.1 with Ag (powder, APS 4–7 micron, Alfa Aesar, 99.9%) instead of Cu as well as the same temperature profile, a low amount of shiny plate-like crystals of $AgCrP_2S_6$ of the size of $2\text{ mm} \times 2\text{ mm} \times 100\text{ }\mu\text{m}$ were grown on the sink site of the ampule (as shown in Fig. 4.9), while most of the material has resolidified in the charge site. Furthermore, some crystals showed the formation of spheres or bubbles on the surface. These bubbles have formed preferably along step edges and could be readily removed by exfoliating the crystal. This implies that the formation of these bubbles has occurred after the surface of the underlying crystal has formed, *i.e.* the growth of the larger crystals has already stopped.

To improve the crystal size and increase the yield of the growth experiment, the temperature regime of the crystal growth phase was changed from 750–700 °C to 800–700 °C, 850–750 °C and 900–800 °C expecting an increase in the growth speed. Temperatures at the sink site for the inverse gradient phase were adjusted to be always 50 °C higher than the charge site temperature. However for all these growth regimes, only a few small crystals of $AgCrP_2S_6$ were obtained, which mostly had secondary phase bubbles on the surface. Consequently, the parameters for the crystal growth of $AgCrP_2S_6$ via CVT are in need of further optimization in the future.

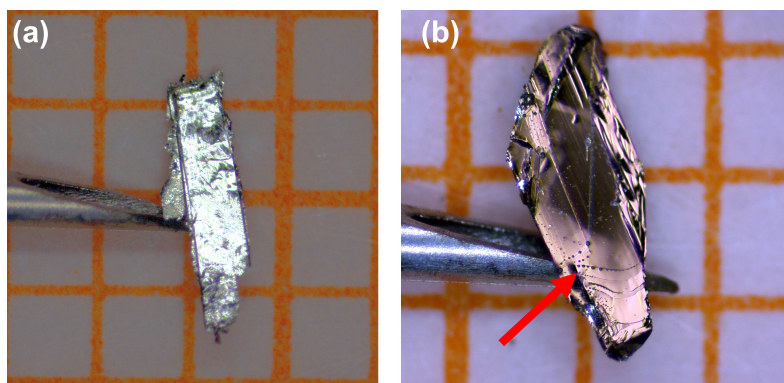


Fig. 4.9.: Single crystals of AgCrP_2S_6 as obtained from the CVT growth experiment. The red arrow in (b) marks an area with several bubbles on the surface of the crystal. One orange square in the background corresponds to $1 \times 1 \text{ mm}^2$ for scale.

4.2.2. Characterization

Crystal Morphology and Compositional Analysis

Crystals obtained from all temperature profiles were investigated by SEM regarding their morphology and chemical homogeneity. Using the topographic contrast mode (SE detector), the surface of the actual crystals was generally flat, typically with some steps or terraces indicating the layered morphology of the crystal. If present, the bubbles are clearly sitting on top of the crystal surface, as shown in the Fig. 4.10(b) and (c). The bigger bubbles in Fig. 4.10(b) are located along lines which most likely correspond to a step on the surface of the underlying crystal. As areas of high surface energy, steps on the surface of a crystal are prone to act as additional nucleation centers *e.g.* for secondary phases. As shown in the zoomed-in view in Fig. 4.10(c), the bubbles either have a rough surface themselves or a lot of small particles deposited on their surface.

The chemical contrast on the crystal surface is homogeneous, as observed in the images with chemical contrast (BSE detector) in Fig. 4.10(d)–(f). For the crystal in Fig. 4.10(a) and (d) without bubbles on the surface, the few spots of different contrast in the SEM(BSE) image can be clearly attributed to particles on the surface in agreement with the SEM(SE) image. This demonstrates that the crystals do not exhibit intergrowth of different phases. For the crystal with bubbles on the surface in Fig. 4.10(e), the bubbles on top of the crystal surface exhibit a much brighter contrast than the crystal in the BSE image, signaling that the bubbles have a chemical composition which is distinctly different from the underlying crystal. The bubbles themselves exhibit a homogeneous contrast as shown in Fig. 4.10(f), demonstrating that they all have the same chemical composition. Additionally, the SEM(BSE) image shows some spots of darker contrast than the underlying crystal which are also located on top of the crystal surface as observed in comparison with the SEM(SE) image. These dark spots are a second secondary phase.

The chemical composition of the crystal as well as of the two secondary phases was further investigated by EDX spectroscopy. The crystal composition was measured on 25 spots

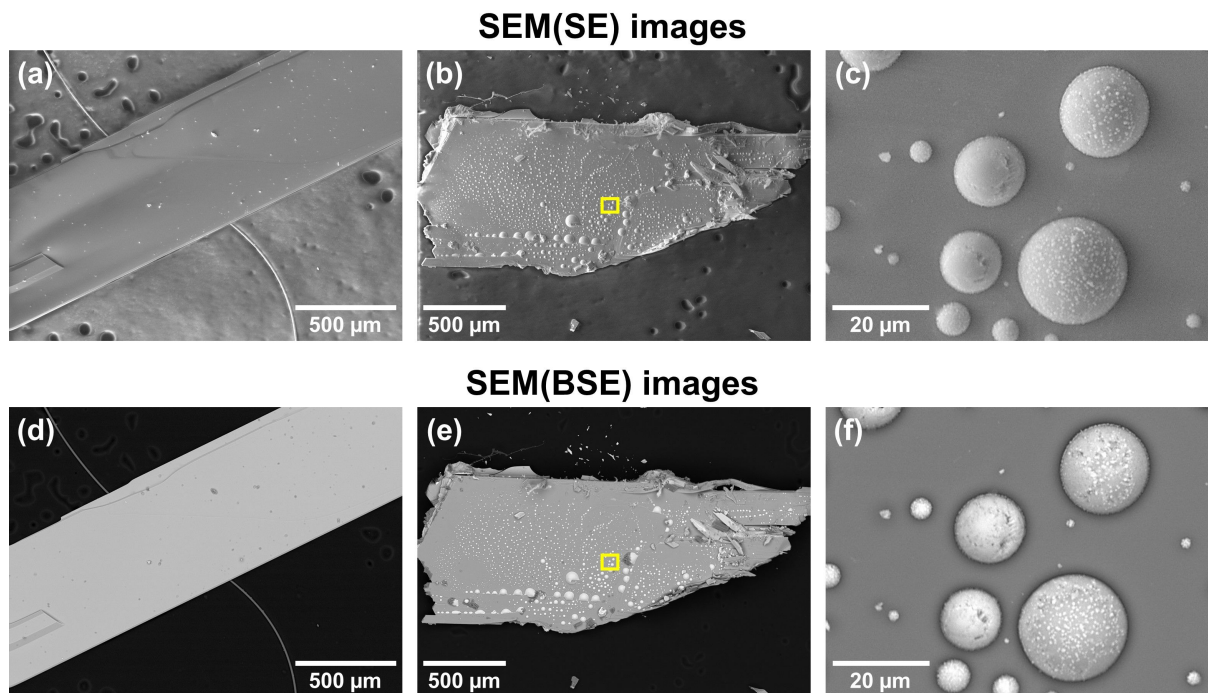


Fig. 4.10.: SEM images of a $AgCrP_2S_6$ crystals using the topographic contrast mode (*i.e.* SE-detector) in (a)–(c) and the chemical contrast mode (*i.e.* BSE-detector) in (d)–(f). In (a)/(d), a crystal with clean surface is shown while the crystal in (b)/(e) exhibits several bubbles on its surface. The yellow rectangle in (b)/(e) corresponds to the area shown in (c)/(f) which offers a zoomed-in view on the bubbles on the surface of this crystal.

on different crystals grown in different temperature regimes and a mean composition of $Ag_{10.3(2)}Cr_{10.6(2)}P_{20.3(2)}S_{58.8(1)}$ was obtained from all these measurements. This composition is in ideal agreement with the expected composition of $Ag_{10}Cr_{10}P_{20}S_{60}$. The small standard deviations demonstrate that the composition of the $AgCrP_2S_6$ is not affected by the changes in the temperature range of the growth profile. Several measurements on crystals with secondary phase bubbles on the surface demonstrated that also these crystals have the desired composition. The composition of the bubbles is approximately $Ag_{35}P_{13}S_{38}I_{14}$ containing no appreciable amounts of chromium. Possibly, this composition corresponds to a phase closely related to Ag_3PS_4 [162] (*i.e.* $Ag_{37}P_{13}S_{50}$) with S being partly substituted by I. The composition of the dark secondary phase observed in Fig. 4.10(e) is $P_{28}S_{72}$ in ideal agreement with the expected composition of the phase P_2S_5 (*i.e.* $P_{29}S_{71}$) [163].

It is most likely that these secondary phases have formed after the crystal growth phase during cooling down the furnace due to their location exclusively on the surface of some crystals. The presence of appreciable amounts of iodine in the phase of the bubbles supports this consideration. As iodine is supposed to act as transport agent for the transition elements in the CVT growth of $AgCrP_2S_6$, no noticeable crystal growth of the target phase would be expected if iodine would immediately form a stable compound with Ag, P and S. As at least some small crystals of $AgCrP_2S_6$ are grown, this indicates that iodine initially participated in the crystal growth as transport agent and the condensation of the iodine containing phase happened in a later phase of the growth process. If the secondary phases indeed form after the crystals have grown, their formation on the surface of the crystals can be reduced or even

avoided by a final inversion of the temperature gradient. By keeping the sink site temperature the same as during the crystal growth phase and cooling the charge site below the sink site temperature (*e.g.* 100 °C cooler than the sink site) and then cooling both sites with this gradient remaining constant, the condensation of the vapor phase would take place on the cooler charge site. As the secondary phases form on the charge site, the surface of the crystals on the sink site should remain pristine.

Furthermore, if the above scenario depicts reality, then the secondary phases are closely related to the composition of the gaseous phase in the ampule at the end of the crystal growth phase. Accordingly, the gaseous phase would have contained Ag, P, S and I, lacking chromium. However, as the elements were weighed in stoichiometric amounts with respect to AgCrP_2S_6 and neither the target phase nor any secondary phase were rich in chromium, this indicates that an increased amount of chromium is left in the charge site. Hence, the composition of the secondary phases may indicate that the formation of the volatile Ag_xI_y vapor transport species is significantly favored over the formation of the Cr_uI_v species. In this line of argumentation, the formation of the chromium containing vapor transport species would be the rate-limiting step of the crystal growth of AgCrP_2S_6 . Consequently, it could be worthwhile to optimize the growth parameters ensuring that the formation of both transition element halide species is energetically equally possible. This may significantly improve the crystal growth speed and, subsequently, the size of crystals that can be grown in a reasonable amount of time.

Structural Analysis

pXRD was measured on pulverized crystals of AgCrP_2S_6 which were exfoliated before grinding to avoid secondary phase contributions to the pattern. As shown in Fig. 4.11(a), using this procedure a phase pure pattern of AgCrP_2S_6 was obtained. As reported by Colombet *et al.* [148], Ag and Cr form zig-zag chains on the honeycomb lattice along the crystallographic a direction in AgCrP_2S_6 . As explained in Sect. 1.1, this ordering on the honeycomb lattice breaks the mirror symmetry of the $C2/m$ space group, which is typically found for the $M_2P_2S_6$ compounds. Consequently, the stripe-like ordered AgCrP_2S_6 exhibits a structure in the space group $P2/a$ (No. 13).

Due to the loss of centering (C base centered to primitive P), the reflection conditions differ noticeably between $C2/m$ and $P2/a$ which makes distinguishing different potential structural models more straightforward than for CuCrP_2S_6 , which is also C centered and discussed in Sect. 4.1.2. In this line, the pXRD pattern of AgCrP_2S_6 exhibits several reflections in the range of $20^\circ < 2\theta < 25^\circ$ as well as between $30^\circ < 2\theta < 35^\circ$. Assuming a monoclinic unit cell, several of these reflections correspond to Laue indices which are systematically absent for C centering (*i.e.* violate the reflection condition for C centering of hkl : $h + k = 2n$). Examples are the reflections at $2\theta = 22.94^\circ$ corresponding to 120 and at $2\theta = 31.92^\circ$ corresponding to $\bar{2}11$, as shown in Fig. 4.11(b). Consequently, the pXRD pattern is well indexed in the space group $P2/a$, while $C2/m$ is not sufficient to explain all observed reflections.

Table 4.4.: Summary and reliability factors of the Rietveld analysis of the pXRD pattern of $AgCrP_2S_6$.

<i>Experiment & Data Collection</i>	
Temperature (K)	293(2)
Radiation Type & Wavelength (Å)	Cu-K $_{\alpha_1}$; 1.54059
θ_{\min} (°)	10.00
θ_{step} (°)	0.03
θ_{\max} (°)	120.13
<i>Crystal Data</i>	
Crystal System	Monoclinic
Space Group	$P2/a$
a (Å)	5.8832(1)
b (Å)	10.6214(2)
c (Å)	6.7450(3)
β (°)	106.043(2)
<i>Refinement</i>	
Goodness-Of-Fit	2.13
R_p (%)	2.08
wR_p (%)	3.11
R_F (%)	5.45

Table 4.5.: Fractional atomic coordinates, occupancies and isotropic displacement parameters U_{iso} of $AgCrP_2S_6$ at 293 K after Rietveld refinement with estimated standard deviations in parantheses.

Label	Type	Wyck	x	y	z	Occ (%)	U_{iso} ($\times 10^{-3} \text{Å}^2$)
Ag1	Ag	$2e$	0.75	0.4364(2)	0	100	34(1)
Cr1	Cr	$2e$	0.25	0.9229(4)	0	100	20(2)
P1	P	$4g$	0.2979(6)	0.2466(4)	0.1659(6)	100	2(1)
S1	S	$4g$	0.9792(7)	0.2309(5)	0.2336(8)	100	18(2)
S2	S	$4g$	0.9880(5)	0.9233(4)	0.2165(8)	100	7(1)
S3	S	$4g$	0.4777(7)	0.3947(4)	0.2802(7)	100	34(1)

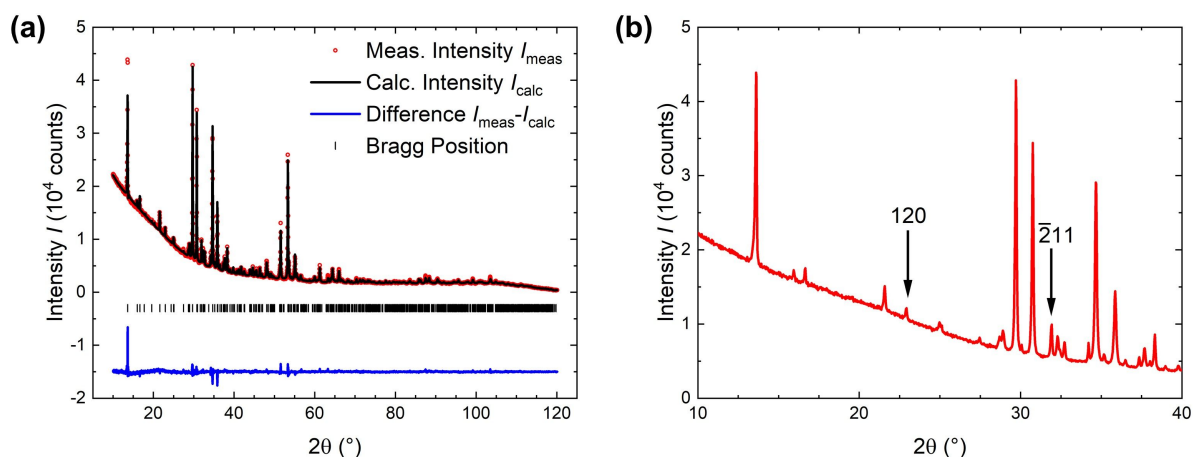


Fig. 4.11.: (a) pXRD pattern from $\text{Cu-K}\alpha_1$ radiation (1.54059 \AA) of pulverized AgCrP_2S_6 crystals (red circles) in comparison to the calculated pattern based on the refined structural model (black line). The black marks below the pattern indicate the Bragg positions of the unit cell of AgCrP_2S_6 in the space group $P2/a$ and the blue line on the bottom corresponds to the difference between experiment and model. (b) Zoomed-in view on the low angle regime of the experimental pattern in (a) with arrows indicating the reflections that violate the reflection conditions for C centering.

Based on the structural model proposed by Colombet *et al.* [148], a refined model is obtained which yields a calculated pattern in good agreement with the experimental pXRD pattern, illustrated in Fig. 4.11(a), and reasonable reliability factors, as shown in Table 4.4. The parameters of the optimized structural model are given in Table 4.5 and a perspective representation of the model is shown in Fig. 4.12. While for CuCrP_2S_6 the difference in the size of the transition elements is relatively small (ionic radii for octahedral coordination: $r(\text{Cu}^{1+}) = 0.77 \text{ \AA}$ and $r(\text{Cr}^{3+}) = 0.62 \text{ \AA}$ [136]), for AgCrP_2S_6 this difference becomes more severe (ionic radii for octahedral coordination: $r(\text{Ag}^{1+}) = 1.15 \text{ \AA}$ and $r(\text{Cr}^{3+}) = 0.62 \text{ \AA}$ [136]). Consequently, the Ag-S bonds are notably longer than the Cr-S bonds which causes a distortion of the structure. In detail, the CrS_6 coordination environments remain antiprismatic with parallel faces perpendicular to c^* , close to octahedral (as shown in Fig. 4.12(a)). However for the AgS_6 as well as the P_2S_6 coordination environments, the faces perpendicular to c^* distort and are found no longer parallel to each other. As shown in the perspective representation of the crystal structure with view along c^* , Cr is found in the center of its sulfur coordination shell, while both Ag as well as P_2 appear to be off-centered in their coordination environments shifted away from the Cr chains along the a direction. This distortion is in agreement with the structure reported by Colombet *et al.* [148].

4.2.3. Magnetic Properties

The magnetic behavior of AgCrP_2S_6 was studied on a single crystal which was exfoliated before the magnetic measurements. Although exfoliation yielded phase pure material for pXRD, the influence of secondary phases on the magnetism should be considered. As both secondary phases observed by SEM and EDX ($\text{Ag}_{35}\text{P}_{13}\text{S}_{38}\text{I}_{14}$ and $\text{P}_{28}\text{S}_{72}$, most likely corresponding to Ag_3PS_4 and P_2S_5) are diamagnetic closed shell systems, no magnetic anomalies are expected

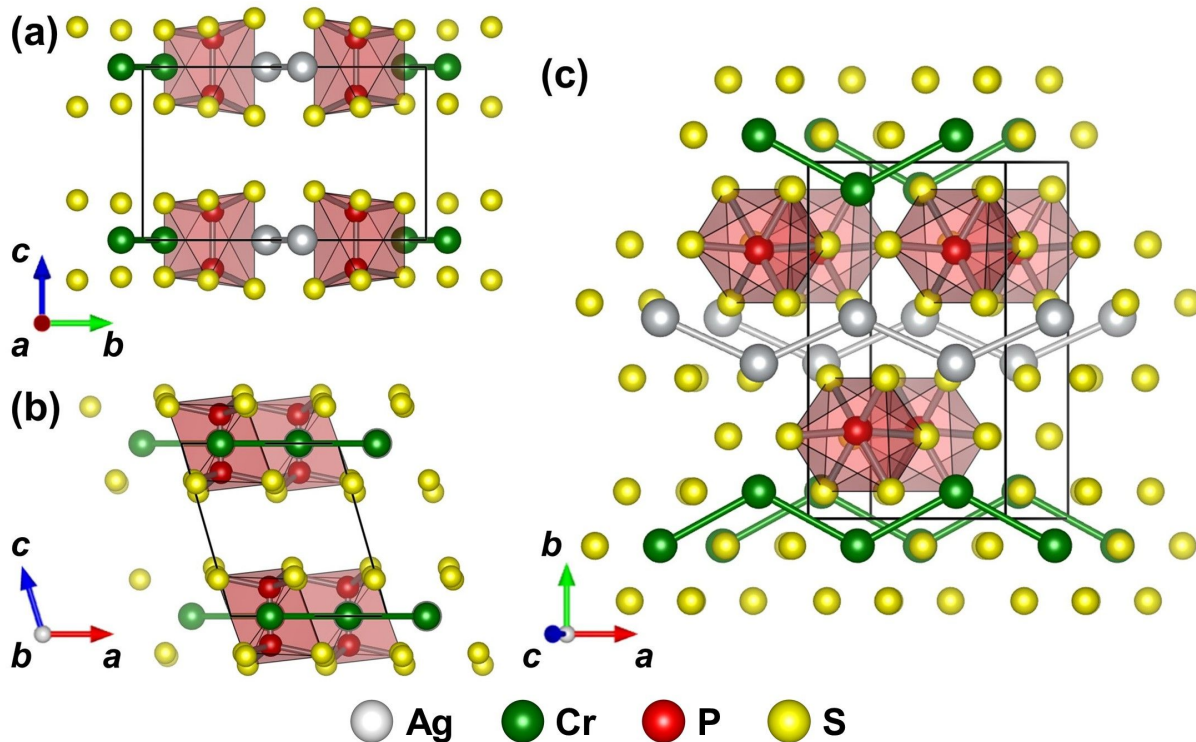


Fig. 4.12.: Perspective drawing of the refined structural model of $AgCrP_2S_6$ after Rietveld refinement with (a) view parallel to the a direction, (b) parallel to the b direction and (c) parallel to the c^* direction. The red antiprisms illustrated the distorted P_2S_6 structural units. Ag–Ag and Cr–Cr connections are shown with lines of the corresponding color to emphasize the zigzag chains along the a direction.

due to these phases. However, their presence influences the absolute magnetic moment by a diamagnetic contribution.

The thermal evolution of the normalized magnetization $MH^{-1}(T)$ of $AgCrP_2S_6$ is shown in Fig. 4.13 for a magnetic field of 1 kOe applied parallel and perpendicular to the crystallographic ab plane. The generic evolution of the normalized magnetization is the same for both directions of the magnetic field. At high temperatures a broad maximum centered at $T_{\max} \approx 250$ K and at low temperatures a steep increase of the magnetization are observed. No notable characteristic anomalies for a magnetic phase transition are found. This generic thermal evolution is in good agreement with Mutka *et al.* [154] and Payen *et al.* [165]. According to these reports, the broad maximum around $T_{\max} \approx 250$ K is attributed to magnetic fluctuations due to the 1D nature of the magnetic structure of $AgCrP_2S_6$ (*i.e.* isolated chains of Cr^{3+}), similar to the maximum observed in the thermal evolution of the magnetization of $Ni_2P_2S_6$ in Sect. 3.1.3. In fact, Smith and Friedberg [166] demonstrated for 1D systems in general that such a maximum is only observed for dominantly antiferromagnetic interactions. The low temperature increase of the magnetization is discussed in the context of a significant contribution of Curie impurities (*i.e.* non-interacting paramagnetic impurity moments) [165].

In the initial report on the magnetic behavior of $AgCrP_2S_6$ by Colombet *et al.* [148], an anomaly indicative of the onset of antiferromagnetic order was observed at 7 K in the temperature dependence of the magnetization. However, this anomaly was neither found in the

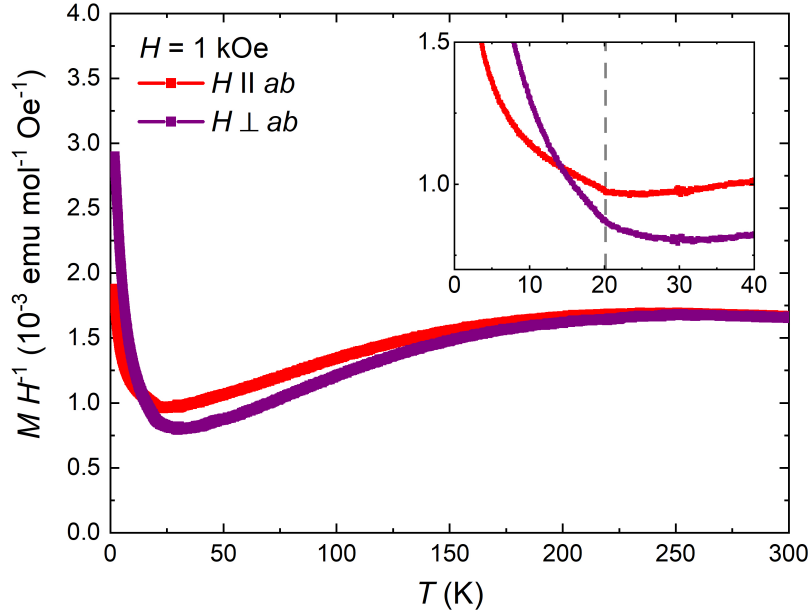


Fig. 4.13.: Thermal evolution of the normalized magnetization of AgCrP_2S_6 measured for a magnetic field of 1 kOe applied parallel and perpendicular to the crystallographic ab plane. The inset shows a zoomed-in view on the temperature regime of the onset of the increase of magnetization towards lowest temperatures with a grey dashed line corresponding to the long-range magnetic ordering temperature at 20 K as reported by Payen *et al.* [164].

follow-up reports by Mutka *et al.* [154] and Payen *et al.* [165] nor is any anomaly present at this temperature in $MH^{-1}(T)$ in this work. Furthermore contradicting the initial finding of Colombet *et al.*, Payen *et al.* [164] reported the onset of long-range antiferromagnetic order in AgCrP_2S_6 already at 20 K, based on neutron diffraction. However, a corresponding anomaly is not unambiguously observed in the thermal evolution of the magnetization, as illustrated in the inset of Fig. 4.13 and in agreement with literature [154, 165]. It is conceivable that the low temperature increase in $MH^{-1}(T)$ superimposes a potential antiferromagnetic downturn in the same temperature range.

The field dependent evolution of the magnetization $M(H)$ of AgCrP_2S_6 at 1.8 K and with a magnetic field of up to 70 kOe is shown in Fig. 4.14. For both $H \parallel ab$ and $H \perp ab$, the magnetization exhibits a saturating field dependence at low fields up to approximately 20–30 kOe and a linear evolution in the saturated regime at higher fields. Such an evolution can be understood considering two contributions — a linear contribution corresponding to the slope at high fields and a contribution described by a Brillouin function corresponding to the saturating component. Considering these two contributions, Mutka *et al.* [167] were able to model the field dependent magnetization of AgCrP_2S_6 at 3 K sufficiently. They attributed the linear component to an isotropic antiferromagnetic contribution and the saturating component to the field dependence of the Curie impurities, which are considered to cause the increase of the magnetization in $MH^{-1}(T)$ in this temperature regime. However, they did not report the parameters for the Brillouin function in their model. In fact, it is also possible to find an excellent agreement between the field dependent magnetization in this work and such a model. However, this requires a total angular momentum of $J \approx 230$ for $H \parallel ab$ and $J \approx 170$ for

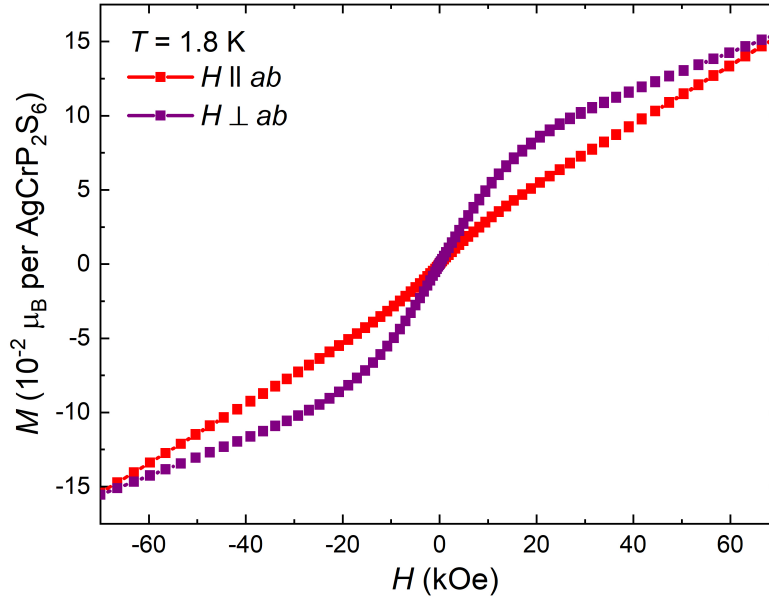


Fig. 4.14.: Field dependence of the magnetization $M(H)$ of $AgCrP_2S_6$ at 1.8 K for magnetic fields up to 70 kOe parallel and perpendicular to the ab plane.

$H \perp ab$ (assuming $g = 2$), which are not physically reasonable values of J . Assuming $J = 3/2$ as expected for Cr^{3+} , which is the only magnetic ion in the compound, the field dependence cannot be expressed by a Brillouin function and a linear term.

Additionally, the direction dependence of the linear component is not in agreement with the interpretation of Mutka *et al.* [167]. As observed in Fig. 4.14 even without the need of modeling, the linear component corresponding to the slope at high fields is anisotropic. Consequently, it cannot be attributed to the field dependence of an isotropic antiferromagnet. In this line, the saturating component of the field dependent magnetization is anisotropic as well, as it is much more pronounced for $H \perp ab$ than for $H \parallel ab$. Yet, assuming this component is caused by Curie impurities, it is expected to be isotropic, as impurity contributions typically do not exhibit any intrinsic anisotropy. The anisotropy of the saturating component in the field dependence is also shown by Mutka *et al.* but is not specifically addressed in their work.

In fact, also the evolution of anisotropy observed in the temperature dependent magnetization contradicts the assumption that $AgCrP_2S_6$ is an isotropic Heisenberg antiferromagnet with isotropic Curie impurities at low temperatures. For $MH^{-1}(T)$, anisotropy sets in below $T_{max} \approx 250$ K, with MH^{-1} for $H \perp ab$ being smaller than MH^{-1} for $H \parallel ab$. Slightly below 20 K, the anisotropy changes sign with MH^{-1} for $H \perp ab$ becoming larger than MH^{-1} for $H \parallel ab$ towards lower temperatures.

It should be mentioned that neither the anisotropic evolution of $MH^{-1}(T)$ nor of $M(H)$ can be purely attributed to shape anisotropy. For the field dependent magnetization, a demagnetizing field correction due to shape anisotropy for a thin platelet sample would only affect the measurement with $H \perp ab$ by increasing its slope (as explained in Sect. 1.2.4). Consequently, the anisotropy would be even more pronounced after such a correction. This implies that

AgCrP_2S_6 exhibits a notable intrinsic magnetocrystalline anisotropy, in disagreement with the isotropic Heisenberg antiferromagnetic character proposed in literature.

The aforementioned discrepancies between the experimental magnetic behavior of AgCrP_2S_6 , especially regarding its magnetic anisotropy, and the expected behavior based on the corresponding literature call for further magnetic investigations of this compound and its anisotropy in the future. Considering these discrepancies, it is possible that another scenario is more suitable to describe the magnetism in AgCrP_2S_6 . For example, a canted antiferromagnetically ordered state below 20 K with a slight ferromagnetic netmagnetization could explain both the increase of magnetization towards low temperatures in $MH^{-1}(T)$ as well as the saturating component in the field dependence. Additionally, such a state would be in agreement with dominant antiferromagnetic interactions, as implied by the broad maximum in $MH^{-1}(T)$, and could cause the anisotropic magnetic behavior. As the increase of magnetization towards low temperatures and the saturating component in the field dependence are intrinsic features of this model, it would be evident why they have been observed for every investigated sample of AgCrP_2S_6 (in this work and in literature). Assuming that these features are due to extrinsic paramagnetic impurity contributions, it remains elusive why they are always observed with the same characteristics in different samples. However, this alternative scenario is only a hypothesis for the magnetic order in AgCrP_2S_6 and is in need of further experimental investigation in the future.

4.3. Polycrystalline $(Cu_{1-x}Ag_x)CrP_2S_6$

Hereafter, the solid state synthesis for polycrystalline samples of $(Cu_{1-x}Ag_x)CrP_2S_6$ with $x = 0, 0.25, 0.5, 0.75$ & 1 is introduced in Sect. 4.3.1. The corresponding samples were analyzed regarding the phases that have been formed during synthesis, which is shown and discussed in Sect. 4.3.2. SEM, EDX and pXRD were used complementing each other to identify and characterize the main and secondary phases for each nominal composition. Based on the phase evaluation, the phase evolution in the nominal composition regime of $(Cu_{1-x}Ag_x)CrP_2S_6$ was extracted.

4.3.1. Synthesis

Polycrystalline samples with a nominal composition of $(Cu_{1-x}Ag_x)CrP_2S_6$ with $x = 0, 0.25, 0.5, 0.75$ & 1 were prepared by solid state synthesis.

In a glove box under argon atmosphere, a total amount of 3 g of the elemental constituents Ag, Cu, Cr, P and S was weighed in stoichiometric quantities with respect to $(Cu_{1-x}Ag_x)CrP_2S_6$ (S was used with an excess of 5 mol-%). The mixture was homogenized in an agate mortar and subsequently pressed to pellets of 1 cm diameter at approximately 30 kN using a hydraulic press. After the total mass of the pellets after pressing was determined, the pellets were loaded in a quartz ampule (10 mm inner diameter, 3 mm wall thickness; previously baked out at 800 °C for at least 12 h). The ampule was transferred out of the glove box to a pump where it was sealed under a partial argon pressure of approx. 300 mbar (at 20 °C). The ampule containing the pellets was placed inside a horizontal tube furnace. Initially, the furnace was slowly heated to 150 °C with 20 °C/h and dwelled at this temperature for 24 h to ensure prereaction of the volatile elements P and S with the transition elements and to reduce changes in the chemical composition of the pellets due to evaporation. Subsequently, the furnace was heated to 450 °C with 20 °C/h and dwelled for 72 h at this temperature. Then the furnace was shut off and the pellets were furnace cooled to room temperature. After the heat treatment, the ampule was opened inside of a glove box. For all degrees of substitution, small amounts of yellow material had been condensed on the inner walls of the ampule. Weighing the pellets after the heat treatment typically indicated a mass loss of the order of 50–100 mg. The pellets were then pulverized in an agate mortar and the phase formation was investigated by pXRD using pattern matching.

As samples for all degrees of substitution contained multiple crystallographic phases after the first heat treatment, the procedure described before was repeated with a modified temperature profile for the heat treatment. The loss of mass was covered by adding the mass difference in sulfur to the powdered material. This mixture was then homogenized and pressed to pellets which were weighed and then sealed in an ampule as described before. The ampule was placed in a tube furnace and heated to 200 °C with 50 °C/h, dwelled for 6 h and then heated to 600 °C with 50 °C/h, dwelled for 72 h before the furnace was turned off and the pellets were furnace cooled to room temperature. The pellets were then removed from the ampule and the mass loss was determined before the phase composition was analyzed by pXRD. This procedure

Table 4.6.: Comparison between the nominal composition and the experimental mean sample composition from EDX of the polycrystalline $(\text{Cu}_{1-x}\text{Ag}_x)\text{CrP}_2\text{S}_6$ samples.

x_{nom}	Nominal Composition	Mean Sample Composition from EDX
0	$\text{Cu}_{10}\text{Cr}_{10}\text{P}_{20}\text{S}_{60}$	$\text{Cu}_{10.6(4)}\text{Cr}_{11.4(3)}\text{P}_{19.6(5)}\text{S}_{58.4(2)}$
0.25	$(\text{Cu}_{7.5}\text{Ag}_{2.5})\text{Cr}_{10}\text{P}_{20}\text{S}_{60}$	$\text{Cu}_{8.0(7)}\text{Ag}_{2.6(2)}\text{Cr}_{12.5(1.8)}\text{P}_{18.7(1.4)}\text{S}_{58.3(3)}$
0.50	$(\text{Cu}_{5.0}\text{Ag}_{5.0})\text{Cr}_{10}\text{P}_{20}\text{S}_{60}$	$\text{Cu}_{5.5(4)}\text{Ag}_{5.0(3)}\text{Cr}_{11.2(3)}\text{P}_{19.8(2)}\text{S}_{58.6(1)}$
0.75	$(\text{Cu}_{2.5}\text{Ag}_{7.5})\text{Cr}_{10}\text{P}_{20}\text{S}_{60}$	$\text{Cu}_{3.0(1)}\text{Ag}_{7.0(1)}\text{Cr}_{11.1(1)}\text{P}_{20.1(1)}\text{S}_{58.8(1)}$
1	$\text{Ag}_{10}\text{Cr}_{10}\text{P}_{20}\text{S}_{60}$	$\text{Ag}_{10.0(1)}\text{Cr}_{11.6(2)}\text{P}_{19.5(2)}\text{S}_{58.9(1)}$

was repeated four times until no more major changes to the pXRD pattern could be observed. Subsequently, these polycrystalline samples were studied in detail regarding their elemental and crystallographic phase composition.

4.3.2. Phase Analysis

The evolution of crystallographic phases in these polycrystalline samples was investigated combining SEM, EDX and pXRD analysis. Samples of the polycrystalline material for SEM and EDX were prepared as explained in Sect. 2.3.2. Using the chemical contrast mode in SEM (*i.e.* BSE detector), areas of different compositions in the polycrystalline grains could be detected. By EDX, the elemental composition of these areas was detected. Additionally, pXRD was measured on a sample of each nominal degree of substitution. Using these techniques complementary allows to reliably detect different crystallographic phases in one sample, which poses a challenge relying only on pXRD alone due to the high number and overlap of reflections of different phases or relying only on SEM and EDX due to allotropes and different phases with virtually the same composition.

Compositional Phase Analysis by SEM and EDX

For all samples of this substitution series, the mean sample composition was obtained from several EDX measurements over large areas (nearly whole polycrystalline grains) on multiple grains for each degree of substitution. As shown in Table 4.6, these mean sample compositions are in agreement with the expected nominal composition, in the limits of reliability of EDX. This implies that no sample suffered from a notable shift in stoichiometry due to the evaporation of volatile components.

However, all samples (except of nominal AgCrP_2S_6) do not just contain a single phase but multiple phases, as revealed by a more detailed SEM(BSE) and EDX investigation and as illustrated by different elemental contrasts in the BSE images of the nominal samples CuCrP_2S_6 and $(\text{Cu}_{0.25}\text{Ag}_{0.75})\text{CrP}_2\text{S}_6$ in Fig. 4.15. For $(\text{Cu}_{0.75}\text{Ag}_{0.25})\text{CrP}_2\text{S}_6$ and $(\text{Cu}_{0.50}\text{Ag}_{0.50})\text{CrP}_2\text{S}_6$, the secondary phases do not yield a notable different BSE contrast to the main phase, such that the BSE image is not sufficient to clearly show all phases. Yet for these samples, EDX mappings, as shown in Fig. 4.16 and 4.17, were used to identify and visualize the different phases.

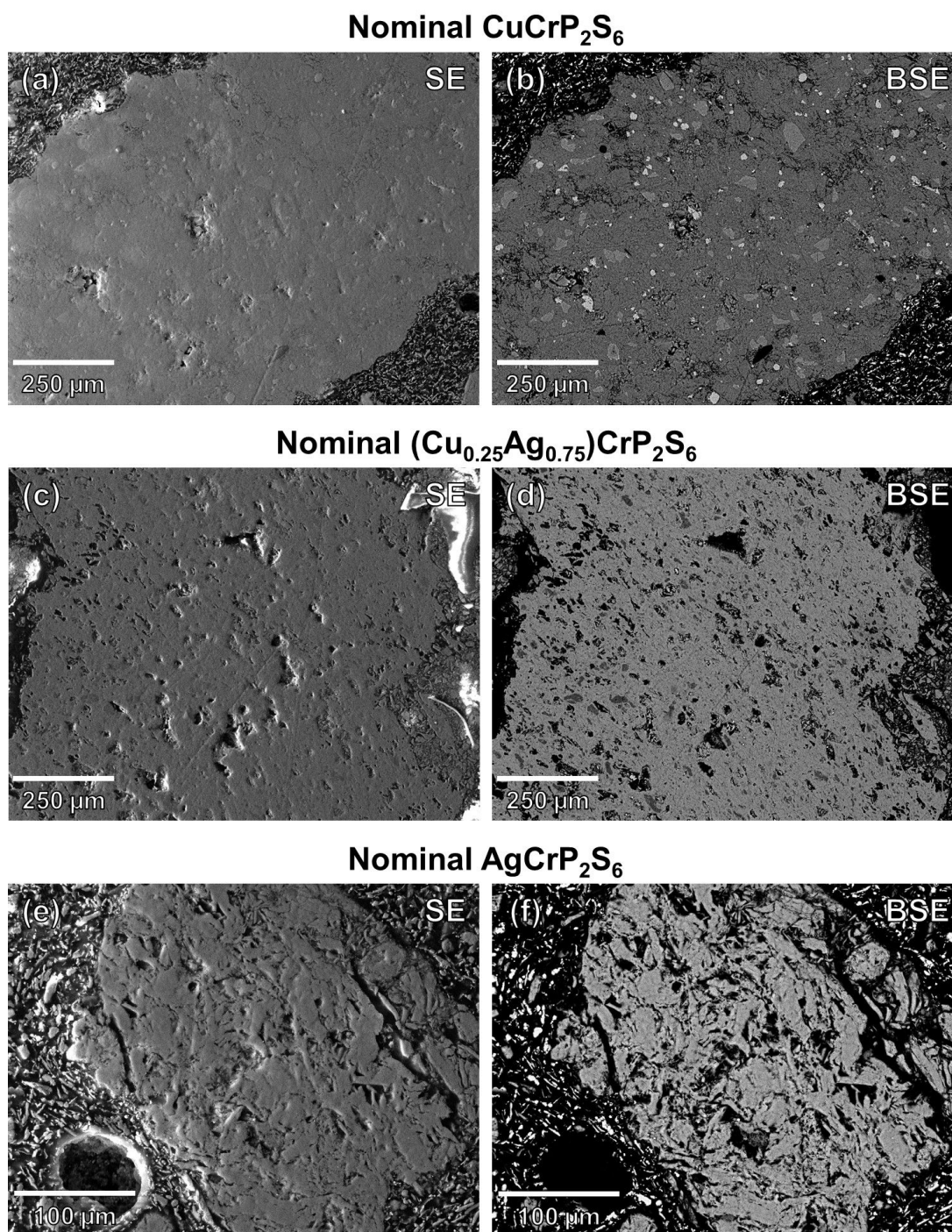


Fig. 4.15.: Representative SEM images using the SE detector for topographical contrast (left) and the BSE detector for chemical contrast (right) for the samples with a nominal composition of $CuCrP_2S_6$ in (a) and (b), a nominal composition of $(Cu_{0.25}Ag_{0.75})CrP_2S_6$ in (c) and (d) and a nominal composition of $AgCrP_2S_6$ in (e) and (f). Please note that the small particles (bright contrast in BSE) observed in the top left and bottom right corner of (a) and (b) as well as on the left side of (e) and (f) are Ni particles which were embedded in the resin as described before.

Table 4.7.: Summary of the compositional phase analysis for the polycrystalline samples of the $(\text{Cu}_{1-x}\text{Ag}_x)\text{CrP}_2\text{S}_6$ substitution series with possible known phases corresponding to the composition of the different phases in the samples.

	Composition from EDX	Possible Phase
<i>Nominal CuCrP_2S_6</i>		
Main Phase	$\text{Cu}_{10.2(2)}\text{Cr}_{11.0(8)}\text{P}_{20.3(2)}\text{S}_{58.5(4)}$	$(\text{Cu,Ag})\text{CrP}_2\text{S}_6$
Secondary Phases	$\text{Cu}_{37.8(7)}\text{Cr}_{0.5(1)}\text{P}_{12.6(2)}\text{S}_{49.1(5)}$	Cu_3PS_4
	$\text{Cu}_{0.9(4)}\text{Cr}_{39.6(4)}\text{P}_{1.4(4)}\text{S}_{58.1(3)}$	Cr_2S_3
<i>Nominal $(\text{Cu}_{0.75}\text{Ag}_{0.25})\text{CrP}_2\text{S}_6$</i>		
Main Phase	$\text{Cu}_{7.43(2)}\text{Ag}_{3.3(1)}\text{Cr}_{10.4(3)}\text{P}_{19.9(3)}\text{S}_{59.0(1)}$	$(\text{Cu,Ag})\text{CrP}_2\text{S}_6$
Secondary Phases	$\text{Cu}_{32.2(1.5)}\text{Ag}_{0.2(2)}\text{Cr}_{2.3(1.3)}\text{P}_{14.1(7)}\text{S}_{51.4(6)}$	Cu_3PS_4
	$\text{Cu}_{2.7(2)}\text{Ag}_{0.7(4)}\text{Cr}_{33.0(2.4)}\text{P}_{5.0(2.3)}\text{S}_{58.7(4)}$	Cr_2S_3
<i>Nominal $(\text{Cu}_{0.50}\text{Ag}_{0.50})\text{CrP}_2\text{S}_6$</i>		
Main Phases	$\text{Cu}_{2.0(1)}\text{Ag}_{9.5(1)}\text{Cr}_{10.5(1)}\text{P}_{20.6(1)}\text{S}_{57.5(2)}$	$(\text{Cu,Ag})\text{CrP}_2\text{S}_6$
	$\text{Cu}_{8.8(4)}\text{Ag}_{1.9(5)}\text{Cr}_{10.6(1)}\text{P}_{20.7(1)}\text{S}_{58.1(1)}$	$(\text{Cu,Ag})\text{CrP}_2\text{S}_6$
Secondary Phases	$\text{Cu}_{29.8(2.5)}\text{Ag}_{0.9(5)}\text{Cr}_{4.0(1.0)}\text{P}_{14.5(1.1)}\text{S}_{50.9(1.4)}$	Cu_3PS_4
	$\text{Cu}_{0.6(2)}\text{Ag}_{0.5(3)}\text{Cr}_{38.3(1.9)}\text{P}_{2.0(9)}\text{S}_{58.6(5)}$	Cr_2S_3
<i>Nominal $(\text{Cu}_{0.25}\text{Ag}_{0.75})\text{CrP}_2\text{S}_6$</i>		
Main Phase	$\text{Cu}_{2.8(5)}\text{Ag}_{7.4(4)}\text{Cr}_{10.7(4)}\text{P}_{20.2(1)}\text{S}_{58.9(1)}$	$(\text{Cu,Ag})\text{CrP}_2\text{S}_6$
Secondary Phase	$\text{Cu}_{0.7(4)}\text{Ag}_{1.5(1.1)}\text{Cr}_{16.6(9)}\text{P}_{17.4(4)}\text{S}_{63.8(1.2)}$	CrPS_4
<i>Nominal AgCrP_2S_6</i>		
Main Phase	$\text{Ag}_{10.4(5)}\text{Cr}_{10.9(6)}\text{P}_{19.5(4)}\text{S}_{59.2(4)}$	$(\text{Cu,Ag})\text{CrP}_2\text{S}_6$

The results of the phase analysis by SEM and EDX are summarized in Table 4.7 and discussed hereafter. Based on EDX, the composition of the main phase of each sample of $(\text{Cu}_{1-x}\text{Ag}_x)\text{CrP}_2\text{S}_6$ agrees well with the expected composition for $(\text{Cu,Ag})\text{CrP}_2\text{S}_6$. A special scenario is observed for nominal $(\text{Cu}_{0.50}\text{Ag}_{0.50})\text{CrP}_2\text{S}_6$, as this is the only sample containing two main phases, both corresponding to the general composition of $(\text{Cu,Ag})\text{CrP}_2\text{S}_6$. However, one of these phases exhibits a lower degree of Ag vs. Cu substitution and the other one a higher degree than expected from the nominal composition. As shown in Fig. 4.17, these two phases exist adjacent to each other with well defined phase boundaries. Additional to the main phase, all samples (except of AgCrP_2S_6) exhibit small amounts of at least one secondary phase. Regarding their composition, these secondary phases agree well with the expected compositions for the phases Cu_3PS_4 [168], CrPS_4 [169] and Cr_2S_3 [170].

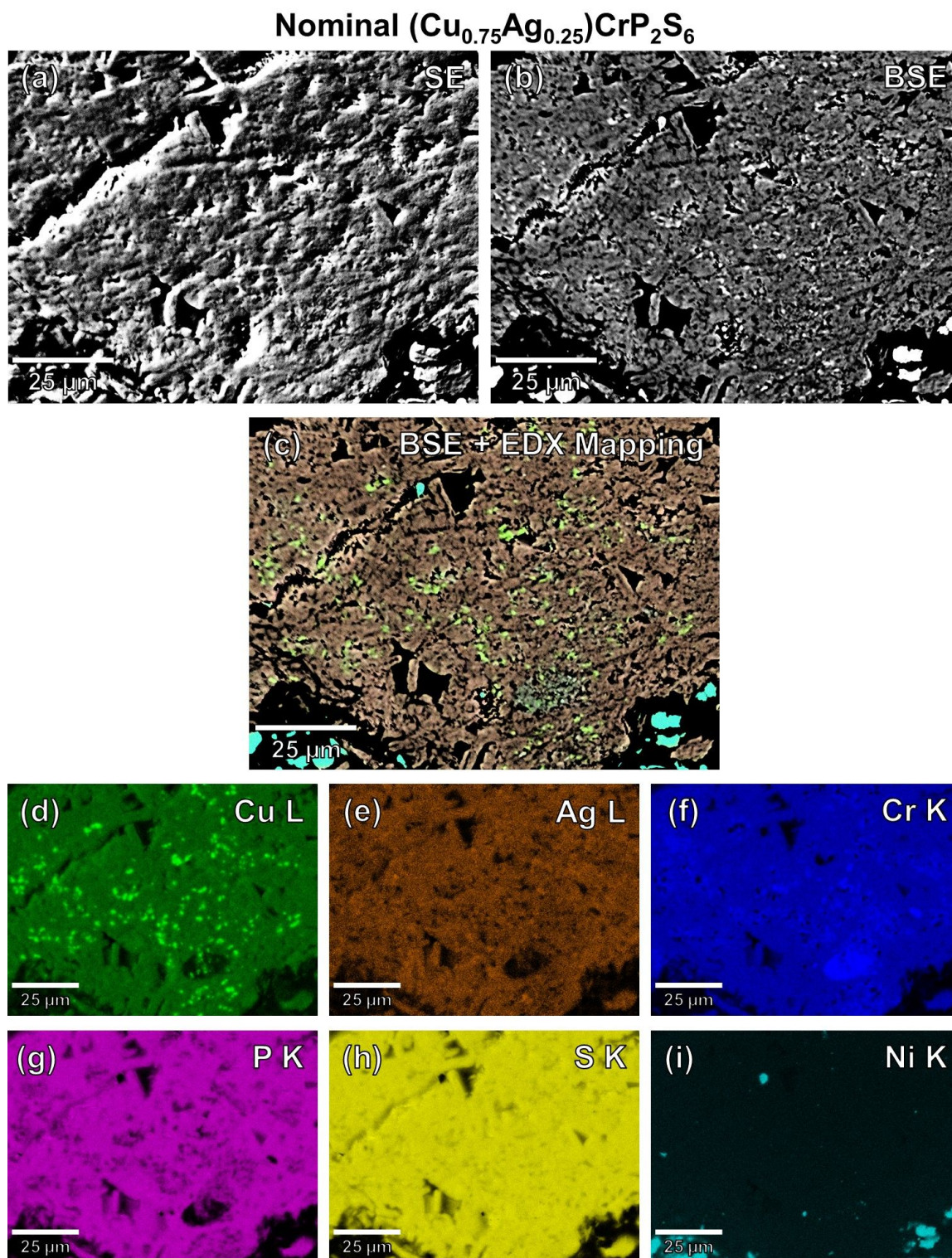


Fig. 4.16.: SEM images of the sample with a nominal composition of $(Cu_{0.75}Ag_{0.25})CrP_2S_6$ using the SE detector for topographical contrast in (a) and the BSE detector for chemical contrast in (b) showing the area of the EDX mapping. (c) shows the same BSE image as in (b) but overlaid by the element maps (d)-(i), each showing a spatial resolved image of the distribution of an element *via* the intensity at a corresponding characteristic X-ray energy as denoted in the images.

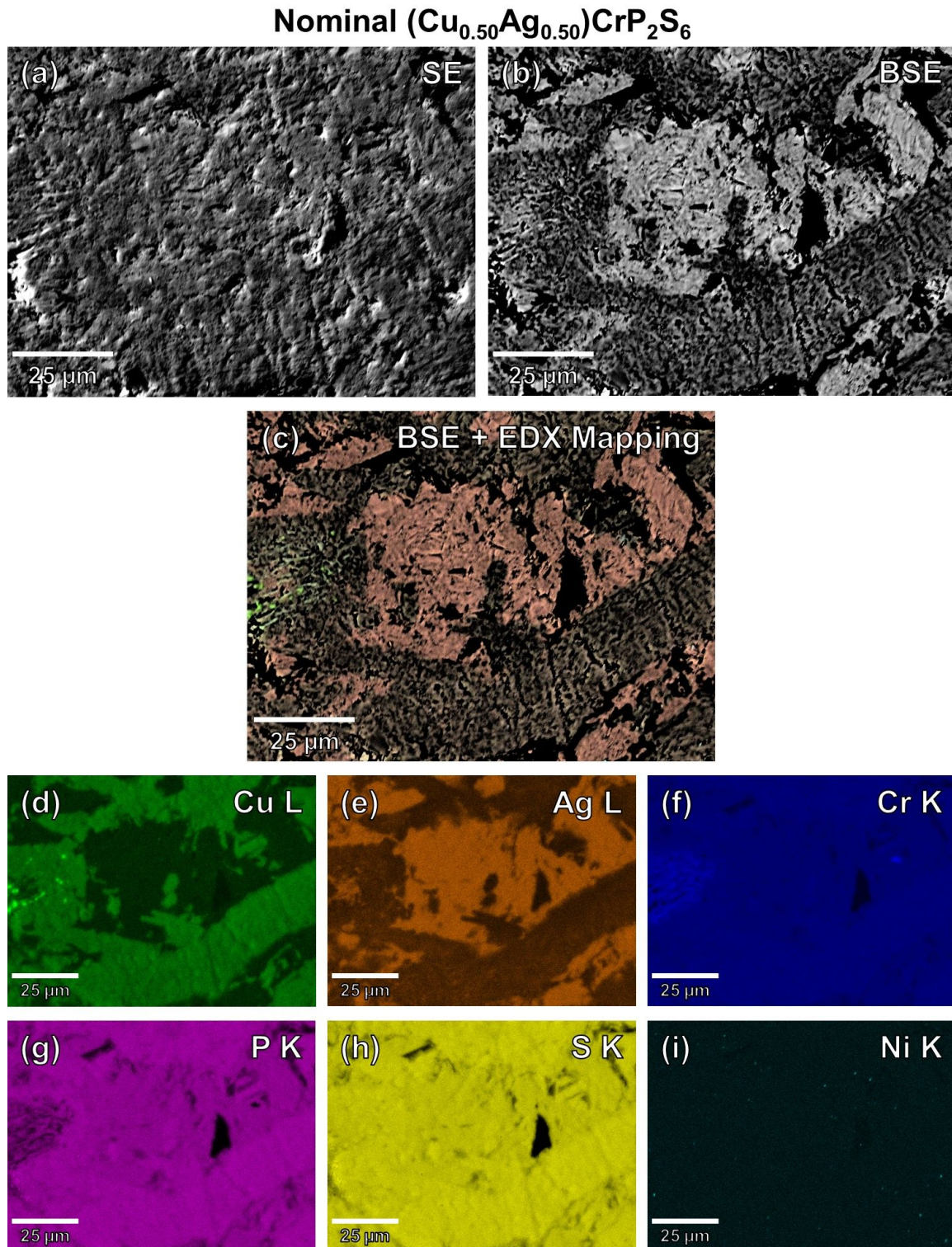


Fig. 4.17.: SEM images of the sample with a nominal composition of $(\text{Cu}_{0.50}\text{Ag}_{0.50})\text{CrP}_2\text{S}_6$ using the SE detector for topographical contrast in (a) and the BSE detector for chemical contrast in (b) showing the area of the EDX mapping. (c) shows the same BSE image as in (b) but overlaid by the element maps (d)-(i), each showing a spatial resolved image of the distribution of an element *via* the intensity at a corresponding characteristic X-ray energy as denoted in the images.

Structural Phase Analysis by pXRD

The pXRD patterns of all $(Cu_{1-x}Ag_x)CrP_2S_6$ samples were evaluated based on the phases that were identified in the compositional analysis. For the sample with the nominal composition of $CuCrP_2S_6$, all observed reflection could be ascribed to $CuCrP_2S_6$ [58] and the secondary phases Cu_3PS_4 [168] and Cr_2S_3 [170]. For the sample on the other end of the substitution regime, nominal $AgCrP_2S_6$, the main reflections correspond to $AgCrP_2S_6$ [148]. Additionally, some small reflections could be ascribed to the secondary phase Cr_2S_3 , which could not be observed in this sample in the SEM and EDX investigation. For the sample of the nominal composition $(Cu_{0.25}Ag_{0.75})CrP_2S_6$, the main reflections are attributed to $AgCrP_2S_6$, while some secondary reflections correspond to $CrPS_4$ [169]. For these samples the aforementioned phases were sufficient to describe all notable reflections. This allowed for a multiphase Rietveld refinement, which yielded simulated pXRD patterns that are in good agreement with the experimental patterns, as shown in Fig. 4.18 and indicated by the reliability factors in Table 4.8. For these refinements, the atomic models for the main and secondary phases were taken from literature and were not further optimized to minimize the amount of free parameters of the refinement. Such refinements allowed to obtain the lattice parameter of the main phase as well as an estimate for the phase fractions, as shown in Table 4.8.

The pXRD patterns of the samples with the nominal composition $(Cu_{0.75}Ag_{0.25})CrP_2S_6$ and the nominal composition $(Cu_{0.50}Ag_{0.50})CrP_2S_6$ are shown in Fig. 4.19. The pattern of the former sample does neither exhibit the reflections expected for $CuCrP_2S_6$ nor for $AgCrP_2S_6$, as illustrated in Fig. 4.20(a). Most prominently for $CuCrP_2S_6$, the 002 reflection at $2\theta \approx 13.8^\circ$ and the 130 reflection at $2\theta \approx 30.6^\circ$ are not observed. For $AgCrP_2S_6$, the 001 reflection at $2\theta \approx 13.6^\circ$ as well as the 131 reflection at $2\theta \approx 34.6^\circ$ are missing. While some small reflections can be attributed to the secondary phases Cu_3PS_4 and Cr_2S_3 , the phase corresponding to the main intensity reflections remains unknown. Due to the presence of secondary phase reflections, a further investigation of the space group and crystal structure of the unknown main phase is not reliably possible, as several secondary phase reflections overlap with the reflections of the main phase. Nevertheless, this pXRD pattern implies that the phase with the experimental composition of $Cu_{7.43(2)}Ag_{3.3(1)}Cr_{10.4(3)}P_{19.9(3)}S_{59.0(1)}$ (from EDX) crystallizes in a different crystal structure than both parent compounds of this substitution series, $CuCrP_2S_6$ and $AgCrP_2S_6$.

The sample with the nominal composition $(Cu_{0.50}Ag_{0.50})CrP_2S_6$ exhibits several high intensity reflections that are well explained by the $P2/a$ phase of $AgCrP_2S_6$, as shown in Fig. 4.19. Some low intensity reflection can be attributed to the secondary phases Cu_3PS_4 and Cr_2S_3 . However, this leaves several high intensity reflections not attributed to any phase. Comparing the pXRD pattern of nominal $(Cu_{0.50}Ag_{0.50})CrP_2S_6$ to nominal $(Cu_{0.75}Ag_{0.25})CrP_2S_6$, as shown in Fig. 4.20(b), demonstrates that these unaccounted reflections are the same as the reflections of the unknown main phase in nominal $(Cu_{0.75}Ag_{0.25})CrP_2S_6$. It is most likely, that the reflections corresponding to the $P2/a$ phase are caused by the Ag-rich main phase with the experimental composition of $Cu_{2.0(1)}Ag_{9.5(1)}Cr_{10.5(1)}P_{20.6(1)}S_{57.5(2)}$ (from EDX), while the reflections corresponding to the unknown phase are caused again by a Cu-rich phase (EDX composition: $Cu_{8.8(4)}Ag_{1.9(5)}Cr_{10.6(1)}P_{20.7(1)}S_{58.1(1)}$), in agreement with the observations for nominal $(Cu_{0.75}Ag_{0.25})CrP_2S_6$.

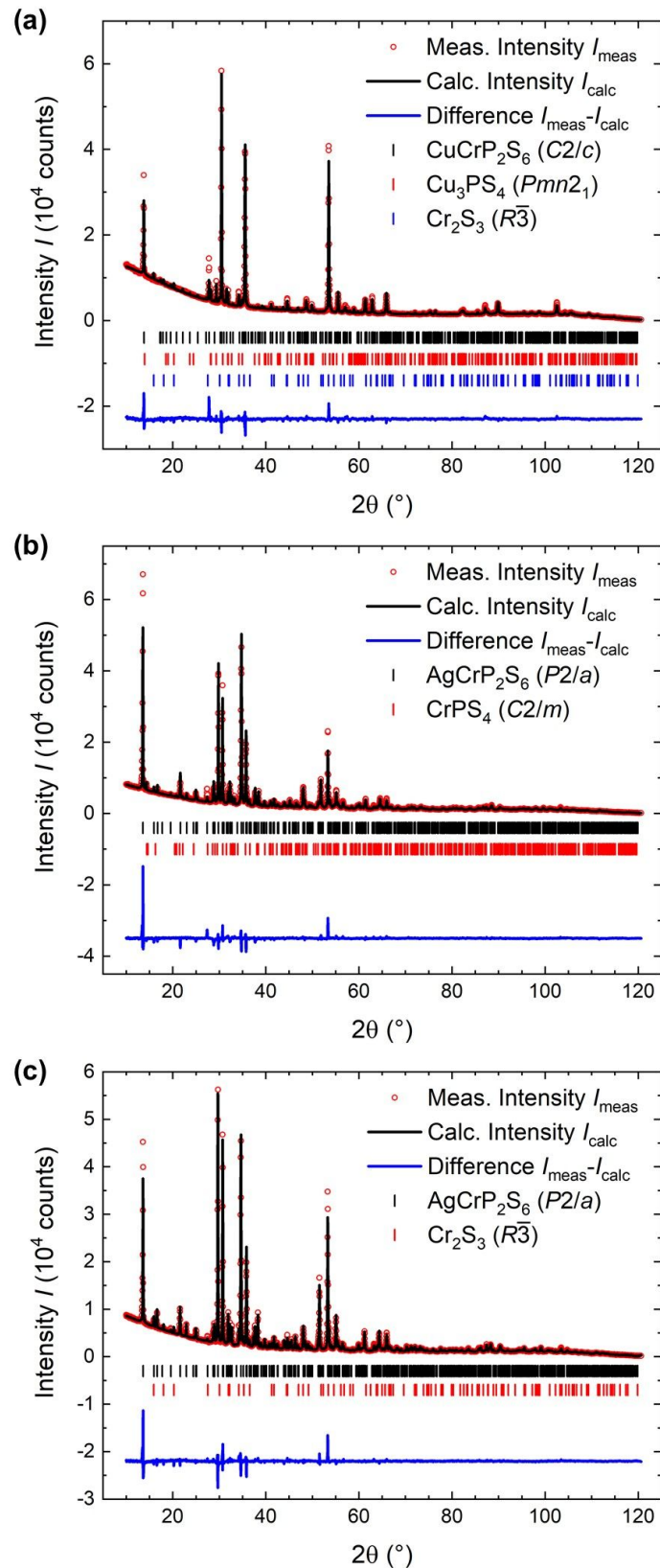


Fig. 4.18.: pXRD pattern from Cu- $K\alpha_1$ radiation (1.54059 Å) from the samples with a nominal composition of (a) CuCrP_2S_6 and (b) $(\text{Cu}_{0.25}\text{Ag}_{0.75})\text{CrP}_2\text{S}_6$ and (c) AgCrP_2S_6 (red circles) compared to the calculated pattern from a multiphase Rietveld refinement (black line).

Table 4.8.: Summary of the multiphase Rietveld analysis of the pXRD patterns for the samples with a nominal composition of $CuCrP_2S_6$ ($x = 0$), $(Cu_{0.25}Ag_{0.75})CrP_2S_6$ ($x = 0.75$) and $AgCrP_2S_6$ ($x = 1$).

$(Cu_{1-x}Ag_x)CrP_2S_6$	$x = 0$	$x = 0.75$	$x = 1$
<i>Experiment and Data Collection</i>			
Temperature (K)		293(2)	
Radiation Type & Wavelength (Å)		Cu- $K_{\alpha 1}$; 1.54059	
θ_{\min} (°)		10.00	
θ_{step} (°)		0.03	
θ_{\max} (°)		120.64	
<i>Crystal Data (Main Phase)</i>			
Crystal System		Monoclinic	
Space Group	$C2/c$	$P2/a$	$P2/a$
a (Å)	5.9231(3)	5.8926(2)	5.8869(2)
b (Å)	10.2571(5)	10.5748(3)	10.6283(3)
c (Å)	13.4219(7)	6.7703(3)	6.7518(2)
β (°)	107.280(3)	106.165(2)	106.044(2)
R_F (Main Phase) (%)	14.21	6.07	4.95
<i>Phase Fractions</i>			
Main Phase (mass-%)	92	97	97
Cu_3PS_4 (mass-%)	4		
Cr_2S_3 (mass-%)	4		3
$CrPS_4$ (mass-%)		3	
<i>Refinement</i>			
Goodness-Of-Fit	2.99	3.62	2.92
R_p (%)	3.64	4.48	3.79
wR_p (%)	5.18	7.09	5.68

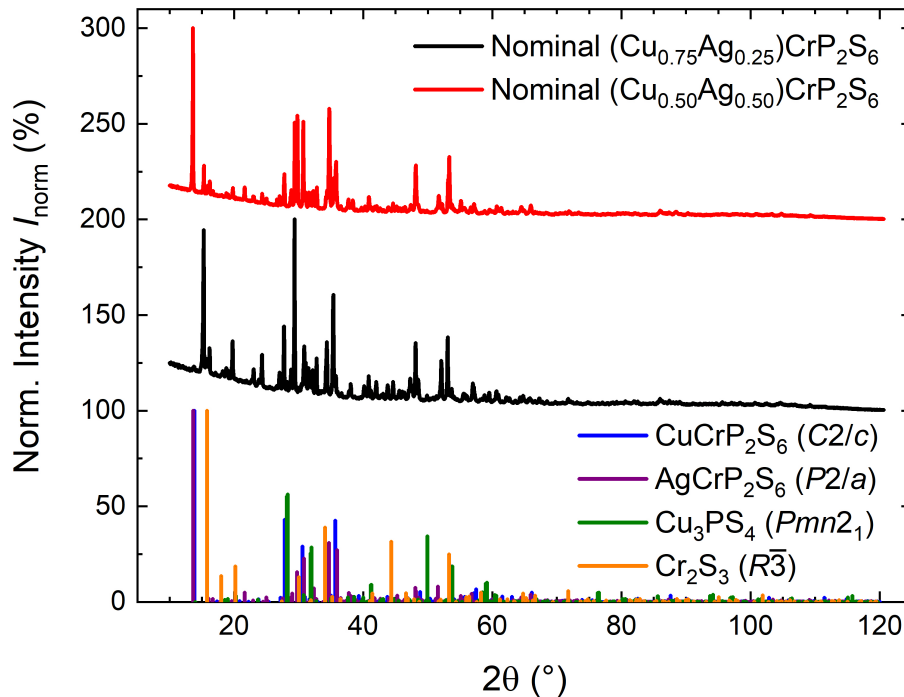


Fig. 4.19.: pXRD pattern from Cu- $K\alpha_1$ radiation (1.54059 Å) of the samples with nominal composition of $(\text{Cu}_{0.75}\text{Ag}_{0.25})\text{CrP}_2\text{S}_6$ (black) and $(\text{Cu}_{0.50}\text{Ag}_{0.50})\text{CrP}_2\text{S}_6$ (red). The intensity is normalized to the reflection of highest intensity of each pattern. On the bottom, the theoretical patterns for the parent phases CuCrP_2S_6 and AgCrP_2S_6 and the secondary phases detected by the EDX analysis are shown for comparison.

Conclusion on the Phase Analysis

Following from the phase analysis of the polycrystalline samples in the quasi-binary $(\text{Cu}_{1-x}\text{Ag}_x)\text{CrP}_2\text{S}_6$ phase diagram, two miscibility gaps have to exist in this regime of the phase diagram, as schematically illustrated in Fig. 4.21. CuCrP_2S_6 and $(\text{Cu}_{0.75}\text{Ag}_{0.25})\text{CrP}_2\text{S}_6$ crystallize in different structures, which implies the existence of a phase transition and, thus, a miscibility gap between these phases. Furthermore, the structure of the other parent compound AgCrP_2S_6 also differs from the structure of the intermediate phase, $(\text{Cu}_{0.75}\text{Ag}_{0.25})\text{CrP}_2\text{S}_6$, implying another miscibility gap between these phases. This second miscibility gap is pinpointed around a nominal composition of $(\text{Cu}_{0.50}\text{Ag}_{0.50})\text{CrP}_2\text{S}_6$, as the corresponding sample simultaneously contains two different $(\text{Cu}_{1-x}\text{Ag}_x)\text{CrP}_2\text{S}_6$ phases of different degrees of Ag vs. Cu substitution. Finally, $(\text{Cu}_{0.25}\text{Ag}_{0.75})\text{CrP}_2\text{S}_6$ exhibits the same crystal structure as AgCrP_2S_6 , indicating that a solid solution regime of the corresponding $P2/a$ structure exists between these phases.

Beyond that it is observed that all samples exhibit a small fraction of secondary phases. The identified secondary phases are rich in transition elements and deficient in at least one of the more volatile elements P and S relative to the corresponding main phase of $(\text{Cu}_{1-x}\text{Ag}_x)\text{CrP}_2\text{S}_6$. It is likely, that the formation of the secondary phases is related to the loss of these volatile components during heat treatment. The corresponding shift in composition is likely small,

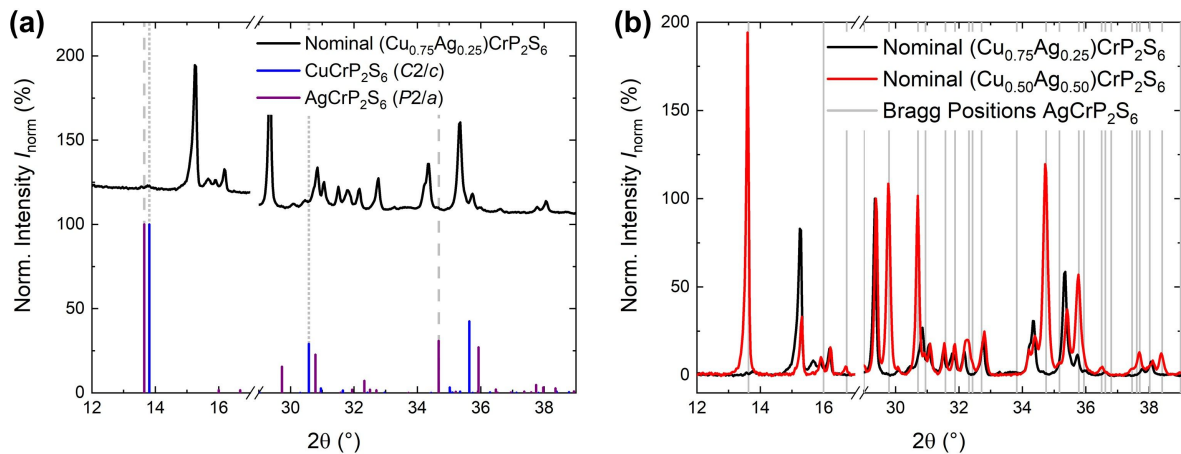


Fig. 4.20.: (a) Zoomed-in view of two regimes ($2\theta = 12\text{--}17^\circ$ and $2\theta = 29\text{--}39^\circ$) of the pXRD pattern of nominal $(\text{Cu}_{0.75}\text{Ag}_{0.25})\text{CrP}_2\text{S}_6$ compared to the expected reflection positions for the $C2/m$ and $P2/a$ phases of CuCrP_2S_6 and AgCrP_2S_6 . The grey dashed and dotted lines correspond to the positions of the missing reflections mentioned in the text. (b) Comparison of the same two angular regimes of nominal $(\text{Cu}_{0.50}\text{Ag}_{0.50})\text{CrP}_2\text{S}_6$ and nominal $(\text{Cu}_{0.75}\text{Ag}_{0.25})\text{CrP}_2\text{S}_6$ after background subtraction using the method proposed by Sonneveld and Visser [171]. Both patterns are normalized to the intensity of the common reflection at $2\theta = 29.4^\circ$.

as for all samples the mean sample composition was the same as the starting composition in the margin of reliability of the EDX technique. Apparently, smallest changes of composition are, however, sufficient to yield the formation of secondary phases. Although an excess of sulfur was used in the starting material (5 mol-%) and in between heat treatments the mass loss of the pellets was covered by addition of sulfur, the formation of secondary phases could not be completely prevented. As all secondary phases are poor in phosphorus, it may be worthwhile to add an excess of phosphorus in the solid state synthesis of these samples in future experiments, additional to the excess of sulfur.

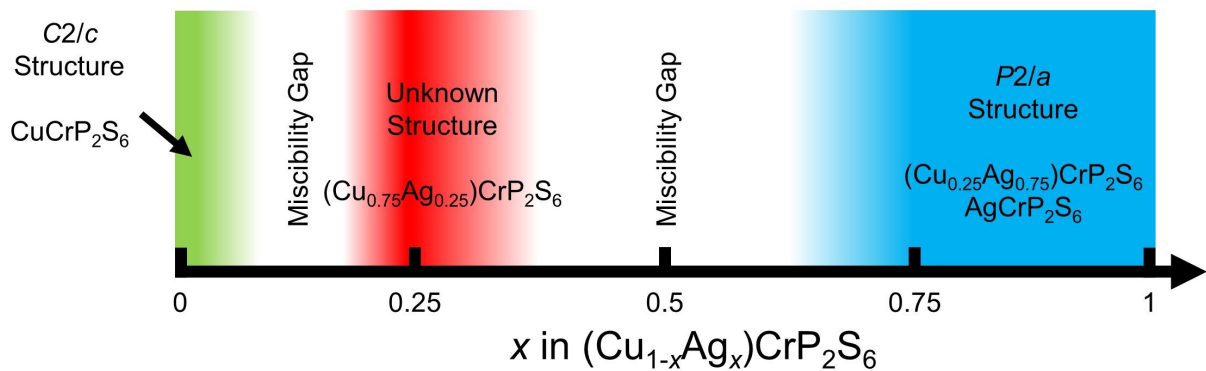


Fig. 4.21.: Schematic illustration of the structural evolution in the composition range of $(\text{Cu}_{1-x}\text{Ag}_x)\text{CrP}_2\text{S}_6$ with $0 \leq x \leq 1$.

4.4. Summary and Outlook

In summary, single crystals of two quaternary compounds of the general formula $M^{1+}M'^{3+}P_2S_6$, $CuCrP_2S_6$ and $AgCrP_2S_6$, were grown by the chemical vapor transport (CVT) technique using iodine as transport agent. This is the first report on the successful single crystal growth of these phases by CVT. While the corresponding growth conditions yielded pristine $CuCrP_2S_6$ crystals, the presence of a secondary phase on the $AgCrP_2S_6$ crystals indicates that the conditions for this phase can be further optimized. However as the impurity phase has only been grown on the surface of the crystals, phase pure crystalline samples of $AgCrP_2S_6$ could be obtained by exfoliation.

For both phases, the crystal structures (*i.e.* $C2/c$ structure for $CuCrP_2S_6$ and $P2/a$ structure for $AgCrP_2S_6$) were found in overall agreement with literature [58, 148]. Yet for $CuCrP_2S_6$, the distinction between the reported $C2/c$ structure and a $C2/m$ structure without the ordering of Cu and Cr on the honeycomb is challenging based on pXRD alone. However in the context of the structural features of the low temperature crystal structure [155] and the magnetic properties, the $C2/c$ structure most likely corresponds to the actual structure of $CuCrP_2S_6$ at room temperature. Furthermore for $CuCrP_2S_6$, a displacement of a fraction of the Cu atoms along the c^* direction away from the center towards the top and bottom faces of the surrounding S_6 octahedra is reported [58]. Including this displacement in the corresponding structural model for the Rietveld refinement yields an improved agreement between model and experiment. Further investigations of the structure of $CuCrP_2S_6$ especially focusing on the Cu displacement may be worthwhile. Firstly, the formation of Cu_2S_6 units (structurally analogous to the P_2S_6 dumbbells) in this compound was discussed before in literature [172] but their existence could not be unambiguously demonstrated [155]. Furthermore, for the low temperature structure of $CuCrP_2S_6$ the displaced Cu atoms order (*i.e.* alternating top and bottom position in a layer along (110)) [155]. Consequently, it is conceivable that this order may not be completely lost for the room temperature structure but remains as a structural modulation, *i.e.* a gradual shift of the Cu position over multiple unit cells. Such a long range ordering of Cu in $CuCrP_2S_6$ could be of interest for the related physical properties, as the Cu displacement causes a local displacement of the electrical dipole moment as demonstrated for the low temperature structure [173].

The thermal evolution of the normalized magnetization $MH^{-1}(T)$ of $CuCrP_2S_6$ indicates an antiferromagnetic ground state. However, positive values of Θ_{CW} indicate dominant ferromagnetic interactions for $H \parallel ab$ as well as for $H \perp ab$. For $H \parallel ab$, $M(H)$ at low temperatures (1.8 K and 5 K) and low fields exhibits a curvature typical for spin-flop transition, as expected for the magnetically easy direction/plane in an antiferromagnetic state. Concluding from the remaining anisotropy in the field dependent magnetization after considering the effect of shape anisotropy, the magnetic anisotropy in $CuCrP_2S_6$ contains a notable contribution of magnetocrystalline anisotropy. At an external field of approximately 65 kOe, magnetic saturation sets in for $H \parallel ab$. The low saturation field compared to other antiferromagnets implies that the spin system is easily polarized, in agreement with notable ferromagnetic contributions as implied by Θ_{CW} . Both the magnetic saturation moment $M_{sat} = 3\mu_B$ per $CuCrP_2S_6$ and the effective moment ($\mu_{eff} \approx 3.78\mu_B$ per $CuCrP_2S_6$ for $H \parallel ab$; $\mu_{eff} \approx 3.89\mu_B$ per $CuCrP_2S_6$ for $H \perp ab$) obtained from the Curie-Weiss analysis demonstrate that the magnetic ion in the sys-

tem is $S = 3/2$ as expected for Cr^{3+} , which agrees with the oxidation states of $Cu^{1+}Cr^{3+}P_2S_6$. The overall magnetic behavior of $CuCrP_2S_6$ is in ideal agreement with the behavior observed by Colombet *et al.* on a polycrystalline sample [58]. Colombet discussed this behavior in terms of dominantly ferromagnetic interactions in the structural layers while adjacent layers order antiferromagnetically, as already well established for similar layered Cr^{3+} compounds, which exhibit virtually the same characteristic features in the evolution of the magnetic properties [156–161]. Further investigations of the magnetic properties in the future may validate such a magnetic structure in $CuCrP_2S_6$. In the context of such a magnetic structure, it may be worthwhile in future to investigate the magnetic properties of $CuCrP_2S_6$ while thinning down the sample towards few layers or even the monolayer. As the antiferromagnetic contribution is related to interactions between layers, it may be weakened by reducing the amount of layers in the sample. Potentially on the monolayer, the material may act as a ferromagnet down to lowest temperatures as no interlayer antiferromagnetic interactions are possible. In this context, the presence of magnetocrystalline anisotropy in $CuCrP_2S_6$ is promising to stabilize long range magnetic order even on the monolayer.

The thermal evolution of the normalized magnetization of $AgCrP_2S_6$ exhibits the characteristic features reported in literature [148, 154, 165]. A broad maximum is observed in the thermal evolution of the normalized magnetization $MH^{-1}(T)$ centered at around 250 K. According to literature [148, 154, 166], this maximum is attributed to low dimensional short range correlations (as already observed for $Ni_2P_2S_6$ in Sect. 3.1.3) and indicates dominantly antiferromagnetic interactions. Below approximately 25–30 K an increase of the normalized magnetization is observed, which was discussed in terms of non-interacting paramagnetic Curie impurities in literature [148, 165]. Below 20 K long-range antiferromagnetic order sets in according to neutron diffraction experiments [164] but no corresponding anomaly is observed. The field dependence of the magnetization of $AgCrP_2S_6$ at 1.8 K exhibits a non-linear evolution up to approximately 20–30 kOe and a linear evolution above these fields. Mutka *et al.* attributed this behavior to a linear component caused by an isotropic antiferromagnet and a saturating component due to paramagnetic Curie impurities, following the evolution described by the Brillouin function. Yet, neither can the experimental field dependence in this work be described by a Brillouin function with physically reasonable parameters nor does the anisotropy of the field dependence agree with the assumption of an isotropic antiferromagnet. In the same line of argumentation, the anisotropic evolution of the temperature dependence does also not agree well with isotropic Curie impurities causing the increase of magnetization towards low temperatures. Consequently, further investigations of the magnetic behavior of $AgCrP_2S_6$ are necessary in the future to show if the low temperature magnetic features are indeed heavily influenced by contributions of Curie impurities or if they have another potentially intrinsic origin. An intrinsic origin for the low temperature upturn might also explain the absent anomaly at the onset of antiferromagnetic ordering.

To investigate the quasi-binary $(Cu_{1-x}Ag_x)CrP_2S_6$ section of the corresponding phase diagram for regions of miscibility and immiscibility, polycrystalline samples of the nominal composition of $(Cu_{1-x}Ag_x)CrP_2S_6$ with $x = 0, 0.25, 0.50, 0.75$ & 1 were synthesized by solid state synthesis. The phases in these polycrystalline samples were thoroughly analyzed by SEM and EDX regarding their composition and phase relation as well as by pXRD regarding their crystal structure. Based on this analysis, it is likely that two regions of immiscibility are present in the quasi-binary $(Cu_{1-x}Ag_x)CrP_2S_6$ phase diagram. The first miscibility gap is located between

CuCrP_2S_6 in the $C2/c$ structure and $(\text{Cu}_{0.75}\text{Ag}_{0.25})\text{CrP}_2\text{S}_6$ in an unknown structure. The second miscibility gap is found between the aforementioned phase of $(\text{Cu}_{0.75}\text{Ag}_{0.25})\text{CrP}_2\text{S}_6$ and $(\text{Cu}_{0.25}\text{Ag}_{0.75})\text{CrP}_2\text{S}_6$ in the $P2/a$ structure reported for AgCrP_2S_6 . In agreement with this, the sample with the nominal composition of $(\text{Cu}_{0.5}\text{Ag}_{0.5})\text{CrP}_2\text{S}_6$ is found in the miscibility gap, containing simultaneously two $(\text{Cu}_{1-x}\text{Ag}_x)\text{CrP}_2\text{S}_6$ phases with different degrees of Cu vs. Ag substitution. A regime of miscibility potentially exists between $(\text{Cu}_{0.25}\text{Ag}_{0.75})\text{CrP}_2\text{S}_6$ and AgCrP_2S_6 as both compounds exhibit the same $P2/a$ crystal structure. Consequently, this regime may be of interest in the future to indirectly tune the magnetic properties of AgCrP_2S_6 by substitution of Cu vs. Ag on the non-magnetic sublattice. Furthermore, the synthesis and potentially crystal growth of phase pure $(\text{Cu}_{0.75}\text{Ag}_{0.25})\text{CrP}_2\text{S}_6$ followed by the determination of the crystal structure by scXRD and pXRD is worthwhile to further verify the aforementioned scenario of two miscibility gaps.

5. $M_2(\text{Ge,Si})_2\text{Te}_6$

The $M_2(\text{Ge,Si})_2\text{Te}_6$ compounds form a subclass in the family of van der Waals layered metal trichalcogenides and crystallize in a trigonal structure with a space group of either $P\bar{3}$ (No. 147) [54, 174] or $R\bar{3}$ (No. 148) [37, 51, 175]. As mentioned in Sect. 1.1, the higher symmetry compared to the monoclinic $M_2\text{P}_2\text{S}_6$ compounds is related to a more rigid stacking order, while the structure of the layers stays virtually the same. The AA stacking of the $P\bar{3}$ structure and the ABC stacking of the $R\bar{3}$ structure are illustrated in Fig. 5.1.

Table 5.1.: Compounds of the $M_2(\text{Ge,Si})_2\text{Te}_6$ subclass with corresponding space groups (SG) according to the ICSD.

Compound	SG	ICSD Code	Ref.
Main-group metal compounds			
$\text{Al}_2\text{Si}_2\text{Te}_6$	$P\bar{3}$	75001	[54]
$\text{In}_2\text{Si}_2\text{Te}_6$	$P\bar{3}$	66356	[174]
$\text{In}_2\text{Ge}_2\text{Te}_6$	$R\bar{3}$	195343	[51]
Transition metal compounds			
$\text{Cr}_2\text{Si}_2\text{Te}_6$	$R\bar{3}$	62379	[175]
$\text{Cr}_2\text{Ge}_2\text{Te}_6$	$R\bar{3}$	79268	[37]

Table 5.1 shows the members of this subclass that are experimentally validated and listed in the ICSD¹. Additionally, Sandre *et al.* report a trigonal unit cell for $\text{Sc}_2\text{Si}_2\text{Te}_6$ [54], which is not found in the ICSD.

$\text{In}_2\text{Si}_2\text{Te}_6$ [176], $\text{In}_2\text{Ge}_2\text{Te}_6$ [177], $\text{Cr}_2\text{Ge}_2\text{Te}_6$ [37] and $\text{Cr}_2\text{Si}_2\text{Te}_6$ [151] are reported to be electrical insulators. For the closed shell main-group metal compounds and $\text{Sc}_2\text{Si}_2\text{Te}_6$, diamagnetism is expected. However for the chromium compounds, Cr^{3+} is $S = 3/2$ and a ferromagnetic ground state is stabilized.

In the course of this work, two of these compounds, the main-group metal compound $\text{In}_2\text{Ge}_2\text{Te}_6$ and the transition metal compound $\text{Cr}_2\text{Ge}_2\text{Te}_6$ were grown as single crystals and their structure as well as their magnetic behavior were investigated. Hereafter, each system and the corresponding investigations are shortly introduced and the results of the experimental studies are presented.

5.1. $\text{Cr}_2\text{Ge}_2\text{Te}_6$

In 1995, Carteaux *et al.* reported the first synthesis of polycrystalline $\text{Cr}_2\text{Ge}_2\text{Te}_6$ as well as its structural and bulk magnetic characterization [37]. The honeycomb layered crystal structure could be solved in the space group $R\bar{3}$ and ferromagnetic order was found below $T_C = 61$ K with a magnetic easy axis perpendicular to the structural layers (as illustrated in Fig. 5.2).

¹Inorganic Crystal Structure Database (<http://icsd.fiz-karlsruhe.de>) [107], accessed June 2020.

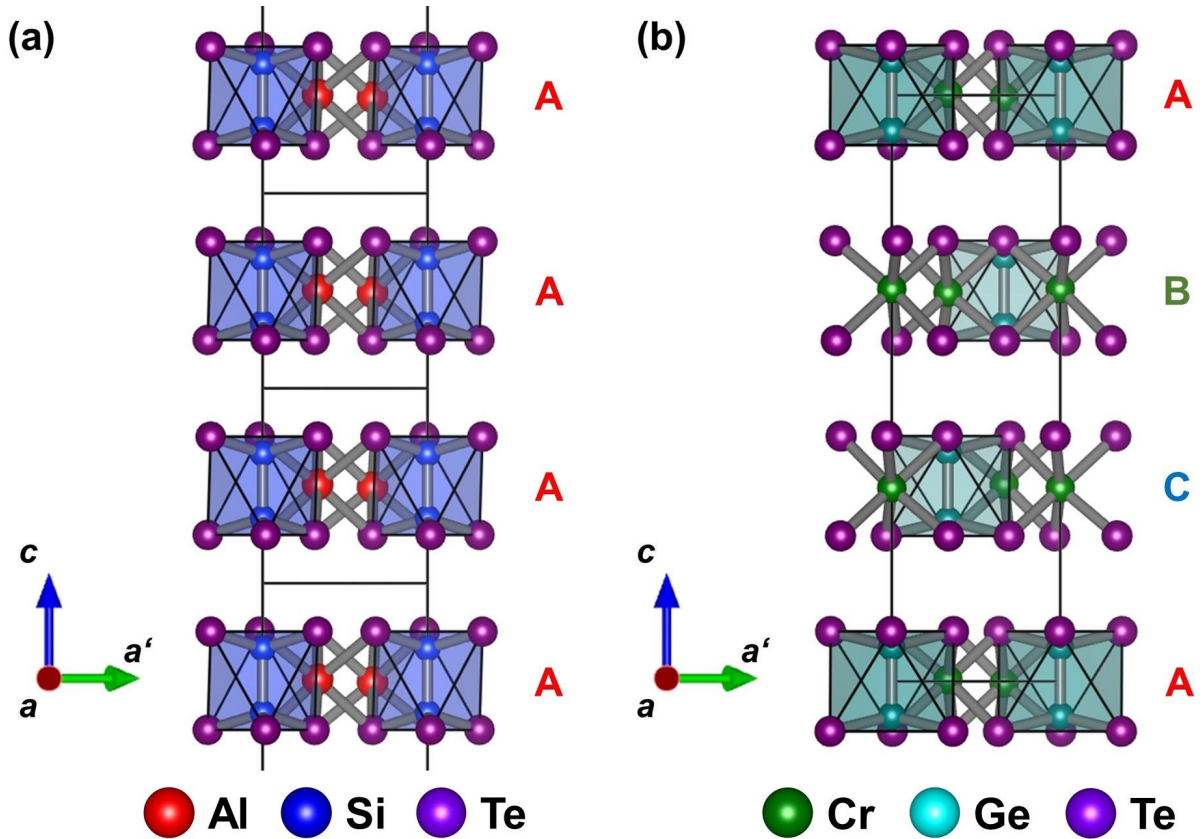


Fig. 5.1.: Perspective drawing of the structure of (a) $\text{Al}_2\text{Si}_2\text{Te}_6$ in $P\bar{3}$ and (b) $\text{Cr}_2\text{Ge}_2\text{Te}_6$ in $R\bar{3}$ with view along the a direction. Note that (a) shows four unit cells of the $P\bar{3}$ structure while (b) shows only one unit cell in the $R\bar{3}$ structure, corresponding to the same number of layers. The differences in the stacking order are best observed based on the shift of the $(\text{Ge,Si})_2\text{Te}_6$ unit between layers.

Additionally the insulating ground state could be probed by the thermal evolution of the resistivity and an activation energy of 0.2 eV was extracted. The first successful growth of bulk crystals is reported by Ji *et al.* [178] in 2013 using a self flux growth attempt with excessive Ge and Te.

However, it was the discovery of intrinsic ferromagnetism in bilayers of $\text{Cr}_2\text{Ge}_2\text{Te}_6$, as reported by Gong *et al.* in 2017 [29], that moved this compound into the focus of research. As explained in the context of the Mermin-Wagner theorem in Sect. 1.2.5, magnetic anisotropy plays a crucial role in the stabilization of long range magnetic order in 2D systems. Consequently, understanding the magnetic anisotropy in $\text{Cr}_2\text{Ge}_2\text{Te}_6$ is essential for the functionality of future applications as well as for the search of new 2D ferromagnets. In this line, a common feature of all known 2D ferromagnetic compounds is a peculiar decrease of the magnetization towards lower temperatures with an onset just below the Curie-temperature for external fields applied along the magnetic hard plane.

To investigate the magnetic anisotropy as well as the peculiar behavior in the magnetization of $\text{Cr}_2\text{Ge}_2\text{Te}_6$, single crystals were grown as discussed in Sect. 5.1.1 and extensively characterized by SEM, EDX spectroscopy and pXRD (see Sect. 5.1.2). The magnetic ground-state was characterized by SQUID magnetometry and specific heat measurements as presented

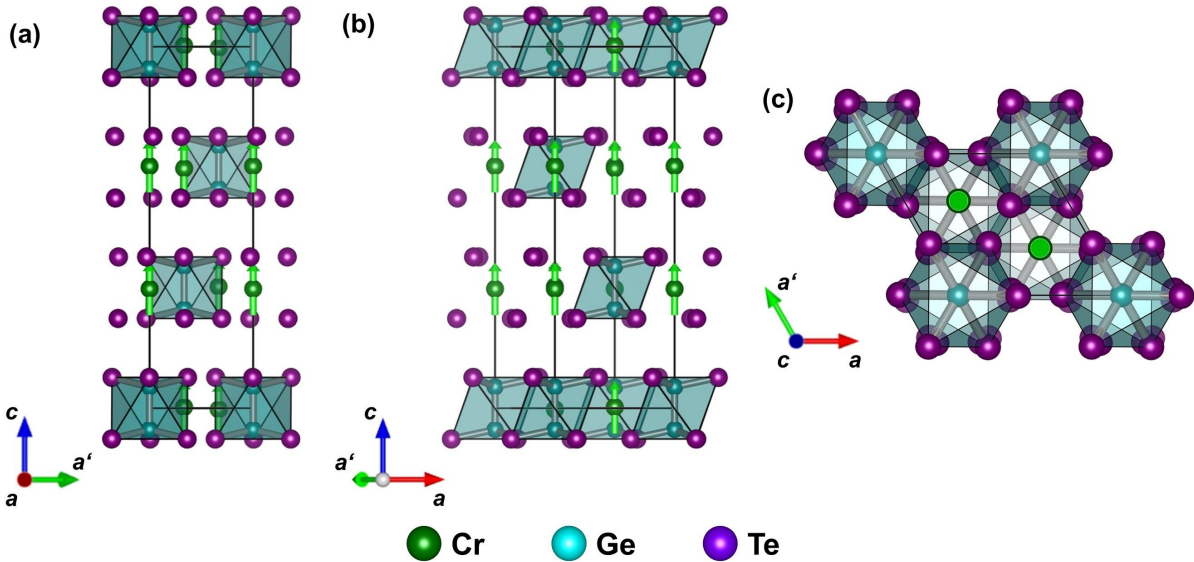


Fig. 5.2.: Perspective drawing of the crystal structure of $\text{Cr}_2\text{Ge}_2\text{Te}_6$. View along (a) the a direction, (b) the b^* direction ($\perp ac$ plane) and (c) the c direction. The cyan octahedra show the Ge_2Te_6 structural units. Cr–Te bonding is omitted. Additionally, bright green arrows illustrate the preferred orientation of the magnetic moments in the ferromagnetic state, according to Carteaux *et al.* [37].

in Sect. 5.1.3 allowing for the extraction of the magnetocrystalline anisotropy constant K_U at 1.8 K. Additionally, the evolution of the temperature dependent magnetization with the external field was studied with a special focus on the low field regime as discussed in Sect. 5.1.3. From this, magnetic field-temperature phase diagrams were obtained for fields along and perpendicular to the magnetic easy axis. These phase diagrams are shown and compared to each other in Sect. 5.1.3. Based on these magnetic phase diagrams, the thermal evolution of the magnetic anisotropy could be retraced (Sect. 5.1.3). This investigation demonstrates that the peculiar magnetization behavior as function of temperature in $\text{Cr}_2\text{Ge}_2\text{Te}_6$ is caused by continuous rotation of the magnetization direction as function of external field as well as the interplay between magnetocrystalline anisotropy and temperature, as discussed in Sect. 5.1.3. Additionally, the critical behavior of $\text{Cr}_2\text{Ge}_2\text{Te}_6$ around the ferromagnetic–paramagnetic phase transition is investigated in detail and the corresponding critical exponents are extracted (see Sect. 5.1.4). These exponents imply that the magnetization of $\text{Cr}_2\text{Ge}_2\text{Te}_6$ is best described in terms of the 2D Ising model with non-negligible interlayer coupling.

Parts of the following section have already been published in J. Zeisner,..., S. Selzer *et al.*, *Physical Review B* **99**, 165109 (2019) [179] (crystal growth and characterization) as well as in S. Selzer *et al.*, *Physical Review B* **101**, 014440 (2020) [180] (magnetic phase diagrams and thermal evolution of $K_{U,\text{eff}}$). Furthermore using crystals grown in the course of this work, an investigation of the influence of pressure on the magnetic anisotropy in $\text{Cr}_2\text{Ge}_2\text{Te}_6$ was accepted as T. Sakurai,..., S. Selzer *et al.* 'Pressure control of the magnetic anisotropy of the quasi-2D van der Waals ferromagnet $\text{Cr}_2\text{Ge}_2\text{Te}_6$ ' in *Physical Review B*.

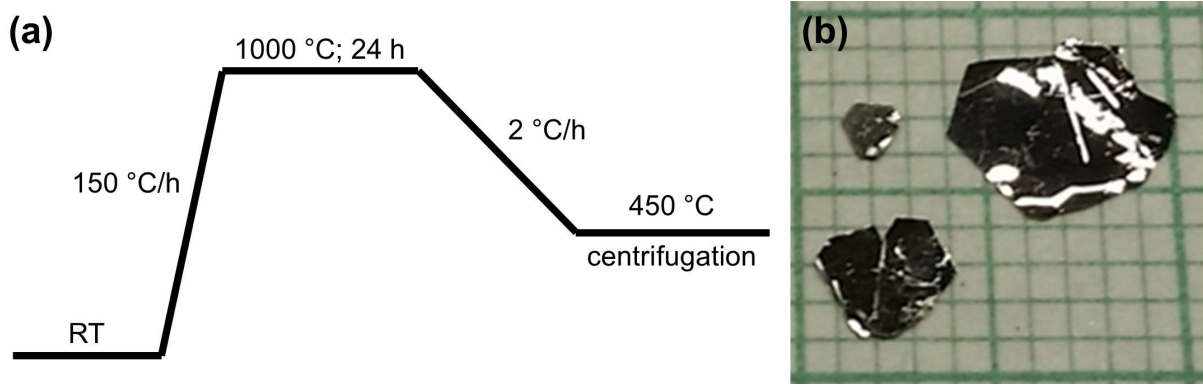


Fig. 5.3.: (a) Schematic representation of the temperature profile used for the self flux growth of $\text{Cr}_2\text{Ge}_2\text{Te}_6$. (b) As-grown plate-like $\text{Cr}_2\text{Ge}_2\text{Te}_6$ crystals obtained from the Ge-Te rich melt. One green square equals $1\text{ mm} \times 1\text{ mm}$ for scale.

5.1.1. Crystal Growth

$\text{Cr}_2\text{Ge}_2\text{Te}_6$ single crystals were grown by the flux growth technique using a Ge-Te rich self flux. A similar approach is reported by Zhang *et al.* [181].

A mixture of chromium (granules, MaTeck, 99.99%), germanium (chips, Sigma Aldrich, 99.999%), and tellurium (lumps, Alfa Aesar, 99.999%) with molar ratios of Cr : Ge : Te = 10 : 13 : 77 were taken in an alumina crucible which was then sealed in a quartz ampule under a partial atmosphere of Ar (approx. 300 mbar). The quartz ampule was placed upright in a box furnace (Nabertherm) and the temperature profile shown in Fig. 5.3(a) was applied. Finally, at $450\text{ }^\circ\text{C}$ excessive melt was centrifuged and shiny, plate-like crystals of $\text{Cr}_2\text{Ge}_2\text{Te}_6$ of up to $6\text{ mm} \times 5\text{ mm} \times 0.2\text{ mm}$ (e.g. in Fig. 5.3(b)) were obtained. The crystals were easy to exfoliate, e.g. by scotch tape, as expected from the van der Waals layered crystal structure of $\text{Cr}_2\text{Ge}_2\text{Te}_6$.

5.1.2. Characterization

Crystal Morphology and Compositional Analysis

The compositional analysis was carried out on as-grown $\text{Cr}_2\text{Ge}_2\text{Te}_6$ crystals by SEM and EDX as explained in Sect. 2.3. Representative SEM(SE) images (*i.e.* topographical contrast) and SEM(BSE) images (*i.e.* chemical contrast) of an as-grown crystal are shown in Fig. 5.4(a) and (b). The SEM(SE) image shows a flat surface and edge facets of $\approx 120^\circ$ (left side of the image) indicative of a trigonal or hexagonal crystal system. In the SEM(BSE) image, the crystal surface exhibits a homogeneous contrast besides some local dark spots. Comparing SEM(BSE) and SEM(SE) images, these dark spots can be clearly attributed to particles on the surface of the crystal and not intrinsic impurities. No further inhomogeneities were resolved.

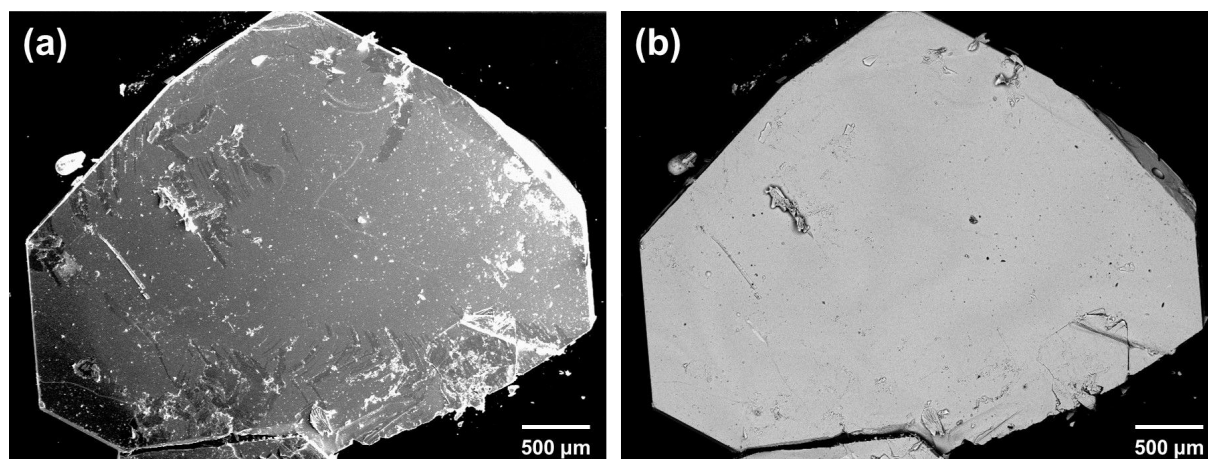


Fig. 5.4.: (a) SEM(SE) (*i.e.* topographical contrast mode) and (b) SEM(BSE) (chemical contrast mode) images of a $\text{Cr}_2\text{Ge}_2\text{Te}_6$ crystal obtained from the aforementioned growth experiment.

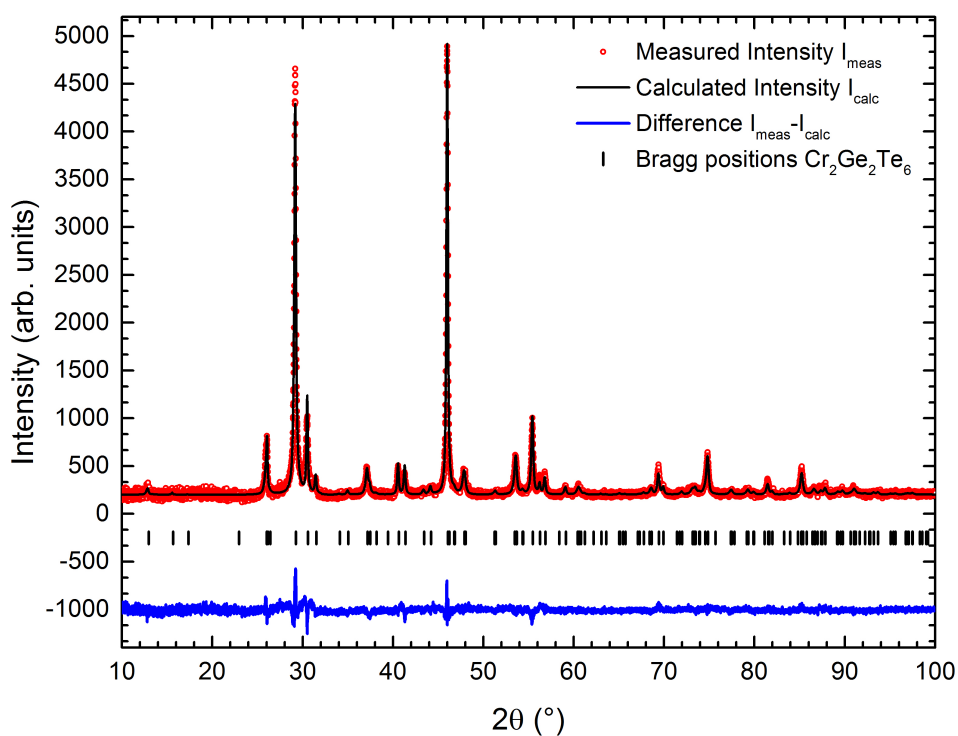


Fig. 5.5.: pXRD pattern from $\text{Cu-K}\alpha_1$ radiation (1.54059 \AA) of pulverized crystals (red dots), calculated pattern of the $R\bar{3}$ structure of $\text{Cr}_2\text{Ge}_2\text{Te}_6$ (black line), difference between measured and calculated intensity (blue line) and expected Bragg positions (black dots).

Table 5.2.: Summary and reliability factors of the Rietveld analysis of the pXRD pattern of $\text{Cr}_2\text{Ge}_2\text{Te}_6$.

<i>Experiment & Data Collection</i>	
Temperature (K)	293(2)
Radiation Type & Wavelength (Å)	Cu-K $_{\alpha_1}$; 1.54059
θ_{\min} (°)	10.00
θ_{step} (°)	0.01
θ_{\max} (°)	101.99
<i>Crystal Data</i>	
Crystal System	Trigonal
Space Group	$R\bar{3}$ (No. 148)
$a = b$ (Å)	6.828(3)
c (Å)	20.572(12)
<i>Refinement</i>	
Goodness-Of-Fit	1.24
R_p (%)	4.76
wR_p (%)	6.15
R_F (%)	9.02

Table 5.3.: Fractional atomic coordinates, occupancies and isotropic displacement parameters U_{iso} of $\text{Cr}_2\text{Ge}_2\text{Te}_6$ at 293 K with estimated standard deviations in parantheses after Rietveld refinement.

Label	Type	Wyck	x	y	z	Occ (%)	U_{iso} ($\times 10^{-3}\text{Å}^2$)
Cr1	Cr	$6c$	0	0	0.3330(30)	100	41(9)
Ge1	Ge	$6c$	0	0	0.0588(13)	100	16(6)
Te1	Te	$18f$	0.6684(11)	0.9691(6)	0.2480(10)	100	29(2)

To quantify the elemental composition of the crystals, EDX spectroscopy was performed on several spots on multiple crystals. The corresponding mean elemental composition of $\text{Cr}_{21.5(2)}\text{Ge}_{19.6(7)}\text{Te}_{58.9(6)}$ agrees well with the expected composition of $\text{Cr}_{20}\text{Ge}_{20}\text{Te}_{60}$. The low standard deviations of the mean ratios are exemplary for a homogeneous elemental distribution. No indications of secondary phases could be found neither from the SEM images nor from EDX spectroscopy.

Structural Analysis

The single phase nature of these crystals is confirmed by the corresponding pXRD pattern, as shown in Fig. 5.5). All reflections can be assigned to the $R\bar{3}$ phase of $\text{Cr}_2\text{Ge}_2\text{Te}_6$ as reported in literature [37] and illustrated before in Fig. 5.2.

To extract further details of the crystal structure, a Rietveld refinement was performed. In the course of this refinement, the experimental pattern could be well described by the crystal structure model proposed by Carreau *et al.* [37]. General information on the refined model as well as corresponding reliability factors are presented in Table 5.2 while details on the atomic model after the refinement are given in Table 5.3. In general, the results from Rietveld analysis are in ideal agreement with literature data on powders and single crystals [37, 182]. Consequently, both crystal structure and elemental composition confirm the successful phase pure formation of crystals of the desired $\text{Cr}_2\text{Ge}_2\text{Te}_6$ phase.

5.1.3. Magnetic Properties

The thermal evolution of the normalized magnetization $MH^{-1}(T)$ of $\text{Cr}_2\text{Ge}_2\text{Te}_6$ was measured at a magnetic field of 1 kOe applied parallel and perpendicular to the crystallographic ab plane and is shown in Fig. 5.6(a). From high to low temperatures, the normalized magnetization starts to notably increase below 100 K for $H \perp ab$. Towards lower temperatures, the slope increases and becomes maximum at 66 K as observed in the first derivative of $MH^{-1}(T)$ (Fig. 5.6(a) bottom) corresponding to an inflection point in $MH^{-1}(T)$. At around 55 K the normalized magnetization saturates. This behavior is typical for a paramagnetic–ferromagnetic transition. The inflection point in $MH^{-1}(T)$ corresponds to the ferromagnetic ordering temperature $T_C = 66 \pm 1$ K (Curie temperature). For $H \parallel ab$, the thermal evolution of the normalized magnetization matches the evolution for $H \perp ab$ down to 64 K. At this temperature, the onset of a downturn is observed for $H \parallel ab$ and the thermal evolution of MH^{-1} becomes anisotropic towards lower temperatures. As the onset of the downturn is of further interest, the corresponding temperature is labeled T^* , which is characterized as $\partial MH^{-1}/\partial T = 0$.

A similar anisotropic behavior is also seen for $\text{Cr}_2\text{Si}_2\text{Te}_6$ [151], CrI_3 [152] and CrBr_3 [152], which are also 2D honeycomb ferromagnets and show a close relation to $\text{Cr}_2\text{Ge}_2\text{Te}_6$ regarding their structure. The similarities regarding structure, magnetic ion and magnetic ordering hint towards a main role of these properties for the origin of the observed anisotropy.

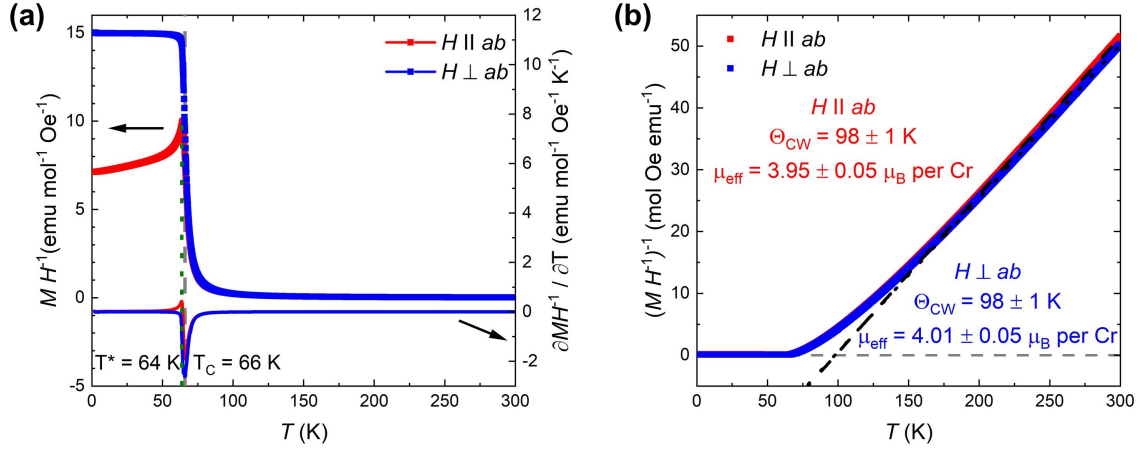


Fig. 5.6.: (a) Top: Normalized magnetization of $\text{Cr}_2\text{Ge}_2\text{Te}_6$ as function of temperature $MH^{-1}(T)$ measured at a magnetic field of 1 kOe applied parallel and perpendicular to the crystallographic ab plane (left y-axis). Bottom: First derivative of $MH^{-1}(T)$ for both directions of the magnetic field (right y-axis). The grey dashed line indicates the temperature of inflection in $MH^{-1}(T)$ corresponding to a minimum in $\partial MH^{-1}/\partial T$ and the ferromagnetic ordering temperature T_C of $\text{Cr}_2\text{Ge}_2\text{Te}_6$. The green dotted line shows the temperature of the onset of the downturn T^* corresponding to $\partial MH^{-1}/\partial T = 0$. (b) Inverse of the normalized magnetization as function of temperature $(MH^{-1})^{-1}(T)$. The black dashed and dotted lines correspond to linear fits of the temperature regime 200–300 K.

The inverse of the normalized magnetization of $\text{Cr}_2\text{Ge}_2\text{Te}_6$ as function of temperature $(MH^{-1})^{-1}(T)$ is shown in Fig. 5.6(b). The linear evolution in the paramagnetic state at high temperatures allows for a Curie-Weiss analysis. From this analysis in the temperature regime of 200–300 K, effective magnetic moments of $\mu_{\text{eff}} = 3.95 \pm 0.05 \mu_B/\text{Cr}$ for $H \parallel ab$ and $\mu_{\text{eff}} = 4.01 \pm 0.05 \mu_B/\text{Cr}$ for $H \perp ab$ are obtained. These values are in ideal agreement with the expected spin-only values of $\mu_{\text{so}}(\text{Cr}^{3+}) = 3.92 \mu_B$ for $H \parallel ab$ and $\mu_{\text{so}}(\text{Cr}^{3+}) = 3.95 \mu_B$ for $H \perp ab$ using $S = 3/2$ and the experimental Landé factors reported by Zeisner *et al.* [179]. Furthermore, the Curie-Weiss analysis yields a Curie-Weiss temperature of $\Theta_{\text{CW}} = 98 \pm 1$ K for both directions, which is in good agreement with literature [183, 184].

The positive Curie temperature indicates a dominant ferromagnetic coupling. In three-dimensional ferromagnets Θ_{CW} is generally close to T_C . The difference between Θ_{CW} and T_C that is found for $\text{Cr}_2\text{Ge}_2\text{Te}_6$ is most likely an indication for the suppression of the magnetic order due to the two-dimensional nature of the compound and thus also of the magnetic interactions. This is in line with current results obtained from ferromagnetic resonance (FMR) and electron spin resonance (ESR) [179], which demonstrated the intrinsic two-dimensional nature of the magnetic interaction in $\text{Cr}_2\text{Ge}_2\text{Te}_6$.

Fig. 5.7 shows the isothermal magnetization of $\text{Cr}_2\text{Ge}_2\text{Te}_6$ at 1.8 K for $H \parallel ab$ and $H \perp ab$. The hysteresis of the magnetization as function of field is negligible, corresponding to a soft ferromagnet. From the high-field region, a saturation magnetization of $M_s \approx 3 \mu_B/\text{Cr}$ is obtained for both orientations. As $S = 3/2$ (Cr^{3+}), this corresponds to a Landé factor of $g \approx 2$, which is in good agreement with the aforementioned experimental g -factors with weak anisotropy [179]. The saturation field is found as the x -component of the intercept of two linear fits, one being a fit to the saturated regime at high fields and one being a fit of the

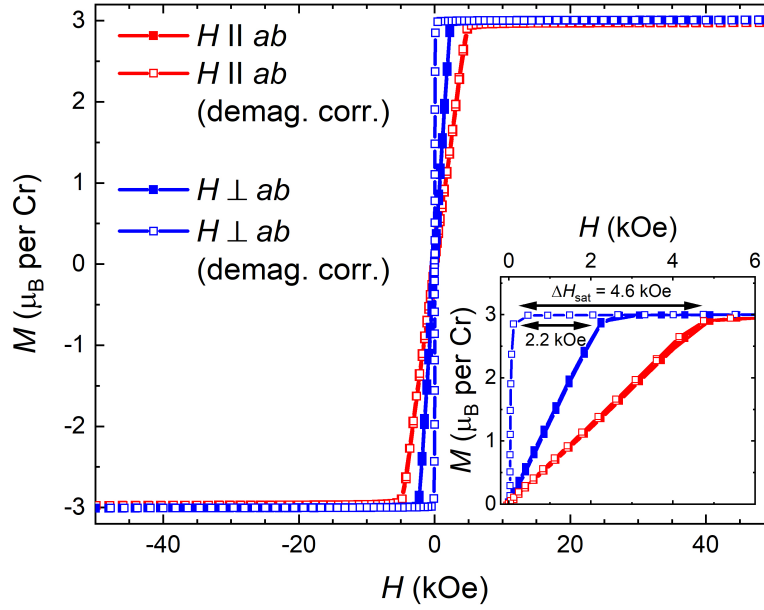


Fig. 5.7.: Field dependence of the magnetization $M(H)$ of $\text{Cr}_2\text{Ge}_2\text{Te}_6$ at 1.8 K for magnetic fields parallel and perpendicular to the crystallographic ab plane. Full symbols: no correction; open symbols: after demagnetizing field correction.

unsaturated linear regime at low fields. Consequently, the saturation field is anisotropic and changes from $H_{\text{sat}} = 4.8$ kOe for $H \parallel ab$ to $H_{\text{sat}} = 2.3$ kOe for $H \perp ab$.

This anisotropic behavior in $M(H)$ is related to two different contributions: the intrinsic magnetic anisotropy of the material (magnetocrystalline anisotropy) and the shape anisotropy of the measured sample. As $\text{Cr}_2\text{Ge}_2\text{Te}_6$ grows as thin platelet crystals, the shape anisotropy must be explicitly taken into account. To evaluate the demagnetizing factors the sample's dimensions were measured along its edges from which an equivalent cuboid was constructed. The demagnetizing factors of $N_x = N_y = 0.06$ and $N_z = 0.88$ were then calculated based on the equivalent-ellipsoid method [70, 185].

As seen in Fig. 5.7, this correction strongly reduces the saturation field to 0.1 kOe for the orientation $H \perp ab$, while only a negligible shift to 4.7 kOe is obtained for $H \parallel ab$. The remaining anisotropy is purely originating from the magnetocrystalline anisotropy, showing that the magnetocrystalline easy axis is perpendicular to the crystallographic ab planes (or in turn parallel to the c direction). This easy axis/hard plane magnetic behavior indicates Ising-type anisotropy.

As mentioned before in Sect. 1.2.4, the free energy density of a ferromagnet can be expressed by Eq. 5.1.

$$F = -\mu_0 \cdot M_s \cdot H \cdot \cos(\varphi) + K_U \cdot \sin^2(\varphi - \theta) \quad (5.1)$$

The first term is the Zeeman contribution with the vacuum permeability μ_0 and the second term corresponds to the contribution of the magnetocrystalline anisotropy with the magnetocrystalline anisotropy constant K_U . θ is the angle between the direction of the external field and the magnetocrystalline easy axis and φ is the angle between the direction of the external field and the direction of the magnetization vector. The contribution from the shape anisotropy was explicitly neglected since the field dependent magnetization was already corrected for the effect of shape anisotropy. For an energetically favoured magnetization direction, a minimum of the energy density must be found. Accordingly, Eq. 5.2 and Eq. 5.3 must be fulfilled.

$$\frac{\partial F}{\partial \varphi} = \mu_0 \cdot M_s \cdot H \cdot \sin(\varphi) + K_U \cdot \sin(2\varphi - 2\theta) = 0 \quad (5.2)$$

$$\frac{\partial^2 F}{\partial \varphi^2} = \mu_0 \cdot M_s \cdot H \cdot \cos(\varphi) + 2 \cdot K_U \cdot \cos(2\varphi - 2\theta) > 0 \quad (5.3)$$

The lowest magnetic field to stabilize the saturated magnetic state ($\varphi = 0$) is found at the saturation field H_{sat} . Consequently, the second derivative (Eq. 5.3) becomes equal to zero at H_{sat} . If the external field is additionally applied perpendicular to the magnetic easy axis ($\theta = \pi/2$), Eq. 5.3 simplifies to Eq. 5.4.

$$\frac{2K_U}{M_s} = \mu_0 H_{\text{sat}} \quad (5.4)$$

This equation allows for an estimation of the magnetocrystalline anisotropy constant K_U from the saturation regime in the field dependence of the magnetization. For the field dependence presented in Fig. 5.7 at 1.8 K, $K_U = 47 \pm 1 \text{ kJ/m}^3$ is obtained, which is in good agreement with K_U obtained previously by FMR on $\text{Cr}_2\text{Ge}_2\text{Te}_6$ [179].

In general, it can be expected that the anisotropic anomaly observed in temperature dependent magnetization also manifests in the field dependence for $H \parallel ab$ (via a change of slope). Such a behavior was not resolved in our data at 1.8 K. This can be explained by the field dependence of T^* , which is investigated in detail in Sect. 5.1.3.

Additionally to the magnetic measurements, the zero field thermal evolution of the normalized specific heat $C_p/T(T)^2$ is shown in Fig. 5.8. The temperature of 65 K of the center of the Λ -shape peak, which corresponding to a second order phase transition regarding the shape, is in good agreement with T_C obtained from $MH^{-1}(H)$.

However, the Λ -shape peak is rather small with an estimated integral of approximately $\Delta S \approx 2 \text{ J/mol/K}$ compared to the expected value of the magnetic entropy change at a ferromagnetic ordering of a system with two $S = 3/2$ magnetic ions per unit cell, the latter being $S_{\text{mag}} = 2R \ln(4) = 23.05 \text{ J/mol/K}$. This reduced size of the peak at the magnetic transition

²All measurements of the specific heat C_p as function of temperature and field as well as the evaluation of the data were performed by Dr. Gaël Bastien at IFW Dresden. All corresponding results are shown with his kind permission.

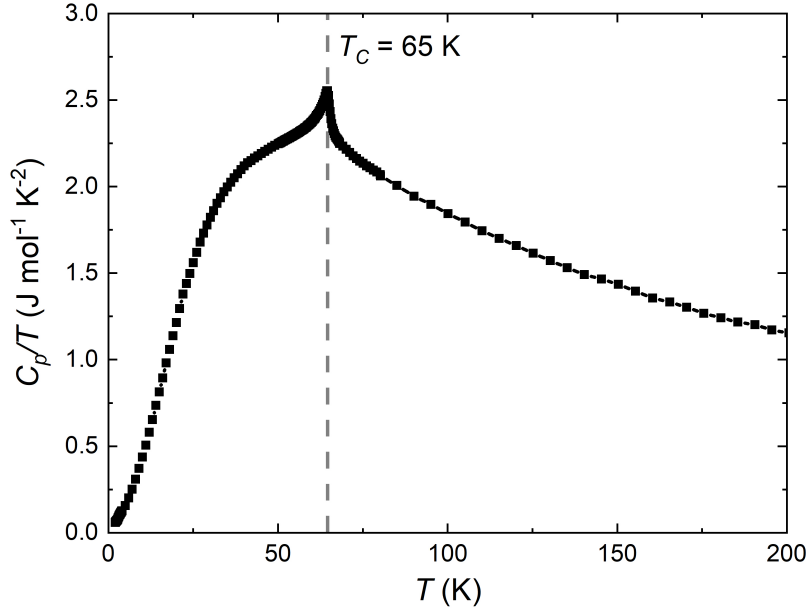


Fig. 5.8.: Thermal evolution of the zero field specific heat divided by the temperature. The dashed line indicates the center of the Λ -shape anomaly which corresponds to T_C .

is a common feature in quasi 2D magnets, which was already observed *e.g.* in the chromium trihalides CrX_3 with $X = \text{Cl}$ [160], Br [186], I [38] and in copper based quasi 2D molecular magnets such as copper pyrazine perchlorate $\text{Cu}(\text{Pz})_2(\text{ClO}_4)_2$ [187]. The missing entropy is most likely from magnetic fluctuations giving an important contribution to the specific heat even far above the magnetic ordering in agreement with the relatively high value of Θ_{CW} and literature [179].

Influence of the Magnetic Field on T_C and T^*

To obtain the magnetic field dependence of T_C and T^* , the thermal evolution of the magnetization and specific heat were measured at several fields.

For the easy axis direction (*i.e.* $H \perp ab$; Fig. 5.9) the usual field dependence of ferromagnetic materials is observed. As observed in the thermal evolution of the magnetization in Fig. 5.9(a), the ferromagnetic–paramagnetic transition temperature T_C (as characterized by the inflection point in $M(T)$) as well as the onset of the upturn monotonically shift towards higher temperatures increasing the magnetic field. $C_p/T(T)$ shows a corresponding shift and additional a notable broadening of the peak, as observed in Fig. 5.9(b). This broadening of the initially Λ -shape anomaly in $C_p/T(T)$ indicates a change of the nature of the corresponding transition from second order to a crossover.

For $H \parallel ab$, the evolution of the ferromagnetic ordering temperature T_C in $M(T)$ is virtually the same as for $H \perp ab$, as shown in Fig. 5.10(a). However up to a magnetic field of 4.5 kOe, additionally a downturn towards lower temperatures with an onset at T^* can be observed

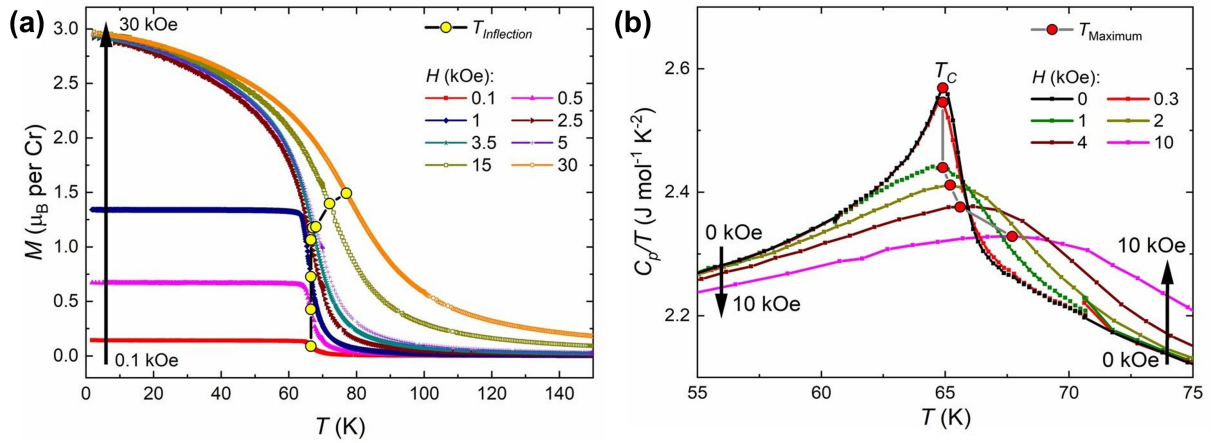


Fig. 5.9.: Thermal evolution of (a) the magnetization M and (b) the normalized specific heat C_p/T of $\text{Cr}_2\text{Ge}_2\text{Te}_6$ under different magnetic fields applied $\perp ab$ (i.e. along the magnetic easy axis). The inflection points in $M(T)$ (corresponding to T_C) in (a) are marked with yellow dots and the red dots in (b) correspond to the maximum of the peak in $C_p/T(T)$.

below T_C in $M(T)$. For the lowest measured magnetic field of 0.1 kOe, T^* is found just below the Curie temperature. By increasing the magnetic field, T^* shifts towards lower temperatures. Furthermore, the maximum in $M(T)$ around T^* gets gradually broader and the downturn itself gets less pronounced increasing the magnetic field. Above 4.5 kOe, no downturn is observed down to 1.8 K and $M(H)$ is found isotropic.

In comparison to $M(T)$, the specific heat only shows one clear phase transition for $H \parallel ab$, together with a change of the shift of the Λ -shaped peak position around 1.7 kOe, as observed in Fig. 5.10(b). By increasing the external field from zero up to 1.3 kOe the position of the maximum shifts towards lower temperatures. By increasing the external field further, the position of the maximum starts to shift towards higher temperatures until an isotropic behavior is observed for fields of 5 kOe and higher. Furthermore, virtually the same progressive broadening of the maximum of C_p/T as for $H \perp ab$ is observed indicating an evolution of the nature of the transition from a second order phase transition to a crossover.

Considering the strength of the downturn observed in the temperature dependent magnetization for $H \parallel ab$, a notable entropy change is expected to go along with its onset. Therefore a corresponding anomaly in $C_p/T(T)$ is expected. In the field range of 0 kOe and 1.3 kOe, only one distinct peak is found in $C_p/T(T)$. However, in this field range T^* and T_C are close to each other (less than 3 K difference) and the Λ -shaped signal in the specific heat has a significant broadness. Therefore, it is not possible to state if only one anomaly is observed or if the signal contains actually two anomalies in this field range. However, as the signal in specific heat shifts towards lower temperatures, a dominant influence of the transition at T^* in this field regime can be expected.

While the crossover resulting from the ferromagnetic–paramagnetic transition shifts towards higher temperatures as seen for $H \perp ab$ for both M and C_p , for $H \parallel ab$ at low fields T^* shifts towards lower temperatures and is accompanied by a corresponding shift in $C_p/T(T)$. However for fields in the range of 1.7 kOe to 5 kOe, the specific heat measurements exhibit no

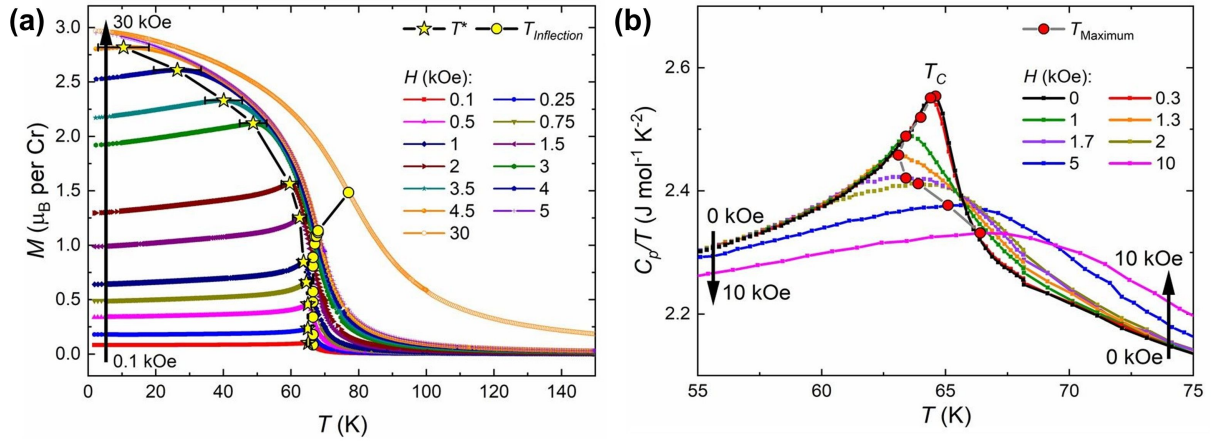


Fig. 5.10.: Thermal evolution of (a) the magnetization M and (b) the normalized specific heat C_p/T of $\text{Cr}_2\text{Ge}_2\text{Te}_6$ under different magnetic fields applied $\parallel ab$ (*i.e.* perpendicular to the magnetic easy axis). The inflection points in $M(T)$ (corresponding to T_C) in (a) are marked with yellow dots, while yellow stars in (a) indicate the maxima observed in $M(T)$ corresponding to T^* . Red dots in (b) illustrate the evolution of the maximum of the peak in $C_p/T(T)$.

clear anomaly corresponding to T^* and the peak follows the changes in T_C . This indicates that T^* is a transition between two states with comparable magnetic entropy. At fields above 5 kOe the specific heat behavior is isotropic for fields parallel and perpendicular to ab , in agreement with $M(T)$.

Low-Field Magnetic Phase Diagrams

The low-field magnetic phase diagrams of $\text{Cr}_2\text{Ge}_2\text{Te}_6$ for $H \parallel ab$ and $H \perp ab$ were constructed from the aforementioned $M(T)$ measurements, allowing for a detailed investigation of the magnetic regimes in this compound. For $H \perp ab$ (*i.e.* along the magnetic easy axis; Fig. 5.11(b)), two phases are observed, *i.e.*, a disordered paramagnetic phase (Phase I) at high temperatures and a ferromagnetic ordered state with $M \parallel H$ (Phase II) at lower temperatures. The transition temperatures from specific heat (peak position) and from magnetization (inflection point) are in good agreement within the range of the measurement uncertainties. In zero field the magnetization direction is supposed to be along the easy axis in the ferromagnetic state. Applying external fields parallel to the magnetic easy axis stabilizes this state for example against thermally activated magnetic fluctuations. Therefore, the observed behavior of Phase II as function of field and temperature is well expected.

However, for $H \parallel ab$ an additional Phase III is observed, as shown in Fig. 5.11(a). While for $H \perp ab$ the iso-magnetization lines are parallel to the T-axis until they deviate towards higher fields very close to T_C , for $H \parallel ab$, these lines first show a trend towards lower fields before they finally deviate towards high fields at elevated temperatures. These kinks are the fingerprints of the maximum seen in the temperature dependent magnetization and are well followed by T^* . This allows to not just define $T^*(H)$ but also $H^*(T)$ in this low temperature/low field regime. Whereas $T^*(H)$ corresponds to the signature of Phase III in temperature dependent magnetization, $H^*(T)$ corresponds to the same signature in field dependent magnetization. Us-

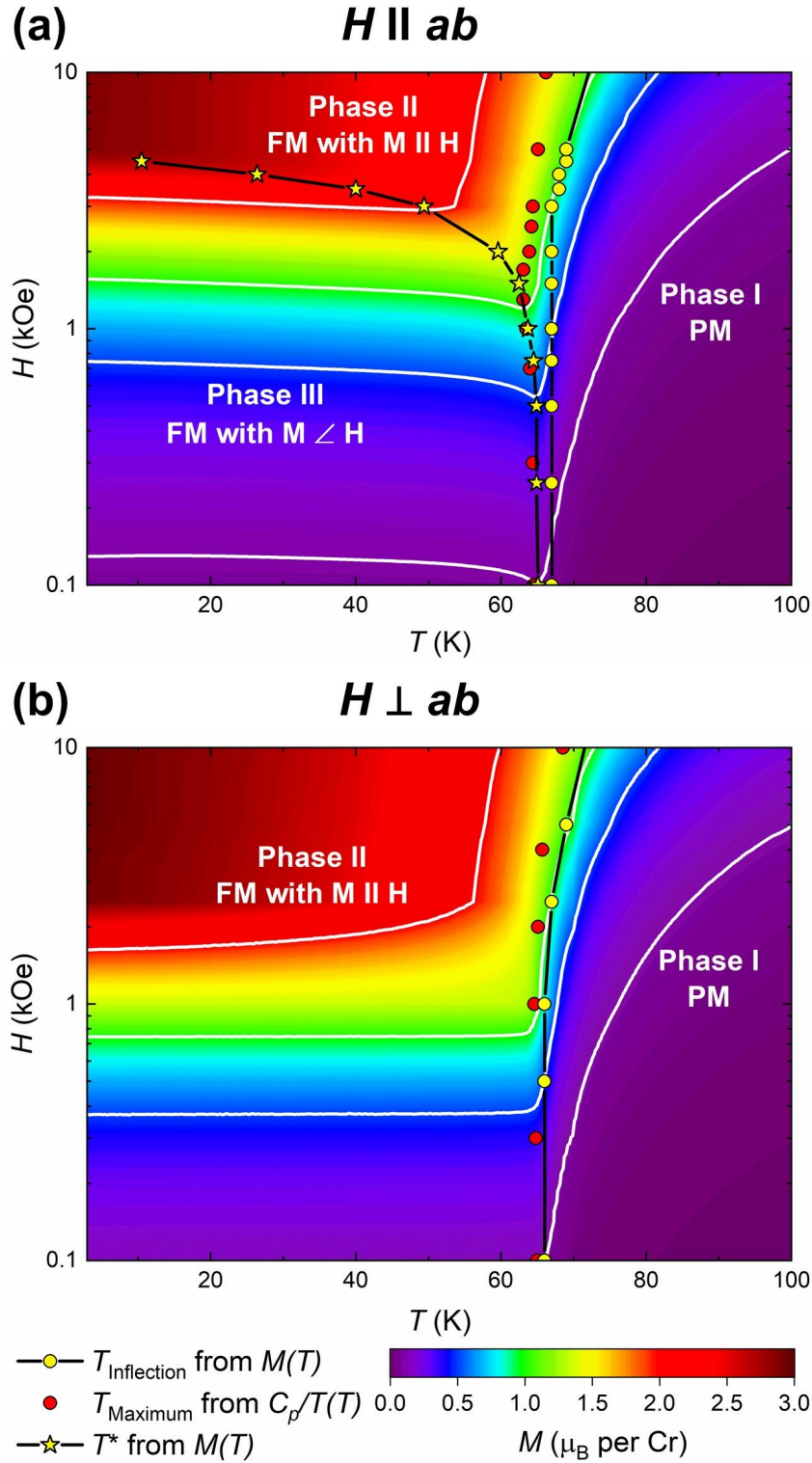


Fig. 5.11.: Low-field magnetic phase diagram of $\text{Cr}_2\text{Ge}_2\text{Te}_6$ for (a) $H \parallel ab$ and (b) $H \perp ab$, where Phase I is the paramagnetic state; Phase II is the ferromagnetic state with $M \parallel H$; Phase III only for $H \parallel ab$ is the ferromagnetic state with $M \perp H$ due to the interplay between $K_{U,\text{eff}}$, H and T . For both phase diagrams iso-magnetization lines at $0.1 \mu_B$, $0.5 \mu_B$, $1 \mu_B$ and $2 \mu_B$ are shown in white. The legend and the color scale at the bottom are applicable to both phase diagrams. Note that the magnetization shown in the phase diagrams is only the magnetization component parallel to H .

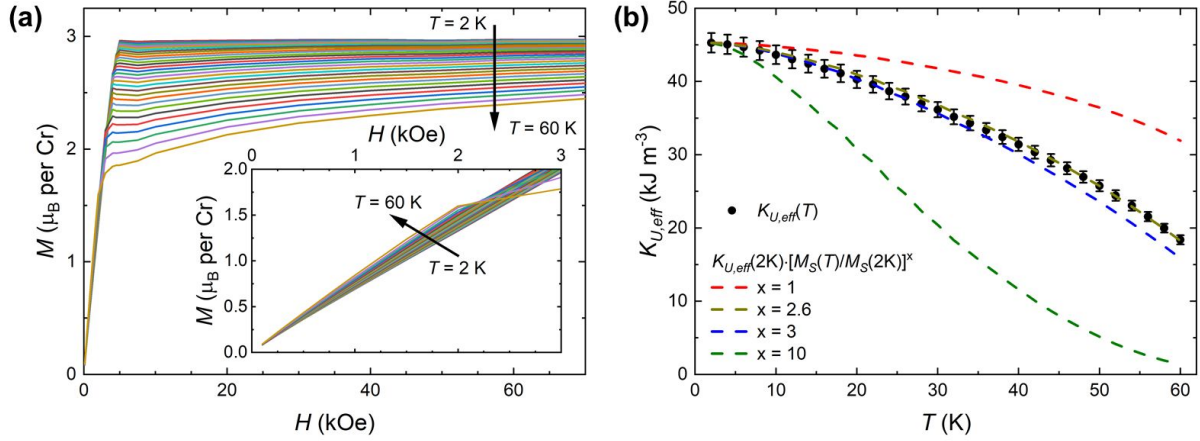


Fig. 5.12.: (a) Isothermal magnetization for $H \parallel ab$ in a range from 2 K to 60 K in 2 K steps extracted from the corresponding magnetic phase diagram. The inset shows a zoomed-in view of the low field regime. (b) Thermal evolution of the effective magnetic anisotropy constant $K_{U,\text{eff}}$ (black points) and the expected scaling of $K_{U,\text{eff}}$ according to the power law behaviour described in Eq. 5.5 using the exponents 1, 2.6, 3 and 10 (dashed lines).

ing the magnetic phase diagram for $H \parallel ab$ to estimate $H^*(1.8 \text{ K})$ explains why no anomaly could be resolved in the corresponding isothermal magnetization in Fig. 5.7, as mentioned before. $H^*(1.8 \text{ K})$ is estimated to be in the range of 4.5–4.7 kOe which is close to the saturation magnetization at this temperature. Consequently the slope of the $M(H)$ curve significantly changes in this field range and a separate anomaly corresponding to the signature of Phase III is not resolved.

Besides the low temperature/low field regime (Phase III) which is separated from the rest of the phase diagram by T^* , both phase diagrams resemble each other. This is best illustrated by the course of the iso-magnetization lines outside of Phase III. Consequently, the magnetization in Phase I and II is considered as isotropic and consequently the direction of the magnetization is parallel to the field for $T^* < T < T_C$ as seen for $H \perp ab$ (Phase II).

Thermal Evolution of the Effective Magnetocrystalline Anisotropy

To be able to describe this peculiar magnetization behavior, a temperature dependent magnetic anisotropy has to be taken into account. The magnetocrystalline anisotropy is caused by the underlying crystallographic lattice which is connected to the electronic spins *via* the spin-orbit coupling. As such, the magnetocrystalline anisotropy constant K_U is considered as a material constant which itself is independent of temperature and field.

However, many ferromagnets (*e.g.* Fe, Co and Ni) exhibit a temperature dependence of the magnetocrystalline anisotropy constant on the macroscopic level. This observation can be understood based on the theory of Zener [188] which describes the effect of temperature fluctuations on the anisotropy of the magnetization. According to his work, temperature leads to independent random fluctuations of local magnetization directions. In turn, this leads to an effective reduction of both macroscopic magnetization and anisotropy in the system. How-

ever, on a local scale the magnetization and magnetic anisotropy are temperature independent. To differentiate between the local temperature independent and the global temperature dependent magnetic anisotropy, $K_{\text{U,eff}}$ is introduced as an effective anisotropy constant which includes the effect of thermal fluctuations on a macroscopic scale and its interplay with the temperature independent K_{U} .

To extract experimental values of $K_{\text{U,eff}}$ at different temperatures, isothermal magnetization curves were reconstructed from the magnetic phase diagram for $H \parallel ab$ in the range of 2 K to 60 K, as shown in Fig. 5.12(a). Based on the aforementioned procedure of estimating the magnetocrystalline anisotropy constant K_{U} from the field dependent evolution of the magnetization using Eq. 5.4, the thermal evolution of $K_{\text{U,eff}}$ shown in Fig. 5.12(b) was obtained.

As both the macroscopic magnetization and anisotropy are affected by thermal fluctuations, a proportionality between their evolution as function of temperature can be expected. According to the theory by Callen and Callen [189], this proportionality can be expressed by a power law behavior as shown in Eq. 5.5.

$$\frac{K_{\text{U,eff}}(T)}{K_{\text{U}}} = \left[\frac{M_{\text{S}}(T)}{M_{\text{s}}} \right]^{\frac{l(l+1)}{2}}. \quad (5.5)$$

Hereinafter, the approximations $K_{\text{U}} \approx K_{\text{U,eff}}(2\text{ K})$ and $M_{\text{s}} \approx M_{\text{S}}(2\text{ K})$ are used. In the case of uniaxial anisotropy $l = 2$ and an exponent of 3 are expected, while for cubic anisotropy $l = 4$ and an exponent of 10 are found.

Fig. 5.12 shows the expected evolution of $K_{\text{U,eff}}(T)$ given by the power law dependence of the saturation magnetization in Eq. 5.5 for exponents 1, 2.6, 3 and 10. The observed temperature dependence of $K_{\text{U,eff}}$ at low temperatures shows a good agreement with the Callen-Callen power law with an exponent of 3, which is expected for purely uniaxial anisotropy. However, at higher temperatures the exponent deviates from 3 towards 2.6. For the exponents 1 and 10 the power law behavior does not follow $K_{\text{U,eff}}(T)$ and therefore direct scaling of the saturation magnetization with $K_{\text{U,eff}}$ as well as cubic anisotropy can be ruled out.

The observed deviation of the exponent from a value of 3 may be attributed to higher order anisotropy contributions. Such contributions need to be considered even in some elemental ferromagnets like nickel [190] or Fe thin-films [191, 192]. One may speculate that materials with more complex crystal structures like $\text{Cr}_2\text{Ge}_2\text{Te}_6$ are more prone to exhibit higher order anisotropic contributions. Another contribution that can influence the temperature dependence of the magnetocrystalline anisotropy is the surface anisotropy. This was demonstrated for example in NiFe_2O_4 nanomagnets [192]. However considering the surface-to-volume ratio, this effect should play only a secondary role in $\text{Cr}_2\text{Ge}_2\text{Te}_6$ bulk crystals compared to nanoparticles. Nevertheless, due to the thin platelet shape of the crystals the surface anisotropy can be expected to be slightly more dominant than in typical 3D crystals.

The agreement between the experimentally determined exponent with a value of 3 confirms that the magnetic anisotropy in $\text{Cr}_2\text{Ge}_2\text{Te}_6$ is uniaxial. Given the non-cubic crystal structure and the good agreement of simulations and experimental values of the angular dependence of

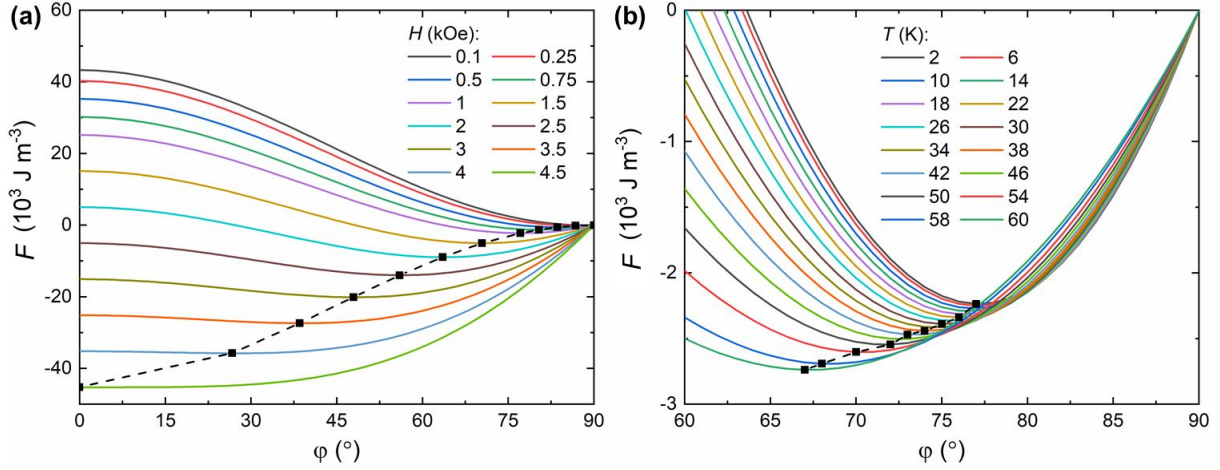


Fig. 5.13.: Evolution of the angular dependence of the free energy density $F(\varphi)$ influenced by (a) varying external magnetic fields at a constant temperature of 2 K and (b) varying temperatures at a constant magnetic field of 1 kOe. For both (a) and (b), $\theta = 90^\circ$ meaning $H \parallel ab$. The black points mark the minimum of $F(\varphi)$ for each field and temperature. The black dashed lines are guide for the eyes.

the resonance field in FMR using an uniaxial model in our previous work [179], this behavior is in accordance with previous work. Therefore, also the observed reduction of the magnetic anisotropy as function of temperature seems to be reliable.

It should be noted that Khan *et al.* also reported a temperature dependent $K_{U,\text{eff}}$ for $\text{Cr}_2\text{Ge}_2\text{Te}_6$ which, however, scales with an exponent 4.71 [193]. They proposed that this deviation from the expected exponent of 3 is due to the role of spin-orbit coupling from Te atoms, which is not observed in our study. Furthermore, our analysis is very similar to N. Richter *et al.* on CrI_3 [152], who also do not see a significant role of spin-orbit coupling on the temperature dependent $K_{U,\text{eff}}$ values in their compound.

Influence of External Fields and Temperature on the Magnetization Direction

Using Eq. 5.1 it is now possible to calculate the dependence of the free energy density F on the angle φ between the direction of H and M for $\text{Cr}_2\text{Ge}_2\text{Te}_6$ for any given field and in the temperature range for which $K_{U,\text{eff}}(T)$ was determined. For example, this is demonstrated for several external fields up to 4.5 kOe at 2 K in Fig. 5.13(a) and for several temperatures up to 60 K for an external field of 1 kOe in Fig. 5.13(b) ($H \parallel ab$ in both scenarios).

As mentioned before, the energetically favoured angle φ corresponds to a minimum of the free energy density F . Accordingly, Fig. 5.13(a) shows the typical field dependence of the magnetization direction, with $M \parallel$ easy axis at zero field ($\theta = \angle(H, \text{easy axis}) = 90^\circ$ and $\varphi = \angle(M, H) = 90^\circ$) and $M \parallel H$ at sufficiently strong external fields ($\theta = 90^\circ$ and $\varphi = 0^\circ$). However due to the thermal evolution of $K_{U,\text{eff}}$, the magnetization direction also changes as function of temperature under constant fields, as seen in Fig. 5.13(b). By increasing the temperature and in turn decreasing $K_{U,\text{eff}}$, M rotates towards the direction of the external field. As SQUID magnetometry is only sensitive to the magnetization component parallel to

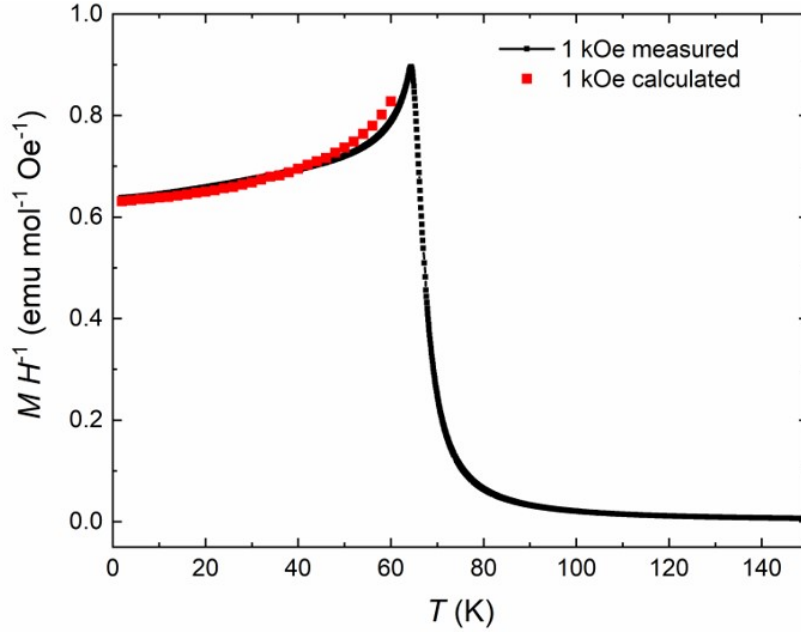


Fig. 5.14.: Comparison between the calculated ab -component of the magnetization vector normalized for the applied field (red dots) and the measured $MH^{-1}(T)$ behavior (black line) for an external field of 1 kOe applied parallel to the ab -plane.

Table 5.4.: Comparison between K_U for different (quasi-)2D honeycomb ferromagnets. Please note that for CrBr_3 and CrI_3 K_U was extracted from isothermal magnetization data at $T = 5$ K while for $\text{Cr}_2\text{Ge}_2\text{Te}_6$ data at $T = 1.8$ K was used.

Compound	K_U [kJ/m ³]	Reference
CrBr_3	86 (± 6)	N. Richter <i>et al.</i> [152]
CrI_3	301 (± 50)	N. Richter <i>et al.</i> [152]
$\text{Cr}_2\text{Ge}_2\text{Te}_6$	47 (± 1)	this work

the applied field, this change of the magnetization direction yields an increase of the measured magnetization in the ferromagnetic state of $\text{Cr}_2\text{Ge}_2\text{Te}_6$ increasing the temperature.

Based on the thermal evolution of φ and the known magnitude of the magnetization vector (M_s), the thermal evolution of the magnetization component parallel to the external field is calculated for $H \parallel ab = 1$ kOe up to 60 K and compared to the respective measurement (see Fig. 5.14). Overall, a good agreement between the experimental and the calculated $M(T)$ behavior is obtained. This demonstrates that the downturn in the thermal evolution of the magnetization for $H \parallel ab$ is caused by a continuous rotation of the magnetization vector as a result of an interplay between the magnetocrystalline anisotropy, temperature and external magnetic field.

A similar scenario was already proposed to explain a similar downturn of the transverse magnetization upon cooling below the Curie temperature in other ferromagnets: the structurally related quasi two-dimensional ferromagnets CrX_3 ($X = \text{Br}, \text{I}$) [152] and the heavy Fermion ferromagnet URhGe [194]. For CrX_3 ($X = \text{Br}, \text{I}$) a similar analysis of $K_{U,\text{eff}}(T)$ was

performed [152]. While the magnetocrystalline anisotropy constants of the chromium halides are larger than the one found for $\text{Cr}_2\text{Ge}_2\text{Te}_6$ (shown in Table 5.4), their temperature dependence is also well described by exponents according to an uniaxial anisotropy. In the case of URhGe, the tilting of the magnetic moment in between the field direction and the easy magnetization axis was directly observed by neutron diffraction [195] and NMR [196]. For URhGe a Ginzburg Landau description of the anisotropic ferromagnet proposed by V. Mineev [197] reproduced the downturn of the magnetization and could possibly also be a promising model for a simple description of the low-field magnetic properties of $\text{Cr}_2\text{Ge}_2\text{Te}_6$. Another material that exhibits a similar anomaly in the temperature dependent magnetization is PbMnBO_4 as reported by A. Pankrats *et al.* [198], where a similar interplay between the temperature dependence of the magnetic anisotropy and the before mentioned anomaly based on the temperature dependence of the anisotropy fields was concluded.

5.1.4. Analysis of the Critical Behavior

The nature of the magnetic interaction is another magnetic property closely related to the magnetic anisotropy, which is as well of crucial interest for the fundamental understanding and for future applications of low dimensional (ferro-)magnetism. One possibility to investigate this property in a system based on magnetic measurements is *via* the critical exponents, which describe the magnetic behavior in the vicinity of a magnetic phase transition (as introduced in Sect. 1.2.6).

Lin *et al.* [184], Liu and Petrovic [183] and Liu *et al.* [199] all reported slightly different values for the critical exponents of $\text{Cr}_2\text{Ge}_2\text{Te}_6$, indicating a magnetic nature in the range of the 2D Ising model to the tricritical mean field model. Due to those differences in literature, it is of interest which exponents are obtained from the crystals investigated in this work. This additional study allows for a comprehensive picture of the magnetic anisotropy and the nature of the magnetic interactions based on the same crystals to ensure the best possible comparability. Furthermore, the critical exponents may give further insight in the dimensionality of the magnetic interactions in $\text{Cr}_2\text{Ge}_2\text{Te}_6$. In the context of different dimensionalities in the magnetic interactions of the two structurally closely related compounds $\text{Cr}_2\text{Si}_2\text{Te}_6$ (2D Ising; [200]) and CrI_3 (3D Ising; [201]), this may be of importance to understand the magnetism in $\text{Cr}_2\text{Ge}_2\text{Te}_6$.

The investigation of the critical behavior and extraction of critical exponents is generally based on the thermal evolution of the field dependent magnetization in the vicinity of the critical temperature T_C . Arrott found that plots of M^2 against H/M yield a set of parallel lines in the high field regime with the line corresponding to the measurement at T_C passing through the origin (Arrott plot) [202]. The other lines either intersect the positive part of the M^2 axis yielding $M_s(T)$ or the H/M axis yielding $\chi_0^{-1}(T)$. However, this is only the case for systems following the mean field model with the critical exponents $\beta = 0.5$ and $\gamma = 1$.

In this line to investigate the nature of the magnetic phase transition in $\text{Cr}_2\text{Ge}_2\text{Te}_6$, a set of isotherms in the temperature range of 55–75 K (1 K steps for 55–60 K and 72–75 K; 0.5 K steps for 60–72 K) was extracted from the magnetic phase diagram with $H \parallel ab$ (see Fig. 5.15(a)).

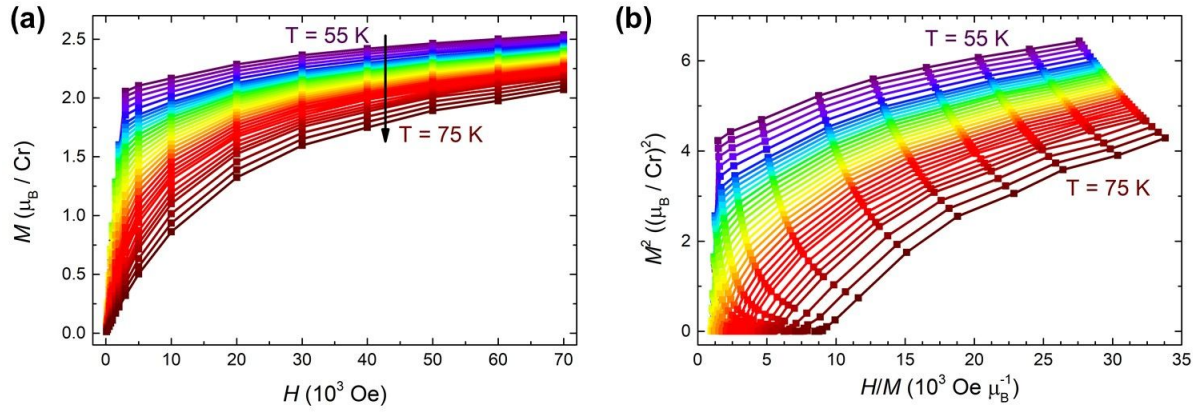


Fig. 5.15.: (a) Isothermal magnetization of $\text{Cr}_2\text{Ge}_2\text{Te}_6$ in the vicinity of the critical temperature (for detailed temperatures see corresponding section) extracted from the magnetic phase diagram for $H \parallel ab$. (b) Arrott plot of the isothermal magnetization of $\text{Cr}_2\text{Ge}_2\text{Te}_6$ shown in (a).

The Arrott plot of these isotherms does not show the expected linearity but still a significant curvature, as shown in Fig. 5.15(b), indicating that the critical behavior of $\text{Cr}_2\text{Ge}_2\text{Te}_6$ cannot be sufficiently described in terms of the mean field model.

Banerjee proposed that the order of a magnetic transition can be estimated from the sign of the slope of the curves in an Arrott plot [203]. Negative slopes correspond to a first order while positive slopes correspond to a second order transition. Accordingly, the magnetic phase transition of $\text{Cr}_2\text{Ge}_2\text{Te}_6$ can be characterized as a second order phase transition in agreement with the results from specific heat measurements discussed before and literature [183].

Although Arrott plots are specific to the mean field model with its corresponding critical exponents, the fundamental concept can be generalized for any set of critical exponents in modified Arrott plots. The Arrott-Noaks equation of state (see Eq. 5.6) describes this generalized approach [204]. Accordingly, plotting a set of isotherms of any system in the vicinity of T_C as $M^{1/\beta}$ vs. $(H/M)^{1/\gamma}$ (with β and γ being suitable critical exponents for the system) yields a set of parallel lines with the aforementioned properties of the Arrott plot.

$$(H/M)^{1/\gamma} = a\varepsilon + bM^{1/\beta} \quad (5.6)$$

Considering the strong easy axis magnetic anisotropy that is observed in the magnetic studies of $\text{Cr}_2\text{Ge}_2\text{Te}_6$ in Sect. 5.1.3 as well as in literature [37, 179, 181] together with quasi-2D layered crystal structure, the 2D-Ising model with $\beta = 0.125$ and $\gamma = 1.75$ could be expected to be suitable to describe the critical behaviour of $\text{Cr}_2\text{Ge}_2\text{Te}_6$ well. However as shown in Fig. 5.16(a), using these values for β and γ does not yield lines in the corresponding modified Arrott plot indicating that the 2D-Ising model is not a sufficient model for the critical behavior of $\text{Cr}_2\text{Ge}_2\text{Te}_6$.

Nevertheless, these values can be used as starting values for an iterative, self-consistent method for the determination of critical exponents based on modified Arrott plots [205]. Linear extrapolations of the high field regime yield $M_s(T)$ from the intercepts with (the positive part

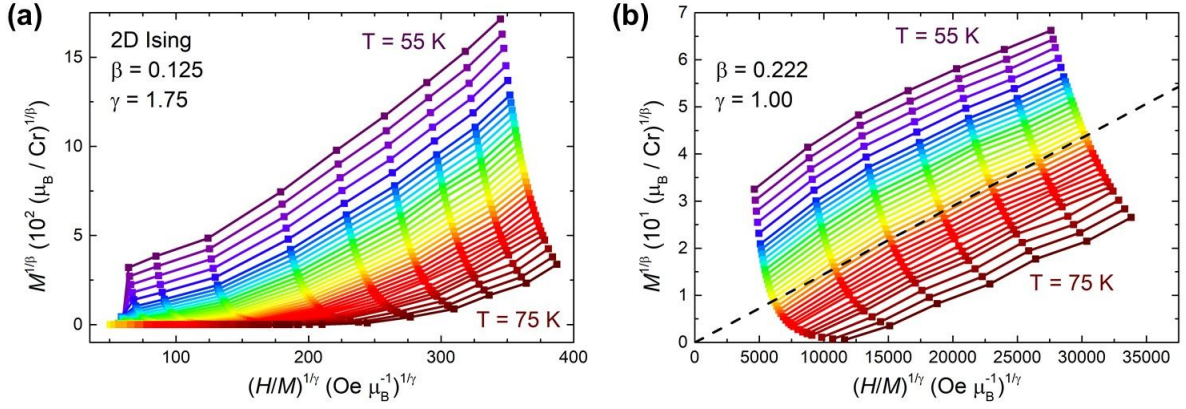


Fig. 5.16.: Modified Arrott plots with (a) $\beta = 0.125$ and $\gamma = 1.75$ (corresponding to the 2D Ising model) as well as (b) $\beta = 0.222$ and $\gamma = 1.00$ for the isotherms of $\text{Cr}_2\text{Ge}_2\text{Te}_6$. The black dashed line in (b) corresponds to the expected isotherm at T_C .

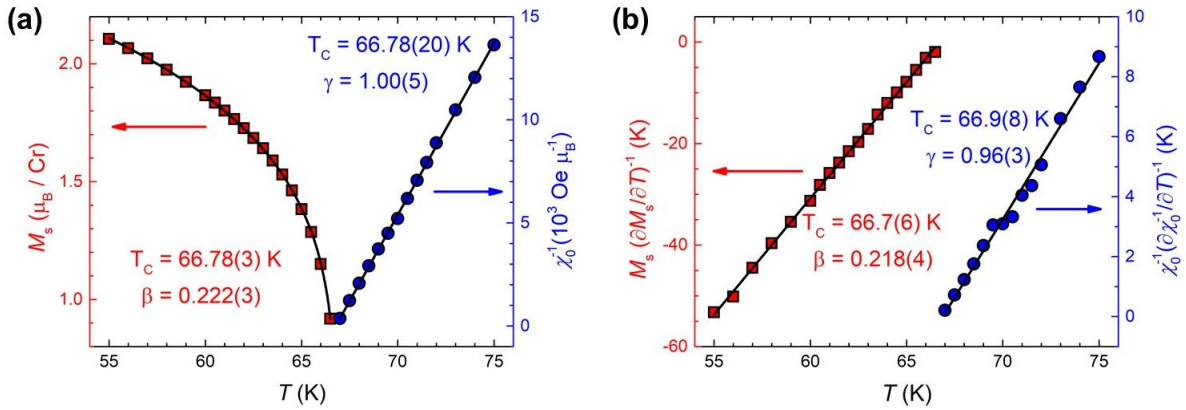


Fig. 5.17.: (a) Evolution of M_s (left axis, red squares) and χ_0^{-1} (right axis, blue circles) as function of temperature extracted from the modified Arrott plot with $\beta = 0.222$ and $\gamma = 1.00$ shown in Fig. 5.16(b). The black lines are fits of M_s and χ_0^{-1} according to Eq. 1.35 and Eq. 1.36, respectively. (b) Kouvel-Fisher plot: Thermal dependence of $M_s(T)(\partial M_s(T)/\partial T)^{-1}$ (left axis, red squares) and $\chi_0^{-1}(\partial \chi_0^{-1}(T)/\partial T)^{-1}$ (right axis, blue circles). The black lines are linear fits in accordance with Eq. 5.7 and Eq. 5.8.

of) the $M^{1/\beta}$ axis and $\chi_0^{-1}(T)$ from the intercepts with $(H/M)^{1/\gamma}$ axis. Based on Eq. 1.35 and Eq. 1.36, new values for β and γ as well as for T_C can be obtained from $M_s(T)$ and $\chi_0^{-1}(T)$, respectively. A new modified Arrott plot is constructed based on the new values of β and γ , which again is used to extract $M_s(T)$ and $\chi_0^{-1}(T)$. This procedure is repeated until constant values of β and γ are obtained.

Following this method, the final modified Arrott plot (see Fig. 5.16(b)) is obtained for $\beta = 0.222$ and $\gamma = 1.00$. From this plot the final $M_s(T)$ and $\chi_0^{-1}(T)$, shown in Fig. 5.17(a), are extracted. Fitting Eq. 1.35 and Eq. 1.36 to these thermal dependencies yields $\beta = 0.222(3)$ and $T_C = 66.78(3)$ K as well as $\gamma = 1.00(5)$ and $T_C = 66.78(20)$ K, respectively.

Another method to determine critical exponents of a magnetic transition is described by Kouvel and Fisher [206]. According to them, $M_s(T)(\partial M_s(T)/\partial T)^{-1}$ and $\chi_0^{-1}(\partial \chi_0^{-1}(T)/\partial T)^{-1}$ evolve linearly in temperature with slopes of $1/\beta$ and $1/\gamma$ as described by Eq. 5.7 and Eq. 5.8.

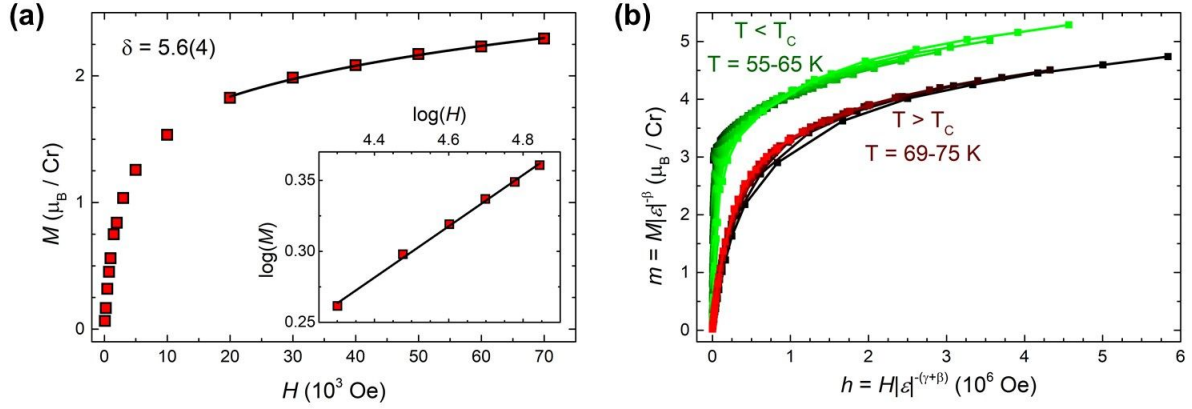


Fig. 5.18.: (a) Isothermal magnetization of $\text{Cr}_2\text{Ge}_2\text{Te}_6$ at 67 K (red squares) and corresponding fit of the high field region according to Eq. 1.37 (black line). The inset shows the high field region with fit on a log-log scale. (b) Scaling plot of the renormalized magnetization m against renormalized field h . All isotherms measured below T_c are shown in green, while all isotherms measured above T_c are shown in red.

$$\frac{M_s(T)}{\partial M_s(T)/\partial T} = \frac{T - T_c}{\beta} \quad (5.7)$$

$$\frac{\chi_0^{-1}(T)}{\partial \chi_0^{-1}(T)/\partial T} = \frac{T - T_c}{\gamma} \quad (5.8)$$

Subsequently, Fig. 5.17(b) shows $M_s(T)(\partial M_s(T)/\partial T)^{-1}$ and $\chi_0^{-1}(\partial \chi_0^{-1}(T)/\partial T)^{-1}$ as function of temperature for $\text{Cr}_2\text{Ge}_2\text{Te}_6$. Overall, a linear evolution is observed for both measures. Corresponding fits yield $\beta = 0.218(4)$ and $T_c = 66.7(6)$ K as well as $\gamma = 0.96(3)$ and $T_c = 66.9(8)$ K in excellent agreement with the critical exponents and T_c extracted from the modified Arrott plot.

The critical exponent δ is obtained from the magnetic isotherm at T_c as seen in Eq. 1.37. To obtain a highly reliable value of δ , a separate measurement of the isotherm exactly at T_c with a high data density in the high fields region is desired. However, in lack of such a measurement, the isotherm at 67 K is used to estimate a value of δ in a first approximation, as shown in Fig. 5.18(a). Accordingly, $\delta = 5.6(4)$ is deduced from the experimental data.

Another way of obtaining a value for the exponent δ is given by the Widom scaling relation (given in Eq. 5.9), which relates the critical exponents β , γ and δ [207]. Consequently using the values of β and γ obtained from the modified Arrott and the Kouvel-Fisher plots, $\delta = 5.50(23)$ and $\delta = 5.40(16)$ can be calculated, respectively. These values of δ compare well to δ obtained from $M(H)$ at 67 K.

$$\delta = 1 + \frac{\gamma}{\beta} \quad (5.9)$$

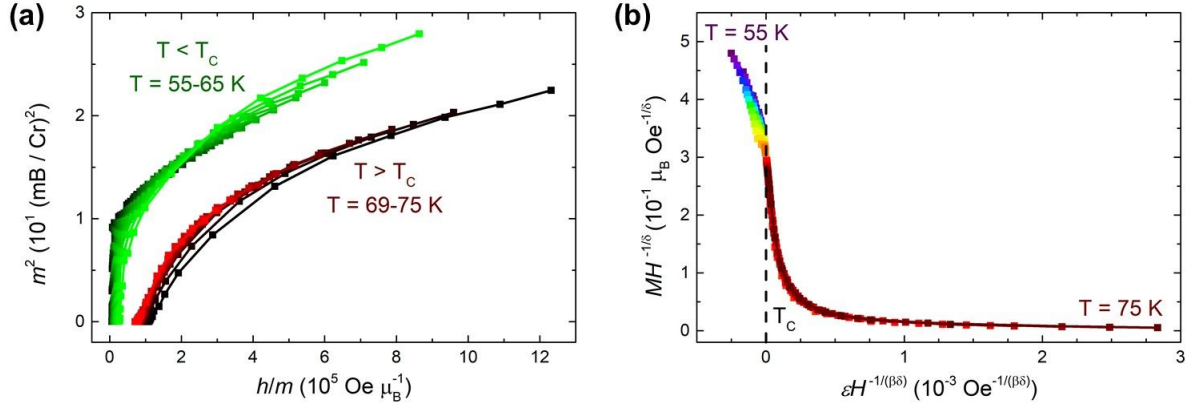


Fig. 5.19.: (a) Renormalized magnetization m and field h plotted as m^2 against h/m as proposed by Kaul [208]. All isotherms measured below T_C are shown in green, while all isotherms measured above T_C are shown in red. (b) Universal scaling of all isotherms in agreement with the reformulated scaling equation of state (Eq. 5.10 for $\beta = 0.222$ and $\delta = 5.50$).

The reliability of the obtained exponents is verified using Eq. 1.39. As mentioned before, suitable values of β , γ and δ are supposed to yield two distinct universal behaviors for the renormalized magnetic equation of state, one below and one above the critical temperature. This is seen in Fig. 5.18(b) showing the renormalized magnetization $m = M|\varepsilon|^{-\beta}$ as function of the renormalized field $h = H|\varepsilon|^{-(\gamma+\beta)}$ for $\beta = 0.222$ and $\gamma = 1.00$. Two distinct trends can be observed, one followed by all isotherms measured at temperatures below T_C (green) and another one followed by all isotherms measured above T_C (red).

A more rigorous method to validate the reliability of these critical exponents is by plotting m^2 against h/m [208]. Again all isotherms measured below (and all measured above) T_C are expected to fall onto one universal curve, which is the case for these exponents as seen in Fig. 5.19(a).

$$\frac{H}{M^\delta} = k\left(\frac{\varepsilon}{M^{1/\beta}}\right) \quad (5.10)$$

The scaling equation of state can be also rewritten as given in Eq. 5.10 with one universal scaling function $k(x)$ [208]. In accordance with Eq. 5.10, plotting $MH^{-1/\delta}$ against $\varepsilon H^{-1/\beta\delta}$ yields one universal curve followed by all isotherms, as shown in Fig. 5.19(b). Consequently, the obtained critical exponents are to be considered reliable and self-consistent.

Table 5.5 summarizes the critical exponents extracted *via* several methods and compares them to theoretical expected critical exponents for various models as well as to critical exponents for $\text{Cr}_2\text{Ge}_2\text{Te}_6$ from literature. Overall, the values extracted in this work compare well with the critical exponents obtained from the tricritical mean field model. This finding is in agreement with Lin *et al.* [184] reporting similar exponents.

A generic feature of all compounds that are magnetically well described by the tricritical mean field model is a tricritical point that separates a regime with a first order from a regime with a second order (ferro-)magnetic phase transition [72]. For example, in the helimagnet

Table 5.5.: Critical exponents of $\text{Cr}_2\text{Ge}_2\text{Te}_6$ extracted *via* several methods (top) compared to different theoretical models (mid) as well as critical exponents for $\text{Cr}_2\text{Ge}_2\text{Te}_6$ from literature (bottom). calc = calculated values using the Widom scaling relation (Eq. 5.9).

Compound/Model	Reference	Technique	T_c (K)	β	γ	δ
$\text{Cr}_2\text{Ge}_2\text{Te}_6$	This work	Mod. Arrott	66.78(12)	0.222(3)	1.00(5)	5.50(23) ^{calc}
		Kouvel-Fisher	66.8(7)	0.218(4)	0.96(3)	5.40(16) ^{calc}
		Critical isotherm				5.6(4)
Tricritical mean field	[203]			0.25	1	5
2D Ising	[209]			0.125	1.75	15
Mean field	[202, 208]	Theory		0.5	1	3
3D Heisenberg	[202, 208]		0.365	1.386	4.8	
3D XY	[202, 208]		0.345	1.316	4.81	
3D Ising	[202, 208]		0.325	1.24	4.82	
$\text{Cr}_2\text{Ge}_2\text{Te}_6$	[184]	Mod. Arrott	67.93(5)	0.242(6)	0.985(3)	5.070(6) ^{calc}
		Kouvel-Fisher	67.90(6)	0.240(6)	1.000(5)	5.167(6) ^{calc}
		Critical isotherm				5.032(5)
	[183]	Mod. Arrott	62.65(6)	0.196(3)	1.32(5)	7.73(15) ^{calc}
		Kouvel-Fisher	62.70(7)	0.200(3)	1.28(3)	7.40(5) ^{calc}
	[199]	Critical isotherm				7.96(1)
	[199]	Magn. entropy change	66.4(3)	0.177(9)	1.746(8)	10.869(5) ^{calc}

MnSi [210] or in some manganites [211–213], all exhibiting critical exponents in agreement with the tricritical model, such behaviour is observed. This is in stark difference to $\text{Cr}_2\text{Ge}_2\text{Te}_6$ for which such a peculiar magnetic behaviour is neither observed in the magnetic phase diagram (see Fig. 5.11) nor reported in literature.

Consequently, another interpretation of the experimentally obtained critical exponents of $\text{Cr}_2\text{Ge}_2\text{Te}_6$ appears to be more likely. The investigation of the magnetocrystalline anisotropy (see Sect. 5.1.3) yields a strong easy axis anisotropy in $\text{Cr}_2\text{Ge}_2\text{Te}_6$, in general agreement with the Ising model. For the isostructural compound $\text{Cr}_2\text{Si}_2\text{Te}_6$, which as well exhibits Ising-type anisotropic magnetization [214], critical exponents well in agreement with the 2D Ising model are reported [200]. Comparing the structural details of these compounds shows that the van der Waals gap between layers shrinks from 3.42 Å for $\text{Cr}_2\text{Si}_2\text{Te}_6$ [215] to 3.36 Å for $\text{Cr}_2\text{Ge}_2\text{Te}_6$ (based on the structural parameters introduced in Sect. 5.1.2 Table 5.2 and Table 5.3) and the height of a layer increases from 3.47 Å for the former to 3.50 Å for the latter. While the increase in the height of the layer goes in hand with the increase of the atomic radius from Si (0.26 Å) to Ge (0.39 Å) [136], the shrinkage of the van der Waals gap may be rather understood as a result of stronger interactions between layers and subsequently a more 3D structure.

In line of this argumentation and in agreement with the Ising anisotropy, the critical exponents of $\text{Cr}_2\text{Ge}_2\text{Te}_6$ may be understood as in between the 2D Ising and 3D Ising model with a non-negligible interlayer interaction. The critical exponents reported by Liu and Petrovic [183] as well as Liu *et al.* [199] are as well found in between the theoretical values obtained from the 2D Ising and 3D Ising model and, in this respect, are in agreement with the exponents extracted here.

5.2. $\text{In}_2\text{Ge}_2\text{Te}_6$

The synthesis and characterization of $\text{In}_2\text{Ge}_2\text{Te}_6$ was first reported in the PhD thesis of S. Seidlmayer in 2009 [51]. By a solid state reaction of a stoichiometric mixture of $\text{In} : \text{Ge} : \text{Te} = 1 : 1 : 3$ at 450°C , a grey powder could be obtained. From this powder, small black crystals could be extracted which were sufficient for a scXRD study and subsequent solution of the crystal structure. $\text{In}_2\text{Ge}_2\text{Te}_6$ was reported as isostructural to $\text{Cr}_2\text{Ge}_2\text{Te}_6$ with a trigonal unit cell in the space group $R\bar{3}$. A (direct) bandgap of 1.6 eV was determined optically. In 2017, Lefèvre *et al.* reported on the low thermal conductivity in $\text{In}_2\text{Ge}_2\text{Te}_6$ [177]. For this study, small crystals from solid state synthesis were used for scXRD and polycrystalline $\text{In}_2\text{Ge}_2\text{Te}_6$ was used for the thermoelectric and transport experiments.

Until now, there are no reports on the growth of macroscopic $\text{In}_2\text{Ge}_2\text{Te}_6$ crystals. Furthermore, the magnetic properties as well as the specific heat capacity of $\text{In}_2\text{Ge}_2\text{Te}_6$ were not investigated yet. Although diamagnetism is expected from the lack of unpaired electrons in $\text{In}_2\text{Ge}_2\text{Te}_6$, experimental confirmation together with the diamagnetic susceptibility is not available in literature. If diamagnetic behaviour is confirmed for $\text{In}_2\text{Ge}_2\text{Te}_6$, the corresponding specific heat is supposed to be only given by the phononic contribution. As both $\text{In}_2\text{Ge}_2\text{Te}_6$ and $\text{Cr}_2\text{Ge}_2\text{Te}_6$ exhibit a significant electronic band gap, the electronic contribution to the specific heat vanishes. Subsequently, it can be expected that the magnetic entropy change ΔS_{mag} of $\text{Cr}_2\text{Ge}_2\text{Te}_6$ can be estimated using the specific heat of the isostructural $\text{In}_2\text{Ge}_2\text{Te}_6$ as an experimental estimate of the phononic contribution to the specific heat of $\text{Cr}_2\text{Ge}_2\text{Te}_6$.

For the single crystal growth of $\text{In}_2\text{Ge}_2\text{Te}_6$ by the flux growth technique, the growth procedure was adopted from the single crystal growth of $\text{Cr}_2\text{Ge}_2\text{Te}_6$ (as discussed in Sect. 5.1.1) and temperatures were derived from the liquidus projection of the germanium-indium-tellurium ternary phase diagram. This is discussed and the corresponding growth experiment is presented in Sect. 5.2.1. The crystals obtained from this growth experiment are characterized in Sect. 5.2.2. In Sect. 5.2.3 the magnetic properties of $\text{In}_2\text{Ge}_2\text{Te}_6$ are presented. Finally in Sect. 5.2.4, the thermal evolution of the specific heat is shown and compared to the expected evolution for only phononic contributions to the specific heat obtained from the Debye model.

5.2.1. Crystal Growth

The liquidus projection of the germanium–indium–tellurium ternary phase diagram³, as reported by Zargarova and Akperov [217], does not show $\text{In}_2\text{Ge}_2\text{Te}_6$ as a congruently melting phase. If the target phase exists, it must be assumed that it melts incongruently. Accordingly, a self flux growth is a viable single crystal growth technique, in similarity to the growth of $\text{Cr}_2\text{Ge}_2\text{Te}_6$ in Sect. 5.1.1.

³Accessed via ASM Alloy Phase Diagram Database (<http://www.asminternational.org>), Unique ID No. 990319 [216].

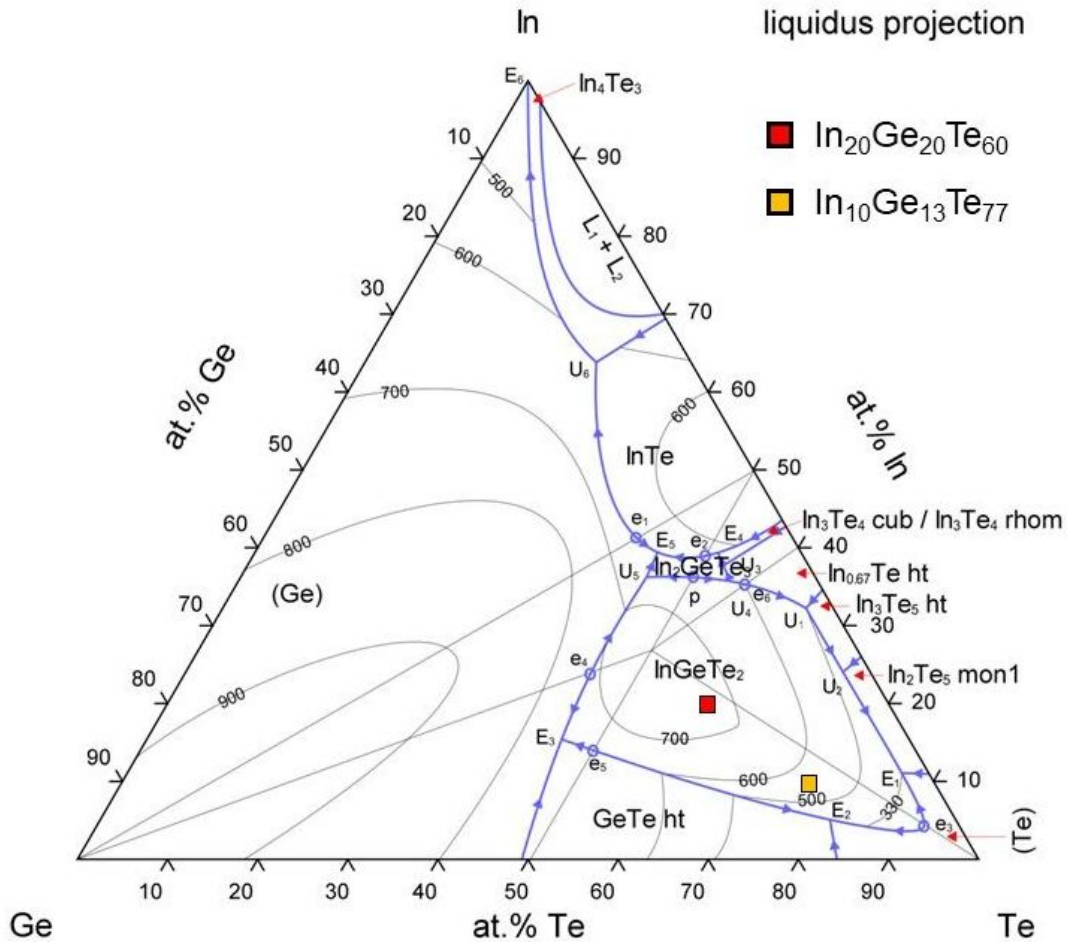


Fig. 5.20.: Liquidus projection of the Ge–In–Te ternary phase diagram as reported by Zargarova and Akperov [217] and accessed *via* the ASM Alloy Phase Diagram Database. The red square corresponds to the composition of the target phase while the yellow square corresponds to the starting composition for the self flux growth experiment.

Based on the curvature of the liquidus surface in the vicinity of In : Ge : Te = 20 at% : 20 at% : 60 at%, the optimal direction for a self flux growth attempt is in the direction of the ternary eutectic point at approximately In : Ge : Te = 5 at% : 15 at% : 80 at%. Consequently, a starting composition of In : Ge : Te = 10 at% : 13 at% : 77 at% was chosen.

A total charge of 3 g containing the respective amounts of indium (shots, MaTeck, 99.9999%), germanium (chips, Sigma Aldrich, 99.999%), and tellurium (lumps, Alfa Aesar, 99.999%) was loaded in an alumina crucible inside a quartz ampule which was then sealed under a partial atmosphere of Ar (approx. 300 mbar). The quartz ampule was placed upright in a box furnace (Nabertherm) and heated to 900 °C for 24 h followed by cooling with a rate of 1 °C/h to 450 °C. At this temperature excessive melt was centrifuged. This temperature profile is derived from the temperatures in the liquidus projection of the germanium–indium–tellurium ternary phase diagram. Shiny, well faceted crystals of up to 7 mm × 5 mm × 1 mm (e.g. in Fig. 5.21(a) and (b)) were obtained using these growth parameters.

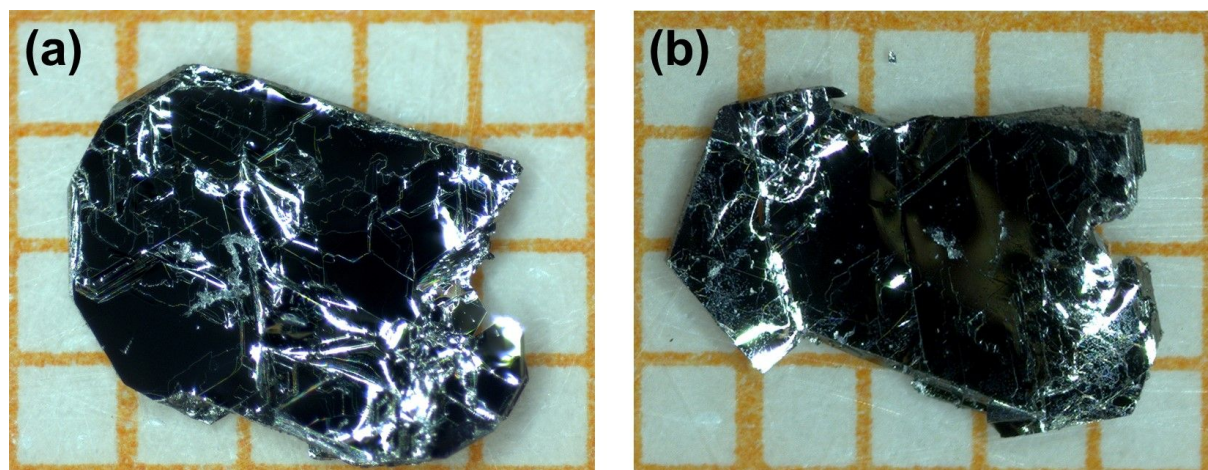


Fig. 5.21.: As grown plate-like $\text{In}_2\text{Ge}_2\text{Te}_6$ crystals obtained from the GeTe rich melt. One orange square in the background is $1\text{ mm} \times 1\text{ mm}$ for scale.

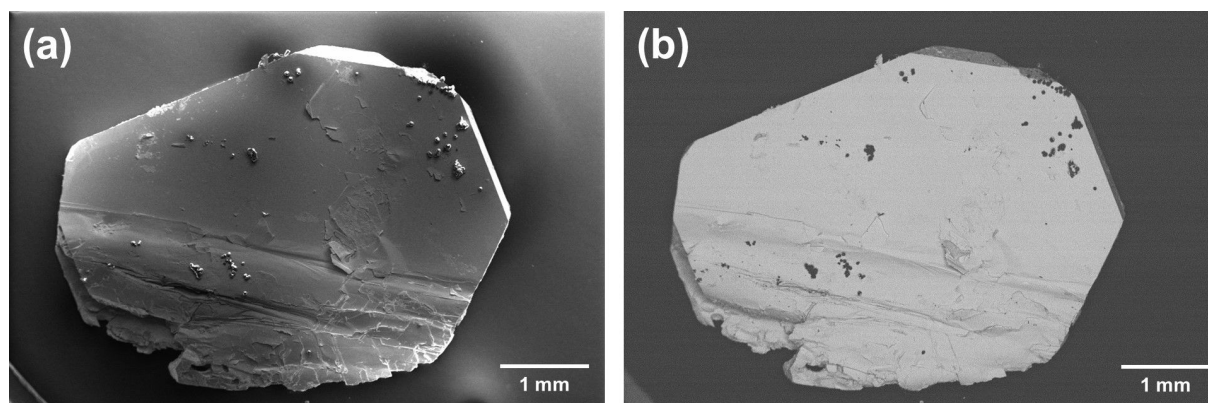


Fig. 5.22.: (a) SEM(SE) image with topographical contrast and (b) SEM(BSE) image with chemical contrast of a $\text{In}_2\text{Ge}_2\text{Te}_6$ crystal obtained from the growth experiment discussed before.

5.2.2. Characterization

Crystal Morphology and Compositional Analysis

As seen in the SEM image with topographical contrast (SE) in Fig. 5.22(a), several steps and terraces on the crystal surface hint at a layered nature of the crystallographic structure. The facet edges of the crystallographic plane shown in Fig. 5.22(a) and (b) exhibit several 120° corners indicative for the ab plane of a trigonal or hexagonal crystal structure in similarity to $\text{Cr}_2\text{Ge}_2\text{Te}_6$ (see Fig. 5.4 for comparison).

However in difference to the latter, these crystals do not only exhibit facets in a certain plane but in all directions. This suggests a more isotropic crystal growth in comparison to $\text{Cr}_2\text{Ge}_2\text{Te}_6$. The SEM image with chemical contrast (BSE) shows a homogeneous contrast of the crystal surface besides some local dark spots. These dark spots in the SEM(BSE) image can be clearly attributed to the spherical particles on top of the crystal surface seen in the corre-

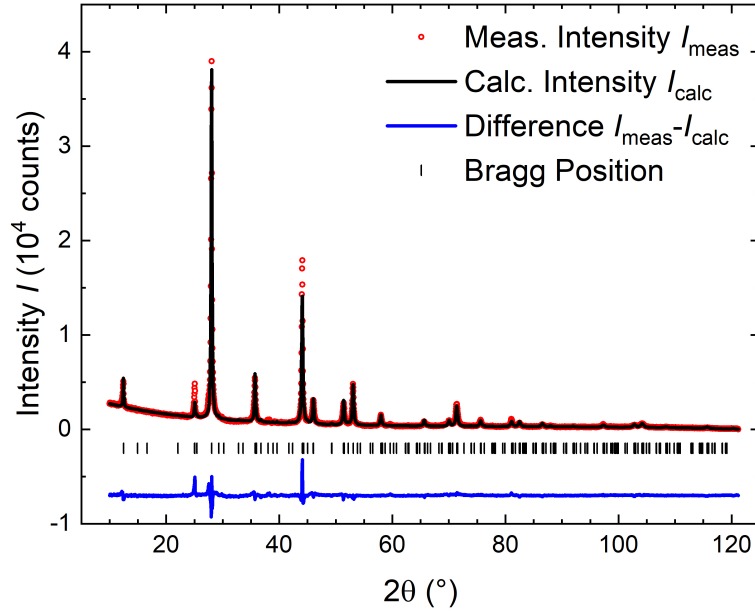


Fig. 5.23.: pXRD pattern from $\text{Cu-K}\alpha_1$ radiation (1.54059 \AA) of pulverized crystals (red dots), calculated pattern of the $R\bar{3}$ structure of $\text{In}_2\text{Ge}_2\text{Te}_6$ (black line), difference between measured and calculated intensity (blue line) and expected Bragg positions (black dots).

sponding SEM(SE) image. The otherwise uniform contrast of the SEM(BSE) image indicates a homogeneous elemental distribution in the crystal.

The mean elemental composition of $\text{In}_{20.0(1)}\text{Ge}_{19.7(2)}\text{Te}_{60.3(1)}$ obtained from EDX spectra measured at several spots on multiple crystals is in excellent agreement with the expected composition of $\text{In}_{20}\text{Ge}_{20}\text{Te}_{60}$. Low standard deviations of the mean elemental composition indicates a homogeneous elemental distribution in agreement with the SEM(BSE) image. In absence of any indication of a secondary phase both from the SEM images as well as from the EDX spectroscopy, the obtained crystals are phase pure.

Structural Analysis

To confirm the phase purity and characterize the crystal structure experimentally, pXRD was measured on pulverized $\text{In}_2\text{Ge}_2\text{Te}_6$ crystals. The corresponding pattern is shown in Fig. 5.23. All observed reflection can be assigned to the trigonal $R\bar{3}$ phase as proposed for $\text{In}_2\text{Ge}_2\text{Te}_6$ in literature [51, 177].

Using the Rietveld method, this pXRD pattern can be well modeled by the crystal structure model proposed by Seidlmayer [51]. The resulting optimized structural parameters are shown in Table 5.6 together with the corresponding reliability factors. Furthermore, Table 5.7 shows the optimized atomic model from the Rietveld refinement. Overall, the optimized atomic model is in good agreement with literature [51, 177] and demonstrates that $\text{In}_2\text{Ge}_2\text{Te}_6$ is in fact isostructural to $\text{Cr}_2\text{Ge}_2\text{Te}_6$.

Table 5.6.: Summary and reliability factors of the Rietveld analysis of the pXRD pattern of $\text{In}_2\text{Ge}_2\text{Te}_6$.

<i>Experiment & Data Collection</i>	
Temperature (K)	293(2)
Radiation Type & Wavelength (Å)	Cu- $\text{K}\alpha_1$; 1.54059
θ_{\min} (°)	10.00
θ_{step} (°)	0.03
θ_{\max} (°)	120.64
<i>Crystal Data</i>	
Crystal System	Trigonal
Space Group	$R\bar{3}$ (No. 148)
$a = b$ (Å)	7.1085(4)
c (Å)	21.280(2)
<i>Refinement</i>	
Goodness-Of-Fit	2.84
R_p (%)	6.96
wR_p (%)	9.58
R_F (%)	10.6

Table 5.7.: Fractional atomic coordinates, occupancies and isotropic displacement parameters U_{iso} of $\text{In}_2\text{Ge}_2\text{Te}_6$ at 293 K with estimated standard deviations in parantheses after Rietveld refinement.

Label	Type	Wyck	x	y	z	Occ (%)	U_{iso} ($\times 10^{-3} \text{Å}^2$)
In1	In	$6c$	0	0	0.3291(11)	100	109(4)
Ge1	Ge	$6c$	0	0	0.0456(10)	100	109(4)
Te1	Te	$18f$	0.6589(8)	0.0030(20)	0.2494(3)	100	38(1)

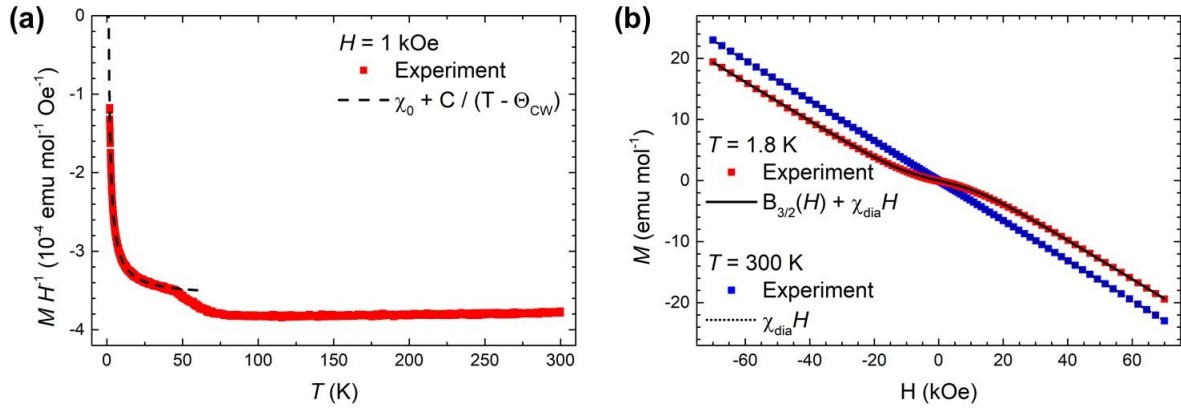


Fig. 5.24.: (a) Normalized magnetization MH^{-1} of $\text{In}_2\text{Ge}_2\text{Te}_6$ as function of temperature at a magnetic field of 1 kOe. The dashed line at low temperatures corresponds to a Curie-Weiss fit of the low temperature behaviour. (b) Field dependent magnetization of $\text{In}_2\text{Ge}_2\text{Te}_6$ at 1.8 K and 300 K. The solid and dashed line correspond to fits to the experimental data as described in the legend. For both (a) and (b) the external field was applied parallel to the crystallographic ab plane.

5.2.3. Magnetic Properties

As shown in Fig. 5.24(a), the negative normalized magnetization over the whole temperature range of the corresponding $MH^{-1}(T)$ measurements at 1 kOe applied parallel to the ab planes indicates diamagnetism for $\text{In}_2\text{Ge}_2\text{Te}_6$. As $\text{In}_2\text{Ge}_2\text{Te}_6$ contains In^{3+} ($S = 0$), this magnetic behavior is well expected in contrast to $\text{Cr}_2\text{Ge}_2\text{Te}_6$ with Cr^{3+} ($S = 3/2$). However, the thermal evolution of MH^{-1} is not temperature independent, as expected for a diamagnet. Below 80 K, the normalized magnetization increases towards lower temperatures with a significant change in slope at around 45 K. The behaviour below 45 K can be well described by the Curie-Weiss law with a Curie-Weiss temperature $\Theta_{\text{CW}} = -0.19(3)$ K, an effective magnetic moment $\mu_{\text{eff}} = 0.061(4) \mu_{\text{B}}$ and a temperature independent contribution $\chi_0 = -3.575(3) \cdot 10^{-4} \text{ emu mol}^{-1}$ as shown by the dashed line in Fig. 5.24(a). Based on the small values of Θ_{CW} and μ_{eff} , the low temperature upturn can be most likely attributed to Curie impurities, crystallographic defects or impurities that lead to nearly non-interacting paramagnetic moments. The second anomaly at slightly higher temperatures indicates the presence of a second magnetic impurity phase in the measured sample besides the aforementioned Curie impurities. Aside from these weak impurity contributions, overall the diamagnetic behavior of $\text{In}_2\text{Ge}_2\text{Te}_6$ is well observed.

In addition, the field dependence of the magnetization of $\text{In}_2\text{Ge}_2\text{Te}_6$ at 1.8 K as well as at 300 K are shown in Fig. 5.24(b). At both temperatures, the negative slopes clearly indicate dominantly diamagnetic contributions. While the linear trend at 300 K corresponds ideally to the behaviour expected for a diamagnet, the field dependence at 1.8 K indicates the contribution of another magnetic phase. Assuming the secondary magnetic phase can be treated as paramagnetic, the Brillouin function $B_J(y)$ can be used to describe this contribution in addition to the linear relation between external field and magnetization of a diamagnet. A corresponding fit to the experimental data with a Landé factor of $g = 2.002$ (free electron) yields excellent agreement with the experiment for $J = 3/2$ and $M_s = 3.21(3) \text{ emu mol}^{-1}$ for the Brillouin contribution and $\chi_{\text{dia}} = -3.244(6) \cdot 10^{-4} \text{ emu mol}^{-1}$ as the diamagnetic molar

susceptibility. This value of χ_{dia} is in good agreement with $\chi_{\text{dia}} = -3.306(3) \cdot 10^{-4} \text{ emu mol}^{-1}$ obtained from a linear regression of the field dependence at 300 K.

Consequently, the diamagnetic groundstate of $\text{In}_2\text{Ge}_2\text{Te}_6$ is confirmed by both the thermal as well as the field dependent evolution of the magnetism and a molar susceptibility of approximately $\chi_{\text{dia}} \approx -3.3 \cdot 10^{-4} \text{ emu mol}^{-1}$ (corresponding volume susceptibility in SI units: $\chi_{\text{V}} \approx 2.2 \cdot 10^{-5}$) is obtained from the latter.

5.2.4. Specific Heat

The specific heat of a solid is in general given by three contributions: The phononic contribution, the contribution of the spin system and the contribution of the electronic system. Here, the the phononic contribution to the specific heat may be estimated by the Debye model (Eq. 5.11).

$$C_{\text{V}}^{\text{Debye}}(T) = 9R \left(\frac{T}{\Theta_{\text{D}}} \right)^3 \int_0^{\Theta_{\text{D}}/T} \frac{x^4 e^x}{(e^x - 1)^2} dx \quad (5.11)$$

Although, the Debye model yields the isochoric specific heat C_{V} and the measurement was performed isobar (C_{p}), the agreement between model and experiment is usually good for solid materials without any change of the state of matter. Assuming all further contributions to the specific heat are zero for the insulating diamagnetic $\text{In}_2\text{Ge}_2\text{Te}_6$, the Debye model is expected to be sufficient to model the experimental specific heat of $\text{In}_2\text{Ge}_2\text{Te}_6$ with a specific Debye temperature Θ_{D} in good agreement.

The specific heat as function of temperature $C_{\text{p}}(T)$ of $\text{In}_2\text{Ge}_2\text{Te}_6$ ⁴ without an applied magnetic field is shown in Fig. 5.25 together with the modeled specific heat from the Debye model using different values of Θ_{D} . Overall, the specific heat of $\text{In}_2\text{Ge}_2\text{Te}_6$ is found featureless implying the absence of any phase transitions in the measured temperature range. However, for no value of Θ_{D} the model is able to sufficiently describe the experimental thermal evolution of C_{p} over the whole temperature range. While $\Theta_{\text{D}} = 160 \text{ K}$ describes the experimental data sufficiently well below 5 K (see inset of Fig. 5.25), at higher temperatures the experimental C_{p} is significantly lower than suggested by the Debye model. For $\Theta_{\text{D}} = 270 \text{ K}$ the high temperature regime of the experiment above 175 K is well described by the Debye model but at lower temperatures the experimental specific heat is significantly higher than suggested by the model. Also intermediate values of Θ_{D} (for instance 200 K and 230 K in Fig. 5.25) do not yield a better agreement between experiment and model.

This disagreement between the Debye model and the experimental specific heat of $\text{In}_2\text{Ge}_2\text{Te}_6$ may implies that further contributions to the specific heat additional to the phononic contribution are at play for the latter. However considering the reported band gap of 1.6 eV and the observed diamagnetic behaviour in agreement with the lack of unpaired electrons in $\text{In}_2\text{Ge}_2\text{Te}_6$,

⁴All measurements of the specific heat C_{p} as well as the evaluation of the data were performed by Dr. Gaël Bastien at IFW Dresden. All corresponding results are shown with his kind permission.

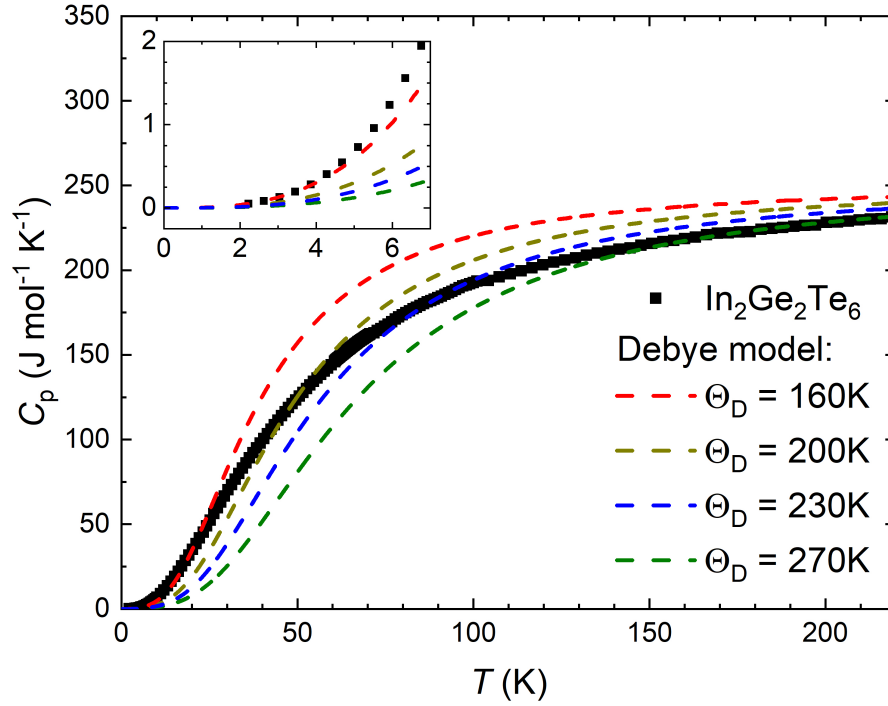


Fig. 5.25.: Zero field specific heat of $\text{In}_2\text{Ge}_2\text{Te}_6$ as function of temperature together with the thermal evolution of the specific heat obtained from the Debye model for different values of Θ_D . The inset shows a zoomed-in view on the low temperature regime up to 7 K.

the origin of any additional contributions to the specific heat of $\text{In}_2\text{Ge}_2\text{Te}_6$ remain elusive. Although the magnetization of $\text{In}_2\text{Ge}_2\text{Te}_6$ as function of temperature and external field shows weak impurity contributions (see Fig. 5.24), these contributions are most likely not sufficient to yield such strong deviations of the specific heat of $\text{In}_2\text{Ge}_2\text{Te}_6$ from the Debye model. Subsequently, further studies are needed to understand the thermal evolution of the specific heat of $\text{In}_2\text{Ge}_2\text{Te}_6$ and its deviations from this model.

5.3. Summary and Outlook

Two members of the $M_2(\text{Ge,Si})_2\text{Te}_6$ compounds, $\text{Cr}_2\text{Ge}_2\text{Te}_6$ and $\text{In}_2\text{Ge}_2\text{Te}_6$, have been successfully grown as single crystals from a GeTe rich melt (*i.e.* self flux) by the flux growth technique. The structural analysis based on pXRD demonstrates that both compounds crystallize isostructurally in a trigonal $R\bar{3}$ structure, in agreement with literature [37, 51].

Magnetization measurements as function of temperature and magnetic field reveal overall diamagnetic behavior for $\text{In}_2\text{Ge}_2\text{Te}_6$ with a temperature independent diamagnetic susceptibility of $\chi_{\text{dia}} \approx -3.3 \cdot 10^{-4} \text{ emu mol}^{-1}$ (corresponding volume susceptibility in SI units: $\chi_V \approx 2.2 \cdot 10^{-5}$). However, additional weak magnetic anomalies at low temperatures are observed, which are most likely attributed to a low amount of magnetic impurities in the corresponding crystal.

Furthermore, a featureless thermal evolution of the specific heat between 2 K and 220 K indicates the absence of any phase transition in this temperature range. This is in agreement with a diamagnetic ground state and the interpretation of the additional anomalies in the magnetic measurements as impurity contribution. However, deviations from the Debye model are observed which may indicate the presence of more than only phononic contributions to the specific heat. The origin of these additional contributions remain elusive and call for further investigations.

In comparison, the magnetic behavior of $\text{Cr}_2\text{Ge}_2\text{Te}_6$ is more complex. $\text{Cr}_2\text{Ge}_2\text{Te}_6$ exhibits a ferromagnetic groundstate with a Curie temperature $T_C = 65 \text{ K}$ according to the thermal evolution of the magnetization and of the specific heat. An effective moment $\mu_{\text{eff}} \approx 4\mu_B/\text{Cr}$ and an isotropic saturation moment $M_s = 3\mu_B/\text{Cr}$ were found, both being in good agreement with the values expected for Cr^{3+} . The difference between $\Theta_{\text{CW}} = 95 \text{ K}$ and T_C as well as the shape of the temperature dependent specific heat indicate low-dimensional magnetic correlations well above the magnetic ordering temperature. The easy-axis nature of the magnetic properties perpendicular to the structural layers in the ab -plane is confirmed in agreement with Ising-type anisotropy. Furthermore, a magnetocrystalline anisotropy constant $K_U = 47 \pm 1 \text{ kJ/m}^3$ is obtained at 1.8 K.

The field and temperature dependence of the magnetization were studied in detail for fields parallel and perpendicular to the hard magnetic plane ab up to fields of 30 kOe. Corresponding magnetic phase diagrams were constructed. The field and temperature dependence for fields along the easy axis $\parallel c$ show the typical behavior of a ferromagnet. However, for fields applied in the hard plane ab below a temperature $T^* < T_C$ a downturn towards lower temperatures is found in magnetization curves below the saturation field $H_{\text{sat},ab} \approx 5 \text{ kOe}$.

To understand the origin of this downturn in the temperature dependent magnetization, the temperature dependence of the effective magnetocrystalline anisotropy $K_{U,\text{eff}}$ was extracted based on the magnetic H, T phase diagram. A good agreement with the expected evolution for uniaxial anisotropy is found according to the power law scaling proposed by Callen and Callen [189]. The peculiar downturn in the magnetization of $\text{Cr}_2\text{Ge}_2\text{Te}_6$ could subsequently be modeled by assuming this temperature dependent anisotropy contribution interacting with

the external applied field and its direction using the energy density equation for ferromagnets. Accordingly, this downturn in the thermal evolution of the magnetization for fields applied in the magnetic hard plane is caused by a temperature dependent magnetization component perpendicular to the applied magnetic field along the magnetic easy axis resulting from the temperature dependence of $K_{U,\text{eff}}$.

A similar anisotropic anomaly was observed for CrX_3 (with $X = \text{Br}, \text{I}$) and also discussed in terms of interplay between $K_{U,\text{eff}}$ and temperature [152]. All these compounds share the same magnetic ion and easy axis $\parallel c$ ferromagnetic ordering together with a similar 2D honeycomb lattice. Thus, the magnetocrystalline anisotropies in these systems are similar, although the magnetocrystalline anisotropy constant K_U shows significant differences in its absolute value for the mentioned compounds. This hints towards a universality of this interplay in quasi two-dimensional ferromagnetic materials. Furthermore, the observed anomaly in the temperature dependence of the magnetization can be considered as a fingerprint of this interplay.

Furthermore, the magnetic H, T phase diagrams allowed for the extraction of the critical exponents describing the second order ferromagnetic phase transition in $\text{Cr}_2\text{Ge}_2\text{Te}_6$. Several methods (modified Arrot, Kouvel-Fisher and critical isotherm) yield the critical exponents $\beta \approx 0.20$, $\gamma \approx 0.98$ and $\delta \approx 5.5$ in agreement with each other. Furthermore, the reliability of these exponents was verified against the magnetic equation of state as proposed in literature [208]. These obtained values for the critical exponents of the magnetic phase transition in $\text{Cr}_2\text{Ge}_2\text{Te}_6$ are found in reasonable agreement with literature [183, 184, 199]. Although this set of critical exponents agrees best with the exponents obtained for the tricritical mean field model, the lack of any other indication of tricritical point in $\text{Cr}_2\text{Ge}_2\text{Te}_6$ leads to another interpretation of these exponents. In line with the Ising-type anisotropy of $\text{Cr}_2\text{Ge}_2\text{Te}_6$, the critical exponents may be best understood as in between the exponents obtained from the 2D Ising model and the 3D Ising model with a non-negligible interlayer interaction. For comparison, the sister compound $\text{Cr}_2\text{Si}_2\text{Te}_6$ [200] exhibits critical exponents in good agreement with the 2D Ising model while the exponents of CrX_3 ($X = \text{Br}$ [218], I [201]) agree with the 3D Ising model.

In conclusion, $\text{Cr}_2\text{Ge}_2\text{Te}_6$ is well characterized as a low dimensional ferromagnet which, however, exhibits non negligible magnetic interlayer interactions. Together with the Curie temperature being the highest out of the before mentioned compounds, this makes $\text{Cr}_2\text{Ge}_2\text{Te}_6$ a highly promising low-dimensional magnet to gain further insight into low-dimensional ferromagnetism in general and for the use in ferromagnetic heterostructures.

6. Conclusion

In this work, the synthesis and crystal growth of different compounds of the class of metal trichalcogenides was investigated and optimized. The chemical vapor transport technique was used to successfully grow crystals of the metal phosphorus sulfides $\text{Fe}_2\text{P}_2\text{S}_6$, $\text{Ni}_2\text{P}_2\text{S}_6$ and the intermediate compounds $(\text{Fe}_{1-x}\text{Ni}_x)_2\text{P}_2\text{S}_6$. Furthermore, crystals of quaternary phosphorus sulfides of the general formula $M^{1+}M^{3+}\text{P}_2\text{S}_6$, *i.e.* CuCrP_2S_6 and AgCrP_2S_6 , were obtained using this technique. The metal germanium tellurides $\text{Cr}_2\text{Ge}_2\text{Te}_6$ and $\text{In}_2\text{Ge}_2\text{Te}_6$ were grown *via* the flux growth technique from a GeTe-rich melt (*i.e.* self-flux).

The elemental composition as well as the layered structure of these compounds, as probed by EDX spectroscopy and X-ray diffraction, are overall in agreement with literature. The structural analysis, especially for $\text{Ni}_2\text{P}_2\text{S}_6$, yields further insight into the structural interactions between adjacent layers in the phosphorus sulfides. In detail, the structure is well ordered in the layers but the stacking between layers is prone to defects (*i.e.* stacking faults) due to the weakness of the interlayer interactions. These stacking faults are a consequence of the intrinsic 2D character of the structure of the metal trichalcogenides, even in bulk crystals. For $\text{Ni}_2\text{P}_2\text{S}_6$, such stacking faults are most likely defined by 120° twinning.

The series of $(\text{Fe}_{1-x}\text{Ni}_x)_2\text{P}_2\text{S}_6$ illustrates the possibility for substitution between isostructural compounds in a subclass of the metal trichalcogenides. Furthermore, the influence of chemical substitution on the magnetic behavior is shown by this example. The ordering of the M^{1+} and M^{3+} sublattices in the quaternary metal trichalcogenides allows to further modify the magnetic structure away from the usual hexagonal honeycomb arrangement of magnetic moments towards triangular or even stripe-like magnetic lattices. CuCrP_2S_6 and AgCrP_2S_6 serve as an example for this more exotic approach of influencing the magnetic interactions and the magnetic structure in metal trichalcogenides. In this context, the phase analysis of the intermediate regime between CuCrP_2S_6 and AgCrP_2S_6 indicates a miscibility regime, which may allow for a partial substitution of Ag against Cu in AgCrP_2S_6 . While this would not directly affect the magnetic Cr sublattice, such a substitution is expected to locally induce strain in the structural lattice and, thus, indirectly influence the magnetic interactions.

The Cr-containing compounds, $\text{Cr}_2\text{Si}_2\text{Te}_6$ and $\text{Cr}_2\text{Ge}_2\text{Te}_6$, are the only known ferromagnetic metal trichalcogenides. The magnetic investigation of $\text{Cr}_2\text{Ge}_2\text{Te}_6$ demonstrates the intrinsic 2D character of the ferromagnetic interactions. Furthermore, an anisotropic downturn in the thermal evolution of the magnetization is identified as a fingerprint for this specific interplay between ferromagnetism and magnetic anisotropy. The isostructural and insulating $\text{In}_2\text{Ge}_2\text{Te}_6$ exhibits diamagnetism as expected for a closed shell system.

Based on the findings in this work, further investigations may be conducted in the future to better understand the structural features and the magnetic behavior of the metal trichalcogenides in general. For the specific compounds investigated in this work, proposals for further investigations as well as open scientific questions are discussed in the separate 'Summary and Outlook' sections of the experimental chapters.

Overall, this work discusses parameters for reproducible synthesis and crystal growth experiments as well as illustrates the variety of magnetic ordering phenomena and magnetic structures that can be realized in the class of metal trichalcogenides. Furthermore, different strategies of tuning the magnetic properties in this class of materials by chemical means are presented. Owing to the flexibility of the magnetic properties in addition to the van der Waals layered 2D crystal structure, the family of the metal trichalcogenides is promising to yield several compounds which will find application in novel 2D devices and heterostructures in the future.

Bibliography

- [1] K. S. Novoselov, A. K. Geim, S. V. Morozov, D. Jiang, Y. Zhang, S. V. Dubonos, I. V. Grigorieva, and A. A. Firsov, *Science* **306**, 666 (2004).
- [2] N. D. Mermin and H. Wagner, *Physical Review Letters* **17**, 1133 (1966).
- [3] L. D. Landau, *Physikalische Zeitschrift der Sowjetunion* **11**, 11 (1937).
- [4] R. E. Peierls, *Annales de l'institut Henri Poincaré* **5**, 177 (1935).
- [5] J. C. Meyer, A. K. Geim, M. I. Katsnelson, K. S. Novoselov, T. J. Booth, and S. Roth, *Nature* **446**, 60 (2007).
- [6] F. Hiebel, P. Mallet, F. Varchon, L. Magaud, and J.-Y. Veullen, *Physical Review B* **78**, 153412 (2008).
- [7] E. Gerstner, *Nature Physics* **6**, 836 (2010).
- [8] Blender Online Community, *Blender - a 3D Modelling and Rendering Package (v2.9)*, Blender Foundation (Stichting Blender Foundation, Amsterdam, 2020).
- [9] A. K. Geim and I. V. Grigorieva, *Nature* **499**, 419 (2013).
- [10] R. Mas-Ballesté, C. Gómez-Navarro, J. Gómez-Herrero, and F. Zamora, *Nanoscale* **3**, 20 (2011).
- [11] M. Osada and T. Sasaki, *Advanced Materials* **24**, 210 (2011).
- [12] Q. H. Wang, K. Kalantar-Zadeh, A. Kis, J. N. Coleman, and M. S. Strano, *Nature Nanotechnology* **7**, 699 (2012).
- [13] K. S. Novoselov, D. Jiang, F. Schedin, T. J. Booth, V. V. Khotkevich, S. V. Morozov, and A. K. Geim, *Proceedings of the National Academy of Sciences* **102**, 10451 (2005).
- [14] M. Xu, T. Liang, M. Shi, and H. Chen, *Chemical Reviews* **113**, 3766 (2013).
- [15] V. K. Sangwan and M. C. Hersam, *Annual Review of Physical Chemistry* **69**, 299 (2018).
- [16] K. F. Mak, C. Lee, J. Hone, J. Shan, and T. F. Heinz, *Physical Review Letters* **105**, 136805 (2010).
- [17] D. A. Bandurin, A. V. Tyurnina, G. L. Yu, A. Mishchenko, V. Zólyomi, S. V. Morozov, R. K. Kumar, R. V. Gorbachev, Z. R. Kudrynskiy, S. Pezzini, Z. D. Kovalyuk, U. Zeitler, K. S. Novoselov, A. Patané, L. Eaves, I. V. Grigorieva, V. I. Fal'ko, A. K. Geim, and Y. Cao, *Nature Nanotechnology* **12**, 223 (2016).
- [18] A. Kuc, N. Zibouche, and T. Heine, *Physical Review B* **83**, 245213 (2011).
- [19] A. Carvalho, R. M. Ribeiro, and A. H. C. Neto, *Physical Review B* **88**, 115205 (2013).
- [20] L. C. Gomes, S. S. Alexandre, H. Chacham, and R. W. Nunes, *The Journal of Physical Chemistry C* **117**, 11770 (2013).
- [21] H. Liu, A. T. Neal, Z. Zhu, Z. Luo, X. Xu, D. Tománek, and P. D. Ye, *ACS Nano* **8**, 4033 (2014).
- [22] H. Chen, Y. Li, L. Huang, and J. Li, *RSC Advances* **5**, 50883 (2015).

- [23] A. S. Rodin, L. C. Gomes, A. Carvalho, and A. H. C. Neto, *Physical Review B* **93**, 045431 (2016).
- [24] K. S. Novoselov, A. Mishchenko, A. Carvalho, and A. H. C. Neto, *Science* **353**, aac9439 (2016).
- [25] J. Wilson, F. D. Salvo, and S. Mahajan, *Advances in Physics* **24**, 117 (1975).
- [26] A. H. C. Neto, *Physical Review Letters* **86**, 4382 (2001).
- [27] B. Sipos, A. F. Kusmartseva, A. Akrap, H. Berger, L. Forró, and E. Tutiš, *Nature Materials* **7**, 960 (2008).
- [28] Y. Liu, N. O. Weiss, X. Duan, H.-C. Cheng, Y. Huang, and X. Duan, *Nature Reviews Materials* **1**, 16042 (2016).
- [29] C. Gong, L. Li, Z. Li, H. Ji, A. Stern, Y. Xia, T. Cao, W. Bao, C. Wang, Y. Wang, Z. Q. Qiu, R. J. Cava, S. G. Louie, J. Xia, and X. Zhang, *Nature* **546**, 265 (2017).
- [30] B. Huang, G. Clark, E. Navarro-Moratalla, D. R. Klein, R. Cheng, K. L. Seyler, D. Zhong, E. Schmidgall, M. A. McGuire, D. H. Cobden, W. Yao, D. Xiao, P. Jarillo-Herrero, and X. Xu, *Nature* **546**, 270 (2017).
- [31] Z. Wang, D. Sapkota, T. Taniguchi, K. Watanabe, D. Mandrus, and A. F. Morpurgo, *Nano Letters* **18**, 4303 (2018).
- [32] M. Gibertini, M. Koperski, A. F. Morpurgo, and K. S. Novoselov, *Nature Nanotechnology* **14**, 408 (2019).
- [33] D. Zhong, K. L. Seyler, X. Linpeng, R. Cheng, N. Sivadas, B. Huang, E. Schmidgall, T. Taniguchi, K. Watanabe, M. A. McGuire, W. Yao, D. Xiao, K.-M. C. Fu, and X. Xu, *Science Advances* **3**, e1603113 (2017).
- [34] T. Song, M. W.-Y. Tu, C. Carnahan, X. Cai, T. Taniguchi, K. Watanabe, M. A. McGuire, D. H. Cobden, D. Xiao, W. Yao, and X. Xu, *Nano Letters* **19**, 915 (2019).
- [35] Z. Wang, I. Gutiérrez-Lezama, N. Ubrig, M. Kroner, M. Gibertini, T. Taniguchi, K. Watanabe, A. Imamoğlu, E. Giannini, and A. F. Morpurgo, *Nature Communications* **9**, 2516 (2018).
- [36] N. Samarth, *Nature* **546**, 216 (2017).
- [37] V. Cartheaux, D. Brunet, G. Ouvrard, and G. Andre, *Journal of Physics: Condensed Matter* **7**, 69 (1995).
- [38] M. A. McGuire, H. Dixit, V. R. Cooper, and B. C. Sales, *Chemistry of Materials* **27**, 612 (2015).
- [39] S. Wakeland, R. Martinez, J. K. Grey, and C. C. Luhrs, *Carbon* **48**, 3463 (2010).
- [40] Z. Cheng, T. A. Shifa, F. Wang, Y. Gao, P. He, K. Zhang, C. Jiang, Q. Liu, and J. He, *Advanced Materials* **30**, 1707433 (2018).
- [41] R. Brec, "Review on Structural and Chemical Properties of Transition Metal Phosphorus Trisulfides MPS₃," in *Intercalation in Layered Materials* (Springer US, 1986), pp. 93–124.
- [42] M. A. Susner, M. Chyasnachyus, M. A. McGuire, P. Ganesh, and P. Maksymovych, *Advanced Materials* **29**, 1602852 (2017).
- [43] A. R. Wildes, V. Simonet, E. Ressouche, G. J. McIntyre, M. Avdeev, E. Suard, S. A. J. Kimber, D. Lançon, G. Pepe, B. Moubaraki, and T. J. Hicks, *Physical Review B* **92**, 224408 (2015).
- [44] J.-U. Lee, S. Lee, J. H. Ryoo, S. Kang, T. Y. Kim, P. Kim, C.-H. Park, J.-G. Park, and H. Cheong, *Nano Letters* **16**, 7433 (2016).
- [45] K. Kim, S. Y. Lim, J.-U. Lee, S. Lee, T. Y. Kim, K. Park, G. S. Jeon, C.-H. Park, J.-G. Park, and H. Cheong, *Nature Communications* **10**, 345 (2019).

- [46] J. M. Kosterlitz and D. J. Thouless, *Journal of Physics C: Solid State Physics* **6**, 1181 (1973).
- [47] J. M. Kosterlitz, *Journal of Physics C: Solid State Physics* **7**, 1046 (1974).
- [48] Of topology and low-dimensionality, *Nature Physics* **12**, 987 (2016).
- [49] H. Falius, *Zeitschrift für anorganische und allgemeine Chemie* **356**, 189 (1968).
- [50] T. Hahn, *International Tables for Crystallography* (Published for the International Union of Crystallography by Springer, Dordrecht, Netherlands, 2005).
- [51] S. Seidlmayer, "Strukturchemische Untersuchungen an Hexachalkogenohypodiphosphaten und verwandten Verbindungen," PhD thesis (Universität Regensburg, 2009).
- [52] R. M. Bozorth, *Journal of the American Chemical Society* **44**, 2232 (1922).
- [53] B. K. Vainshtein, *Fundamentals of Crystals* (Springer Berlin Heidelberg, 2010).
- [54] E. Sandre, V. Carteaux, A. Marie, and G. Ouvrard, *Journal of Alloys and Compounds* **204**, 145 (1994).
- [55] W. Klingen, G. Eulenberger, and H. Hahn, *Zeitschrift für anorganische und allgemeine Chemie* **401**, 97 (1973).
- [56] R. Brec, G. Ouvrard, and J. Rouxel, *Materials Research Bulletin* **20**, 1257 (1985).
- [57] S. Lee, P. Colombet, G. Ouvrard, and R. Brec, *Materials Research Bulletin* **21**, 917 (1986).
- [58] P. Colombet, A. Leblanc, M. Danot, and J. Rouxel, *Journal of Solid State Chemistry* **41**, 174 (1982).
- [59] C.-T. Kuo, M. Neumann, K. Balamurugan, H. J. Park, S. Kang, H. W. Shiu, J. H. Kang, B. H. Hong, M. Han, T. W. Noh, and J.-G. Park, *Scientific Reports* **6**, 20904 (2016).
- [60] R. Brec, D. M. Schleich, G. Ouvrard, A. Louisy, and J. Rouxel, *Inorganic Chemistry* **18**, 1814 (1979).
- [61] M. J. Coak, S. Son, D. Daisenberger, H. Hamidov, C. R. S. Haines, P. L. Alireza, A. R. Wildes, C. Liu, S. S. Saxena, and J.-G. Park, *npj Quantum Materials* **4**, 38 (2019).
- [62] Y. Wang, Z. Zhou, T. Wen, Y. Zhou, N. Li, F. Han, Y. Xiao, P. Chow, J. Sun, M. Pravica, A. L. Cornelius, W. Yang, and Y. Zhao, *Journal of the American Chemical Society* **138**, 15751 (2016).
- [63] C. Haines, M. Coak, A. Wildes, G. Lampronti, C. Liu, P. Nahai-Williamson, H. Hamidov, D. Daisenberger, and S. Saxena, *Physical Review Letters* **121**, 266801 (2018).
- [64] M. Tsurubayashi, K. Kodama, M. Kano, K. Ishigaki, Y. Uwatoko, T. Watanabe, K. Takase, and Y. Takano, *AIP Advances* **8**, 101307 (2018).
- [65] S. Blundell, *Magnetism in Condensed Matter*, 2nd ed. (Oxford University Press, New York, USA, Aug. 1, 2001).
- [66] H. Lueken, *Magnetochemie* (Vieweg+Teubner Verlag, Leipzig, Germany, 1999).
- [67] D. Shriver, P. W. Atkins, and C. H. Langford, *Anorganische Chemie - ein weiterführendes Lehrbuch*, edited by E. Buchholz (VCH (Weinheim, New York, Basel, Cambridge), 1992).
- [68] A. Abragam and B. Bleaney, *Electron Paramagnetic Resonance of Transition Ions* (Oxford University Press, July 1, 2012).
- [69] P. Enis and S. Geisser, *Journal of the American Statistical Association* **66**, 162 (1971).
- [70] J. A. Osborn, *Physical Review* **67**, 351 (1945).
- [71] V. L. Berezinsky, *Zhurnal Eksperimental'noi i Teoreticheskoi Fiziki* **32**, 493 (1970).

- [72] H. Stanley, *Introduction to Phase Transitions and Critical Phenomena* (Oxford University Press, New York, USA, 1987).
- [73] R. B. Griffiths, *Physical Review Letters* **24**, 1479 (1970).
- [74] M. E. Fisher, *Reports on Progress in Physics* **30**, 615 (1967).
- [75] A. R. West, *Solid State Chemistry* (Wiley John + Sons, 2014).
- [76] H. Okamoto, *Journal of Phase Equilibria* **13**, 543 (1992).
- [77] P. Rudolph, *Handbook of Crystal Growth* (Elsevier Science & Technology, 2014).
- [78] K.-T. Wilke and J. Bohm, *Kristallzüchtung*, 1st ed. (VEB Deutscher Verlag der Wissenschaften, Berlin, 1988).
- [79] D. Li, D. Zeng, X. Yin, H. Han, L. Guo, and Y. Yao, *Calphad* **53**, 78 (2016).
- [80] M. Binnewies, R. Glaum, M. Schmidt, and P. Schmidt, *Chemical Vapor Transport Reactions* (Walter de Gruyter GmbH, 2012).
- [81] P. Kleinert, *Zeitschrift für anorganische und allgemeine Chemie* **378**, 71 (1970).
- [82] L. Mond, C. Langer, and F. Quincke, *Journal of the Chemical Society, Transactions* **57**, 749 (1890).
- [83] W. Massa, *Crystal Structure Determination* (Springer Berlin Heidelberg, Berlin, Heidelberg, 2004).
- [84] P. P. Ewald, *Zeitschrift für Physik* **14**, 465 (1913).
- [85] W. H. Bragg and W. L. Bragg, *Proceedings of the Royal Society of London A* **88**, 428 (1913).
- [86] G. Friedel, *Comptes rendus de l'Académie des sciences* **157**, 1533 (1913).
- [87] Bruker AXS Inc., Madison, Wisconsin, USA, *SAINT*, 2004.
- [88] Bruker AXS Inc., Madison, Wisconsin, USA, *APEX2*, 2004.
- [89] G. M. Sheldrick, *SADABS Program for Empirical Absorption Correction of Area Detector Data*, 1996.
- [90] L. Palatinus and G. Chapuis, *Journal of Applied Crystallography* **40**, 786 (2007).
- [91] V. Petříček, M. Dušek, and L. Palatinus, *Zeitschrift für Kristallographie - Crystalline Materials* **229**, 345 (2014).
- [92] G. M. Sheldrick, *Acta Crystallographica Section A* **64**, 112 (2007).
- [93] R. E. Dinnebier and S. J. L. Billinge, eds., *Powder Diffraction: Theory and Practice* (Royal Society of Chemistry, 2008).
- [94] A. T. Macrander and X. Huang, *Annual Review of Materials Research* **47**, 135 (2017).
- [95] J. Goldstein, *Scanning Electron Microscopy and X-ray Microanalysis* (Springer US, Boston, MA, 2003).
- [96] T. E. Everhart and R. F. M. Thornley, *Journal of Scientific Instruments* **37**, 246 (1960).
- [97] F. Eggert, *Standardfreie Elektronenstrahl-Mikroanalyse (mit dem EDX im Rasterelektronenmikroskop)* (Books on Demand, 2005).
- [98] R. Kleiner, *Superconductivity : an Introduction* (Wiley-VCH Verlag GmbH & Co. KGaA, Weinheim, Germany, 2016).
- [99] R. L. Fagaly, *Review of Scientific Instruments* **77**, 101101 (2006).
- [100] Quantum Design, *Accuracy of the Reported Moment: Sample Shape Effects - SQUID VSM Application Note 1500-015*, 2010.

- [101] C. Slichter, *Principles of Magnetic Resonance* (Springer Berlin Heidelberg, Berlin, Heidelberg, 1990).
- [102] G. R. Stewart, *Review of Scientific Instruments* **54**, 1 (1983).
- [103] A. Medina, A. Caldeira, A. Bento, M. Baesso, J. Sampaio, T. Catunda, and F. Gandra, *Journal of Non-Crystalline Solids* **304**, 299 (2002).
- [104] W. Klingen, G. Eulenberger, and H. Hahn, *Die Naturwissenschaften* **57**, 88 (1970).
- [105] B. E. Taylor, J. Steger, and A. Wold, *Journal of Solid State Chemistry* **7**, 461 (1973).
- [106] R. Brec, G. Ouvrard, A. Louisy, and J. Rouxel, *Annales de Chimie* **5**, 499 (1980).
- [107] G. Bergerhoff and I. D. Brown, "ICSD," in *Crystallographic Databases* (F. H. Allen et al., Chester, 1987).
- [108] M. Z. Jandali, G. Eulenberger, and H. Hahn, *Zeitschrift für anorganische und allgemeine Chemie* **447**, 105 (1978).
- [109] W. Klingen, G. Eulenberger, and H. Hahn, *Die Naturwissenschaften* **55**, 229 (1968).
- [110] W. Klingen, R. Ott, and H. Hahn, *Zeitschrift für anorganische und allgemeine Chemie* **396**, 271 (1973).
- [111] G. Ouvrard, R. Fréour, R. Brec, and J. Rouxel, *Materials Research Bulletin* **20**, 1053 (1985).
- [112] G. Ouvrard, R. Brec, and J. Rouxel, *Materials Research Bulletin* **20**, 1181 (1985).
- [113] F. Boucher, M. Evain, and R. Brec, *Journal of Alloys and Compounds* **215**, 63 (1994).
- [114] G. L. Flem, R. Brec, G. Ouvrard, A. Louisy, and P. Segransan, *Journal of Physics and Chemistry of Solids* **43**, 455 (1982).
- [115] A. R. Wildes, B. Roessli, B. Lebech, and K. W. Godfrey, *Journal of Physics: Condensed Matter* **10**, 6417 (1998).
- [116] D. Lançon, H. C. Walker, E. Ressouche, B. Ouladdiaf, K. C. Rule, G. J. McIntyre, T. J. Hicks, H. M. Rønnow, and A. R. Wildes, *Physical Review B* **94**, 214407 (2016).
- [117] D. Lançon, R. A. Ewings, T. Guidi, F. Formisano, and A. R. Wildes, *Physical Review B* **98**, 134414 (2018).
- [118] A. R. Wildes, V. Simonet, E. Ressouche, R. Ballou, and G. J. McIntyre, *Journal of Physics: Condensed Matter* **29**, 455801 (2017).
- [119] Y. Takano, A. Arai, Y. Takahashi, K. Takase, and K. Sekizawa, *Journal of Applied Physics* **93**, 8197 (2003).
- [120] Y. Shemerliuk, "Optimizing the Synthesis and Crystal Growth in 2D Magnets," MA thesis (Vasyl Stefanyk Precarpathian National University, 2019).
- [121] T. Holub, "Synthesis and Characterisation of MPS₃ Materials," MA thesis (V. N. Karazin Kharkiv National University, 2020).
- [122] H. Hahn and W. Klingen, *Die Naturwissenschaften* **52**, 494 (1965).
- [123] D. J. Goossens, D. James, J. Dong, R. E. Whitfield, L. Norén, and R. L. Withers, *Journal of Physics: Condensed Matter* **23**, 065401 (2011).
- [124] J. A. Venables, C. A. English, K. F. Niebel, and G. J. Tatlock, *Le Journal de Physique Colloques* **35**, 113 (1974).

- [125] S. Y. Kim, T. Y. Kim, L. J. Sandilands, S. Sinn, M.-C. Lee, J. Son, S. Lee, K.-Y. Choi, W. Kim, B.-G. Park, C. Jeon, H.-D. Kim, C.-H. Park, J.-G. Park, S. Moon, and T. Noh, *Physical Review Letters* **120**, 136402 (2018).
- [126] P. A. Joy and S. Vasudevan, *Physical Review B* **46**, 5425 (1992).
- [127] A. P. Dioguardi, S. Selter, U. Peeck, S. Aswartham, M.-I. Sturza, R. Murugesan, M. S. Eldeeb, L. Hozoi, B. Büchner, and H.-J. Grafe, *Physical Review B* **102**, 064429 (2020).
- [128] A. March, *Zeitschrift für Kristallographie - Crystalline Materials* **81**, 285 (1932).
- [129] W. A. Dollase, *Journal of Applied Crystallography* **19**, 267 (1986).
- [130] J.-F. Bézar and G. Baldinozzi, *Journal of Applied Crystallography* **26**, 128 (1993).
- [131] M. S. Paterson, *Journal of Applied Physics* **23**, 805 (1952).
- [132] G. E. Pake, *The Journal of Chemical Physics* **16**, 327 (1948).
- [133] T. Masubuchi, H. Hoya, T. Watanabe, Y. Takahashi, S. Ban, N. Ohkubo, K. Takase, and Y. Takano, *Journal of Alloys and Compounds* **460**, 668 (2008).
- [134] R. R. Rao and A. K. Raychaudhuri, *Journal of Physics and Chemistry of Solids* **53**, 577 (1992).
- [135] D. J. Goossens, S. Brazier-Hollins, D. R. James, W. D. Hutchison, and J. R. Hester, *Journal of Magnetism and Magnetic Materials* **334**, 82 (2013).
- [136] R. D. Shannon, *Acta Crystallographica Section A* **32**, 751 (1976).
- [137] L. Vegard, *Zeitschrift für Physik* **5**, 17 (1921).
- [138] C. Berthier, Y. Chabre, and M. Minier, *Solid State Communications* **28**, 327 (1978).
- [139] K. Kurosawa, S. Saito, and Y. Yamaguchi, *Journal of the Physical Society of Japan* **52**, 3919 (1983).
- [140] K. C. Rule, G. J. McIntyre, S. J. Kennedy, and T. J. Hicks, *Physical Review B* **76**, 134402 (2007).
- [141] D. J. Breed, K. Gilijamse, and A. R. Miedema, *Physica* **45**, 205 (1969).
- [142] P. Nordblad, L. Lundgren, E. Figueroa, U. Gäfvert, and O. Beckman, *Physica Scripta* **20**, 105 (1979).
- [143] J. Akimitsu, Y. Ishikawa, and Y. Endoh, *Solid State Communications* **8**, 87 (1970).
- [144] R. J. Birgeneau, H. J. Guggenheim, and G. Shirane, *Physical Review Letters* **22**, 720 (1969).
- [145] D. C. Johnston, R. K. Kremer, M. Troyer, X. Wang, A. Klümper, S. L. Bud'ko, A. F. Panchula, and P. C. Canfield, *Physical Review B* **61**, 9558 (2000).
- [146] S. B. Roy and M. K. Chattopadhyay, *Physical Review B* **79**, 052407 (2009).
- [147] Z. Ouli, A. Leblanc, and P. Colombet, *Journal of Solid State Chemistry* **66**, 86 (1987).
- [148] P. Colombet, A. Leblanc, M. Danot, and J. Rouxel, *Nouveau Journal de Chimie* **7**, 333 (1983).
- [149] N. Menyuk, K. Dwight, R. J. Arnett, and A. Wold, *Journal of Applied Physics* **37**, 1387 (1966).
- [150] N. W. Grimes and E. D. Isaac, *Philosophical Magazine* **35**, 503 (1977).
- [151] L. D. Casto, A. J. Clune, M. O. Yokosuk, J. L. Musfeldt, T. J. Williams, H. L. Zhuang, M.-W. Lin, K. Xiao, R. G. Hennig, B. C. Sales, J.-Q. Yan, and D. Mandrus, *APL Materials* **3**, 041515 (2015).
- [152] N. Richter, D. Weber, F. Martin, N. Singh, U. Schwingenschlögl, B. V. Lotsch, and M. Kläui, *Physical Review Materials* **2**, 024004 (2018).
- [153] W. Kleemann, V. V. Shvartsman, P. Borisov, J. Banys, and Y. M. Vysochanskii, *Physical Review B* **84**, 094411 (2011).

- [154] H. Mutka, C. Payen, and P. Molinié, *Europhysics Letters (EPL)* **21**, 623 (1993).
- [155] V. Maisonneuve, V. B. Cajipe, and C. Payen, *Chemistry of Materials* **5**, 758 (1993).
- [156] P. Bongers, C. V. Bruggen, J. Koopstra, W. Omloo, G. Wiegers, and F. Jellinek, *Journal of Physics and Chemistry of Solids* **29**, 977 (1968).
- [157] B. van Laar and D. Ijdo, *Journal of Solid State Chemistry* **3**, 590 (1971).
- [158] B. V. Laar and F. Engelsman, *Journal of Solid State Chemistry* **6**, 384 (1973).
- [159] F. Engelsman, G. Wiegers, F. Jellinek, and B. V. Laar, *Journal of Solid State Chemistry* **6**, 574 (1973).
- [160] M. A. McGuire, G. Clark, S. KC, W. M. Chance, G. E. Jellison, V. R. Cooper, X. Xu, and B. C. Sales, *Physical Review Materials* **1**, 014001 (2017).
- [161] J. Zeisner, K. Mehlawat, A. Alfonsov, M. Roslova, T. Doert, A. Isaeva, B. Büchner, and V. Kataev, *Physical Review Materials* **4**, 064406 (2020).
- [162] S. Jörgens and A. Mewis, *Solid State Sciences* **9**, 213 (2007).
- [163] A. Vos, R. Olthof, F. van Bolhuis, and R. Botterweg, *Acta Crystallographica* **19**, 864 (1965).
- [164] C. Payen, H. Mutka, J. Soubeyroux, P. Molinié, and P. Colombet, *Journal of Magnetism and Magnetic Materials* **104-107**, 797 (1992).
- [165] C. Payen, P. Molinie, P. Colombet, and G. Fillion, *Journal of Magnetism and Magnetic Materials* **84**, 95 (1990).
- [166] T. Smith and S. A. Friedberg, *Physical Review* **176**, 660 (1968).
- [167] H. Mutka, C. Payen, and P. Molinié, *Journal of Magnetism and Magnetic Materials* **140-144**, 1677 (1995).
- [168] A. Pfitzner and S. Reiser, *Zeitschrift für Kristallographie - Crystalline Materials* **217**, 51 (2002).
- [169] P. Toffoli, P. Khodadad, and N. Rodier, *Acta Crystallographica Section B* **33**, 285 (1977).
- [170] M. Widenmeyer, E. Meissner, A. Senyshyn, and R. Niewa, *Zeitschrift für anorganische und allgemeine Chemie* **640**, 2801 (2014).
- [171] E. J. Sonneveld and J. W. Visser, *Journal of Applied Crystallography* **8**, 1 (1975).
- [172] Y. Mathey, H. Mercier, A. Michalowicz, and A. Leblanc, *Journal of Physics and Chemistry of Solids* **46**, 1025 (1985).
- [173] Y. Lai, Z. Song, Y. Wan, M. Xue, C. Wang, Y. Ye, L. Dai, Z. Zhang, W. Yang, H. Du, and J. Yang, *Nanoscale* **11**, 5163 (2019).
- [174] E. Sandre, V. Carteaux, and G. Ouvard, *Comptes Rendus de l'Académie des Sciences Paris* **314**, 1151 (1992).
- [175] G. Ouvrard, E. Sandre, and R. Brec, *Journal of Solid State Chemistry* **73**, 27 (1988).
- [176] T. Suriwong, K. Kurosaki, and S. Thongtem, *Journal of Alloys and Compounds* **735**, 75 (2018).
- [177] R. Lefèvre, D. Berthebaud, O. Lebedev, O. Pérez, C. Castro, S. Gascoin, D. Chateigner, and F. Gascoin, *Journal of Materials Chemistry A* **5**, 19406 (2017).
- [178] H. Ji, R. A. Stokes, L. D. Alegria, E. C. Blomberg, M. A. Tanatar, A. Reijnders, L. M. Schoop, T. Liang, R. Prozorov, K. S. Burch, N. P. Ong, J. R. Petta, and R. J. Cava, *Journal of Applied Physics* **114**, 114907 (2013).
- [179] J. Zeisner, A. Alfonsov, S. Selter, S. Aswartham, M. P. Ghimire, M. Richter, J. van den Brink, B. Büchner, and V. Kataev, *Physical Review B* **99**, 165109 (2019).

- [180] S. Selter, G. Bastien, A. U. B. Wolter, S. Aswartham, and B. Büchner, *Physical Review B* **101**, 014440 (2020).
- [181] X. Zhang, Y. Zhao, Q. Song, S. Jia, J. Shi, and W. Han, *Japanese Journal of Applied Physics* **55**, 033001 (2016).
- [182] D. Yang, W. Yao, Q. Chen, K. Peng, P. Jiang, X. Lu, C. Uher, T. Yang, G. Wang, and X. Zhou, *Chemistry of Materials* **28**, 1611 (2016).
- [183] Y. Liu and C. Petrovic, *Physical Review B* **96**, 054406 (2017).
- [184] G. T. Lin, H. L. Zhuang, X. Luo, B. J. Liu, F. C. Chen, J. Yan, Y. Sun, J. Zhou, W. J. Lu, P. Tong, Z. G. Sheng, Z. Qu, W. H. Song, X. B. Zhu, and Y. P. Sun, *Physical Review B* **95**, 245212 (2017).
- [185] D. C. Cronmeyer, *Journal of Applied Physics* **70**, 2911 (1991).
- [186] L. D. Jennings and W. N. Hansen, *Physical Review* **139**, A1694 (1965).
- [187] T. Lancaster, S. J. Blundell, M. L. Brooks, P. J. Baker, F. L. Pratt, J. L. Manson, M. M. Conner, F. Xiao, C. P. Landee, F. A. Chaves, S. Soriano, M. A. Novak, T. P. Papageorgiou, A. D. Bianchi, T. Herrmannsdörfer, J. Wosnitza, and J. A. Schlueter, *Physical Review B* **75**, 094421 (2007).
- [188] C. Zener, *Physical Review* **96**, 1335 (1954).
- [189] H. Callen and E. Callen, *Journal of Physics and Chemistry of Solids* **27**, 1271 (1966).
- [190] W. J. Carr, *Physical Review* **109**, 1971 (1958).
- [191] D. P. Pappas, *Journal of Vacuum Science & Technology B* **14**, 3203 (1996).
- [192] B. K. Chatterjee, C. K. Ghosh, and K. K. Chattopadhyay, *Journal of Applied Physics* **116**, 153904 (2014).
- [193] S. Khan, C. W. Zollitsch, D. M. Arroo, H. Cheng, I. Verzhbitskiy, A. Sud, Y. P. Feng, G. Eda, and H. Kurebayashi, *Physical Review B* **100**, 134437 (2019).
- [194] F. Hardy, D. Aoki, C. Meingast, P. Schweiss, P. Burger, H. v. Löhneysen, and J. Flouquet, *Physical Review B* **83**, 195107 (2011).
- [195] F. Lévy, I. Sheikin, B. Grenier, and A. D. Huxley, *Science* **309**, 1343 (2005).
- [196] H. Kotegawa, K. Fukumoto, T. Toyama, H. Tou, H. Harima, A. Harada, Y. Kitaoka, Y. Haga, E. Yamamoto, Y. Ōnuki, K. M. Itoh, and E. E. Haller, *Journal of the Physical Society of Japan* **84**, 054710 (2015).
- [197] V. P. Mineev, *Physical Review B* **83**, 064515 (2011).
- [198] A. Pankrats, K. Sablina, M. Eremin, A. Balaev, M. Kolkov, V. Tugarinov, and A. Bovina, *Journal of Magnetism and Magnetic Materials* **414**, 82 (2016).
- [199] W. Liu, Y. Dai, Y.-E. Yang, J. Fan, L. Pi, L. Zhang, and Y. Zhang, *Physical Review B* **98**, 214420 (2018).
- [200] B. Liu, Y. Zou, L. Zhang, S. Zhou, Z. Wang, W. Wang, Z. Qu, and Y. Zhang, *Scientific Reports* **6**, 33873 (2016).
- [201] Y. Liu and C. Petrovic, *Physical Review B* **97**, 014420 (2018).
- [202] A. Arrott, *Physical Review* **108**, 1394 (1957).
- [203] B. K. Banerjee, *Physics Letters* **12**, 16 (1964).
- [204] A. Arrott and J. E. Noakes, *Physical Review Letters* **19**, 786 (1967).
- [205] A. K. Pramanik and A. Banerjee, *Physical Review B* **79**, 214426 (2009).

-
- [206] J. S. Kouvel and M. E. Fisher, *Physical Review* **136**, A1626 (1964).
- [207] B. Widom, *The Journal of Chemical Physics* **41**, 1633 (1964).
- [208] S. N. Kaul, *Journal of Magnetism and Magnetic Materials* **53**, 5 (1985).
- [209] J. C. L. Guillou and J. Zinn-Justin, *Physical Review B* **21**, 3976 (1980).
- [210] L. Zhang, D. Menzel, C. Jin, H. Du, M. Ge, C. Zhang, L. Pi, M. Tian, and Y. Zhang, *Physical Review B* **91**, 024403 (2015).
- [211] J. Fan, L. Ling, B. Hong, L. Zhang, L. Pi, and Y. Zhang, *Physical Review B* **81**, 144426 (2010).
- [212] J. Yang, Y. Lee, and Y. Li, *Physical Review B* **76**, 054442 (2007).
- [213] D. Kim, B. Revaz, B. L. Zink, F. Hellman, J. J. Rhyne, and J. F. Mitchell, *Physical Review Letters* **89**, 227202 (2002).
- [214] V. Carreaux, F. Moussa, and M. Spiesser, *Europhysics Letters (EPL)* **29**, 251 (1995).
- [215] R. E. Marsh, *Journal of Solid State Chemistry* **77**, 190 (1988).
- [216] M. I. Zargarova and M. M. Akperov, "Ge-In-Te Phase Diagram Liquidus Projection," in *ASM Alloy Phase Diagrams Database* (P. Villars (editor-in-chief), H. Okamoto and K. Cenzual (section editors), Materials Park, OH, 2016).
- [217] M. I. Zargarova and M. M. Akperov, *Inorganic Materials* **9**, 1012 (1973).
- [218] J. T. Ho and J. D. Litster, *Journal of Applied Physics* **40**, 1270 (1969).

List of Publications

- **S. Selter**, G. Bastien, A. U. B. Wolter, S. Aswartham and B. Büchner, '*Magnetic anisotropy and low-field magnetic phase diagram of the quasi-two-dimensional ferromagnet $\text{Cr}_2\text{Ge}_2\text{Te}_6$* ', Physical Review B **101**, 014440 (2020)
- J. Zeisner, A. Alfonsov, **S. Selter**, S. Aswartham, M. P. Ghimire, M. Richter, J. van den Brink, B. Büchner and V. Kataev, '*Magnetic anisotropy and spin-polarized two-dimensional electron gas in the van der Waals ferromagnet $\text{Cr}_2\text{Ge}_2\text{Te}_6$* ', Physical Review B **99**, 165109 (2019)
- T. Sakurai, B. Ruprecht, L. T. Corredor, R. Takehara, M. Yasutani, J. Zeisner, A. Alfonsov, **S. Selter**, S. Aswartham, A. U. B. Wolter, B. Büchner, H. Ohta and V. Kataev, '*Pressure control of the magnetic anisotropy of the quasi-two-dimensional van der Waals ferromagnet $\text{Cr}_2\text{Ge}_2\text{Te}_6$* ', Physical Review B **103**, 024404 (2021)
- A. P. Dioguardi, **S. Selter**, U. Peeck, S. Aswartham, M.-I. Sturza, R. Murugesan, M. S. El-deeb, L. Hozoi, B. Büchner and H.-J. Grafe, '*Quasi-two-dimensional magnetic correlations in $\text{Ni}_2\text{P}_2\text{S}_6$ probed by ^{31}P NMR*', Physical Review B **102**, 064429 (2020)
- **S. Selter**, F. Scaravaggi, R. Kappenberger, M. Naumann, V. V. Romaka, M. Knupfer, S. Aswartham, A. U. B. Wolter, S. Wurmehl and B. Büchner, '*Evolution of Structure and Electronic Correlations in a Series of BaT_2As_2 ($T = \text{Cr-Cu}$) Single Crystals*', Inorganic Chemistry **59**, 16913 (2020)
- R. Hussain, G. Prando, **S. Selter**, S. Aswartham, B. Büchner and P. Carretta, '*Magnetically-induced local lattice anomalies and low-frequency nematic fluctuations in the Mott insulator $\text{La}_2\text{O}_3\text{Fe}_2\text{Se}_2$* ', *arXiv:2010.00968* (2020) (submitted to Physical Review Letters)

Acknowledgements

First and foremost, I want to express my deep gratitude to Prof. Bernd Büchner for giving me the opportunity to work on this interesting topic under excellent scientific conditions at the Institute for Solid State Research at the Leibniz IFW Dresden. Furthermore, I thank him for acting as first examiner for my doctoral thesis.

I am sincerely thankful to Jun.-Prof. Anna Isaeva for her willingness to become the second examiner for my doctoral thesis.

I deeply thank Saicharan Aswartham, group leader of the 'Materials Development Group' at the Leibniz IFW Dresden, for the supervision of my scientific work and the plentiful ideas for new compounds to synthesize, grow and investigate.

My sincere gratitude for financial support goes to Prof. Hans-Henning Klauß as representative of the graduate academy GRK-1621 of the *deutsche Forschungsgemeinschaft* (DFG). Beyond that, I am thankful to the GRK-1621 and its fellows for the extensive scientific exchange and interesting discussions in the framework of the seminars of the graduate academy.

I thank my colleagues of the 'Materials Development Group' at the Leibniz IFW Dresden, namely Mihai-Ionut Sturza, Grigory Shipunov and Yuliia Shemerliuk, as well as the former members of the group, B. Roman Piening and Tamara Holub, for the pleasant working atmosphere and for plenty of helpful scientific discussions. To Mihai-Ionut Sturza, I want to express special thanks for the conduction of the single crystal X-ray diffraction experiments and the useful discussions regarding the structural refinement process. Furthermore, I want to express my sincere gratitude to Grigory Shipunov for his scientific and personal advises and his resilience with my naive questions, especially on crystallography and diffractometry.

Beyond that, my thanks are addressed to all members of the 'Synthesis and Crystal Growth Research Team' at the Leibniz IFW Dresden. Especially, I want to deeply thank Sabine Wurmehl and Silvia Seiro for scientific and personal advises and that their doors were always open for discussions. Furthermore, I want to thank the technical staff of this research team, namely Robert Kluge, Rowena Wachtel, Sabine Müller-Litvanyi, Jochen Werner and Christian G. F. Blum, as well as the former staff member Dietmar Meiler for running the laboratories and scientific devices as well as for their support of my work. Especially, I want to thank Robert Kluge for conducting the solid state synthesis experiments for the substitution series $(\text{Ag}_{1-x}\text{Cu}_x)\text{CrP}_2\text{S}_6$ as well as for several SEM and EDX investigations on short notice. Also, I want to separately express my deep gratitude to Christian G. F. Blum for sharing his vast knowledge on crystal growth, inorganic chemistry and diffractometry with me and for

all the helpful discussions which have been the foundation for several investigations that are presented in this doctoral thesis.

I express my gratitude to Gaël Bastien, Bastian Rubrecht, Laura T. Corredor and Anja U. B. Wolter of the 'Thermodynamics Group' as well as Julian Zeisner, Alexey Alfonsov and Vladislav Kataev of the 'Electron Spin Resonance Group' of the Leibniz IFW Dresden for the pleasant and productive collaborations regarding the investigation of the magnetic properties of $\text{Cr}_2\text{Ge}_2\text{Te}_6$. Especially, I want to thank Julian Zeisner and Alexey Alfonsov for all the exceptionally helpful scientific discussions on magnetism in general and its interplay with crystal structures.

Furthermore, I am grateful to Adam P. Dioguardi, Ulrich Peeck and Hans-Joachim Grafe of the 'Nuclear Magnetic Resonance Group' of the Leibniz IFW Dresden for the excellent joint work regarding $\text{Ni}_2\text{P}_2\text{S}_6$ and other $M_2\text{P}_2\text{S}_6$ compounds. Also, I want to thank Adam P. Dioguardi for all the scientific and non-scientific discussions and his positive and uplifting attitude.

For the access to devices at the Leibniz IFW Dresden, I want to acknowledge Anja U. B. Wolter from the Institute for Solid State Research (magnetometers) as well as Daria Mikhailova and Lars Giebeler from the Institute for Complex Materials (STOE STADI powder X-ray diffractometers). Furthermore, I thank Prof. Jochen Geck from the TU Dresden for access to the single crystal diffractometer. In this course, I also want to thank all colleagues who maintained and serviced the devices and helped me with technical support, especially Sebastian Gaß. In addition, I am grateful to Ivan Kaban and Brigit Opitz from the Institute for Complex Materials of the Leibniz IFW Dresden for conducting the powder X-ray diffraction measurement of $\text{Ni}_2\text{P}_2\text{S}_6$ in reflection geometry.

Furthermore, I want to thank all my fellow PhD students, who contributed to the nice and friendly working atmosphere at the Leibniz IFW. Especially, I will remember the countless scientific and non-scientific discussions during coffee breaks and social gatherings like the PhD seminars, IFW summer schools, *et cetera*.

Special thanks are attributed to my parents and my sister, who supported me during my bachelor and master studies and afterwards during my time at the Leibniz IFW. Without them, my studies would not been possible, which I sincerely acknowledge.

Finally, I thank my girlfriend, Patrizia Fritsch, for bearing with me during all the ups and downs in my time as PhD student and, especially, during the period of writing this thesis. Her resilient support and encouragement as well as her caring attitude contributed greatly to the successful completion of this work. Beyond that, she did not only provide invaluable support to me as a partner, but also aided my doctoral work with innumerable scientific discussions as a colleague over the last years, for which I cannot be grateful enough.

Eidesstattliche Erklärung

Hiermit versichere ich, dass ich die vorliegende Arbeit unter der wissenschaftlichen Betreuung von Herrn Prof. Dr. Bernd Büchner sowie Herrn Dr. Saicharan Aswartham am Institut für Festkörperforschung des Instituts für Festkörper- und Werkstoffforschung, Leibniz IFW Dresden ohne unzulässige Hilfe Dritter und ohne Benutzung anderer als der angegebenen Hilfsmittel angefertigt habe; die aus fremden Quellen direkt oder indirekt übernommenen Gedanken sind als solche kenntlich gemacht.

Die Arbeit wurde bisher weder im Inland noch im Ausland in gleicher oder ähnlicher Form einer anderen Prüfungsbehörde vorgelegt. Es haben keine früheren erfolglosen Promotionsverfahren stattgefunden.

Ich erkenne die Promotionsordnung des Bereichs Mathematik und Naturwissenschaften der Technischen Universität Dresden vom 23.02.2011 an.

Sebastian Selter

Dresden, January 2021

A. Appendix

A.1. Scanning Electron Microscopic Images

A.1.1. $(\text{Fe}_{1-x}\text{Ni}_x)_2\text{P}_2\text{S}_6$

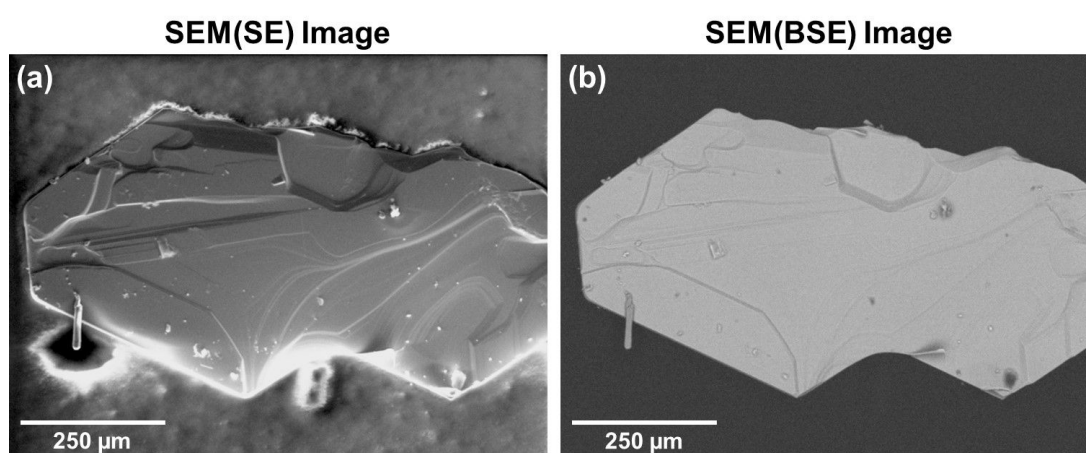


Fig. A.1.: Electron microscopy images of a $\text{Fe}_2\text{P}_2\text{S}_6$ crystal in topographic mode (SE detector) in (a) and in chemical contrast mode (BSE detector) in (b).

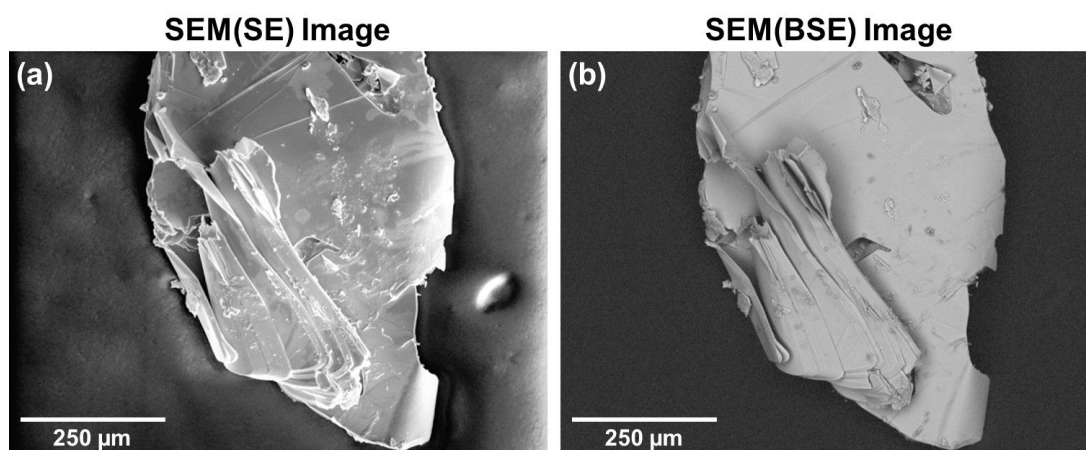


Fig. A.2.: Electron microscopy images of a $(\text{Fe}_{0.5}\text{Ni}_{0.5})_2\text{P}_2\text{S}_6$ crystal in topographic mode (SE detector) in (a) and in chemical contrast mode (BSE detector) in (b).

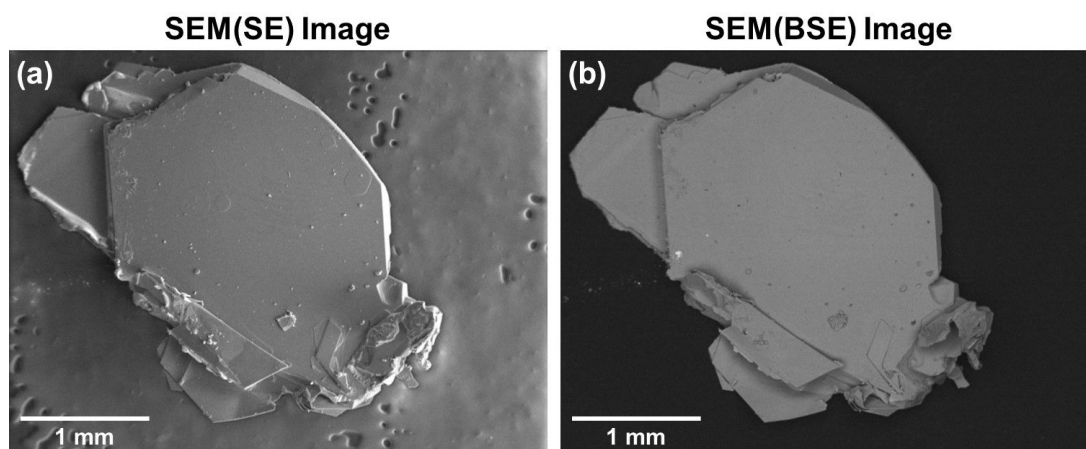


Fig. A.3.: Electron microscopy images of a $(\text{Fe}_{0.3}\text{Ni}_{0.7})_2\text{P}_2\text{S}_6$ crystal in topographic mode (SE detector) in (a) and in chemical contrast mode (BSE detector) in (b).

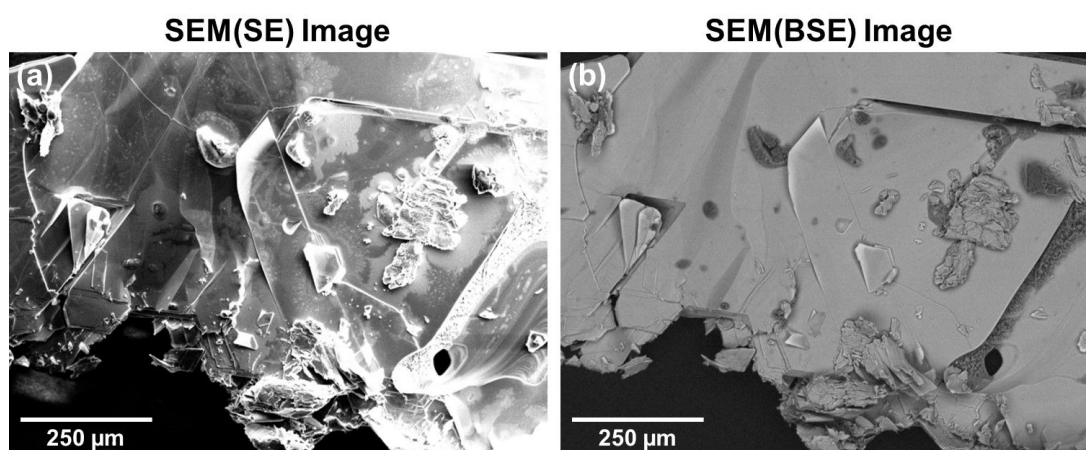


Fig. A.4.: Electron microscopy images of a $(\text{Fe}_{0.1}\text{Ni}_{0.9})_2\text{P}_2\text{S}_6$ crystal in topographic mode (SE detector) in (a) and in chemical contrast mode (BSE detector) in (b).

A.2. scXRD

A.2.1. $(\text{Fe}_{1-x}\text{Ni}_x)_2\text{P}_2\text{S}_6$ **Table A.1.:** Summary of crystallographic data and structural refinement for $(\text{Fe}_{1-x}\text{Ni}_x)_2\text{P}_2\text{S}_6$ with $x = 0, 0.3, 0.5, 0.7, 0.9, 1$ from scXRD at 293(2) K.

x_{nom}	0.0	0.3	0.5	0.7	0.9	1
<i>Experiment & Data Collection</i>						
Temperature (K)	293(2)					
Radiation Type & Wavelength (Å)	Mo-K α_1 ; 0.71073					
θ_{min} (°)	3.18	3.20	3.20	3.20	3.20	3.22
θ_{max} (°)	36.33	45.68	41.99	41.55	41.65	43.23
Completeness to θ (%)	100	100	100	99.7	99.7	100
	($\theta = 25.24^\circ$)	($\theta = 25.24^\circ$)	($\theta = 25.24^\circ$)	($\theta = 25.24^\circ$)	($\theta = 25.24^\circ$)	($\theta = 26.64^\circ$)
Reflections Collected	3833	15048	14173	12380	10948	19885
Independent Reflections	994	1615	1321	1313	1216	1438
R_{int} (%)	2.29	4.71	6.33	4.62	4.84	4.47
Index Ranges	$-9 \leq h \leq 9$ $-15 \leq k \leq 17$ $-11 \leq l \leq 11$	$-10 \leq h \leq 11$ $-20 \leq k \leq 20$ $-13 \leq l \leq 13$	$-11 \leq h \leq 11$ $-18 \leq k \leq 16$ $-12 \leq l \leq 12$	$-10 \leq h \leq 10$ $-18 \leq k \leq 17$ $-12 \leq l \leq 12$	$-9 \leq h \leq 9$ $-18 \leq k \leq 18$ $-11 \leq l \leq 12$	$-11 \leq h \leq 11$ $-19 \leq k \leq 19$ $-12 \leq l \leq 12$
$F(000)$	355	356	364	359	362	362
Absorption Coefficient (mm^{-1})	5.604	6.306	6.363	6.541	6.827	7.075
<i>Crystal Data</i>						
Crystal System	monoclinic					
Space Group	$C2/m$ (No. 12)					
a (Å)	5.9345(10)	5.8544(2)	5.8602(2)	5.8671(2)	5.8481(3)	5.8165(7)
b (Å)	10.2942(17)	10.1487(2)	10.1497(4)	10.1658(3)	10.1219(3)	10.0737(12)
c (Å)	6.7092(11)	6.6563(2)	6.6518(2)	6.6663(2)	6.6534(3)	6.6213(8)
β (°)	107.069(11)	107.139(4)	107.069(3)	107.086(3)	107.127(6)	107.110(6)
Volume (Å ³)	391.82(11)	377.92(2)	378.22(2)	380.06(2)	376.38(3)	370.80(10)
Empirical Formula	$\text{Fe}_{2.00}\text{P}_{1.97}\text{S}_6$	$\text{Fe}_{1.45}\text{Ni}_{0.62}\text{P}_{1.98}\text{S}_6$	$\text{Fe}_{0.99}\text{Ni}_{0.99}\text{P}_{2.00}\text{S}_6$	$\text{Fe}_{0.60}\text{Ni}_{1.39}\text{P}_{1.96}\text{S}_6$	$\text{Fe}_{0.20}\text{Ni}_{1.78}\text{P}_{2.00}\text{S}_6$	$\text{Ni}_{2.00}\text{P}_{1.96}\text{S}_6$
Formula Weight (g mol^{-1})	365.0	371.4	367.8	368.5	370.0	370.2
Z	2	2	2	2	2	2
Density (Calculated) (g cm^{-3})	3.094	3.264	3.230	3.220	3.265	3.315
Site Disorder Ratio r_{disorder} (%)	6	0 (fixed)	2	14	2	4
<i>Refinement</i>						
Method	Full-matrix least squares on F^2					
Data / Restraints / Parameters	994 / 0 / 44	1615 / 0 / 30	1321 / 0 / 34	1313 / 0 / 46	1216 / 0 / 45	1438 / 0 / 45
Goodness-Of-Fit	1.13	2.30	1.61	2.55	1.93	1.28
R_{obs} (%)	1.70	2.32	3.50	2.67	2.93	2.17
wR_{obs} (%)	4.07	6.16	8.48	7.49	6.65	4.64
R_{all} (%)	2.52	2.53	4.21	3.22	4.10	2.97
wR_{all} (%)	4.37	6.21	8.75	7.61	6.82	4.87
Largest Diff. Peak and Hole (e \AA^{-3})	0.36 and -0.25	0.88 and -1.07	2.04 and -1.60	1.17 and -0.75	1.22 and -1.09	1.07 and -0.87

Table A.2.: Fractional atomic coordinates, occupancies and equivalent isotropic displacement parameters U_{eq} of $(\text{Fe}_{1-x}\text{Ni}_x)_2\text{P}_2\text{S}_6$ at 293(2) K with estimated standard deviations in parentheses.

Label	Type	Wyck	x	y	z	Occ (%)	U_{eq} ($\times 10^{-3}\text{\AA}^2$)
$\text{Fe}_2\text{P}_2\text{S}_6$							
Fe1	Fe	4g	0	0.3326(1)	0	94(1)	14(1)
P1	P	4i	0.0565(1)	0	0.1696(1)	89(1)	7(1)
S1	S	4i	0.7503(1)	0	0.2471(1)	100	10(1)
S2	S	8j	0.2482(1)	0.1659(1)	2483(1)	100	11(1)
Fe2	Fe	2a	0	0	0	11(1)	20(1)
P2	P	8j	0.0594(10)	0.3328(6)	0.1719(10)	5(1)	16(2)
$(\text{Fe}_{0.7}\text{Ni}_{0.3})_2\text{P}_2\text{S}_6$							
Fe1	Fe	4g	0	0.3328(1)	0	73(1)	16(1)
Ni1	Ni	4g	0	0.3328(1)	0	31(1)	16(1)
P1	P	4i	0.0575(1)	0	0.1699(4)	99(1)	13(1)
S1	S	4i	0.7446(1)	0	0.2445	100	15(1)
S2	S	8j	0.2507	0.1686(1)	0.2451(1)	100	15(1)
Fe2	Fe	2a	-	-	-	-	-
Ni2	Ni	2a	-	-	-	-	-
P2	P	8j	-	-	-	-	-
$(\text{Fe}_{0.5}\text{Ni}_{0.5})_2\text{P}_2\text{S}_6$							
Fe1	Fe	4g	0	0.3328(1)	0	49(1)	14(1)
Ni1	Ni	4g	0	0.3328(1)	0	49(1)	14(1)
P1	P	4i	0.0571(1)	0	0.1698(1)	97(1)	10(1)
S1	S	4i	0.7463(1)	0	0.2452(1)	100	13(1)
S2	S	8j	0.2499(1)	0.1677(1)	0.2461(1)	100	13(1)
Fe2	Fe	2a	0	0	0	2(1)	14(1)
Ni2	Ni	2a	0	0	0	2(1)	14(1)
P2	P	8j	0.0590(40)	0.3350(30)	0.1730(40)	1	10(1)
$(\text{Fe}_{0.3}\text{Ni}_{0.7})_2\text{P}_2\text{S}_6$							
Fe1	Fe	4g	0	0.3330(1)	0	26(1)	11(1)
Ni1	Ni	4g	0	0.3330(1)	0	60(1)	11(1)
P1	P	4i	0.0572(1)	0	0.1697(1)	75(1)	8(1)
S1	S	4i	0.7460(1)	0	0.2447(1)	100	11(1)
S2	S	8j	0.2498(1)	0.1678(1)	0.2453(1)	100	11(1)
Fe2	Fe	2a	0	0	0	8(1)	19(1)
Ni2	Ni	2a	0	0	0	19(1)	19(1)
P2	P	8j	0.0567(4)	0.3335(2)	0.1713(4)	12(1)	11(1)
$(\text{Fe}_{0.1}\text{Ni}_{0.9})_2\text{P}_2\text{S}_6$							
Fe1	Fe	4g	0	0.3329(1)	0	10(1)	12(1)
Ni1	Ni	4g	0	0.3329(1)	0	87(1)	12(1)
P1	P	4i	0.0577(1)	0	0.1702(1)	96(1)	9(1)
S1	S	4i	0.7428(1)	0	0.2436(1)	100	12(1)
S2	S	8j	0.2514(1)	0.1696(1)	0.2440(1)	100	12(1)
Fe2	Fe	2a	0	0	0	0(1)	20(4)
Ni2	Ni	2a	0	0	0	4(1)	20(4)
P2	P	8j	0.0570(70)	0.3320(30)	0.1690(50)	2(1)	40(13)
$\text{Ni}_2\text{P}_2\text{S}_6$							
Ni1	Ni	4g	0	0.3331(1)	0	96(1)	9(1)
P1	P	4i	0.0578(1)	0	0.1702(1)	91(1)	7(1)
S1	S	4i	0.7421(1)	0	0.2432(1)	100	9(1)
S2	S	8j	0.2517(1)	0.1698(1)	0.2433(1)	100	9(1)
Ni2	Ni	2a	0	0	0	8(1)	9(1)
P2	P	8j	0.0574(10)	0.3329(6)	0.1734(9)	3(1)	7(1)

Table A.3.: Anisotropic displacement parameters U_{ij} for $(\text{Fe}_{1-x}\text{Ni}_x)_2\text{P}_2\text{S}_6$ at 293(2) K with estimated standard deviations in parentheses.

Label	Type	U_{11}	U_{22}	U_{33}	U_{12}	U_{13}	U_{23}
($\times 10^{-3} \text{\AA}^2$)							
$\text{Fe}_2\text{P}_2\text{S}_6$							
Fe1	Fe	12(1)	12(1)	17(1)	0	5(1)	0
P1	P	6(1)	6(1)	10(1)	0	4(1)	0
S1	S	9(1)	10(1)	13(1)	0	5(1)	0
S2	S	10(1)	9(1)	14(1)	-2(1)	4(1)	-1(1)
Fe2	Fe	20(2)	20(2)	22(2)	0	6(1)	0
P2	P	11(3)	15(3)	19(3)	1(2)	1(2)	-1(2)
$(\text{Fe}_{0.7}\text{Ni}_{0.3})_2\text{P}_2\text{S}_6$							
Fe1	Fe	15(1)	15(1)	20(7)	0	6(1)	0
Ni1	Ni	15(1)	15(1)	20(7)	0	6(1)	0
P1	P	12(1)	12(1)	15(1)	0	5(1)	0
S1	S	14(1)	15(1)	18(1)	0	7(1)	0
S2	S	14(1)	14(1)	18(1)	-2(1)	4(1)	-2(1)
Fe2	Fe	-	-	-	-	-	-
Ni2	Ni	-	-	-	-	-	-
P2	P	-	-	-	-	-	-
$(\text{Fe}_{0.5}\text{Ni}_{0.5})_2\text{P}_2\text{S}_6$							
Fe1	Fe	10(1)	14(1)	18(1)	0	5(1)	0
Ni1	Ni	10(1)	14(1)	18(1)	0	5(1)	0
P1	P	7(1)	10(1)	14(1)	0	4(1)	0
S1	S	9(1)	14(1)	16(1)	0	6(1)	0
S2	S	9(1)	13(1)	16(1)	-2(1)	3(1)	-2(1)
Fe2	Fe	10(1)	14(1)	18(1)	0	5(1)	0
Ni2	Ni	10(1)	14(1)	18(1)	0	5(1)	0
P2	P	7(1)	10(1)	14(1)	0	4(1)	0
$(\text{Fe}_{0.3}\text{Ni}_{0.7})_2\text{P}_2\text{S}_6$							
Fe1	Fe	9(1)	10(1)	16(1)	0	5(1)	0
Ni1	Ni	9(1)	10(1)	16(1)	0	5(1)	0
P1	P	6(1)	7(1)	12(1)	0	4(1)	0
S1	S	9(1)	11(1)	15(1)	0	6(1)	0
S2	S	10(1)	10(1)	15(1)	-1(1)	4(1)	-1(1)
Fe2	Fe	18(1)	13(1)	24(1)	0	7(1)	0
Ni2	Ni	18(1)	13(1)	24(1)	0	7(1)	0
P2	P	11(1)	7(1)	15(2)	0(1)	4(1)	0(1)
$(\text{Fe}_{0.1}\text{Ni}_{0.9})_2\text{P}_2\text{S}_6$							
Fe1	Fe	11(1)	7(1)	18(1)	0	6(1)	0
Ni1	Ni	11(1)	7(1)	18(1)	0	6(1)	0
P1	P	9(1)	5(1)	14(1)	0	4(1)	0
S1	S	11(1)	9(1)	17(1)	0	6(1)	0
S2	S	12(1)	7(1)	17(1)	-1(1)	4(1)	-1(1)
Fe2	Fe	10(5)	35(7)	14(6)	0	1(4)	0
Ni2	Ni	10(5)	35(7)	14(6)	0	1(4)	0
P2	P	50(20)	25(14)	40(20)	9(11)	16(17)	1(10)
$\text{Ni}_2\text{P}_2\text{S}_6$							
Ni1	Ni	8(1)	8(1)	13(1)	0	4(1)	0
P1	P	6(1)	6(1)	9(1)	0	3(1)	0
S1	S	8(1)	9(1)	11(1)	0	4(1)	0
S2	S	8(1)	7(1)	12(1)	-1(1)	3(1)	-1(1)
Ni2	Ni	11(1)	9(1)	16(1)	0	5(1)	0
P2	P	6(1)	6(1)	9(1)	0	3(1)	0